Physics Area - PhD course in AstroParticle Physics

SISSA, Trieste

Probing the regularization of spacetime singularities

Supervisor:
Stefano Liberati

Candidate:
Vania Vellucci

ACADEMIC YEAR 2023/2024

Actually, we are the white rabbit
being pulled out of the hat.
The only difference between us and the white
rabbit is that the rabbit does not realize it is
taking part in a magic trick. Unlike us.
We feel we are part of something mysterious
and we would like to know how it all works.
—— Jostein Gaarder

Acknowledgments

I would like to thank my collaborators, especially Julio Arrechea, Raùl Carballo Rubio, Edgardo Franzin, and Jacopo Mazza, without whom this work would not have been possible. I have learned so much from each of you, and I am proud of what we have been able to understand together. In particular, I am extremely grateful to my supervisor Stefano Liberati for guiding me on this journey, always finding the right words, the right coordinate system, the right paper. The hours spent discussing physics, time, and life have allowed me to grow tremendously both scientifically and personally.

I would also like to thank all the wonderful people who have accompanied me on this journey at SISSA. I won't list all the names because, fortunately, there are so many of you. It is said that difficulties bring people together, and we have faced so much life together: curfews, QFT exercises, grappa Luigia, Bora, first hard-won publications, skiing injuries, the longest train in the largest seaside square in Europe, Barcolane and Barcollande. You are the thing I will miss most about Trieste, and I hope that one day our paths will cross again. Among all, a special thanks to Diego for the kindness, support, and love you continue to give me every day, even during the toughest times. Meeting you made me realize that talent and competence do not necessarily come with overconfidence and arrogance. I must also thank Max for always managing to create that atmosphere of joy and companionship in my daily life, even during our "domeniche tristine", and for teaching me to appreciate the joys and pains of living away from home.

During these years, I have not lost the support of my lifelong friends, to whom I owe a huge thank you. In particular, a thanks to Elsa and Gessica, and to Giorgia who welcomed me to Trieste in the first months, bringing a bit of home, a bit of Gaeta, here as well. And then, no thanks would be enough for my Iole and my sister Giorgia, despite the geographical distance, I feel like I have carried you both with me throughout this adventure. At every obstacle, pain, or achievement, those two WhatsApp chats were always there.

A special thanks to my parents for the unconditional support you have continued to show me over the years and for transmitting me that love for culture and knowledge that is the driving force behind my studies and work.

Finally, even though she can no longer read it, I want to dedicate this work to my grandmother and to all the women and men who, like her, knew so little of this world. Her affection continues to stay with me today, and everything I have been able and will be able to study, learn, and see, I dedicate to her.

Ringraziamenti

Vorrei ringraziare i miei collaboratori, in particolare Julio Arrechea, Raùl Carballo Rubio, Edgardo Franzin e Jacopo Mazza, senza i quali questo lavoro non sarebbe stato possibile. Ho imparato tantissimo da ognuno di voi e sono fiera di ciò che siamo riusciti a capire insieme. In particolar modo, sono estremamente grata al mio supervisor Stefano Liberati per avermi guidata in questo percorso, trovando sempre le parole giuste, il sistema di coordinate giusto, l'articolo giusto. Le ore passate a discutere di fisica, di tempo, di vita passata e futura mi hanno permesso di crescere tantissimo scientificamente e personalmente.

Vorrei poi ringraziare tutte le persone meravigliose che mi hanno accompagnato in questo percorso in SISSA. Non riporterò tutti i nomi perchè per fortuna siete tantissimi. Si dice che le difficoltà uniscano le persone e noi abbiamo affrontato tanta vita insieme: coprifuoco, esercizi di QFT, grappa Luigia, Bora, prime sofferte pubblicazioni, infortuni sugli sci, il trenino più lungo nella piazza sul mare più grande d'europa, barcolane e barcollande. Siete la cosa che più mi mancherà di Trieste e spero che un giorno le nostre strade possano rincrociarsi. Tra tutti, un ringraziamento speciale a Diego per la gentilezza, il sostegno e l'amore che continui a darmi ogni giorno, anche nei momenti più difficili. Averti conosciuto mi ha permesso di capire che il talento e la competenza non sono necessariamente accompagnati da eccessiva sicurezza e arroganza. Non può poi mancare un ringraziamento a Max per essere sempre riuscito a creare quell'atmosfera di festa e di compagnia nella mia quotidianeità, addirittura durante le nostre domeniche tristine, e per avermi insegnato ad apprezzare le gioie e i dolori della vita fuorisede.

Durante questi anni non ho poi perso l'appoggio dei miei amici di sempre a cui non può mancare un enorme grazie. In particolar modo, un ringraziamento a Elsa, e Gessica e a Giorgia che mi ha accolto a Trieste nei primi mesi, portandomi un po di casa, un po di Gaeta anche qui. E poi qualsiasi ringraziamento non sarebbe abbastanza per la mia Iole e per mia sorella Giorgia, nonostante la distanza geografica mi sembra di avervi portate con me durante tutta questa avventura. ad ogni ostacolo, dolore o traguardo quelle due chat su whatsapp non potevano mancare.

Un ringraziamento speciale ai miei genitori, per il supporto incondizionato che avete continuato a mostrarmi in questi anni e per avermi trasmesso da sempre l'amore per la cultura e la conoscenza, motore primo dei miei studi e del mio lavoro.

Infine, anche se non può più leggerlo, voglio dedicare questo lavoro a mia nonna e a tutte le donne e gli uomini che come lei hanno potuto conoscere poco di questo mondo. Il suo affetto continua ad accompagnarmi oggi e tutto quello che ho potuto e potrò studiare, conoscere e vedere, lo dedico a lei.

Abstract

In General relativity (GR), the formation of spacetime singularities is proved to be inevitable in the gravitational collapse of very compact objects and in the early universe. These singularities are considered the sign of the breakdown of the theory and the proof of its intrinsic incompleteness. The common belief is that their formation will be prevented in a full, potentially quantum, completion of GR. In this view, it is reasonable to assume that non-singular, or regular, metrics can provide an effective description of the outcome of gravitational collapse and of the early universe, providing a valid alternative to the Big Bang and to singular black holes. This thesis covers various aspects of this theme.

Firstly we deal with a classification of the possible local regularization of spacetime singularities. Indeed, in recent years, a systematic, quantum gravity agnostic, study has been carried out to catalogue all the conceivable non-singular, continuous geometries arising from evading Penrose's focusing theorem in gravitational collapse. In this study, we extend this inquiry by systematically examining all potential non-singular, continuous extensions into the past of an expanding Friedmann–Lemaître–Robertson–Walker (FLRW) metric.

Subsequently, we discuss the construction of global regular metrics that embody the aforementioned possible local regularizations of black holes singularities. In particular, we present a new rotating regular black hole whose inner horizon has zero surface gravity for any value of the spin parameter, and is therefore stable against mass inflation.

Finally we study the phenomenological properties of these regular alternatives to singular black holes, to which we refer as black hole mimickers. Namely we investigate the gravitational waves signal generated by their merger, in particular their ringdown signal. This is characterized by a different spectrum of quasinormal modes (QNMs) with respect to singular black holes and, in the case of horizonless mimickers, by the appearance of echoes after the prompt ringdown, that is a series of secondary pulses with progressively smaller amplitudes. We compute this spectrum of QNMs enlightening a common misunderstanding regarding the study of gravitational perturbations in such regular spacetimes. We also investigate the effect of non-linear interactions on the echoes part of the signal and its sensitivity to the internal structure of the emitting object. In particular, we find that if one considers the increase of the central object mass due to the partial absorption of the energy carried by perturbations, the echo signal can be quite different and non-periodic. Furthermore, when gravitational perturbations are assumed to travel thorough the object instead of being reflected at the surface, the echoes signal appears to be very sensitive to the structure of the innermost region of the mimicker.

This research fits into the broader context of exploring alternatives to classical cosmological and black hole models, aiming to test new (quantum) physics beyond General Relativity in extreme density and curvature environments.

Contents

Acronyms

GR General relativity

GWs Gravitational waves

BH black hole

RBH regular black hole

SNR signal to noise ratio

QNMs quasinormal modes

NJP Newman-Janis procedure

SV Simpson-Visser

FLRW Friedmann–Lemaître–Robertson–Walker

ISCO innermost stable circular orbit

ADM Arnowitt–Deser–Misner

SET stress-energy tensor

RSET renormalized stress-energy tensor

ECO exotic compact object

PN Post Newtonian

Conventions: We use "geometrodynamics units" units in which $c = G = 1$. For this reason in Chapter 8 we also have for the Planck mass $M_p^2 = \hbar$. The signature of the metric is $(-,+,+,+)$. Spacetime indeces run from 0 to 3 and are denoted with Greek letters.

Publications

This thesis is based on the following list of publications:

Chapter 2: Raúl Carballo-Rubio, Stefano Liberati, Vania Vellucci. *Geodesically complete universes* [arXiv:2404.13112 [gr-qc]].

Chapter 4: Edgardo Franzin, Stefano Liberati, Jacopo Mazza and Vania Vellucci. *Stable rotating regular black holes* Phys.Rev.D 106 (2022) 10, 104060, [arXiv:2207.08864 [gr-qc]].

Chapter 6: Edgardo Franzin, Stefano Liberati, Vania Vellucci. *From regular black holes to horizonless objects: quasinormal modes, instabilities and spectroscopy* JCAP 01 (2024) 020 [arXiv:2310.11990 [gr-qc]].

Chapter 7: Vania Vellucci, Edgardo Franzin and Stefano Liberati. *Echoes from backreacting exotic compact objects.* Phys.Rev.D 107 (2023) 4, 044027, [arXiv:2205.14170 [gr-qc]].

Chapter 8: Julio Arrechea, Stefano Liberati, Vania Vellucci. *Whispers from the quantum core: the ringdown of semiclassical stars* [arXiv:2407.08807 [gr-qc]].

Part I

Introduction: the problem of singularities in General Relativity

Everything straight lies',
murmured the dwarf disdainfully.
'All truth is crooked,
time itself is a circle.
—— Friedrich Nietzsche

General Relativity as an incomplete theory

The gravitational force, albeit weaker then the other interactions, dominate our macroscopic world, keeping us grounded on Earth, building planets, galaxies and cosmic structures.

So, not surprisingly, among what we call fundamental interactions, gravity was the first to be formally studied, in the 17th century by Newton.

Despite this, in certain respects, a complete and deep understanding of gravity still remains the main challenge of contemporary physics. Indeed, even if the theory of General Relativity was developed over a century ago, its integration into a comprehensive quantum field theory, as achieved with other interactions, remains elusive.

Beside being non-renormalizabile as a quantum field theory, GR presents also several conceptual and observational issues. One of the main ones is certainly its intrinsic incompleteness. Indeed, GR predicts the formation of singularities in different physical scenarios. To understand why this implies incompleteness of the theory, we need to better investigate the concept of singularity.
One straightforward approach might be to define a singularity as a point where the metric becomes singular, failing to be adequately differentiable. This means that there must exist some local observable quantities (some curvature scalar) whose (position-dependent) value "blows up" in the vicinity of a certain point. However, this approach presents a challenge: we could simply remove these singular points and argue that the remaining manifold encompasses all of spacetime.

However, even though we exclude singular points from our definition of spacetime, we can still detect the "gaps" left behind by their removal through the presence of incomplete geodesics. Therefore, it appears logical to base our definition of spacetime singularities on the notion of geodesic incompleteness. A geodesic is defined incomplete if it cannot be extended beyond a finite value of the affine parameter, i.e. it is possible to reach the end of such geodesic at a finite value of its affine parameter. While the incompleteness of spacelike geodesics lacks specific physical significance given their unimportance in the theory of relativity, the incompleteness of timelike and null geodesics, that represents the trajectories of massive and massless particles, holds significant implications. It suggests the potential existence of particles whose trajectories cease to exist after (or before) a certain period of time, as measured by them. In essence, these particles would seemingly be annihilated or created at the singularity. Thus it is clear that geodesic incompleteness entails a loss of predictability of the theory.

These singularities appear in different solutions of the Einstein equations as the Schwarschild and Kerr metric describing respectively static and rotating black holes or the Friedmann-Lemaître-Robertson-Walker metric describing an homogeneous and isotropic universe. However the existence of singular solutions alone does not imply that these singularities really exist in nature. To really prove that GR is an incomplete theory failing to predict what happens at the center of a black hole and at the beginning of the universe we need to prove that the formation of these singularities is inevitable under generic assumptions. This proof resides in a series of singularity theorems, developed throughout the 1960s and '70s by Penrose and Hawking, which we will discuss in more detail in the next section.

Due to these theorems it is possible to conclude that in the framework of General Relativity singularities are both conceptually problematic and inevitably present in different physical scenario. For this reason, the idea that they represent the breakdown of GR and of our understanding of the gravitational interaction is largely diffused.

The common belief is that new (quantum) physics beyond General Relativity will definitely address the issues related to spacetime singularities.

In particular, considerable effort has been directed into investigating the hypothesis that this singularities regularization, even if realized through some unknown mechanisms beyond GR, can be captured effectively within the standard tools of differential geometry. Indeed, under this hypothesis, it is possible to construct and study regular effective models that serve as alternatives to singular black holes to describe the dark compact objects populating our universe.

These models, to which one usually refer as black hole mimickers, may exhibit horizons, and thus represent regular black holes, or they may lack horizons, in which case they are referred as horizonless compact objects. In both cases they are expected to present phenomenological differences with respect to singular models.

For these reason, the Gravitational waves (GWs) signal coming from the coalescences of compact objects could be a powerful tool to probe the regularization of spacetime singularities. Such observations could allow us to test the hypothesis that the merging compact objects are not singular GR black holes but rather some regular alternatives, and potentially they could even provide us some hints about any new (quantum) physics responsible for this regularization.

From the first GWs observed signal in 2015 [1], the three ground-based observatory LIGO, Virgo and KAGRA have detected more than 90 events, comprising the multimessenger event GW170817 [2–4], and they have now started the fourth observing run.

Other potentially useful observations could come from the electromagnetic emission of the matter surrounding these compact objects. Through the observation of this emission, the Event Horizon Telescope team succeeded in generating the first "image" of the supermassive black holes M87* [5–12] and Sgr A*, at the center of our galaxy [13–18].

So far, the accuracy of all these observations has not been sufficient to impose strict constraints on the nature of the dark compact objects sourcing them. However, future ground-based [19–24] and space-based [25–27] gravitational-wave detectors have been planned. These will reach higher signal to noise ratio (SNR) potentially leading to detection of new physics.

This thesis is inserted in such flourishing context. Its aim is to explore the theory and phenomenology of regular solutions, intended as tools for the investigation of new physics beyond General Relativity. We will start by reviewing the definite proof of GR incompleteness: the singularities theorems. From this, we will see how the introduction of new physics beyond General Relativity allows for the evasion of the theorems, the construction of regular alternative models and the study of their phenomenological signatures.

Singularity theorems

In this section, we review the assumptions and the main content of the first singularity theorem. Before entering in its precise statement, we will recall some important geometric concepts, useful in the study of the causal structure of a spacetime and thus central in the derivation of the singularity theorems, as well as in the search for possible ways to evade them, as we will see in Chapter 1 and Chapter 2.

The expansion parameter and the Raychaudhuri equations

The action of gravity on a multidimensional set of neighbouring timelike or null geodesics is described by the Raychaudhuri equations. Such set, to which we usually refer as a congruence, describe the trajectory of a bundle of photons or of a cloud of massive particles. For every geodesic of the congruence we can define a normalized tangent vector $u^\mu = \frac{dx^\mu}{d\lambda}$, such that $u^\mu u_\mu = 1$ (or $u^\mu u_\mu = 0$ for null congruences), and we shall assume that the geodesics are affinely parametrized $u^\mu \nabla_\mu u^\nu = 0$. The expansion of such congruence is defined as $\theta = \nabla_\mu u^\mu$ and it tells us how much our cloud of particle is expanding or contracting isotropically. Its evolution along the geodesic and affinely parametrized congruence is given by the Raychaudhuri equation:

$$\frac{d\theta}{d\lambda} = -\frac{\theta^2}{3} - \sigma_{\mu\nu}\sigma^{\mu\nu} + \omega_{\mu\nu}\omega^{\mu\nu} - R_{\mu\nu}u^\mu u^\nu \tag{0.0.1}$$

for time-like geodesics, and

$$\frac{d\theta}{d\lambda} = -\frac{\theta^2}{2} - \sigma_{\mu\nu}\sigma^{\mu\nu} + \omega_{\mu\nu}\omega^{\mu\nu} - R_{\mu\nu}u^\mu u^\nu \tag{0.0.2}$$

for null geodesics.

Here $\sigma_{\mu\nu}$ is the shear tensor that tells us how things get elongated or squashed along the congruence and $\omega_{\mu\nu}$ is the twist tensor describing the rotation of the particles of the cloud as they move forward along the congruence. They can be defined in terms of the gradient tensor $B_{\mu\nu} \equiv \nabla_\nu u_\mu$: the shear is its symmetric and traceless part, the twist is its antisymmetric part and the expansion is its trace. Also the evolution of the shear and of the twist along the congruence is given by the other two Raychaudhuri equations that we don't report here but can be found for instance in [28, 29].

Note that the expansion parameter we have denoted here can be seen exactly as the variation of the volume orthogonal to a given congruence. Thus it is given by:

$$\theta = \frac{1}{\delta V^{(3)}}\frac{\delta V^{(3)}}{\delta\lambda} \tag{0.0.3}$$

for timelike geodesics and

$$\theta = \frac{1}{\delta A^{(2)}}\frac{\delta A^{(2)}}{\delta\lambda} \tag{0.0.4}$$

for null geodesics (since the submainfold orthogonal to a null vector is two-dimensional).

Trapping surfaces and horizons

The expansion parameter that we just introduced allows us to define a new important local concept connected with the presence of horizons and singularities: future (past) closed trapped surfaces. These are closed spacelike surfaces such that their area tends to decrease locally along any possible future (past) direction.

We shall now explain more rigorously what does this mean in the case of future trapped surface, the definition of a past trapped surface is exactly dual.

If we draw the future-directed null geodesics orthogonal to a closed space-like two-surface (we draw the lightcones departing from each point of the surface), we see that all the vectors emanating from a certain point can be expressed as a linear combination of two future directed null vectors $V^{\mu}_{\pm}$. In flat spacetime, one of them is pointing inward toward the internal region delimited by the surface and we call it ingoing, while the other is pointing outward and we call it outgoing. The expansion of ingoing geodesic θ_{-} is always negative while in flat spacetime the expasion of outgoing geodesic θ_{+} is positive.

In strong gravity regimes, lightcones can tilt towards the interior of the two-surface in such a way that also θ_{+} is negative. In this case the surface will be trapped. Indeed, since time-like observers are forced to travel inside the light cones, if these cones become enough tilted, any timelike observer in the surface will be causally connected with a smaller region in the future, in other worlds it will not be able to exit (to escape) the region delimited by the two-surface.

Summirizing, a closed trapped surface is a *closed, spacelike, two-surface such that both ingoing and outgoing geodesics are converging (have negative expasion).* The limit case in which $\theta_{+} = 0$, is called a marginally trapped surface.

The set of all the points on a three-surface Σ through which a trapped surface passes is called *trapped region.* The boundary of a trapped region is an *apparent horizon*, thus it is an outer marginally trapped surface. The extension of an apparent horizon towards the past and the future of Σ is a three dimensional surface called the trapping horizon of the spacetime.

For a stationary black hole, the apparent horizon coincides with the event horizon but in general they are two different concepts, as instance, during a collapse, the apparent horizon is always included inside the event horizon. Indeed, the event horizon is defined as the border of the region that is not causally connected with future null infinity and thus is a global notion, in order to define it we need to know a priori what is the infinite future evolution of our spacetime.

Contrary, the apparent horizon is a local notion, and as such in principle observable. In practice, the apparent horizon is the boundary of a region through which at some time anything cannot escape from, the event horizon is the boundary of a region through which at any time anything cannot escape from.

Global hyperbolicity

The first singularity theorem rely on a quite strong but physically justified assumption about the causal structure of the spacetime: global hyperbolicity. Let S be a closed, achronal set. We define the future (past) domain of dependence of S as the set of all points p such that every past (future) inextendible causal curve through p intersects S. The full

domain of dependence of S, is the union of the past and future domain of dependence.

A closed achronal set for which the full domain of dependence covers all the mainfold is called a Cauchy hypersurface. A spacetime that admits a Cauchy hypersurface is said to be globally hyperbolic. The complete history of causal observers is predictable in a global hyperbolic spacetime given appropriate initial data on the Cauchy hypersurface. In a generic spacetime, there might be limits to the Cauchy evolution: these are called Cauchy horizons. If a spacetime is not globally hyperbolic, the full domain of dependence of each surface will be limited and will not cover all the mainfold, in this case the boundary of the full domain of dependence is a Cauchy horizon. As we will see in Section 3.4.1, Cauchy horizons are expected to be unstable because of a phenomena called mass inflation. For this reason it is usually believed that all physical spacetime are actually global hyperbolic.

The Penrose theorem

We are now ready to discuss the first singularity theorem developed by Penrose in the original paper [30].

According to this theorem, a spacetime $(M, g_{\mu\nu})$ cannot be null geodesically complete if:

- The "null convergence condition", $R_{ab}k^a k^b \geqslant 0 \ \forall$ null vector k^a, holds. This implies in GR the null energy condition, i.e. the energy density measured along any null curve must be non-negative.
- The manifold is a time orientable, globally hyperbolic spacetime, $\mathcal{M} = R \times \Sigma^3$ admitting a non-compact Cauchy hypersurface.
- At some point, a closed trapped surface $\mathcal{T}^2$ forms.

The proof of the theorem then proceeds in two steps. The first one consists in showing that an initial negative expansion (on the trapped surface) and the null convergence condition are enough to prove, via the Raychaudhuri equation, that the expansion will become infinitely negative in the future for some finite value of the affine parameter of a null congruence orthogonal to $\mathcal{T}^2$. This point at which the expansion goes to $-\infty$ is called focusing point. The second step consisted in a ingenious use of topological arguments to prove that assuming the regularity of the focusing point is incompatible with the presence of a non-compact Cauchy hypersurface.

The original singularity theorem above summarized, actually proves that at the end of a gravitational collapse, either the spacetime is geodesically incomplete or it must develop a Cauchy horizon so that the presence of a non-compact Cauchy hypersurface cannot hold.

This motivated Penrose and Hawking to formulate a second theorem in 1970 not relying on Cauchy hypersurfaces, and hence also extendible to closed universes, where non-compact Cauchy hypersurfaces are absent [31]. We will not enter in the detail of this theorem because as we will see, also when we will deal with closed universe, for spatially homogeneous and isotropic spacetimes, the framework provided by the original Penrose theorem suffices to the scope of our work.

Beyond the singularity theorems

The singularities theorems proved that, in the GR framework, the formation of singularities is inevitably in different physical scenario.

When considering General Relativity as an effective field theory, these singularities emerge in a high curvature regime where higher-order corrections to GR would become substantial.

This implies that the formation of singularities could potentially be avoided in theories that extend beyond GR. In these theories, higher-order terms will modify the Einstein equations. If one interpret this modifications as an effective stress-energy tensor, the equations of motion in this theories can be cast as:

$$R_{\mu\nu} - \frac{1}{2} g_{\mu\nu} R = T_{\mu\nu} + T^{\text{eff}}_{\mu\nu} \tag{0.0.5}$$

This effective stress-energy tensor can generally violate the null energy condition, which is one of the key assumptions in singularity theorems. Therefore, these theorems might be circumvented, leading to a scenario where the final state of gravitational collapse (or the initial state of an expanding universe) could result in a regular, singularity-free geometry.

This idea becomes even more plausible when considering quantum effects. As already mentioned, it is reasonable to expect that a full quantum gravity theory, in whatever form it takes, will provide insights into the nature of singularities.

We must say however, that there is no certainty in this expectation, mainly because quantum gravity might not be expressible in the conventional language of differential geometry.

Despite this uncertainty, adopting the following assumptions seems like a sensible working hypothesis for this thesis:

- General Relativity is extended by incorporating some form of "new physics" which could be related to quantum gravity.
- Gravitational phenomena can be effectively described using the traditional tools of pseudo-Riemannian geometry, specifically a spacetime manifold and a Lorentzian metric.

Under this assumptions it is possible to study and classify the possible non-singular geometries evading the singularity theorems, as regular black holes, horizonless compact objects and regular expanding universes, with the main purpose of understanding which could be the possible phenomenological effects of this regularization.

This type of classification has already been performed for static and spherically symmetric black hole spacetime in [32] and we will summarize the results in the first part of this thesis in Chapter 1. Then we will extend this classification to homogeneous and isotropic cosmological spacetimes in Chapter 2.

In the second part of the thesis we will move to the specific construction of global solutions that embody the previously classified regularizations and we will discuss about their self-consistency and stability. After an introduction on the topic in Chapter 3, we will introduce a specific regular metric describing a rotating black hole in Chapter 4. Even if other solutions of rotating regular black holes were already present in literature, they

suffered several issues, in particular they described objects unstable under a phenomenon known as mass inflation. With our new solution we wanted to prove that it is possible to construct a spacetime in which this unstable process can not take place.

In the third part, we will move to investigate some phenomenological features of the previously introduced regular alternatives to GR black holes in order to understand if and how it could be possible, through GWs observations, to prove that the astrophysical compact objects that populate our universe are not singular black holes. In particular in Chapter 5 we will summarize background knowledge on the topic. In Chapter 6 we will focus on the effects of regularization on the ringdown signal and their possible detectability with the next future gravitational detectors. In the case of horizonless solutions the usual ringdown is expected to be followed by a series of "echoes", in Chapter 7 we will discuss how for the correct study of this part of the signal, non linear effects and back-reaction should definitely be taken into account. Furthermore, in Chapter 8 we will show that this echoes signal can carry information about the structure of the innermost region of the emitting object, a region where quantum gravity effects are expected to dominate.

Part II

Classification of the possible regularizations

Not knowing when the Dawn will come,
I open every Door
—— Emily Dickinson

Chapter 1

Background: classification of regular alternatives to black holes

Following the Penrose Theorem as a guide, we want to understand how to avoid the formation of a singularity at the end of a gravitational collapse.

One possibility to evade the theorem is certainly to violate the last of its assumptions that is not to form any closed trapped surface during the collapse, meaning there will be no black hole (no horizon). This kind of regularization leads to the formation of an horizonless compact object (sometimes referred to as exotic compact object (ECO)). In literature, there is a notable number of examples of horizonless models, developed in the framework of candidate quantum gravity theories or considering the effect of new exotic degrees of freedom. We will briefly review their general features in Section 1.2.

The other possibility, chosen in [32], is to consider that even if a trapped surface is formed, the violation of the null convergence condition allows to evade the theorem and to avoid reaching a focusing point at finite affine distance. In this case the resulting spacetime will be a regular black hole (RBH), in the sense that it will present a trapped region (an thus an horizon) but it will be geodesically complete. In [32] it has been proven that the taxonomy of this kind of regular geometries is remarkably short. We will now briefly review their analysis in Section 1.1.

1.1 Null expansion-based classification of regular black holes

In addition to the general working assumptions of this thesis I, the authors of [32] assume for their classification global hyperbolicity, spherical symmetry and the presence of a trapped surface. In this set-up we can classify different geometries depending on the behavior of radial null congruences. Starting from a reference value of the affine parameter λ_* along an outgoing null congruence, from Eq. (0.0.4), the rate of change of the area element δA orthogonal to the congruence for $\lambda = \lambda_0 > \lambda_*$ is determined by the following equation:

$$\ln\left(\frac{\delta A_+|_{\lambda=\lambda_0}}{\delta A_+|_{\lambda=\lambda_*}}\right) = \int_{\lambda_*}^{\lambda_0} \mathrm{d}\lambda\, \theta_+(\lambda). \tag{1.1.1}$$

where $\theta_+(\lambda)$ is the expansion of the congruence at λ. Note that we are choosing a reference point λ_* for which $\delta A_+|_{\lambda=\lambda_*} \neq 0$. As it was shown in [32], a corollary of this equation is

that a congruence has a focusing point at a finite affine distance $\lambda = \lambda_0$ ($\delta A_+|_{\lambda=\lambda_0} = 0$) if and only if $\theta_+|_{\lambda=\lambda_0} = -\infty$. Since we are assuming that a trapped surface is present in our spacetime, there will be a value of λ for which the expansion θ_+ vanishes. From that point on, outgoing geodesics will tend to focus: inside the trapped region θ_+ will be negative and δA will continue to decrease until one reach the focusing point. In order to avoid that the spacetime is geodesically incomplete we need to modify the spacetime geometry in the vicinity of the focusing point, either creating a defocusing point ($\theta_+ = 0$ and changes sign again) or displacing the focusing point to infinite affine distance. We can thus proceed to a systematic consideration of all the possible regularization based on three parameters, i.e., the value of the affine parameter $\lambda_{\rm defocus}$ for which we have a defocusing of the outgoing congruence, the value of the radius $R(\lambda_{\rm defocus})$ of the area element orthogonal to the congruence at that point, and the value of the ingoing congruence expansion at that point, $\theta_-(\lambda_{\rm defocus}) = \bar{\theta}$.

Case A Defocusing point at a finite affine distance, $\lambda_{\rm defocus} = \lambda_0$.

A.I: $(\lambda_0, R_0, \bar{\theta} < 0)$: The expansion θ_+ vanishes and changes sign at a finite affine distance $\lambda = \lambda_0$ or, in terms of the radius of the area element orthogonal to the null outgoing congruence, at a value $R_0 = R(\lambda_0) > 0$. On the other hand, the expansion of the intersecting ingoing radial null geodesics remains negative until (and including) λ_0, so that $\bar{\theta} = \theta_-|_{\lambda=\lambda_0} < 0$.

A.II: $(\lambda_0, R_0, \bar{\theta} \geqslant 0)$: The only difference with respect to the previous case is that the expansion of the intersecting ingoing radial null geodesics does not remain negative at $R_0 = R(\lambda_0)$, $\bar{\theta} = \theta_-|_{\lambda=\lambda_0} \geqslant 0$.

Case B Defocusing point at an infinite affine distance, $\lambda_{\rm defocus} = \infty$.

B.I: $(\infty, R_\infty, \bar{\theta} < 0)$: The expansion θ_+ vanishes in the limit $\lambda \to \infty$, in a manner such that the integral in Eq. (1.1.1) is convergent. The corresponding asymptotic value of the radius of the area element orthogonal to the outgoing null congruence is $R_\infty = \lim_{\lambda_0\to\infty} R(\lambda_0) > 0$. The expansion of the intersecting ingoing radial null geodesics remains negative there, so that $\bar{\theta} = \theta_-|_{\lambda\to\infty} < 0$.

B.II: $(\infty, R_\infty, \bar{\theta} \geqslant 0)$: The only difference with respect to the previous case is that the expansion of the intersecting ingoing radial null geodesics does not remain negative at $R_\infty = \lim_{\lambda_0\to\infty} R(\lambda_0)$, $\bar{\theta} = \theta_-|_{\lambda\to\infty} \geqslant 0$.

B.III: $(\infty, 0, \bar{\theta} < 0)$: The expansion θ_+ vanishes in the limit $\lambda \to \infty$, in a manner such that the integral in Eq. (1.1.1) is divergent. Thus, the radius of the area element orthogonal to the congruence vanishes asymptotically along these geodesics (in other words, there is an asymptotic focusing point), $R_\infty = \lim_{\lambda_0\to\infty} R(\lambda_0) = 0$. The expansion of the intersecting ingoing radial null geodesics remains negative at 0, so that $\bar{\theta} = \theta_-|_{\lambda\to\infty} < 0$.

B.IV: $(\infty, 0, \bar{\theta} \geqslant 0)$ The only difference with respect to the previous sub-case is that the expansion of the intersecting ingoing radial null geodesics does not remain negative, $\bar{\theta} = \theta_-|_{\lambda\to\infty} \geqslant 0$.

Case C No defocusing point, $\lambda_{\rm defocus} = \emptyset$.

C.I: $(\emptyset, 0, \bar{\theta} < 0)$: The expansion θ_+ remains negative (but finite) in the limit $\lambda \to \infty$, which in particular implies that the integral in Eq. (1.1.1) is divergent. Thus, the radius of the area element orthogonal to the congruence vanishes asymptotically along these geodesics. The expansion of the intersecting ingoing radial null geodesics continues to be negative, so $\bar{\theta} = \theta_-|_{\lambda\to\infty} < 0$.

C.II: $(\emptyset, 0, \bar{\theta} \geqslant 0)$: The only difference with respect to the previous sub-case is that the expansion of the intersecting ingoing radial null geodesics does not remain negative, $\bar{\theta} = \theta_-|_{\lambda\to\infty} \geqslant 0$.

We will now briefly discuss these different cases separately in order to understand in more detail the properties of these spacetimes.

Case A.I and B.I: simply connected regularizations

In Case A.I, the defocusing point is attained at a finite affine distance and the ingoing congruence exhibits negative expansion there. An inner trapping horizon develops within the outer trapping horizon; the two horizons eventually merge within a finite time, leaving no black hole behind. This scenario represents a black hole (BH) that exists for a limited amount of time and stays regular throughout. Note that our geometric analysis does not provide any hint about the dynamical process behind this disappearance of the black hole. Such process could either be Hawking radiation or some other process taking place in shorter time scales, for instance the transition to a white hole [33, 34]. The limiting case (B.I), where the two horizons merge in infinite time, is referred to as an everlasting horizon. A spacetime entering these cases will be simply connected i.e. its topology will be the same as Mikowski spacetime.

Case A.II and B.II: multiply connected regularizations

In Case A.II, the defocusing point is attained at a finite affine distance as before but the expansion of the ingoing congruence is non-negative at that point, implying it must be zero at some location along the congruence between the trapped surface and the defocusing point. Consequently, the two-spheres orthogonal to the two null congruences never shrink to a point, their radius exhibits a local minimum as a function of the affine parameters along the two congruences. This minimum forms a (dynamical) wormhole throat, but since the throat is situated behind a trapping horizon, the wormhole is considered "hidden" (and the throat can only be crossed in one direction). The extreme case (B.II) where the throat is infinitely distant is referred to as an asymptotic hidden wormhole. A spacetime entering these cases, containing a wormhole throath, will be path-connected but not simply connected. Indeed, a closed path that winds around the wormhole throat cannot be shrunk to a point, this kind of spacetime is said to be multiply connected.

Remaning singular cases

In practical terms, sub-cases B.III and C.I fall into the same category, as both of these situations can be understood as the limiting case in which the focusing point is pushed to an infinite affine distance along outgoing null geodesics. The same comment applies to

cases B.IV and C.II, that only differ from the previous sub-cases in the behavior of the expansion of the null congruence θ_-. All these cases can be proven to describe a spacetime that presents a curvature singularity at infinite affine distance along outgoing null geodesics, but generally finite affine distance along ingoing null geodesics.

In conclusion, under some minimal geometric assumptions it is possible to construct an exhaustive classification of geometries describing in effective terms the regularization of black holes due to quantum gravity effects or new phisics. The result of this classification is that the most generic regular black hole spacetimes can be divided into two classes: simply connected geometries, to which we also refer as evanescent horizons RBHs, and multiple connected geometries to which we also refer as hidden wormholes. These two categories can include geometries that are quite intricate. For example, in the case of evanescent horizons, there might be more than two horizons, nested one inside the other, for this reason from now on we will refer to geometries entering this class as multiple horizons RBHs. However, these horizons must form pairs and merge within a finite time. Similarly, in the hidden wormhole scenario, multiple horizons (on both sides of the throat) and multiple throats may exist.

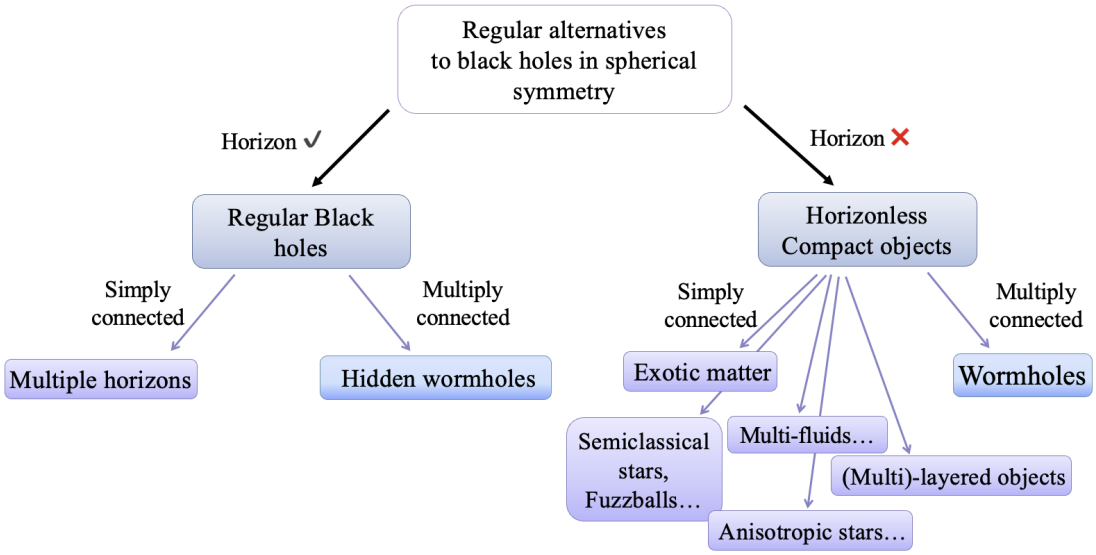

Figure 1.1: Scheme of the possible spherically symmetric regular alternatives to singular black holes. The multiple-horizons RBHs and the simply connected horizonless objects are shown in the same color because in Chapter 3 we will see that they can be often described by the same metric, the same happens for hidden wormholes and horizonless wormholes. The vast zoo of simply-connected horizonless compact objects is summarized here according to the Buchdhal theorem: each box contains some of the known objects violating a particular assumption of the theorem.

1.2 The zoo of horizonless compact objects

The previous analysis focused on how to prevent the formation of a singularity inside a trapped region, violating the weak convergence condition. However, as we mentioned, another possibility to evade the Penrose theorem is to prevent the formation of the trapped region itself.

In General Relativity, a trapping horizon usually forms in a region of relatively low curvature, where the effects of new physics are expected to be minimal, at least at the classical level. However, already incorporating semiclassical effects (in the sense of quantum field theory in curved spacetimes) could significantly change this scenario, allowing for the existence of horizonless compact solutions. Notable examples in literature are gravastars [35–37] or semiclassical stars [38, 39], other examples come from candidate quantum gravity scenarios like fuzzballs [40, 41] or the introduction of exotic matter like boson stars [42, 43]. Most of these horizonless alternatives to BHs are simply connected, but multiply connected models, such as wormholes [44, 45], are also possible. In general the main phenomenological features of an horizonless object are:

- The *size*. For some models a true surface is present and it allows for an unambiguous definition of the radius r_0. In other models the modifications with respect to the black hole geometry extend in all the spacetime, decreasing with the radial distance. However, it is still possible to define an effective radius below which these modifications are of $O(1)$. The size is usually described through a compactness parameter such as $\sigma = \frac{r_0}{r_0^{BH}} - 1$ or $C = 2M/r_0$ with r_0^{BH} the horizon radius for a BH of the same mass M and spin a;

- The *reflection properties of the surface*. These can be encoded in an absorption coefficient κ measuring the fraction of the energy that can be semi-permanently lost inside the region $r \leqslant r_0$. This absorption can be due to the inelastic interaction with the horizonless object, when exciting internal degrees of freedom in the bulk, or simply due to propagation in the interior region.

- The *tails*. These are the modifications with respect to the BH geometry that extend outside the radius. Since at infinite radial distance r we need to recover asymptotic flatness, these tails must decay with the r, typically polynomial but possibly modulated by functions of compact support.

In order for these horizonless compact objects to represent valid black hole mimickers, they need to share some key features of the exterior black-holes spacetime. In addition to asymptotic flatness, a desirable property is to be compact enough to posses a photon sphere, i.e. a circular closed orbit for null geodesics, outside the putative surface of the object. Horizonless objects with such feature are usually indicated as ultra-compact objects.

Finally we want to remark that every horizonless compact object will violate at least one of the assumptions of the Buchdhal theorem [46] that sets an upper limit to the compactness of a spherical distributions of matter in hydrostatic equilibrium. Specifically, it states that a self-gravitating object with compactness higher than $C_{Buch} = 2M/r_0 = 8/9$, must violate at least one of the following assumptions:

- General Relativity
- spherical symmetry
- single perfect fluid description of interior matter
- approximate isotropy of the fluid, i.e the tangential pressure is equal or mildly smaller then the radial one
- non-negative radial pressure and energy density
- decreasing of the energy density as one moves outwards

This is a powerful instrument to navigate through the vast zoo of horizonless compact objects, indeed they can be classified according to which of these assumptions they violate [47].

Chapter 2

Classification of regular alternatives to the Big Bang

The previous classification was restricted to spherically symmetric compact objects, we want now to apply the same analysis to cosmological scenarios. In particular we want to classify the possible regular manifolds describing an expanding and (at least approximately) homogeneous and isotropic universe. These are described by the FLRW metric [48]:

$$ds^2 = -dt^2 + a^2(t)\left[dr^2 + R^2(r)\left(d\theta^2 + \sin^2\theta d\varphi^2\right)\right], \tag{2.0.1}$$

with $R(r) = (\sin r, r, \sinh r)$ if $(k = 1, 0, -1)$ respectively.

2.1 Trapped regions in FLRW geometries

Since they are crucial for our analysis, we will now analyse the congruences of null geodesics of the FLRW metric and the conditions under which a trapped region is formed in such spacetime. The family of past-directed radial null geodesics in a FLRW universe has tangent vector field [49]:

$$V^\mu_\pm = \frac{1}{a(t)}\left(-1, \pm\frac{1}{a(t)}, 0, 0\right) = \frac{dx^a}{d\lambda}, \tag{2.1.1}$$

where $d\lambda = -a(t)dt \pm a(t)^2 dr$ is an affine parameter[1]. Note that the $+$ sign indicates outgoing geodesics, while the $-$ indicates ingoing geodesics. Along such null geodesics, from Eq. (2.0.1) we have $dr/dt = \mp 1/a$ and thus $\lambda = -2\int a(t)dt$.

The expression for the expansion of such geodesics is then[2]

$$\theta_\pm = \frac{2}{a^2(t)}\left[-\dot{a}(t) \pm \frac{\partial R(r)/\partial r}{R(r)}\right], \tag{2.1.2}$$

[1]Note that these two null vectors are defined only up to a multiplicative function of the respective orthogonal null coordinate. The redefinition $V_\pm \to g(u_\mp)V_\pm$, with $g(u_\mp) > 0$ and $du_\pm = -dt/a(t) \pm dr$, stills results into affinely parameterized vector fields. However, $u_\pm$ are constant along the respective orthogonal geodesics, which implies $V^a_\pm \nabla_a g(u_\mp) = 0$. Hence, this redefinition changes expansions by a positive multiplicative factor and therefore does not affect our identification of trapped regions.

[2]The expression provided for the expansion is not the usual one derived as $\partial_t \ln A$, where A is the proper cross-sectional area [28], but it is that divided by $1/a(t)$ in order to coincide with the divergence of the tangent vector normalized as in Eq. (2.1.1).

in terms of the time t, or

$$\theta_{\pm} = \frac{2}{a^2(\lambda)}\left[2a(\lambda)a'(\lambda) \pm \frac{\partial R(r)/\partial r}{R(r)}\right], \tag{2.1.3}$$

in terms of the affine parameter λ. In these expressions as well as in the rest of the chapter, $\dot{a} = da/dt$ and $a' = da/d\lambda$, so that $\dot{a} = -2aa' = -(a^2)'$. Due to the one-to-one relation between λ and t, we can choose any of these variables to parametrize null geodesics. In the following, we will always use t for this purpose. When working with specific geodesic congruences we will always choose, without loss of generality, a reference point $\lambda = \lambda_\star$ such that $t(\lambda_\star) = 0$.

Let us now discuss the structure of trapped surfaces for expanding universes. In the flat and open case, taking into account that $R(r)$ is always a positive and monotonically increasing function in its range of definition, any expanding universe [$\dot{a}(t) > 0$ or $a'(\lambda) < 0$] satisfies

$$\theta_- \leqslant 0, \tag{2.1.4}$$

while

$$\theta_+ \begin{cases} > 0 & \text{if } \partial \ln R(r)/\partial r > \dot{a}, \\ \leqslant 0 & \text{if } \partial \ln R(r)/\partial r \leqslant \dot{a}. \end{cases} \tag{2.1.5}$$

In the closed case, $R(r)$ is no more a monotonically increasing function, and can assume negative values. However, we also have to take into account that, in such universe, $\theta_+ < 0$ does not correspond necessarily to a trapped region since for some values of r outgoing and ingoing geodesics exchange roles, as we shall elaborate in Sec. 2.5. Thus, one has to check the sign of both θ_+ and θ_-, and a trapped region is present only if both of them are negative. We get

$$\theta_+ \begin{cases} > 0 & \text{if } \partial \ln R(r)/\partial r > \dot{a}, \\ \leqslant 0 & \text{if } \partial \ln R(r)/\partial r \leqslant \dot{a}. \end{cases} \tag{2.1.6}$$

$$\theta_- \begin{cases} > 0 & \text{if } \partial \ln R(r)/\partial r < -\dot{a}, \\ \leqslant 0 & \text{if } \partial \ln R(r)/\partial r \geqslant -\dot{a}. \end{cases} \tag{2.1.7}$$

The function $\partial \ln R(r)/\partial r$ goes from $+\infty$ at $r = 0$ to 0 at $r = \infty$ for the flat case ($k = 0$), from $+\infty$ to 1 in the open case ($k = -1$) and from $+\infty$ and $-\infty$ for the closed case ($k = 1$). Hence, both flat and closed expanding universes always have trapped surfaces with the structure depicted in Fig. 2.1, which is also shared by open universes with $\dot{a} > 1$.[3]

Figure 2.2 shows the causal structure of a decelerating FLRW metric and its trapped region, which will exist for the open case only for $\dot{a} > 1$. Trapped surfaces appear for sufficiently large distances to the reference point $r = 0$ being used. However, due to homogeneity and isotropy, the choice of reference point is fiduciary and has no physical meaning. This is different with respect to spherically-symmetric black holes, in which the gravitational potential has a defined center. Hence, in a FLRW spacetime it is enough to show that a point belongs to a trapped surface to conclude that all points belong to trapped surfaces. In other words, there are no trapped regions in the usual sense: either

[3]Note that, as we have chosen k to be dimensionless following standard conventions, $a(t)$ has dimensions of length. As we are also choosing units in which $c = 1$, $\dot{a}(t)$ is dimensionless.

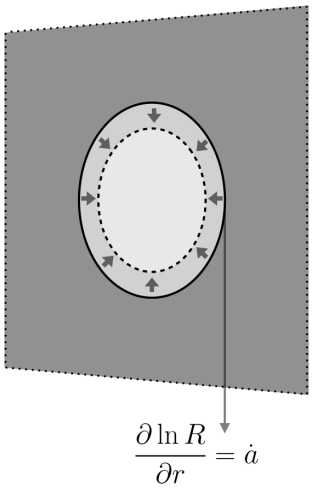

Figure 2.1: Structure of trapped surfaces (dark gray) in a given slice of constant time t of FLRW spacetimes (for open universes, it is necessary that $\dot{a} > 1$ for trapped surfaces to exist). The solid circle indicates the location of the marginal trapped surface for a given value of $\dot{a}$, and the arrows pointing to the dashed line indicate how this location changes as $\dot{a}$ increases.

all points are trapped, or no points are trapped.

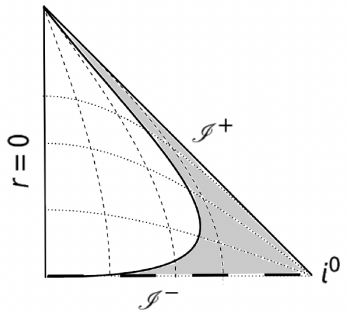

Figure 2.2: Penrose diagram of a singular decelerating universe. The shaded region is the one containing trapped surfaces (which, for open universes, requires $\dot{a} > 1$ in order to exist). Note that the shading indicates trapped points with respect to a fiduciary reference point which has no physical meaning: due to homogeneity and isotropy, either all points are trapped, or no points are trapped.

Finally, regardless of the spatial curvature and the structure of the trapping surfaces, imposing regularity of curvature invariants implies some further constraints on the nature of the scale factor as a function of time. The Ricci scalar $\mathcal{R}$ takes the form

$$\mathcal{R} = \frac{6\left[k + a(t)\ddot{a}(t) + \dot{a}^2(t)\right]}{a(t)^2}, \tag{2.1.8}$$

while the Kretschmann scalar $\mathcal{K}$ reads

$$\mathcal{K} = \frac{12\left[a^2(\ddot{a})^2 + (k + \dot{a}^2)^2\right]}{a^4}. \tag{2.1.9}$$

As a consequence, $a(t)$ must be at least a C^2 function to avoid curvature singularities.

2.2 Null expansions-based classification of regular cosmological spacetimes

We shall now analyze the possible conditions under which a singularity in the past of a FLRW universe can be avoided, starting with some general considerations.

For flat and open universes (that is, well approximated by either $k = 0$ or $k = -1$ FLRW spacetimes), the discussion is parallel to the one for spherical static black holes in Chapter 1, with the only difference that we will consider congruences of past-directed (instead of future-directed) null geodesics. Hence, the different geometric possibilities for these cases are in one-to-one correspondence to the possible ways in which spacetimes can be deformed to avoid focusing points (see the classification in Section 1.1). For general closed universes, Penrose's theorem does not apply, and therefore the aforementioned classification would not apply without further considerations. However, as discussed in Sec. 2.5, this classification is still meaningful for homogeneous and isotropic closed universes.

As explained in Sec. 2.1, moving to bigger values of the affine parameter along the considered past-directed null congruences corresponds to move towards the past (i.e., to smaller values of t), and in the following equations we will always choose, without loss of generality, a reference point $\lambda = \lambda_\star$ such that $t(\lambda_\star) = 0$. As we start with negative expansion for some of the past directed outgoing null geodesics (we start in a past trapped region), the avoidance of a focusing point requires at some point a change of sign for θ_+ and hence that the latter vanishes.

However, differently from the black-hole cases studied, for cosmological spacetimes, the expansion does not vanish at the same value of the affine parameter for all null geodesics. We shall name the point at which $\theta_+ = 0$ for the most trapped null geodesic, and thus $\theta_+ \geqslant 0$ for all null geodesics, the defocusing point.

We can now proceed to a systematic consideration of all the possible regularizations of FLRW universes. In doing so we shall use the same classification reported in Section 1.1. We will discuss the different cases separately in order to understand in more detail the properties of these spacetimes and, in particular, the implications of the homogeneity and isotropy assumptions. Given the quite different nature of closed universes, we shall treat first the flat and open cases in Sec. 2.3 and 2.4, and consider separately the closed case in Sec. 2.5.

2.3 Regular Flat FLRW universes

We shall now discuss in detail the different cases of Section 1.1 for a flat FLRW universe. We will be using often the expression for the expansion of ingoing and outgoing null geodesics, Eq. (2.1.2), specialized to $k = 0$ so that $R(r) = r$:

$$\theta_\pm = \frac{2}{a^2(t)}\left[-\dot{a}(t) \pm \frac{1}{r(t)}\right] = \frac{2}{a^2(t)r(t)}\left[-\dot{a}(t)r(t) \pm 1\right] . \tag{2.3.1}$$

In order to have a more clear physical interpretation of this expression, it is useful to rewrite it as

$$\theta_{\pm} = \frac{2}{a(t)}\left[-\frac{\dot{a}(t)}{a(t)} \pm \frac{1}{a(t)r(t)}\right] = \frac{2}{a(t)}\left[-H(t) \pm \frac{1}{a(t)r(t)}\right]. \tag{2.3.2}$$

We see that null rays for which the comoving radius $a(t)r(t)$ lies outside the Hubble sphere $1/H(t)$, are trapped. The Hubble sphere is the point in which the recession velocity due to the cosmological expansion equates the speed of light [50, 51] (indeed, the Hubble radius is sometimes called the "speed of light sphere" [50]). Now, consider two past-directed outgoing null geodesics, they have a tendency to move away from each other but, since they are past directed, these experience a contraction of the universe that tends to bring them closer. They will effectively move away from each other only if their velocity is larger than the "contraction" velocity of the universe, that is, if their comoving radius is inside the Hubble sphere. The remaining null geodesics, lying outside $1/H(t)$, will inevitably get closer to each other driven by the "contraction" of the spacetime, and are indeed trapped.

2.3.1 Cases A.I and A.II (λ_0, R_0)

For a given congruence of outgoing null geodesics that is trapped at $t = 0$, it is required that $\theta_+ < 0$, which means that

$$\dot{a}(0) > \frac{1}{r(0)} \rightarrow \dot{a}(0)r(0) > 1. \tag{2.3.3}$$

The existence of a defocusing point at a finite affine distance $t = t_0$ requires the condition

$$\dot{a}(t_0) = \frac{1}{r(t_0)} \rightarrow \dot{a}(t_0)r(t_0) = 1. \tag{2.3.4}$$

Hence, a relative deceleration towards the past is required. Also, it is necessary that the decreasing scale factor does not vanish in the interval $t \in [0, t_0)$. Otherwise, we would have $\theta_+(t) = -\infty$, thus signaling the formation of a focusing point, which we were trying to avoid (the limiting case in which $a(t_0) \rightarrow 0$ slow enough so that $\theta_+(t_0) \rightarrow 0$ is discussed below). The condition in Eq. (2.3.4) must be satisfied for some value of t_0 along all congruences. As shown next, this imposes a stronger constraint on $\dot{a}(t)$.

Proposition: All congruences of null geodesics are untrapped at finite affine distance λ corresponding to time t if and only if the derivative of the scale factor with respect to the time, $\dot{a}(t)$, vanishes.

Proof: Let us assume that $\dot{a}(t)$ does not vanish for any value of t, and show that this implies the existence of at least a past-directed null geodesic that does not have a defocusing point at finite affine distance. Let us take a reference geodesic, for which

$$1 - \dot{a}(0)r(0) < 0, \tag{2.3.5}$$

thus implying that $\theta_+(0) < 0$, while

$$1 - \dot{a}(t_0)r(t_0) \tag{2.3.6}$$

has an indefinite sign. Let us now multiply $r(t)$ by a positive constant factor N, which yields another geodesic with a larger value of the radius. We still have that

$$1 - \dot{a}(0)Nr(0) = 1 - \dot{a}(0)r(0) - (N-1)\dot{a}(0)r(0) < 0, \tag{2.3.7}$$

so this second congruence was still trapped originally. Moreover, it always exists a value of N such that

$$1 - \dot{a}(t_0)Nr(t_0) < 0. \tag{2.3.8}$$

This holds for any finite value of t_0, thus showing that there always exists a past-directed outgoing null geodesic that remains trapped, thus reaching a contradiction.

Regarding the converse implication, if we impose $\dot{a}(t_0) = 0$, then the expansion of any past-directed congruence of null geodesics is positive. □

Hence, spacetimes in this class are geodesically complete if and only if the derivative of the scale factor vanishes at some $t = t_0$, while the scale factor remains non-zero at $t = t_0$. Indeed, the limiting case in which also the scale factor vanishes is not admissible — as it would entail a manifest curvature singularity. For $t < t_0$, in order to avoid the formation of further trapped surfaces, $\dot{a}(t) \leqslant 0$. Hence, spacetimes in this class describe a bounce between a contracting and an expanding universe where a future trapped region is continuously connected with a past trapped region, being both delimited by the trapping horizon $r = \pm 1/a(t)$.

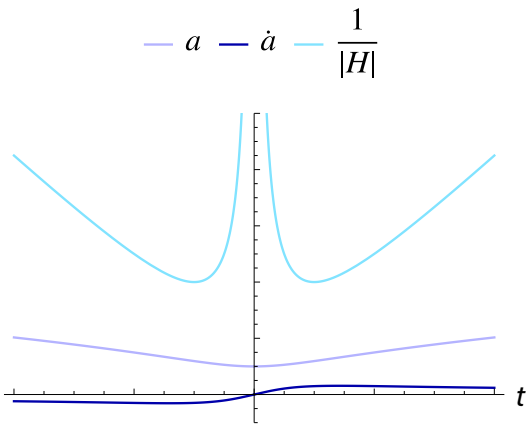

Figure 2.3: Bouncing universe: behavior of the scale factor $a(t)$, of its derivative to respect to time and of the Hubble radius $1/|H(t)| = a(t)/\dot{a}(t)$. The defocusing point $\dot{a}(t) = 0$ is reached in a finite affine distance and it is preceded by a "contracting" phase in which $\dot{a}(t) < 0$.

Note that we are implicitly assuming that the scale factor is an analytic function of time which, if dropped, would allow also the possibility that $a(t)$ vanishes in a closed interval or half-line (in the latter case, the geometry describes an expanding universe emerging from a stationary phase [52]). Analytical solutions that are effectively emergent are however possible, for example the expansion can be preceded by an oscillatory phase in which $\dot{a}$ is 0 on average (see [53] for a specific realization). These solutions embody a hybrid nature, drawing from both emergent and bouncing universe scenarios, as $\dot{a}$ assumes also negative values during the "emergent" phase.

As we have mentioned above, the expansion does not vanish at the same value of

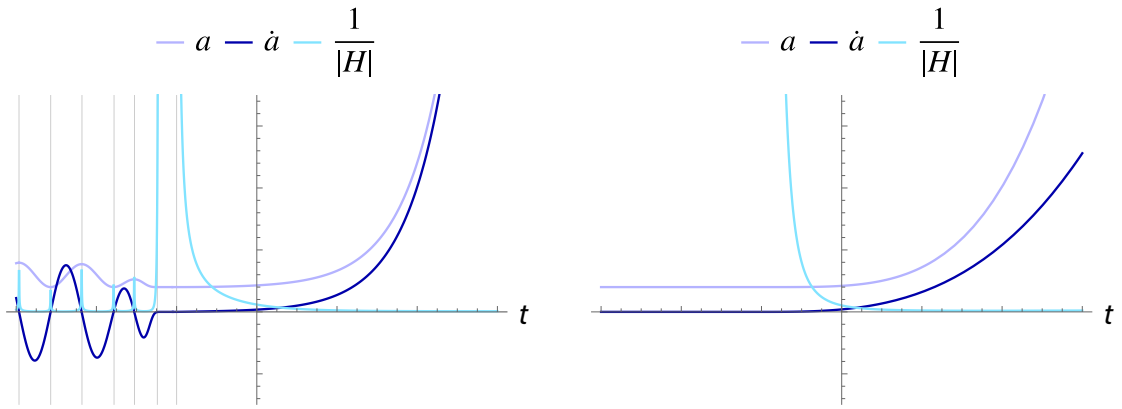

Figure 2.4: Effectively emergent universe and emergent universe: behavior of the scale factor $a(t)$, of its derivative to respect to time and of the Hubble radius $1/|H(t)| = a(t)/\dot{a}(t)$. The defocusing point $\dot{a}(t) = 0$ is reached in a finite affine distance and it is preceded either by a "stationary" phase in which $\dot{a}(t)$ is 0 on average (in the effectively emergent case — left panel) or exactly 0 (in the emergent case — right panel).

the affine parameter for all null outgoing geodesics. Furthermore, the homogeneity and isotropy assumptions strongly constrain the behavior of ingoing geodesics with respect to the outgoing ones. Indeed, if $\theta_+(t) = 0$, then

$$\theta_-(t) = -\frac{4}{a^2(t)r(t)} \leqslant 0. \tag{2.3.9}$$

Hence, it is not possible to achieve at the same time $\theta_+(t) = 0$ and $\theta_-(t) \geqslant 0$ for all null geodesics (Case A.II) within the family of geometries being considered.

An analogous reasoning leads to the same conclusions also for the case B.II, B.IV and C.II, thus we neglect this discussion about ingoing geodesics in the next sections.

2.3.2 Cases B.I and B.II (∞, R_∞)

This case is similar to A.I, but now the defocusing point is at an infinite affine distance $\lambda_{\text{defocus}} = \infty$. Since $a(t)$ is always finite, this means that $t_{\text{defocus}} = -\infty$. We have that the integral

$$\lambda_{\text{defocus}} = \lambda_* + 2\int_{-\infty}^{0} \mathrm{d}t\, a(t) \tag{2.3.10}$$

is divergent, while the integral

$$\ln\left(\frac{\delta A_+|_{\lambda=\infty}}{\delta A_+|_{\lambda=\lambda_*}}\right) = \int_{-\infty}^{0} \mathrm{d}t\, a(t)\theta_+(t) = \int_{-\infty}^{0} \mathrm{d}t \frac{2}{a(t)}\left(-\dot{a}(t) + \frac{1}{r(0) + \int_t^0 \mathrm{d}t'/a(t')}\right) \tag{2.3.11}$$

must not be negatively divergent ($> -\infty$), where we have used the expression $r(t) = r(0) + \int_t^0 \mathrm{d}t'/a(t')$ obtained along geodesics, with tangent vector given by Eq. 2.1.1.

Proposition: All congruences of null geodesics are untrapped at infinite affine distance if and only if the derivative of the scale factor with respect to the time, $\dot{a}(t)$, vanishes for

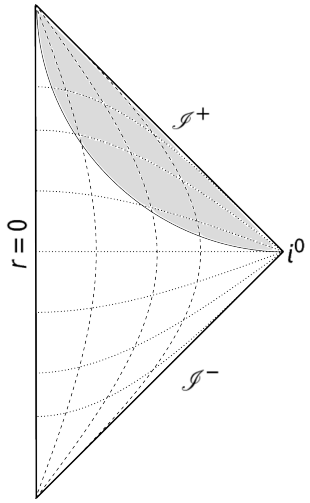

Figure 2.5: Penrose Diagram of a bouncing or emergent universe.

$t \to -\infty$.

Proof: The proof proceeds as the one for Case A.I simply putting $t_0 = -\infty$. □

Example: Let us require to have a regular expanding universe at any time thus $\dot{a}(t) \geqslant 0$ and $a(t) > 0$ for any t. In order to have the defocusing at infinite affine distance we then need $\lim_{t\to-\infty} \dot{a}(t) = 0$. A simple analytic profile for $a(t)$ is then $a(t) = a_0 + b_0 e^{Ht}$, that is a sort of "regularized inflation". With this choice the integral in Eq. (2.3.11) goes

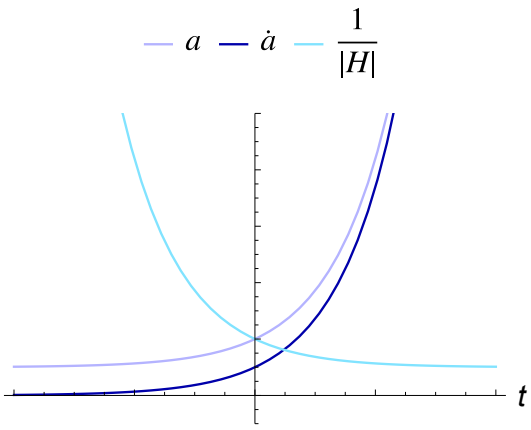

Figure 2.6: Regular inflating universe: behavior of the scale factor $a(t)$, of its derivative to respect to time and of the Hubble radius $1/|H(t)| = a(t)/\dot{a}(t)$. The defocusing point $\dot{a}(t) \to 0$ is reached in an infinite affine distance.

to $+\infty$. It is possible to prove that this is a generic feature of each regular spacetime entering this case.

Proposition: For a regular expanding flat FLRW spacetime with complete defocusing at infinite affine distance [$\dot{a}(t)$ vanishes for $t \to -\infty$] the integral in Eq. (2.3.11) diverges positively, $\ln\left(\delta A_+|_{\lambda=\infty} / \delta A_+|_{\lambda=\lambda_*}\right) = +\infty$.

Proof: If the spacetime is regular, $a(t) \neq 0$ $\forall t$, then the first term in the integral

Eq. (2.3.11),

$$\int_{-\infty}^{0} \mathrm{d}t\Big(-2\frac{\dot{a}(t)}{a(t)}\Big), \tag{2.3.12}$$

is negative but finite. Indeed, if $a(t) \neq 0$ the integrand in the equation above is finite, thus the integral from 0 to t_B with t_B arbitrarily small, but finite, cannot diverge. On the other hand, since $a(t)$ is a monotonically increasing function in the interval $t \in [-\infty, t_B]$ and it starts from a value $a(-\infty) > 0$, we have

$$\int_{-\infty}^{t_B} \mathrm{d}t\Big(-2\frac{\dot{a}(t)}{a(t)}\Big) > \int_{-\infty}^{t_B} \mathrm{d}t\Big(-2\frac{\dot{a}(t)}{a(-\infty)}\Big) = -2\Big(\frac{a(t_B)}{a(-\infty)} - 1\Big) > -\infty. \tag{2.3.13}$$

Let us therefore focus on the second term:

$$\int_{-\infty}^{0} \frac{2\,\mathrm{d}t}{a(t)\left[r(0) + \int_t^0 \mathrm{d}t'/a(t')\right]}. \tag{2.3.14}$$

As mentioned before, we are choosing a reference point λ_* corresponding to $t = 0$ at which δA is finite[4] and thus $a(t = 0) = a_0$ is a finite positive number. Since $a(t)$ is a monotonically increasing function from $-\infty$, $a(t) < a_0$ in all the interval $[0, -\infty)$ thus

$$\int_{-\infty}^{0} \frac{2\,\mathrm{d}t}{a(t)\left[r(0) + \int_t^0 \mathrm{d}t'/a(t')\right]} > \int_{-\infty}^{0} \frac{2\,\mathrm{d}t}{a_0\left[r(0) + \int_t^0 \mathrm{d}t'/a(t')\right]}. \tag{2.3.15}$$

We can split this integral into two pieces by defining a negative value of t, t_{B1},

$$\int_{-\infty}^{0} \frac{2\,\mathrm{d}t}{a_0\left[r(0) + \int_t^0 \mathrm{d}t'/a(t')\right]} = \int_{t_{\mathrm{B1}}}^{0} \frac{2\,\mathrm{d}t}{a_0\left[r(0) + \int_t^0 \mathrm{d}t'/a(t')\right]} + \int_{-\infty}^{t_{\mathrm{B1}}} \frac{2\,\mathrm{d}t}{a_0\left[r(0) + \int_t^0 \mathrm{d}t'/a(t')\right]}, \tag{2.3.16}$$

with the first term being finite, so that any divergent behavior (if present) is isolated in the second term. Let us therefore focus on this second term, introducing another auxiliary value of the time $t_{\mathrm{B2}} > t_{\mathrm{B1}}$ and expanding $a(t)$ near $-\infty$ as $a(t) = a_{-\infty} + a_1/t + a_2/t^2 + ...$, so that

$$\begin{aligned}
&\int_{-\infty}^{t_{\mathrm{B1}}} \frac{2\mathrm{d}t}{a_0\left[r(0) + \int_t^0 \mathrm{d}t'/a(t')\right]} \\
&= \int_{-\infty}^{t_{\mathrm{B1}}} \frac{2\mathrm{d}t}{a_0\left[r(0) + \int_{t_{\mathrm{B2}}}^0 \mathrm{d}t'/a(t') + \int_t^{t_{\mathrm{B2}}} \mathrm{d}t'/\left(a_{-\infty} + a_1/t' + a_2/t'^2 + \dots\right)\right]} \\
&= \int_{-\infty}^{t_{\mathrm{B1}}} \frac{2\mathrm{d}t}{a_0\left[r(t_{\mathrm{B2}}) + \int_t^{t_{\mathrm{B2}}} \mathrm{d}t'\left(1/a_{-\infty} + b_1/t' + b_2/t'^2 + \dots\right)\right]} \\
&= \int_{-\infty}^{t_{\mathrm{B1}}} \frac{2\mathrm{d}t}{a_0\left[g(t_{\mathrm{B2}}) - t/a_{-\infty} - b_1 \ln|t| + b_2/t + \dots\right]},
\end{aligned} \tag{2.3.17}$$

where we introduced $g(t_{\mathrm{B2}}) = r(t_{\mathrm{B2}}) + t_{\mathrm{B2}}/a_{-\infty} + b_1 \ln|t_{\mathrm{B2}}| - b_2/t_{\mathrm{B2}}$ that is not a function

[4] This is always possible through a linear rescaling of the time coordinate $t \to t + c$ with c an arbitrary constant.

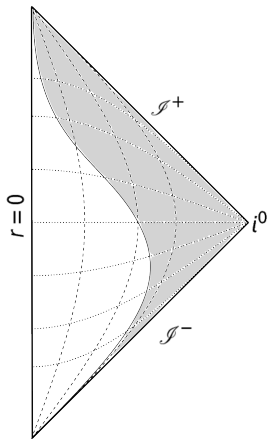

Figure 2.7: Penrose diagram of a regular universe of Case B.I (asymptotic defocusing e.g. $a(t) = a_0 + b_0 e^{Ht}$)

of t. Since the integrand goes to 0 in the $t \to -\infty$ limit at most as $1/t$, the integral in the last line is divergent.

This analysis is general enough for being in principle applicable also to the case B.II. Nonetheless, as explained at the end of Sec. 2.3.1, case B.II, cannot be realized, within the family of geometries being here considered, given that the conditions $\theta_+ = 0$ and $\theta_- \geqslant 0$ are never realized simultaneously for all null geodesics.

2.3.3 Cases B.III and B.IV $(\infty, 0)$

In this cases, the defocusing point is at an infinite affine distance and the integral in Eq. (2.3.11) is divergent $(-\infty)$. As discussed below, these case are singular.

Proposition: If the integral in Eq. (2.3.11) is negatively divergent (it goes to $-\infty$), then $a(t) \to 0$ for some t, and thus the spacetime is also singular.

Proof: We will prove the equivalent proposition: if $a(t) \neq 0 \ \forall t$ (including the limit $t \to -\infty$), then the integral Eq. (2.3.11) cannot be negatively divergent. Indeed, the term proportional to $1/r(t)$ is always positive thus, to prove that the integral is greater than $-\infty$, we only need to focus on the following piece

$$\int_{-\infty}^{0} \mathrm{d}t \Big(-2\frac{\dot{a}(t)}{a(t)} \Big). \tag{2.3.18}$$

which however, as already proved, is never negatively divergent [see, in particular, Eq. (2.3.13) in the previous section].

Finally note, that the above reasoning is strictly needed for case B.III only, given that case B.IV, as explained at the end of Sec. 2.3.1, is not realizable within the family of geometries being considered.

2.3.4 Cases C.I and C.II $(\emptyset, 0)$

In this case, there is some geodesic for which θ_+ remains negative for $\lambda \to +\infty$ $(t \to -\infty)$. This can happen only if $\dot{a}(t)$ remains positive in the infinite domain $(-\infty, 0]$. Thus, if $a(t)$

is finite at the point $t = 0$, it must have crossed or reached the value of 0 at some point in the past. This proves that there is a curvature singularity, and therefore these spacetimes cannot be regular.

Note that, as explained at the end of Sec. 2.3.1, aside from this singular behavior, it would not be possible to realize Case C.II within the family of geometries being considered.

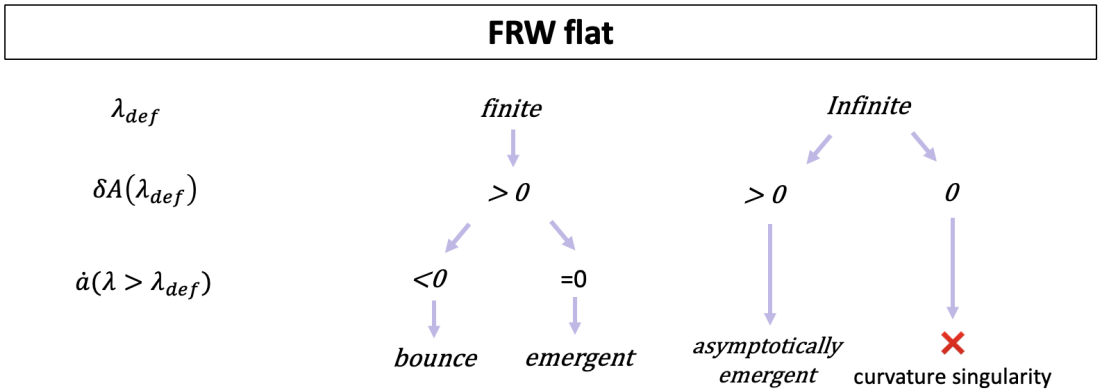

Figure 2.8: Scheme of the allowed flat homogeneous and isotropic regular geometries. These geometries are classified according to: i) the value of the affine parameter at which all outgoing null geodesics are defocused λ_{def} so that $\theta_+(\lambda_{def}) = 0$; ii) the area element orthogonal to the congruence at λ_{def}; iii) the derivative of the scale factor for $\lambda > \lambda_{def}$ that is in the past with respect to the defocusing ($t < t_{def}$).

2.4 Regular Open FLRW universes

We shall now discuss in detail the different cases of Section 1.1 for an open FLRW universe. The expansion of ingoing and outgoing null geodesics, Eq. (2.1.2), particularized to $k = -1$, i.e. $R(r) = \tan r$, is

$$\theta_\pm(t) = \frac{2}{a^2(t)}\left[-\dot{a}(t) \pm \frac{1}{\tanh r(t)}\right] = \frac{2}{a^2(t)\tanh r(t)}\left[1 - \dot{a}(t)\tanh r(t)\right]. \tag{2.4.1}$$

2.4.1 Cases A.I and A.II (λ_0, R_0)

Proposition: All congruences of null geodesics are untrapped at finite affine distance λ corresponding to time t if and only if $\dot{a}(t) \leqslant 1$.

Proof: Let us assume that $\dot{a}(t)$ remains greater than 1 for any value of t, and show that this implies the existence of at least a past-directed null geodesic that does not have a defocusing point at finite affine distance. Let us take a reference geodesic, for which

$$1 - \dot{a}(0)\tanh r(0) < 0, \tag{2.4.2}$$

thus implying that $\theta_+(0) < 0$, while

$$1 - \dot{a}(t_0)\tanh r(t_0) = 0. \tag{2.4.3}$$

Let us now multiply $r(t)$ by a positive constant factor N, which yields another geodesic with a larger value of the radius. Then we have that:

$$\tanh Nr(t) = M \tanh r(t) \tag{2.4.4}$$

with $M > 1$ since $\tanh(x)$ is monotonically increasing in $[0, +\infty)$. Thus we still have that

$$\begin{aligned} &1 - \dot{a}(0) \tanh Nr(0) = 1 - 2M\dot{a}(0) \tanh r(0) = \\ &1 - \dot{a}(0) \tanh r(0) - \dot{a}(0)(M-1) \tanh r(0) < 0, \end{aligned} \tag{2.4.5}$$

so this second geodesic was still trapped originally. Moreover, it always exists a value of N such that

$$1 - \dot{a}(t_0) \tanh Nr(t_0) = 1 - M\dot{a}(t_0) \tanh r(t_0) < 0. \tag{2.4.6}$$

This holds for any finite value of t_0, thus showing that there always exists a past-directed outgoing null geodesic that remains trapped, thus reaching a contradiction. Regarding the converse implication, if we impose $\dot{a}(t_0) \leqslant 1$, then $\dot{a}(t_0) \tanh r(t_0) \leqslant \tanh r(t_0) \leqslant 1$ and thus the expansion of any past-directed null geodesic is positive. □

Note that, for open universes, it is possible to have singular spacetimes without trapped regions if $a(t)$ vanishes, for instance $a(t) = e^t$. In this case there is a naked curvature singularity at $t = -\infty$ where $\theta_\pm = \pm\infty$, which is therefore not a focusing point. Hence, the condition $\dot{a} \leqslant 1$ is necessary, but not sufficient for regularity.

As in the flat case, the homogeneity and isotropy assumptions strongly constrain the behavior of ingoing geodesics with respect to the outgoing ones. Indeed, if $\theta_+(t) = 0$, then

$$\theta_-(t) = -\frac{4}{a^2(t) \tanh r(t)} \leqslant 0. \tag{2.4.7}$$

Hence, it is not possible to achieve at the same time $\theta_+(t) = 0$ and $\theta_-(t) \geqslant 0$ for all null geodesics within the family of geometries being considered, and therefore case A.II cannot be realized.

An analogous reasoning leads to the same conclusions for cases B.II, B.IV and C.II, thus we will not repeat explicitly this discussion about ingoing geodesics in the next sections.

2.4.2 Cases B.I and B.II (∞, R_∞)

In this case, the defocusing point is at an infinite affine distance, and the integral in Eq. (2.3.11) is convergent.

Proposition: This case cannot be realized, if one pushes the defocusing point to ∞ then the integral in Eq. (2.3.11) diverges.

Proof: To have the defocusing point at ∞, $\dot{a} \to 1$ for $t \to -\infty$. This can be seen following the proof of Case A.I simply putting $t_0 = -\infty$. If $\dot{a} \to 1$ for $t \to -\infty$ it always remains positive in the infinite domain $(-\infty, t(0)]$, thus if $a(t)$ is finite at the point $t = 0$, it must have crossed or reached the value of 0 at some point in the past. This proves that the integral in Eq. (2.3.11) diverges and that there must be a curvature singularity.

As explained at the end of Sec. 2.4.1, Case B.II cannot be achieved within the family of geometries being considered.

2.4.3 Cases B.III and B.IV $(\infty, 0)$

The defocusing point is at an infinite affine distance and the integral in Eq. (2.3.11) is divergent (it goes to $-\infty$).

Proposition: This case is singular.

Proof: If $\dot{a} \to 1$ for $t \to -\infty$ it always remain positive in the infinite domain $(-\infty, t(0))$, thus if $a(t)$ is finite at the point $t = 0$, it must have crossed or reached the value of 0 at some point in the past. This proves that there must be a curvature singularity.

Note that, as explained at the end of Sec. 2.4.1, it is not possible to achieve Case B.IV within the family of geometries being considered.

2.4.4 Cases C.I and C.II $(\emptyset, 0)$

This case is singular, and the proof proceeds as for case B.III.

As discussed at the end of Sec. 2.4.1, it is impossible to achieve case C.II within the family of geometries being considered.

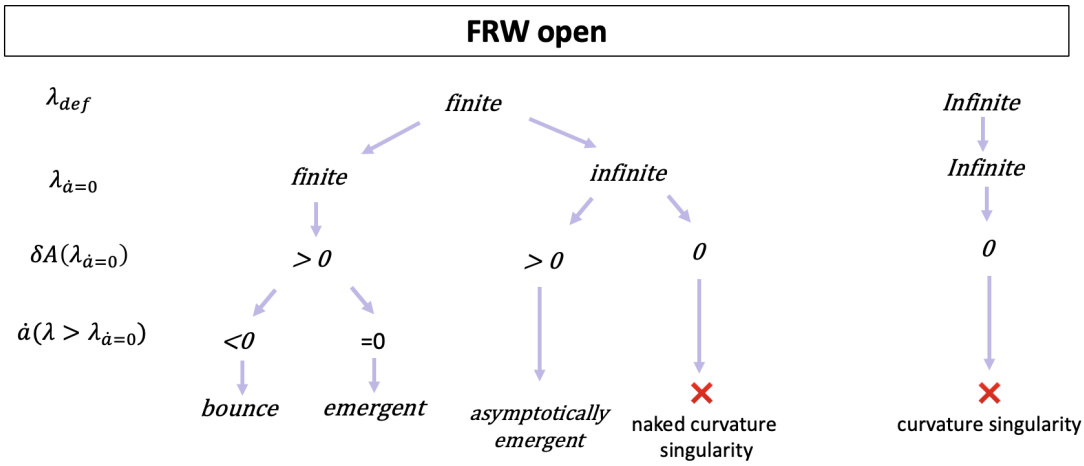

Figure 2.9: Scheme of the allowed open homogeneous and isotropic regular geometries. These geometries are classified according to: i) the value of the affine parameter at which all outgoing geodesics are defocused $\lambda_{def}|\ \theta_+(\lambda_{def}) = 0$; ii) the value of the affine parameter at which the universe ceases to contract/expand that is $\lambda_{\dot{a}=0}$; iii) the area element orthogonal to the congruence at λ_{def}; iv) the derivative of the scale factor for $\lambda > \lambda_{def}$, i.e. for $t < t_{def}$.

2.5 Regular Closed FLRW universes

In the case of a closed universe, the non-compactness assumption of the Penrose theorem is no more guaranteed, thus in general we would have to rely on the Hawking-Penrose theorem. However, as we will show in the following, in the specific case of a homogeneous and isotropic universe (describable by the FLRW metric), simpler assumptions suffice to prove the presence of a singular focusing point.

The first part of Penrose's theorem makes no use of the presence of a non-compact Cauchy hypersurface, and thus is also valid for any generic closed spacetime, it shows that

an initial negative expansion and the null convergence condition are enough to prove the presence of a focusing point in which the expansion will become infinitely negative. What is no more guaranteed for closed spacetimes is that this focusing point is singular.

The expansion of null geodesics in a closed FLRW spacetime is given by:

$$\theta_{\pm} = \frac{2}{a^2(t)}\left[-\dot{a}(t) \pm \frac{1}{\tan r(t)}\right]. \tag{2.5.1}$$

Note that $1/\tan r$ is a periodic function thus we can evaluate it in $r \in [0, \pi]$, taking values ∞ for $r \to 0$, 0 for $r \to \pi/2$ and $-\infty$ for $r \to \pi$. Both poles (0 and π) correspond to $R(r) = 0$, and the reason for which the expansions there blow up with different signs is geometrical and essentially the same reason for which the expansion of geodesics in flat Minkowski blows up at $r = 0$. These points are then regular focusing points.

Using this expression for the expansions we now show that, in presence of a trapped region where both expansions $\theta_{\pm}$ are negative, a singular focusing point is always present if the timelike convergence condition holds (this implies the strong energy condition in GR). In order to isolate the divergent behavior at the focusing point, while avoiding the divergences caused by the poles, it is useful to introduce the following quantity:

$$\theta = \theta_+ + \theta_- = -\frac{2\dot{a}(t)}{a^2(t)}. \tag{2.5.2}$$

If both $\theta_{\pm}$ are negative initially, and thus a trapped surface is present, then also θ will have an initial negative value $\theta_0 < 0$. On the other hand, θ is the expansion of a past-directed time-like congruence of geodesics with tangent vector $U^a = (-2, 0, 0, 0)/a(t))$ and, as such, it satisfies the Raychaudhuri equation with zero twist and shear:

$$\frac{d\theta}{d\lambda} = -\frac{\theta^2}{3} - R_{\mu\nu}U^{\mu}U^{\nu}. \tag{2.5.3}$$

From the timelike convergence condition ($R_{\mu\nu}u^{\mu}u^{\nu} \geqslant 0 \quad \forall u^{\mu}$ timelike) — or the strong energy condition if one assumes the Einstein field equations — we have that

$$\frac{d\theta_{\pm}}{d\lambda} \leqslant -\frac{\theta_{\pm}^2}{3}, \tag{2.5.4}$$

so that, in the best case scenario (the expansion taking the least negative value possible), we have

$$\frac{d\theta}{d\lambda} = -\frac{\theta^2}{3}. \tag{2.5.5}$$

Solving this differential equation results in the expression

$$\theta^{-1} = \theta_0^{-1} + \frac{\lambda}{3}, \tag{2.5.6}$$

which indicates that θ will reach $-\infty$ for a finite value of the affine parameter (in particular, $-3\theta_0^{-1}$).

On the other hand, taking a look at the functional form of θ in Eq. (2.5.2), we see that it can reach $-\infty$ only if $a(t) = 0$ or $\dot{a}(t) \to +\infty$. Both cases correspond to a divergence of the Ricci scalar in Eq. (2.1.8) and thus this focusing point is associated with a curvature

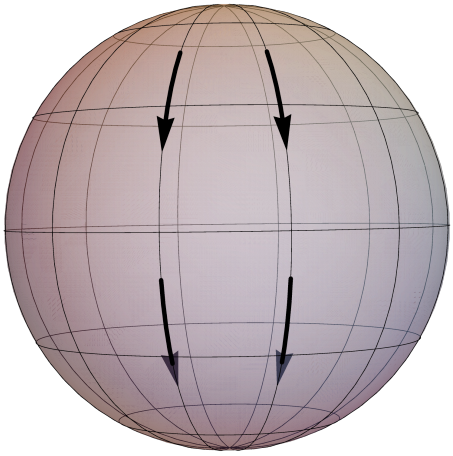

Figure 2.10: Path of geodesics in a two-dimensional closed spacetime. As we can see the ingoing/outgoing nature of trajectories changes at the equator and the poles.

singularity.

In summary, we have proved that a spacetime satisfying the following assumptions cannot be geodesically complete:

- It is a homogeneous and isotropic solution of Einstein equations.
- The timelike convergence condition holds.
- At some point a closed past-trapped surface forms.

Based on this result, let us continue with our aim of characterizing the different possible regular solutions with a trapped region, following the classification discussed in Section Section 1.1.

2.5.1 Case A

The reasoning is similar to the corresponding case for flat spacetime but taking into account that now $\theta_+ < 0$ does not correspond necessarily to a trapped region, since outgoing and ingoing geodesics exchange roles for some values of r (see Fig. 2.10). We thus have to check the sign of both θ_+ and θ_-, and a trapped region is indeed present if both are negative.

Proposition: All congruences of null geodesics are untrapped at finite affine distance λ corresponding to time t *if and only if* the derivative of the scale factor with respect to the time, $\dot{a}(t)$, vanishes.

Proof: Let us assume that $\dot{a}(t)$ does not vanish but remains positive for any value of t. Then for any t all the geodesics for which $-\dot{a}(t) < 1/\tan r(t) < \dot{a}(t)$ would have $\theta_\pm < 0$ and thus would be trapped. These trapped geodesics always exist. Indeed since, for the periodic nature of the metric functions, r can be taken in the finite interval $[0, \pi]$, it is always possible to choose an initial value for the photon position $r(0)$ such that $r(t)$ is sufficiently near $\pi/2$ to satisfy the previous trapping condition. Conversely, if $\dot{a}(t)$ becomes negative, $\theta_+ < 0$ only for geodesics with $1/\tan r(t) < \dot{a}(t) < 0$ while $\theta_- < 0$ only for geodesics with $1/\tan r(t) > -\dot{a}(t) > 0$. Thus there are no geodesics for which both θ_+ and θ_- are negative, and therefore no trapping region if $\dot{a}(t)$ becomes negative.

Hence, also for the closed case, this class describes a bounce with $\dot{a}(t)$ vanishing between a contracting and an expanding universe (or, if we drop the assumption that the scale factor is an analytic function of time, an expanding universe emerging from a stationary phase).

For what regards the distinction between case A.I and A.II, we saw that in a closed universe outgoing and ingoing geodesics exchange roles for some values of r (see Fig. 2.10).

The homogeneity and isotropy assumption strongly constrain the behavior of one family of geodesics with respect to the other. Indeed, if $\theta_+(t) = 0$, then

$$\theta_-(t) = -\frac{4}{a^2(t)\tan r(t)}, \tag{2.5.7}$$

and if $\theta_-(t) = 0$, then

$$\theta_+(t) = -\frac{4}{a^2(t)\tan r(t)}. \tag{2.5.8}$$

Hence, it is not possible to achieve at the same time $\theta_+(t) = 0$ and $\theta_-(t) \geqslant 0$ (or $\theta_-(t) = 0$ and $\theta_+(t) \geqslant 0$) for all null geodesics (case A.II) within the family of geometries being considered.

An analogous reasoning leads to the same conclusions also for the case B.II, B.IV and C.II thus we neglect this discussion about ingoing geodesics in the next sections.

2.5.2 Case B

Analogously to the Case A, all congruences of null geodesics are untrapped at infinite affine distance if and only if the derivative of the scale factor with respect to the time, $\dot{a}(t)$, vanishes for $t \to -\infty$. The proof proceeds as in Case A, simply considering $t \to -\infty$.

Differently from the flat and open case, we can no longer use the integral in Eq. (1.1.1) to distinguish between cases B.I (no focusing point) and B.III (asymptotic focusing point) since in this case this integral always diverges for long enough geodesics (even for regular spacetimes), due to the divergent behavior of the term $1/\tan[r(t)]$ in the expansion. However, the presence of a singularity can be still detected in the behavior of geodesics since it is signaled by the vanishing of the universe radius $a(t)$ that causes the negative divergence of both expansions, $\theta_\pm \to -\infty$.

Note that, as explained in 2.5.1, it is not possible to achieve Case B.II and B.IV within the family of geometries being considered.

2.5.3 Case C

We can show that curvature invariants must be singular in this case. By definition, there is now some congruence for which both $\theta_\pm$ remain negative for $\lambda \to +\infty$ ($t \to -\infty$). From Eq. (2.5.1), we can conclude that this can happen only if $\dot{a}(t)$ remains positive in the semi-infinite domain $(-\infty, 0]$. As a consequence, if $a(t)$ is finite at $t = 0$, it must have crossed or reached the value of 0 at some point in the past due to its derivative being definite positive in a semi-infinite domain. This proves that there is a curvature singularity.

Note that, as explained in 2.5.1, it is not possible to achieve Case C.II within the family of geometries being considered.

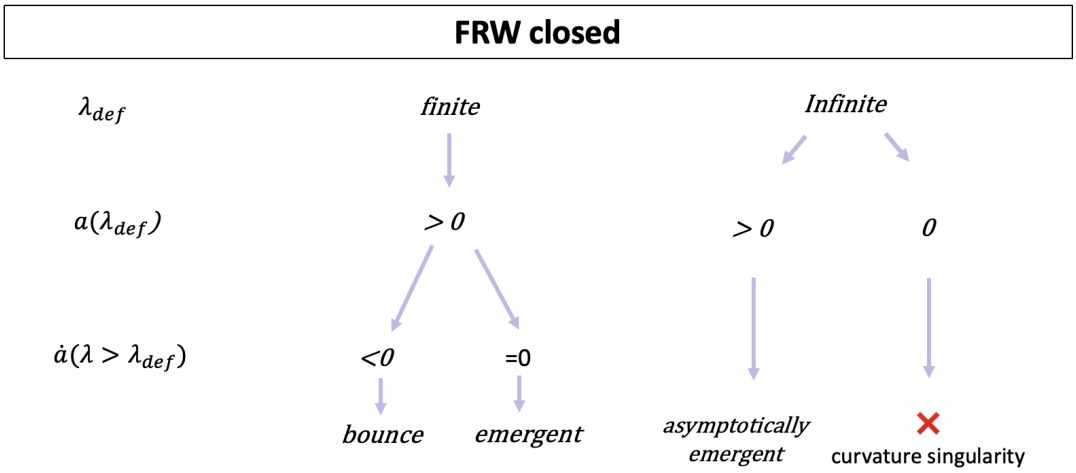

Figure 2.11: Scheme of the allowed closed homogeneous and isotropic regular geometries. These geometries are classified accprding to: (i) the value of the affine parameter at which all outgoing geodesics are defocused λ_{def}, so that $\theta_+(\lambda_{def}) = 0$; (ii) $a(\lambda_{def})$ or equivalently the value of both expansions for the same value of the affine parameter [note that, if $a(\lambda_{def}) = 0$, then $\theta_\pm(\lambda_{def}) = -\infty$]; (iii) the derivative of the scale factor for $\lambda > \lambda_{def}$, i.e. for $t < t_{def}$.

2.6 Conclusions

This chapter delves into the behavior of null geodesics within various spacetime geometries in the context of cosmology. The investigation primarily focused on the behavior of the expansion of null congruences with the aim of classifying from a geometric standpoint the possible regularizations of the initial singularity. Distinct scenarios emerged based on the behavior of the expansion and the presence and extension of trapped regions. These scenarios are:

- A bouncing universe.
- An expanding universe emerging from a stationary phase.
- An asymptotically emergent universe where the scale factor is always decreasing towards the past but never vanishes. An example of scale factor with these characteristics is an inflating universe, with a characteristic exponential behavior of the scale factor but with the addition of a constant that corresponds to the asymptotic value of $a(t)$ towards the past.

The analysis of closed universes presented unique challenges due to the violation of the non-compactness assumption and to the diverging nature of certain functions influencing geodesic expansions. Despite this, it was established that, also in this case, true defocusing points at finite or infinite affine distance are contingent upon specific behaviors of the scale factor derivative with respect to time. Moreover, the absence of defocusing leads to the inevitable occurrence of a curvature singularity.

Regarding the physical interpretation of the bouncing solutions, it is interesting to keep in mind the following consideration. The metric alone does not provide any real information regarding the direction in which time flows. GR is time-symmetric, as flipping

the t-direction on a globally hyperbolic manifold results in another valid solution to the field equations.[5]

The scenario of a universe contracting to a minimum scale factor and then expanding stems from the implicit assumption that the direction of time remains the same before and after the bounce. However, it is possible to imagine a scenario in which the two parts of spacetime separated by the defocusing point have opposite time directions. In this case, we would have two identical expanding bouncing universes joined at the defocusing point (the bounce). The reason why we expect the inversion of time direction to be possible at the bounce is because, besides being a stationary point for the expansion of the universe, it is also a point at which we expect quantum gravitational effects to play an important role, causing this possible inversion. If for example, as in the Hartle-Hawking no boundary proposal [54], near the would-be-singularity time becomes imaginary, it would lose any privileged direction there, making the subsequent appearance of an opposite arrow of time more natural. Furthermore, this scenario seems also to connect to similar ideas advanced to address the so called "arrow of time" problem [55, 56].

In conclusion, this study elucidates the diverse range of regular possibilities within cosmological models, shedding light on the interconnections between geodesic behavior, singularities, and the evolution of the universe. These findings not only contribute to our theoretical understanding of the universe's behavior but also pave the way for refining cosmological models based on observational data and theoretical considerations. Efforts to probe these possible regularizations with empirical observations and astrophysical data would be instrumental in refining and validating cosmological models. Even if it seems difficult to test such a remote region of the cosmological spacetime, there are already works showing how quantum gravitational effects responsible for the regularization of the initial singularity can leave some imprints on observables of the late-time universe [57–59]

[5]Note that, due to the fact that at the bounce $\dot{a}(t) = 0$, this would be possible while keeping the metric components at least C^1, and could be possibly fine-tuned so that at the bounce one also has $\ddot{a}(t) = 0$ so as to ensure regularity of curvature tensors as well.

Part III

Global solutions and their stability

All things by immortal power,
Near or far,
Hiddenly
To each other linked are,
That thou canst not stir a flower
Without troubling of a star
— Francis Thompson

Chapter 3

Background: constructing regular alternatives to black holes

In this chapter, we show how to construct specific global solutions that embody the previously classified local regularizations and we will discuss about their self-consistency and stability. We will focus on metrics describing both static and rotating compact objects. Instead, we will not delve into the specifics of the aforementioned global regular metric describing cosmological spacetime as bouncing or emergent universes. For further information, in addition to the previously cited literature, refer also to [60–63].

Conditions for the regularity of the curvature scalars

In order to prove the regularity of the considered alternative models, we will always check the absence of curvature singularities.

In spacetimes that are both static and spherically symmetric, the Kretschmann scalar, being a sum of squares, is always non-negative. For this reason, it can be demonstrated that in such spacetimes, the Kretschmann scalar is bounded if and only if all the components of the Riemann tensor in an orthonormal frame are also bounded. Thus, in a static and spherically symmetric spacetime, the boundedness of the Kretschmann scalar suffices to guarantee that all scalar polynomials constructed from the Riemann tensor (along with the metric and the Levi-Civita fully antisymmetric tensor) are also bounded [64].

When these symmetry assumptions are removed, the situation becomes significantly more complex. In a generic spacetime, there are seventeen algebraically independent curvature invariants. A comprehensive set of these invariants has been provided in [65]. To assert that a spacetime is devoid of scalar polynomial curvature singularities, theoretically, the boundedness of all these invariants must be verified. Fortunately, the effective models examined in this thesis exhibit a high degree of symmetry, thus obviating the need for this laborious verification process in most instances. For example, the most frequently encountered simply connected rotating regular black holes are classified as Petrov type D and Segre type [(1, 1), (1, 1)]. In such cases, the number of independent curvature invariants is reduced to four [66, 67]. Similarly, in multiply connected models, the regularization process is generally designed in such a manner that the boundedness of curvature invariants is immediately apparent.

The effective matter content

Based on the assumptions outlined in Part I, the effective models we aim to develop do not necessarily have to be solutions of General Relativity. Nevertheless, Einstein's equations can still be utilized to study the geometries and, specifically, to measure the deviations from vacuum GR. Our models are intended to represent, to a first approximation, isolated astrophysical objects, and any deviation from vacuum GR should be attributed to the hypothetical new physics assumed to prevent singularity formation — rather than to the presence of ordinary matter. In some cases, we will calculate the Einstein tensor and set it equal to the stress-energy tensor of what we refer to as effective sources. This term is chosen for its convenience and intuitiveness, but it should be understood that we do not assume the existence of any real matter source. Therefore, one should not be concerned if the effective sources appear 'exotic', for example, due to the violation of some energy conditions. In fact, from our perspective, the violation of energy conditions is not a disadvantage but rather a necessary feature of singularity regularization. As we will see, it is often feasible to find classical theories that incorporate these effective models as solutions. Generally, these theories consist of GR supplemented with some form of non-linear electrodynamics, meaning the Lagrangian is a non-linear function of the Maxwell scalar, and potentially a phantom scalar field, i.e. one whose kinetic term has an opposite sign compared to conventional scalar fields [68–71]. Additionally, such solutions have been derived in certain specific alternative gravity theories [72–77].

3.1 Spherically symmetric and static models

A static spacetime can be foliated by hypersurfaces orthogonal to a timelike Killing vector field, denoted as χ_μ. Spherical symmetry indicates that these hypersurfaces can themselves be foliated by two-dimensional spheres. One can then introduce a time coordinate t associated with the orbits of χ_μ and two coordinates θ and ϕ analogous to standard spherical coordinates. A fourth coordinate r can be introduced to label the different spheres within a constant-t hypersurface. This coordinate, termed "radius" for simplicity, generally lacks direct physical interpretation. In these coordinates, the metric becomes diagonal and can be expressed as:

$$ds^2 = -e^{-2\phi(r)} f(r) dt^2 + \frac{dr^2}{f(r)} + h(r)(d\theta^2 + \sin\theta^2 d\varphi^2) \tag{3.1.1}$$

One can always redefine the radial coordinate to "gauge away" one between ϕ and h, since in literature there are examples of both "gauge" choices we will keep both ϕ and h as free functions in this section. The requirement of asymptotic flatness and of a clearly defined Newtonian limit can be expressed as straightforward criteria on the free functions f, ϕ, and h:

$$f(r) \xrightarrow{r\to\infty} 1 - \frac{2M}{|r|} + O(r^{-2}), \quad e^{-2\phi(r)} \xrightarrow{r\to\infty} 1 + O(r^{-2}), \quad h(r) \xrightarrow{r\to\infty} r^2(1 + O(|r|^{-3}) \tag{3.1.2}$$

This general metric can posses horizons and wormhole throats. To formally characterise them we need to analyse the expansion of null geodesics. For this purpose, we chose two

future-directed radial null geodesics with tangent vectors normalized as $V_+V_- = -1$:

$$V_+^\mu = \left(-\frac{e^{\phi(r)}}{2}, \frac{f(r)}{2}, 0, 0\right) \quad V_-^\mu = \left(-\frac{1}{e^{-\phi(r)}f(r)}, -1, 0, 0\right), \tag{3.1.3}$$

The expansion of such geodesics is then:

$$\theta_+ = \frac{f(r)h'(r)}{h(r)} \quad \theta_- = -\frac{h'(r)}{h(r)} \tag{3.1.4}$$

The horizons corresponds to marginally trapped surfaces at which θ_+ vanishes, this happens when $f(r) = 0$. Wormhole throats corresponds to the surfaces at which both expansions vanish, this happens when $h'(r) = 0$.

3.1.1 Simply connected solutions: from multiple horizons RBHs to horizonless stars

In literature a vast variety of simply connected solutions (i.e. of the "multiple horizons" type) has been explored [78–82]. The defining characteristic of a simply connected spacetime is that any closed path can be contracted to a point, therefore the spheres centred at the origin will also be contractible to a point, which cannot be anything but the origin $r = 0$. Hence, it must be $h(0) = 0$. Usually a choice of minimal deviation from Schwarzschild is performed putting

$$\phi(r) = 0, \quad h(r) = r^2, \tag{3.1.5}$$

and in analogy with the Schwarzschild metric we can write:

$$f(r) = 1 - \frac{2m(r)}{r}. \tag{3.1.6}$$

Thus the regularization consist in substituting the usual mass parameter M with what is usually called Misner-Sharp mass function m(r) [83, 84]. From asymptotic flatness we require

$$\lim_{r\to\infty} m(r) = M. \tag{3.1.7}$$

As previously explained, in order to ensure curveture regularity in spherically symmetric spacetimes it is sufficient to require the boundedness of the Kretschmann scalar. In this case it reads:

$$R^{\mu\nu\alpha\beta}R_{\mu\nu\alpha\beta} = f''(r)^2 + 4\frac{f'(r)^2}{r^2} + 4\frac{(1-f(r))^2}{r^4}. \tag{3.1.8}$$

Imposing the boundedness of $R^{\mu\nu\alpha\beta}R_{\mu\nu\alpha\beta}$ translates in a simple requirement on the Misner-Sharp mass close to $r = 0$:

$$m(r) = c\ell^{-2}r^3 + O(r^4), \tag{3.1.9}$$

Model	$m(r)$
Bardeen [78]	$M\frac{r^3}{(r^2+\ell^2)^{3/2}}$
Hayward [79]	$M\frac{r^3}{r^3+2M\ell^2}$
Dymnikova [80]	$M\left[1-\exp(-\frac{r^3}{2M\ell^2})\right]$
Fan–Wang [81]	$M\frac{r^3}{(r+\ell)^3}$

Table 3.1: Some of the most popular RBH models. More examples e.g. in Refs. [89–93]

with c a dimensionless number of order one and ℓ a non-negative length scale to which we will refer as "regularizing" or "regularization" parameter[1].
Thus, for small r, the metric reads:

$$ds^2 = -[1 - 2c\ell^{-2}r^2 + O(r^3)]dt^2 + [1 + 2c\ell^{-2}r^2 + O(r^3)]dr^2 + r^2(d\theta^2 + \sin\theta^2 d\varphi^2), \tag{3.1.10}$$

describing a de Sitter core if $c > 0$, an anti de Sitter core if $c = 0$ or a Minkowsky core if $c = 0$. Indeed, the Einstein tensor for small r becomes the one corresponding to a (effective) cosmological constant:

$$G_{\mu\nu} = \Lambda_{\text{eff}} g_{\mu\nu} = \frac{6c}{\ell^2}. \tag{3.1.11}$$

It is important to note that these geometries are generally non-singular only for $r \geqslant 0$. If the coordinate r is allowed to take negative values, spacetime singularities might still occur, either as divergences in curvature or through geodesic incompleteness [87, 88]. The restriction of the domain of r to $[0, +\infty)$ aligns with the interpretation of r as a radius. Some widely studied choices of $m(r)$ are summarized in Table 3.1.

For all models, in the limit $\ell \to 0$ the Schwarzschild metric is recovered. Also the presence/absence and the number of horizons depend on the value of ℓ. Indeed the horizons are determined by the roots of $f(r) = 0$. Since $f(r)$ goes to 1 both at the center and at infinity and it is continuous, horizons will always be in pair: for any outer event horizon there will be an inner horizon. Note however that the position of the two horizons can coincide resulting in a single degenerate horizon. Concluding, depending on the value of ℓ, we can have three different cases:

- ℓ is in $(0, \ell_*)$ for some model dependent threshold ℓ_* and the spacetime presents multiple horizons.
- $\ell = \ell_*$ the horizons degenerates into a single extremal (i.e. with vanishing surface gravity) horizon.
- $\ell > \ell_*$ and the spece-time presents no horizons, it describes a regular, horizonless

[1] In some studies a less stringent regularity condition is imposed: singularities in the curvature scalars can be present but the stress energy tensor must be integrable [85, 86]. In these case the condition on the mass parameter near 0 reduces to $m(r) \propto r^2$

exotic compact object.

3.1.2 Multiply connected solutions: from hidden wormholes to traversable wormholes

For this case we will initially work in the gauge in which $\phi(r) = 0$ but $h(r)$ is non-trivial, we will see however that an equivalent choice is to put $h(r) = r^2$ but $\phi(r) \neq 0$. Differently from the previous case, in multiply connected spacetime the aerial radius $\sqrt{h}$ never reduces to zero. We will assume to have two asymptotically flat regions for $r \to \pm\infty$ connected through a global minimum of h, which we locate without loss of generality at $r = 0$. This means that:

$$h(0) = \ell^2 \quad h'(0) = 0 \quad \text{and} \quad h''(0) \geqslant 0 \tag{3.1.12}$$

with ℓ a length scale that, as in the case of simply connected solutions, we will call "regularizing" or "regularization" parameter. The Kretschmann scalar is then:

$$R^{\mu\nu\alpha\beta}R_{\mu\nu\alpha\beta} = \frac{3f^2h'^4}{4h^4} + f''^2 - fh'^2\frac{2 + f'h' + 2fh''}{h^3} + \frac{4 + f'^2h'^2 + 2ff'h'h'' + 2f^2h''^2}{h^2} \tag{3.1.13}$$

from which it is clear that no curvature singularities are present if $h(r) \neq 0$ for $r \in (-\infty, +\infty)$. Usually in literature we find minimal models in which:

$$f(r) = 1 - \frac{2M}{\sqrt{h(r)}}. \tag{3.1.14}$$

In these models the geometry of the core will depend on the choice of $h(r)$ and in general it will not possess any clear interpretation in terms of the three simple maximally symmetric spaces.

The spacetime presents both horizons located at the roots of $f(r) = 0$ and wormhole throats located at the roots of $h'(r) = 0$, from 3.1.12 is clear that one of these is at $r = 0$.

Depending on the position of the throat with respect to the horizons, we can have an *hidden throat* that is shielded by one or more horizons, a *null throat* that coincide with an horizon or a *traversable throat* that is a timelike hypersurface, not shilded by any horizon and thus crossable in both ways by causal curves. Usually the "regularizing" parameter ℓ will enter the metric functions in such a way that depending on its value the spacetime will interpolate between these three cases. A popular example of this kind of regularization is the Simpson-Visser (SV) metric [64, 94]:

$$ds^2 = -\left(1 - \frac{2M}{\sqrt{r^2 + \ell^2}}\right)dt^2 + \frac{dr^2}{\left(1 - \frac{2M}{\sqrt{r^2+\ell^2}}\right)} + (r^2 + \ell^2)(d\theta^2 + \sin^2\theta d\varphi^2). \tag{3.1.15}$$

Similar examples are described in [95–97].

The SV model corresponds to the simple choice $h(r) = r^2 + \ell^2$, it is symmetric under the inversion $r \to -r$ and thus describe two identical universes connected by throat at $r = 0$, we will refer to the positive-r region as *our universe* and to the negative-r region as

the *other universe*. Depending on the value of ℓ, it can describe three different scenarios:

- if $\ell < 2M$ there are two horizons one for each universe and $r = 0$ is an *hidden throat*,
- if $\ell = 2M$ the horizons degenerate in one extremal horizon (with vanishing surface gravity) located at the *null throat*,
- if $\ell > 2M$ there are no horizon and the throat at $r = 0$ is a *traversable throat*.

For phenomenological applications it is useful to rewrite the SV metric in a different gauge that correspond to the change of coordinates $\sqrt{r^2 + \ell^2} \to \tilde{r}$. In this gauge the radial coordinate is defined in $[0, +\infty)$ and every value of $\tilde{r}$ describe a couple of points $\pm r$ one for each universe of the old gauge. The new metric line reads:

$$ds^2 = -\left(1 - \frac{2M}{\tilde{r}}\right) dt^2 + \frac{d\tilde{r}^2}{\left(\frac{\tilde{r}^2 - \ell^2}{\tilde{r}^2}\right)\left(1 - \frac{2M}{\tilde{r}}\right)} + \tilde{r}^2(d\theta^2 + \sin^2\theta d\varphi^2) \tag{3.1.16}$$

that correspond to the line element 3.1.1 with:

$$\phi(r) = \frac{1}{2}\ln\left(1 - \frac{\ell^2}{r^2}\right), \quad f(r) = 1 - \frac{2}{r}\left[M\left(1 - \frac{\ell^2}{r^2}\right) + \frac{\ell^2}{2r}\right], \quad h(r) = r^2. \tag{3.1.17}$$

We will use this other gauge in Chapter 6.

3.2 Rotating models

Although precisely measuring the spin of astrophysical black holes can be challenging, it is well established that their angular momentum is generally non-zero. Consequently, any phenomenologically relevant model of compact objects must incorporate rotation . However, this introduces significant challenges, even within General Relativity. For instance, consider the problem of determining the metric for a star: Birkhoff's theorem guarantees that in spherical symmetry, the vacuum metric outside the star is the Schwarzschild metric, so one only needs to solve Einstein's equations for the star's interior. In contrast, with only axial symmetry, there is no assurance that the exterior metric is Kerr, as no analogous theorem to Birkhoff's exists in this scenario. Departing from GR, the complications only increase, making the construction of rotating models from scratch particularly difficult.

Luckily, there exist a method, the Newman-Janis procedure (NJP), to find the stationary and axially symmetric "counterpart" of a given static spacetime. The NJP was first identified in the 1960s as a method to connect the Schwarzschild solution with the Kerr solution. Shortly after, it was employed to derive the Kerr–Newman metric from the Reissner–Nordström solution [98]. Importantly, the method has been widely applied to create rotating solutions in alternative gravity theories [99–101] (although see [102]) and rotating regular black holes [103, 104]. Despite its achievements, the method contains some perplexing arbitrariness — which we will discuss in more detail below — and a complete understanding of its mechanism is still missing. Some foundational work has been done in [105], and further insights were provided by [106–108], more recently, new perspectives have emerged from the study of scattering amplitudes [109, 110]. Nevertheless, the status of the NJP remains highly controversial to this day.

In our framework, spacetimes generated using the NJP are valid examples since we are considering them from an "effective" perspective and we are focusing on phenomenological uses only; however, the method's limitations are significant and must be acknowledged.

There exist two version of the NJP, for the details about both of them, we refer the reader to the original papers [111–113]. Here we only report the final form of the rotating version of the metric 3.1.1 obtained with the most modern version of the method:

$$ds^2 = \frac{\Psi}{\Sigma}\left[-\left(1-\frac{2H}{\Sigma}\right)\mathrm{d}t^2 + \frac{\Sigma}{\Delta}\mathrm{d}r^2 + \Sigma\mathrm{d}\theta^2 + \frac{A\sin^2\theta}{\Sigma}\mathrm{d}\varphi^2 - \frac{4Ha\sin^2\theta}{\Sigma}\mathrm{d}t\ \mathrm{d}\varphi\right], \quad (3.2.1)$$

where

$$\Sigma = K + a^2\cos^2\theta, \quad 2H(r) = K - f(r)h(r), \quad \Delta = f(r)h(r) + a^2,$$
$$A = \left(K + a^2\right)^2 - a^2\Delta\sin^2\theta, \quad K = h(r)e^{\phi(r)}.$$

The previously mentioned arbitrariness of the method is encoded in the arbitrary conformal factor $\Psi(r,\theta)$. In order to recover the Kerr metric from the Schwarschild one, we need to impose $\Psi(r,\theta) = \Sigma(r,\theta)$ that seems to be a very natural choice. Furthermore, if a metric can be interpreted as solution of some non-linear electrodynamics, that is the case for many regular black holes metrics, the field equations imply the same condition $\Psi = \Sigma$. However more generally one can impose only to recover the original static metric in the limit $a \to 0$ which means to impose

$$\lim_{a\to 0}\Psi(r,\theta) = r^2. \quad (3.2.2)$$

3.2.1 Simply connected solutions

Using as static seed the popular simple connected regular solutions described in Section 3.1.1 ($f(r) = 1 - \frac{2m(r)}{r}$, $\phi(r) = 0$ and $h(r) = r^2$) and making the simple choice $\Psi = \Sigma$ one obtains from 3.2.1 a metric similar to the Kerr one but with a mass function $m(r)$ in place of the mass parameter, the so called Gürses-Gürsey metric:

$$ds^2_{GG} = -\left(1 - \frac{2m(r)r}{\Sigma}\right)\mathrm{d}t^2 + \frac{\Sigma}{\Delta}\mathrm{d}r^2 + \Sigma\mathrm{d}\theta^2 - \frac{4m(r)a\sin^2\theta}{\Sigma}\mathrm{d}t\ \mathrm{d}\varphi + \frac{A\sin^2\theta}{\Sigma}\mathrm{d}\varphi^2 \quad (3.2.3)$$

where

$$\Sigma = r^2 + a^2\cos^2\theta, \quad \Delta = r^2 + a^2 - 2m(r)r$$
$$A = \left(r^2 + a^2\right)^2 - \Delta a^2\sin^2\theta$$

Note however that there can be motivations to take into account also a possible angular dependence of the mass function (assuming $m = m(r,\theta)$), for example if one wants to obtain a solution that respects the locality principle [114–116]. The general properties of the spacetime in 3.2.3 have been investigated in [117, 118]. It is Petrov type D and thus it has four independent second-order curvature invariants. Imposing their boundedness we obtain the same conditions that guaranteed regularity for the static and spherically

symmetric case:

$$m(0) = m'(0) = m''(0) = 0 \tag{3.2.4}$$

However if we take $m(r) = c\ell^{-2}r^3$ as for the static case, the curvature invariants exhibit a bizarre behavior near the would-be singularity (i.e. $r = 0$ and $\theta = \frac{\pi}{2}$). Specifically, they are typically proportional to:

$$\frac{r^2}{r^2 + a^2\cos^2\theta}. \tag{3.2.5}$$

This means that the limit $r \to 0$, $\theta \to \pi/2$ does not exist. Indeed if one take before the limit $r \to 0$ keeping θ fixed one gets zero while if one takes before $\theta \to \pi/2$ and then $r \to 0$ one gets a finite non-zero result. In other words, the curvature invariants are bounded but not continuous at the would-be singularity. Moreover, since in these models the ring $r = 0$ can be crossed in finite proper time for any $\theta \neq \pi/2$, the maximal analytical extension of these spacetimes generally reaches negative values of r, similar to the Kerr spacetime. In this domain, the Killing vector related to rotational symmetry can become timelike, suggesting that the spacetime can contain closed timelike curves. Additionally, various commonly adopted forms of $m(r)$ exhibit poles in the $r < 0$ region, potentially indicating new spacetime singularities [87, 88]. Both these problems can be circumvented introducing an angular dependence in the mass function as in the examples previously cited [114–116].

3.2.2 Multiply connected solutions

Using as static seed one of the most popular model of multiply connected regular solutions, i.e. the SV model described in Section 3.1.2 ($f(r) = \frac{2M}{\sqrt{r^2+\ell^2}}$, $\phi(r) = 0$ and $h(r) = r^2 + \ell^2$), and making the simple choice $\Psi = \Sigma$, one obtains from 3.2.1 the following line element:

$$\mathrm{d}s^2 = -\left(1 - \frac{2M\sqrt{r^2+\ell^2}}{\Sigma}\right)\mathrm{d}t^2 + \frac{\Sigma}{\Delta}\mathrm{d}r^2 + \Sigma\mathrm{d}\theta^2 - \frac{4Ma\sin^2\theta\sqrt{r^2+\ell^2}}{\Sigma}\mathrm{d}t\ \mathrm{d}\varphi + \frac{A\sin^2\theta}{\Sigma}\mathrm{d}\varphi^2, \tag{3.2.6}$$

where now Σ, Δ and A are

$$\begin{aligned}
\Sigma &= r^2 + \ell^2 + a^2\cos^2\theta \\
\Delta &= r^2 + \ell^2 + a^2 - 2M\sqrt{r^2+\ell^2}, \\
A &= \left(r^2 + \ell^2 + a^2\right)^2 - \Delta a^2\sin^2\theta.
\end{aligned}$$

This spacetime is not algebraically special, however its regularity is manifest in these coordinates. Indeed, for every value of $\ell \neq 0$ the Kerr singularity is excised and $r = 0$ becomes a regular surface of finite size (ℓ^2) which observers may cross: a wormhole throat. Like in the corresponding static model, r is defined in $(-\infty, \infty)$ and the metric is symmetric under the reflection $r \to -r$, thus the spacetime is composed of two identical universes glued at $r = 0$ where the wormhole throat lies. This throat can be traversable or null and can or cannot be shielded by one, two (one for each universe) or four (two for each universe) horizons, depending on the value of ℓ and a. Indeed, the horizons lies at roots

of $\Delta = 0$:

$$r_{\pm}^2 = \left(M \pm \sqrt{M^2 - a^2}\right)^2 - \ell^2 \tag{3.2.7}$$

For further details see the original papers. [104, 119]

3.3 The "regularization" parameter

We have observed that regularizing the singularity usually introduces a new length scale ℓ, which influences the curvature near the would-be singularity. In the simply connected case, ℓ^2 is proportional to the inverse of the effective cosmological constant associated with the dS or AdS core geometry. In the multiply connected case, ℓ^2 represents the area of the throat that replaces the singularity.

To better understand the significance of this regularization scale, consider the gravitational collapse of some energy density, assuming simplistically that the collapse follows General Relativity predictions until a certain threshold, beyond which new physical effects dominate. If these new effects are related to quantum gravity, might be linked to the Planck scale, the presumed scale of quantum gravity. Choosing a specific Planck-scale quantity involves assumptions about quantum gravity's behavior. A natural choice is $\ell \sim \ell_{planck}$, implying quantum effects become dominant when the collapsing object's radius is around the Planck length. This aligns with perturbative quantum gravity results, which suggest metric fluctuations become significant at lengths smaller than the Planck length and the theory becomes strongly coupled at the Planck mass energy scale.

An alternative, suggested by loop quantum cosmology, identifies the threshold with reaching Planckian density [34, 120]. In this scenario, $\ell \sim \ell_P \, (M/m_P)^{1/3}$ where M is the collapsing matter's mass, resulting in a larger ℓ than the previous scenario. However, for astrophysically relevant masses, ℓ would still be much smaller than M. Indeed it would be of order of $10^{-26} M_\odot$ while typical astrophysical black hole masses, range from about $3M_\odot$ to $10^2 M_\odot$ for stellar black holes observed by LIGO-Virgo-Kagra, and up to $10^{10} M_\odot$ for supermassive black holes.

In such scenarios, gravitational collapse always leads to the formation of an horizon whenever GR predicts it. The resulting regular black hole geometries are likely similar to GR solutions, with deviations too small to be observable.

However, these assumptions might be too simplistic. A regularization at the Planck scale could be followed by a dynamic process leading to a stable configuration, possibly unrelated to the quantum gravity scale. This process could preserve or destroy the horizon, resulting in a regular black hole or an horizonless object [121]. Another possibility is the emergence of new physics and semiclassical effects before reaching the Planckian regime, potentially preventing horizon formation altogether [122–125].

Therefore, these regularized models aim to provide a reasonable phenomenological description of astrophysical black holes, and one should remain open to the scale of new physics, considering values of ℓ that could be comparable to the object's mass.

Finally, the choice to use a length scale is somewhat arbitrary, motivated by the equivalence of length and mass/energy dimensions in $c = G = 1$ units and the natural association of new physics with high-energy or small-distance GR extensions. However, regulariza-

tion actually require an area scale ℓ^2, roughly corresponding to the upper bound of the curvature.

3.4 Viability and Instabilities

Both the classification of the possible geometrical regularization done in Chapter 1 and the construction of specific models performed in this chapter were purely geometric in nature and thus they not address the dynamical mechanisms that are needed in order to form and to stably maintain in existence (or not) these objects.

If analysed through the lens of General Relativity or semiclassical gravity these models can indeed presents some issues and instabilities. Even if one can think that the modified quantum gravity dynamic would prevent the onset of such instabilities, it is still reasonable to expect that far from the high curvature region of the would be singularity (and from the high energy regime of the collapse) the effective dynamic of these objects should not significantly deviate from the one predicted by GR. For this reason, a brief discussion about these dynamical issues is in order.

Instead, we will not discuss the related issue of the formation mechanisms for these objects. As explained, most models are built in a phenomenological way, simply correcting classical solutions. The lack of a robust quantum gravity framework at the foundations of these solutions translates into an almost complete ignorance of the physical dynamical mechanisms necessary in order to prevent the formation of the singularity or even of the horizon during the collapse. As mentioned in Section 3.3, some attempts to deal with this problem in loop quantum gravity or in the semiclassical framework can be found in [34, 120–126].

3.4.1 Mass inflation

Many of the models described in this chapter, in particular all the ones with simply connected topology, present an inner horizons behind the event horizon. This raised some debate about their stability because of a phenomenon known as *mass inflation* that is an unlimited growth of mass caused by the presence of small perturbations near the inner horizon. This phenomenon is usually analyzed using two simplified models: the "double-shell" model by Poisson and Israel [127], and a variant by Ori [128].

In the double-shell model, perturbations to a spherically symmetric background are represented by two null shells, one ingoing and the other outgoing, which intersect at a point. At this crossing point, junction conditions are imposed on the metric components to maintain continuity. These conditions, along with assumptions about the late-time behavior of the ingoing shell (such as satisfying Price's law), demonstrate that the Misner–Sharp mass between the two shells increases without bound as the crossing point approaches the inner horizon. This exponential divergence affects the curvature and its timescale is determined by the inner horizon's surface gravity.

Ori's model replaces the ingoing null shell with a more realistic continuous influx of null dust. The analysis follows a similar process and yields comparable results. Consequently, it is generally believed that in General Relativity, the back-reaction of perturbations on the geometry causes the inner horizon to shrink to $r = 0$.

Both models were initially designed to study the stability of the Reissner–Nordström inner horizon but are also applicable to RBHs with inner horizons.

Some researchers argue that certain RBHs show a polynomial, rather than exponential [129], divergence, which is much milder, especially when considering Hawking evaporation [130]. However it was later understood that that although the divergence may appear polynomial at late times, it is always preceded by an exponential phase [131, 132].

Additionally, the classical mechanism has a semiclassical counterpart suggesting different outcomes [133–135]. When quantum perturbation back-reaction is considered, the inner horizon appears to be pushed outward, making the fate of perturbed inner horizons unclear. Furthermore the timescale of the semiclassical mass inflation instability seems to depend on the difference between the surface gravity of the two horizons rather then uniquely on the inner horizon one.

In Chapter 4 we will discuss how the instability related to classical mass inflation could be quenched. We will do so by constructing a rotating model of a RBH whose inner horizon has been appropriately engineered. The resulting "inner-extremal" RBH could seem somewhat artificial, and it should be considered as a proof of concept that models of simply connected RBHs without classical mass inflation are in principle viable. The construction of models free of the semiclassical mass inflation instability is instead performed in [136].

3.4.2 Lightring instability

A common feature of horizonless ultracompact objects, like wormholes and exotic stars, is the presence of a stable lightring, i.e. of a stable circular orbit for massless particles in addition to the standard unstable one (located at $r \sim 3M$ for spherically symmetric objects). This additional stable orbit corresponds to a minimum in the potential of the field equation for massless linear perturbations causing them to accumulate near this stable lightring. Indeed the analysis of linear perturbations of numerous horizonless compact objects [137–139] pointed out the presence of long-living perturbations, semi-trapped in the minimum and slowly leaking out. In time domain these perturbations decay slower than $\frac{1}{t}$, this leads to the breaking of linear approximation and it is considered an hint of a non-linear instability.

An intuitive way to see it is the following. In perturbation theory each order is the source of the next one in the linearized Einstein field equations, then if $h^{(n)}$ is the perturbation at the n-th order, one has

$$\Box h^{(2)} \propto h^{(1)} \propto \frac{1}{t^q} \quad \rightarrow \quad h^{(2)} \propto \frac{1}{t^{q-2}} \tag{3.4.1}$$

thus if $q \leqslant 1$ then $h^{(2)}$ will be increasing with t, so eventually breaking the perturbative order-expansion.

For the specific case of boson stars, numerical simulations [140] seems to confirm the presence of a non-linear instability. Furthermore, in the frequency domain these semi-trapped perturbations are described by frequencies with a very small imaginary part and a pseudo-spectrum analysis [141] showed that these type of frequencies can be easily perturbed into unstable modes, i.e. modes with a positive imaginary part. This means

that small fluctuations in the system, caused for example by enviromental effects, may trigger growing modes and thus lead to an instability.

In chapter 6, studying linear perturbations of object described by the metric 3.1.1, we will discuss again of the lightring instability and of its potential connection with another instability that should plague extremal horizons: the Aretakis instability.

3.4.3 Ergoregion instability

Outside the event horizon of any rotating black hole is a region, known as ergoregion, in which the Killing vector that corresponds asymptotically to time translations and is therefore associated with energy conservation, becomes spacelike. This means that in this region it is possible to have negative energy states and since they can exist outside the horizon, in principle it is possible to extract energy from the black hole. Indeed, suppose to have a particle of energy E_0 entering the ergorigion and splitting into two particles, one of energy E_1 escaping the black hole and one of energy E_2 falling into the black hole. Since E_2, can be negative we can have $E_1 > E_0$. This is called the Penrose Process and its field-theoretical analogue is the superradiant scattering that occurs when the amplitude of a scattered waves is greater than that of the incoming waves, resulting in energy being extracted from the object being scattered.

Compact rotating objects that lack an event horizon become unstable when they have an ergoregion [142]. This ergoregion instability occur in every circumstance in which the superradinat process repeats indefinitely. For instance, if a BH is encircled by a "mirror" that reflects the superradiant waves back towards the horizon, amplifying them with each reflection, the total energy extracted grows exponentially over time. This process, known as the BH bomb, continues until the radiation pressure destroys the mirror. If the mirror is within the ergoregion, superradiance can cause an inverted BH bomb, where some superradiant waves escape to infinity carrying positive energy, reducing the energy within the ergoregion and eventually causing instability. This can happen with any rotating star that has an ergoregion, where the mirror can be either the star's surface or its center if the star consists of matter that does not interact with the wave. BHs remain stable likely because the absorption by their event horizon surpasses the superradiant amplification.

The ergoregion instability is present in any star with ergoregions and no horizons but its time-scale strongly depends on the compactness and spin of the object. For ordinary astrophysical rotating stars the instability timescales are longer than the Hubble time [143, 144], making the ergoregion instability too weak to affect the star's evolution significantly. However, this conclusion changes dramatically for ultra-compact stars for which the instability timescale can become of order or seconds [145–150]. This seems to seriously threaten the viability of rotating horizonless alternatives to singular black holes. However, recent works [151, 152] showed that the this instability can be quenched if the horizonless object can absorb part of the incoming radiation. Furthermore, it should be taken into account that when the reflection occurs at the center of the object, because the star's matter does not interact at all with the incoming radiation, the time-scale of the instability strongly depends on the crossing time between the photon sphere and the center. This means that models with big enough crossing time (see Chapter 8) can have a huge time-scale for this instability and thus be effectively stable.

Chapter 4

A stable rotating regular black hole

In Chapter 3, we observed that simply connected RBHs are plagued by the mass inflation instability and that the timescale for such phenomenon is determined by the surface gravity of the inner horizon. This suggests a potential method to mitigate the instability: if the surface gravity is very small, the instability will take longer to develop. If the surface gravity is exactly zero, the instability is absent, at least according to the two models discussed in Section 3.4.1. Ideally, one would want to turn off the inner horizon's surface gravity without affecting the outer horizon's characteristics: specifically, its surface gravity should remain non-zero, and the two horizons should stay distinct. This means considering scenarios other than an extremal black hole. In spherical symmetry, a regular black hole model that achieves this can be easily constructed. This issue is thoroughly examined in [153], which also presents calculations demonstrating the absence of mass inflation.

Extending this result to include rotation, using a Gürses-Gürsey metric, is not straightforward, especially if one aims to maintain $m(r) \propto r^3$ near the center. Furthermore, these metrics present other issues discussed in Section 3.2.

However let us recall that the rotating metric that one obtains using the aforementioned NJP presents additional freedom with respect to the usual Gürses-Gürsey metrics, which can be encoded in an additional conformal factor $\Psi(r, \theta)$:

$$ds^2 = \frac{\Psi}{\Sigma} ds^2_{GG} \tag{4.0.1}$$

Several works in the context of conformal gravity has shown that appropriate choices for a conformal factor can lead to geodesically complete spacetimes [154–156].

Our goal is therefore to show how one can exploit such freedom to build a RBH that is free of the issues presented above: in our proposal, Ψ will be used to improve the appearances of the spacetime close to $r = 0$, while $m(r)$ will be chosen so as to trim the properties of the inner horizon.

Note, incidentally, that adding a conformal factor to Eq. (3.2.3) is by no means disruptive: the spacetime described by the metric (4.0.1) is of Petrov type D, exactly as

Eq. (3.2.3), with double null directions given by

$$l^\mu = \sqrt{\frac{\Sigma}{\Psi}}\frac{1}{\Delta}\left\{r^2+a^2,\Delta,0,a\right\}, \quad n^\mu = \sqrt{\frac{\Sigma}{\Psi}}\frac{1}{\Delta}\left\{r^2+a^2,-\Delta,0,a\right\}; \tag{4.0.2}$$

these two null vectors can be complemented with

$$m^\mu = \sqrt{\frac{\Sigma}{\Psi}}\frac{1}{\sqrt{2}\,(r+\mathrm{i}a\cos\theta)}\left\{\mathrm{i}a\sin\theta,0,1,\mathrm{i}\csc\theta\right\} \tag{4.0.3}$$

and its complex conjugate $\bar{m}^\mu$ to form a Kinnersley-like tetrad. When $\Psi(r,\theta) = \psi_r(r) + \psi_\theta(\theta)$ (i.e. it is "separable"), the geometry admits the non-trivial Killing tensor

$$K_{\mu\nu} = \Psi(r,\theta)\left[l_\mu n_\nu + l_\nu n_\mu\right] + \psi_r(r) g_{\mu\nu}\,. \tag{4.0.4}$$

In this case, the equations of motion for a test particle of Killing energy per unit mass E and Killing angular momentum along the axis of rotation per unit mass L are

$$\dot{t} = \frac{1}{\Psi\Delta}\left[AE - 2m(r)arL\right], \tag{4.0.5}$$

$$\dot{\phi} = \frac{1}{\Psi\Delta}\left[\frac{L}{\sin^2\theta}\left(\Sigma - 2m(r)r\right) + 2m(r)arE\right], \tag{4.0.6}$$

$$\Psi^2\dot{r}^2 = \left[(r^2+a^2)E - aL\right]^2 - \Delta\left(\delta\psi_r + K\right), \tag{4.0.7}$$

$$\Psi^2\dot{\theta}^2 = K - \delta\psi_\theta - \left(aE\sin\theta - \frac{L}{\sin\theta}\right)^2 = Q + \cos^2\theta\left(E^2a^2 - \frac{L^2}{\sin^2\theta}\right) - \delta\psi_\theta\,, \tag{4.0.8}$$

where $\delta = 0$ for massless particles and $\delta = 1$ for massive ones, while K is the conserved quantity associated to the Killing tensor (4.0.4), $K = K_{\mu\nu}\dot{x}^\mu\dot{x}^\nu$, and $Q = K - (Ea - L)^2$. Clearly, planar equatorial orbits are possible only if $\psi_\theta(\pi/2) = 0$.

In the more general case in which Ψ is not separable, the equations of motion are more involved and not separable. Motion with $\ddot{\theta} = \dot{\theta} = 0$ can take place on the equator and on the axis of symmetry if $\partial_\theta\Psi = 0$ there. Note that if Ψ is a function of Σ only this is always the case, since $\partial_\theta\Psi = \Psi'\partial_\theta\Sigma = 2a^2\cos\theta\sin\theta\Psi'$.

4.1 Regularizing the singularity with Ψ

In this section we discuss how the function Ψ can regularize the spacetime, regardless of the specific choice of $m(r)$. We assume such Ψ will satisfy a very minimal set of requirements, namely: $\Psi(r,\theta) > 0$ everywhere, in order to ensure that no additional singularities are introduced; and

$$\frac{\Psi}{\Sigma} = 1 + O\left(\frac{1}{r^2}\right) \text{ as } r \to \infty\,, \tag{4.1.1}$$

so that the spacetime Arnowitt–Deser–Misner (ADM) mass and specific angular momentum are still given by the parameters $M = \lim_{r\to\infty} m(r)$ and a, respectively — this is tantamount to a slightly stricter version of the usual asymptotic-flatness condition. (Note, in particular, that we do not follow the physical interpretation of Refs. [157–159] and hence

we do not impose the partial differential equations that descend from that reasoning.)

Let us now look for a Ψ that regularizes the singularity of the Kerr BH, i.e. one for which

$$ds^2 = \frac{\Psi}{\Sigma}\, ds^2_{\rm Kerr} \tag{4.1.2}$$

is the line element of a spacetime free of scalar polynomial curvature singularities. The same Ψ will also regularize more general metrics characterized by a generic (analytic) $m(r)$. As will become clear momentarily, the function Ψ can also "remove" regions of the spacetime with undesirable features.

A simple example of such Ψ is

$$\Psi = \Sigma + \frac{b}{r^{2z}}\,, \tag{4.1.3}$$

with z a real number, which we will further constrain in a moment, and b a positive constant with dimensions $[M]^{2z+2}$. Note that if $b \to 0$ as $M \to 0$ or as $a \to 0$ one may recover respectively the Minkowski or the Schwarzschild metric. The Ricci scalar has the form

$$R = -\frac{6b\, r^{2z}}{r^2\Sigma^2\left(b + r^{2z}\Sigma\right)^3} P_z\left(r, \cos\theta\right)\,, \tag{4.1.4}$$

where $P_z\left(r, \cos\theta\right)$ is an expression (a polynomial in r and $\cos\theta$ when z is an integer) that goes to zero at least as fast as Σ^2 in the limit $r \to 0,\ \theta \to \pi/2$. Hence, the Ricci scalar never blows up for $z \geqslant 1$. However, $z = 1$ still does not yield a well-defined limit, while for $z > 1$ the limit exists and is zero, irrespective of the path taken to reach the would-be singularity in the r–θ space. Similar remarks hold for the Ricci tensor squared $R^{\mu\nu}R_{\mu\nu}$ and the Kretschmann scalar $R^{\mu}{}_{\nu\rho\sigma}R_{\mu}{}^{\nu\rho\sigma}$.

The ansatz in Eq. (4.1.3) can be written as $\psi_r(r) + \psi_\theta(\theta)$, i.e. it is "separable" in the terminology previously introduced, and hence has the advantage of leading to separable equations of motion.

Note that, with $z > 1$, Ψ is divergent on the whole disk $r = 0$ — which will have consequences for CTCs. The fact that this divergence can in fact cancel the divergences in the curvature scalars is quite remarkable. For these reasons, Eq. (4.1.3) is the choice we will mostly explore in the remainder of the chapter: in particular, we will often consider the "minimal" choice $z = 3/2$, corresponding to the smallest integer exponent of r that yields a well defined limit of the curvature invariants.

It is also worth mentioning that, if one focuses on the non-spinning case only, lower values of the exponent z are required. Indeed, in order to regularize the metric

$$ds^2 = \frac{\Psi}{r^2}\, ds^2_{\rm Schw}\,, \tag{4.1.5}$$

with the $a \to 0$ limit of Eq. (4.1.3)

$$\Psi = r^2 + \frac{b}{r^{2z}}\,, \tag{4.1.6}$$

one must have $z \geqslant 1/2$.

Finally, before moving on, let us add that an interesting alternative to Eq. (4.1.3) can be represented by the ansatz

$$\Psi = \Sigma + \frac{b}{\Sigma^z}\,. \tag{4.1.7}$$

In this case it is easy to check that the Ricci scalar tends to zero for $r \to 0,\ \theta \to \pi/2$ for any $z > 1$. The same holds true for the Ricci tensor squared and the Kretschmann scalar, hence Eq. (4.1.7) seems equivalent to Eq. (4.1.3). Notably, however, in this second case $z = 1$ too yields a well-defined, and finite, limit

$$\lim_{\Sigma\to 0} R = -\frac{24a^2}{b} \tag{4.1.8}$$

and similar results can be found for $R^{\mu\nu}R_{\mu\nu}$ and the Kretschmann.[1] With this choice, Ψ only diverges on the ring $r = 0,\ \theta = \pi/2$, but not on the disk $r = 0,\ \theta \neq \pi/2$. Equation (4.1.7) will be juxtaposed to Eq. (4.1.3) in Section 4.1.1 to highlight the properties that make us prefer the latter.

4.1.1 The spacetime close to $r = 0$

Although the scalar curvatures we computed are everywhere finite, the components of the metric still diverge for $\Sigma = 0$. Previous works [160] have argued that the resulting spacetime is in fact geodesically complete, since the would-be singularity is reached in infinite proper time. Since our choice of conformal factor is slightly different from that discussed in Ref. [160], we sketch the relevant computations below.

Consider first a particle moving on the equatorial plane $\theta = \pi/2$ and falling radially towards $r = 0$. With E and L being the particle energy and angular momentum per unit mass, its radial velocity satisfies

$$\Psi^2\dot{r}^2 = \mathcal{R}_{\rm Kerr} - \delta\Delta(\Psi - r^2)\,. \tag{4.1.9}$$

Here $\delta = 0$ or 1 for massless or massive particles respectively, and $\mathcal{R}_{\rm Kerr}$ is the right-hand side of Eq. (4.0.7) with $\Psi = \Sigma$. The proper time it takes for the particle to fall from r_0 to r is

$$\Delta\tau = -\int_{r_0}^{r} \frac{\Psi}{\left[\mathcal{R}_{\rm Kerr} - \delta\Delta(\Psi - \tilde{r}^2)\right]^{1/2}}\mathrm{d}\tilde{r}\,. \tag{4.1.10}$$

For both our ansatz (Eq. (4.1.3) or Eq. (4.1.7)), one finds that on the equatorial plane $\Psi - r^2 = b\,r^{-2z} > 0$; therefore the infall time for massless particles ($\delta = 0$) is shorter than that for massive particles ($\delta = 1$). (Obviously, this is true as long as $\mathcal{R}_{\rm Kerr} - \delta\Delta(\Psi - r^2) > 0$, i.e. only where the trajectory is classically allowed: where the condition is not met, such motion could not take place.)

Let us then focus on massless particles. At $r = 0$, $\mathcal{R}_{\rm Kerr} = a^2(Ea - L)^2$, while Ψ

[1] To our knowledge, those built with a Ψ are the only examples of rotating RBHs whose curvature scalars are continuous and non-zero at the would-be singularity.

diverges at least as fast as $1/r^2$. We conclude that massless particles reach the would-be singularity in an infinite amount of proper time. Given the inequality above, the conclusion remains true for massive particles.

Next, consider a particle that falls along the axis of symmetry $\theta = 0$. Such particle could reach the disk $r = 0$ without encountering the would-be singularity, and potentially cross it through its center. On-axis motion requires $L = 0$, so the radial velocity now satisfies

$$\Psi^2 \dot{r}^2 = -\delta \Psi \Delta + E^2 (r^2 + a^2)^2 \tag{4.1.11}$$

where Ψ is now evaluated at $\theta = 0$. The infall proper time becomes in this case

$$\Delta\tau = -\int_{r_0}^{r} \frac{\Psi}{\sqrt{(\tilde{r}^2 + a^2)^2 E^2 - \delta \Delta \Psi}} \mathrm{d}\tilde{r} \,. \tag{4.1.12}$$

First of all, we can see that it is still true that massless particles fall in a shorter time than massive ones, therefore we again focus on the former. We have

$$E\Delta\tau_{\text{light}} = -\int \frac{\Psi}{r^2 + a^2} \mathrm{d}r \tag{4.1.13}$$

and with our ansatz we have

$$\frac{\Psi}{r^2 + a^2} = 1 + b \begin{cases} (r^2 + a^2)^{-1} r^{-2z} & \text{for Eq. (4.1.3)} \\ (r^2 + a^2)^{-(z+1)} & \text{for Eq. (4.1.7).} \end{cases} \tag{4.1.14}$$

In the first case, the integrand diverges faster than r^{-2z} as $r \to 0$, hence the particle will reach $r = 0$ in an infinite time. In the second case, instead, the integrand is everywhere finite. For massive particles, one can show that the infall time remains finite in the second case but, according to the inequality above, it is infinite in the first.

Therefore, the two choices of Ψ lead to a very different structure of the region close to the would-be singularity: in the first case, the whole disk $r = 0$ is (regularized and) "sent to infinity"; in the second case, only the ring $r = 0$, $\theta = \pi/2$ is pushed away, so that particles can still cross the disk inside the ring. This is a non-negligible difference as in the case of ansatz Eq. (4.1.3) we end up precluding, to light or matter, access to that region of the Kerr geometry ($r < 0$) characterized by the presence of CTCs.

Let us stress that while usually such a region is taken to be nonphysical in the Kerr geometry, due to the fact that it is shielded by a Cauchy horizon which is widely (albeit non-unanimously) considered unstable, the same region would represent a problem for us once we shall have proceeded to stabilize the RBH inner horizon by making it degenerate. It is henceforth even more pressing for a stable RBH to chose an ansatz such as Eq. (4.1.3) over that of Eq. (4.1.7).

4.2 Stabilizing the inner horizon with $m(r)$

As shown in [153], the mass inflation instability can be turned off if the surface gravity of the inner horizon κ_- is made to vanish thanks to a wise choice of the mass function. The

problem with extending this idea to the rotating case is that we wish to impose several conditions at the same time. Indeed, we want to: remove the ring singularity; avoid close timelike curves appearing in the negative r region; have a well-defined limit at the would-be singularity; and have an inner horizon with vanishing surface gravity. Making all these conditions coexist seems a daunting task. While we do not have a no-go theorem in this sense, it is rather clear to a first investigation that, even if viable, such regular metrics would be too cumbersome for any phenomenological application.

We shall then pursue a different path here, starting from the realization that if we regularize the singularity with the conformal factor as above, the functional form of the mass function is left with very few constraints (namely it must be everywhere finite and it must reduce to the ADM mass M at infinity), and can be easily shaped so to stabilize the inner horizon.

Since the surface gravity of the inner horizon r_- depends on $m(r)$ as

$$k_- \propto \partial_r \Delta|_{r=r_-} \,, \tag{4.2.1}$$

if we assume a rational-function form for the mass function, to have a vanishing k_- the inner horizon must be a degenerate root of Δ

$$\Delta \equiv r^2 - 2m(r)r + a^2 = 0 \implies (r - r_+)(r - r_-)^d = 0 \,, \tag{4.2.2}$$

for some $d \in \mathbb{N}_{\geqslant 2}$. $d = 2$ is not viable, since it implies that $m(r)$ has a pole at some positive r. Thus the minimal choice ends up being $d = 3$ which implies (given also the required asymptotic behavior) a mass function of the form

$$m(r) = M \, \frac{r^2 + \alpha r + \beta}{r^2 + \gamma r + \mu}. \tag{4.2.3}$$

From Eq. (4.2.2), it can been shown that β cannot be zero and thus the limit of $m(r)$ for $r \to 0$ is not zero but the finite value $M\beta/\mu$. In this form, $m(r)$ is parametrized by four coefficients, two of dimension $[M]$ (α and γ) and two of dimension $[M]^2$ (β and μ). However, through Eq. (4.2.2), they can all be expressed as functions of the position of the two horizons

$$\alpha = \frac{a^4 + r_-^3 r_+ - 3a^2 r_-(r_- + r_+)}{2a^2 M} \,, \tag{4.2.4}$$

$$\beta = \frac{a^2(2M - 3r_- - r_+) + r_-^2(r_- + 3r_+)}{2M} \,, \tag{4.2.5}$$

$$\gamma = 2M - 3r_- - r_+ \,, \tag{4.2.6}$$

$$\mu = \frac{r_-^3 r_+}{a^2} \,. \tag{4.2.7}$$

If we choose $r_+ = M + \sqrt{M^2 - a^2}$, i.e. the outer horizon to coincide with its Kerr analog, our family of metrics can be parametrized in terms of r_- only. It is quite remarkable, and very relevant for phenomenological studies, that in spite of being located beyond a trapping horizon, the position of the inner horizon can matter for observables in the outside geometry. An example of this can be exposed by looking at the large-r behavior

of the mass function:

$$m(r) \sim M + \frac{M(\alpha - \gamma)}{r} + O(1/r^2)\,, \quad (r \to \infty)\,. \tag{4.2.8}$$

The second term in the above expansion could be interpreted as an electric charge, and could lead to a different quadrupole moment with respect to a Kerr BH.

The choice $\alpha = \gamma$ must be discarded as it forces the inner horizon to coincide with the Kerr one, and in turn implies a non-zero inner horizon surface gravity (actually the usual one for the Kerr geometry) making the conformal Kerr metric still unstable to mass inflation.

Nonetheless, we can introduce a parameter controlling the difference between the inner-horizon position in our geometry and in Kerr. This parameter will in turn control the difference $\alpha - \gamma$. Let us write then

$$r_- \equiv \frac{a^2}{M + (1-e)\sqrt{M^2 - a^2}}\,, \tag{4.2.9}$$

with $e \neq 0$ and $e < 2$ in order to ensure $0 < r_- < r_+$. Further requiring the mass function to have no poles implies

$$-3 - \frac{3M}{\sqrt{M^2 - a^2}} < e < 2\,, \tag{4.2.10}$$

where in the positive (negative) part of the interval r_- is larger (smaller) than the Kerr inner horizon.

With the above choice, it follows that $\alpha - \gamma = O(e^3)$ — the same holds true for all the other coefficients in the large-r expansion. This suggests that sizable deviations of r_- from its Kerr value could translate into measurable differences in the value of the quadrupole moment, or in the periastron precession and the orbital frequency in a binary system [161]. Such differences would all be $O(e^3)$, which entails that values of $|e|$ close to one or smaller might be phenomenologically favored; but the possible impact of e on astrophysical observables certainly deserves further scrutiny, which we leave for the future.

Let us also note that, with the parametrization (4.2.9), the mass function becomes $m(r) = M + O(e^3)$ and in particular $m(r_+) = M$. This entails, among other things, that the outer-horizon angular velocity is the same as in Kerr, while its surface gravity is

$$k_+ = \frac{\partial_r \Delta(r_+)}{2(r_+^2 + a^2)} = k_+^{\rm Kerr} + O(e^3)\,. \tag{4.2.11}$$

Moreover, $e \to 2$ is an extremal limit similar to $a \to M$, since in this limit $r_- \to r_+$ and $k_+ \to 0$.

Of course, different choices from Eq. (4.2.9) for r_- are in principle possible but they are strongly limited by a series of sanity requirements: the inner horizon must lie within the outer horizon for all values of a; $m(r)$ must go to M asymptotically; the denominator of $m(r)$ must have no zeros (for all $r > 0$), that is $\gamma^2 < 4\mu$; all the coefficients of $m(r)$ must be finite for all values of a; the extremal limit $a \to M$ should remain thermodynamically unattainable and thus also the surface gravity of r_+ should become zero in this limit —

indeed this is possible only if $r_- \to r_+$ for $a \to M$.

In conclusion, the complete form of our rotating "inner-degenerate" metric is

$$ds^2 = \frac{\Psi}{\Sigma}\left[-\left(1-\frac{2m(r)r}{\Sigma}\right)\mathrm{d}t^2 - \frac{4a\,m(r)r\sin^2\theta}{\Sigma}\mathrm{d}t\mathrm{d}\varphi + \frac{\Sigma}{\Delta}\mathrm{d}r^2 + \Sigma\mathrm{d}\theta^2 + \frac{A\sin^2\theta}{\Sigma}\mathrm{d}\varphi^2\right], \tag{4.2.12}$$

with $m(r)$ given in Eq. (4.2.3) and

$$\Psi = \Sigma + \frac{b}{r^3}, \quad \Sigma = r^2 + a^2\cos^2\theta, \quad \Delta = r^2 - 2m(r)r + a^2, \quad A = (r^2+a^2)^2 - \Delta a^2\sin^2\theta\,, \tag{4.2.13}$$

where for the power law of Ψ we have chosen the lowest integer that makes the curvature scalars continuous and finite (see Section 4.1).

Fixing $r_+ = r_+^{\mathrm{Kerr}}$ and choosing r_- as in Eq. (4.2.9), this metric represents a family of stable, rotating, CTC-free, regular spacetimes with two free parameters (beyond the usual spin one): the "Kerr-deviation parameter" e and the "conformal parameter" b. Notice that for $a \to M$ the metric becomes conformal to the extremal Kerr, while for $a \to 0$ the metric becomes conformal to Schwarzschild.

4.3 The rotating "inner-degenerate" RBH as a Kerr black hole mimicker

In this section we investigate the extent to which our metric (4.2.12) can mimic a Kerr BH: first we describe the causal structure; then the effective matter content; the position of ergosurfaces; and finally the location of the light rings and of the innermost stable circular orbit (ISCO).

4.3.1 Causal structure

To study the casual structure of this spacetime we introduce ingoing null coordinates

$$\mathrm{d}v = \mathrm{d}t + \frac{r^2+a^2}{\Delta}\,\mathrm{d}r, \quad \mathrm{d}\psi = \mathrm{d}\varphi + \frac{a}{\Delta}\,\mathrm{d}r\,, \tag{4.3.1}$$

that are regular at the horizons. In Fig. 4.1 we plot the equatorial principal null geodesics in the r–t_*^v plane where t_*^v is defined as

$$\mathrm{d}t_*^v = \mathrm{d}v - \mathrm{d}r\,. \tag{4.3.2}$$

We see that, even if the inner horizon has zero surface gravity, we still have peeling of geodesics there, the difference with respect to Kerr is in the peeling trend. Since $k_- \propto \partial_r\Delta|_{r_-} = 0$ and $\partial_r^2\Delta|_{r_-} = 0$ this peeling is no longer exponential but scales as $1/t^{1/2}$. In fact for the principal null geodesics

$$\frac{\mathrm{d}r}{\mathrm{d}t} = \pm\frac{\Delta}{r^2+a^2}\,. \tag{4.3.3}$$

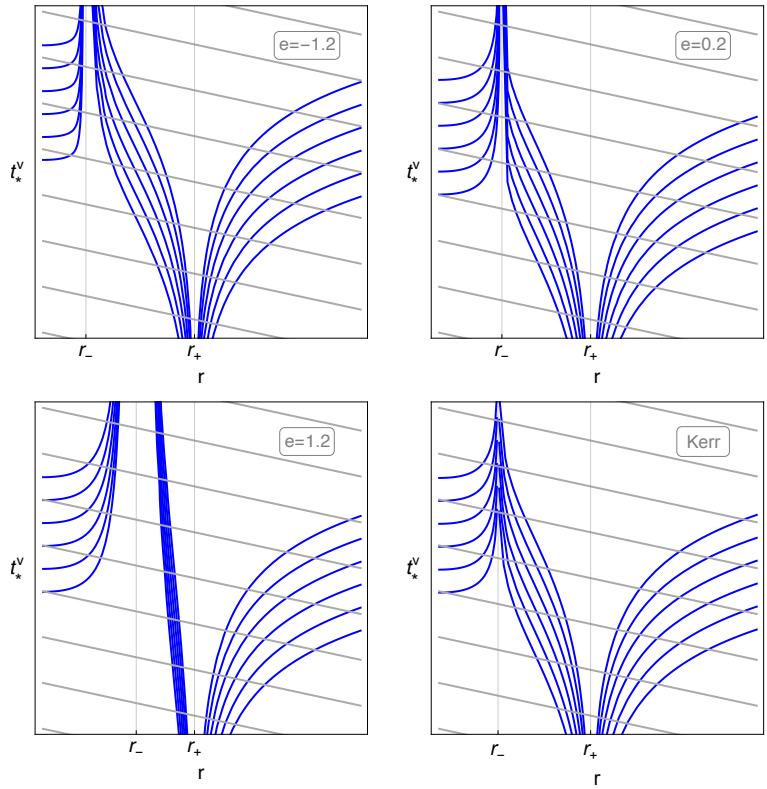

Figure 4.1: Ingoing (gray) and outgoing (blue) null rays near the horizons for selected values of the "Kerr-deviation parameter" e compared with the Kerr ones in the bottom right panel. The spin parameter is set to $a = 0.9M$.

Thus near the inner horizon

$$\frac{\mathrm{d}r}{\mathrm{d}t} = \pm\frac{\partial_r^3\Delta|_{r_-}}{r_-^2 + a^2}\,(r - r_-)^3 + O(r - r_-)^4\,. \tag{4.3.4}$$

The causal structure of the spacetime is summarized by the Penrose diagram of Fig. 4.2. The diagram is completely analogous to that of the Kerr spacetime, except for the fact that the surface $r = 0$ — which is timelike — is not a singularity and it can be reached only after an infinite amount of proper time by any infalling observer. In order to hint at these differences, we choose to represent $r = 0$ as a branch of hyperbola instead of a straight line.

4.3.2 Effective matter content

Clearly, the metric we are considering is not a vacuum solution of GR. Yet, as discussed in Chapter 3, the Einstein equations can be used to characterize the spacetime by interpreting the Einstein tensor $G^\mu{}_\nu = R^\mu{}_\nu - \frac{1}{2}R\,\delta^\mu{}_\nu$ as an effective stress–energy tensor and to quantify deviations of our candidate spacetime with respect to the Kerr one. To properly characterize the effective matter content, one first needs to project the Einstein tensor onto an orthonormal tetrad, e.g. the one of Refs. [157–159]. The behavior of the orthonormal components close to spatial infinity is particularly relevant: since the spacetime is asymptotically flat, they must all tend to zero as $r \to \infty$, but they do so at different rates.

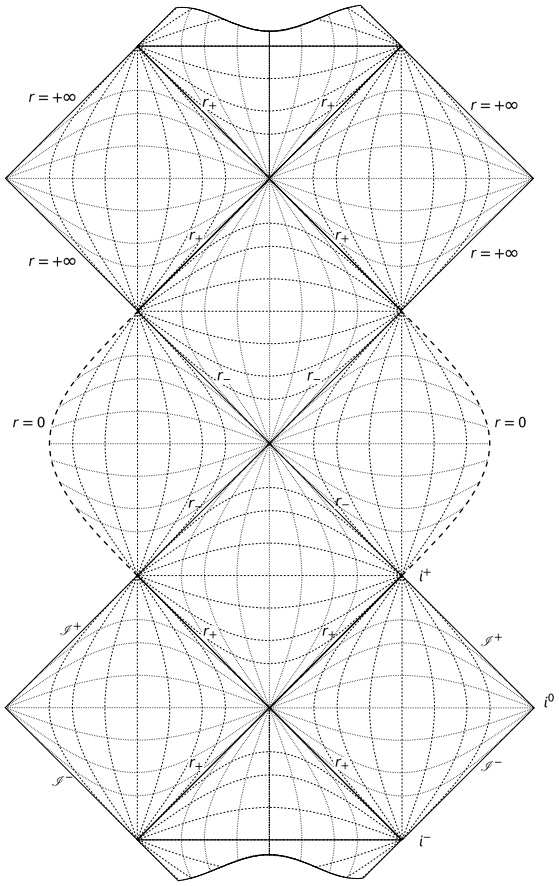

Figure 4.2: Penrose diagram of the rotating RBH in Eq. (4.2.12). The hypersurface $r = 0$ is timelike, but reached in infinite proper time by any infalling observer: for this reason it is drawn not as a straight line but as a curve.

In particular, the slowest decaying (non-zero) components are those on the diagonal, all the others being of higher order in powers of $1/r$. Such components, at infinity, are the effective energy density and pressures:[2]

$$\rho = -p_r = p_\theta = p_\phi = -\frac{2M(\alpha - \gamma)}{r^4} + O(1/r^5)\,. \tag{4.3.5}$$

Note that these quantities fall off quickly as $r \to \infty$, meaning that quantum-gravity-induced deviations from the GR vacuum solution are sizable only in a region close to the object. Moreover, they are $O(e^3)$ and do not depend on b; the next-to-leading order $O(1/r^5)$ also does not depend on b. Equation (4.3.5) can lead to violations of the null energy condition (NEC), which requires $\rho + p_i \geqslant 0$, if $\alpha - \gamma > 0$. When the NEC is

[2]Technically, the energy density and pressures are defined in terms of the eigenvalues of the orthonormalized Einstein tensor, when these are real. In asymptotically flat spacetimes, this procedure and the one presented in the text agree at leading order.

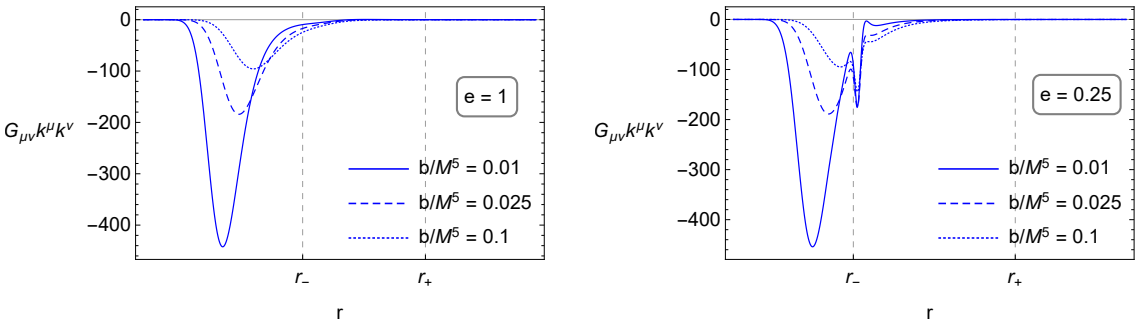

(a) (b)

Figure 4.3: Effective energy density as measured along a null equatorial trajectory, with $L = 0$, that falls into a RBH with spin $a/M = 0.9$. Each plot is relative to a particular choice of the deviation parameter e and displays curves corresponding to three values of the conformal parameter b. The two vertical lines mark the location of the inner and outer horizons.

violated, all the other classical energy conditions are violated too. When instead $\gamma > \alpha$, not only the null but also the weak (NEC + $\rho \geqslant 0$) and dominant ($\rho \geqslant |p_i|$) energy conditions are met; the strong energy condition (NEC + $\rho + 3p_i \geqslant 0$) instead is always violated. Notice also that the above effective matter distribution does not correspond to any simple realistic matter content. This is not surprising, as this effective stress–energy tensor gives an insight to the higher-order terms in the still unknown gravitational action.

Moving closer to $r = 0$, the simple interpretation in terms of energy density and pressures is not always viable, since there are regions in which the Einstein tensor cannot be diagonalized over the real numbers: in these regions, the effective matter content is of type IV in the Hawking–Ellis classification [162]. (The existence of these regions is entirely due to the presence of the conformal factor: when $\Psi = \Sigma$, the effective stress–energy tensor is of Hawking–Ellis type I for any $m(r)$.)

In order to circumvent this problem, we select particular geodesics and investigate the effective matter content as measured along them. We focus first on null geodesics: calling k^μ their tangent vector, the contraction

$$G_{\mu\nu}k^\mu k^\nu \tag{4.3.6}$$

is always real and can be interpreted as the energy density measured along the geodesic. When this quantity is non-positive, the null energy condition is violated. For simplicity, we choose a geodesic that lies on the equatorial plane ($k^\theta = 0$) and that falls towards the BH with zero angular momentum ($L = 0$) — cf. Eqs. (4.0.5) to (4.0.8). Clearly, this choice represents a loss of generality, but is sufficiently illustrative for our purposes.

The result is displayed in Fig. 4.3, for $a/M = 0.9$ and some choices of the parameters e and b. The effective energy density measured along the null geodesic is mostly negligible outside of the BH; inside the outer horizon, it becomes large and negative, signaling a substantial violation of the null energy condition; and it is exactly zero at $r = 0$ (although that point is reached only at infinite affine parameter). The plot of Fig. 4.3a is representative of all the cases $|e| \gtrsim 1$: increasing e slightly moves the negative trough to the right;

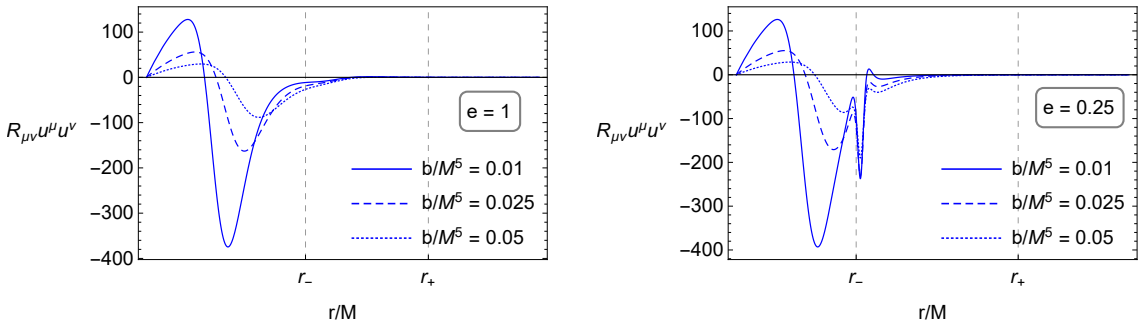

(a) (b)

Figure 4.4: Contraction of the Ricci tensor with the tangent vector of a particular timelike equatorial trajectory ($L = 0,\ E = 1$) that falls into a RBH with spin $a/M = 0.9$. Each plot is relative to a particular choice of the deviation parameter e and displays curves corresponding to three values of the conformal parameter b. The two vertical lines mark the location of the inner and outer horizons.

increasing b, instead, tends to smooth out the trough; but the overall shape of the curve is not greatly affected. When $|e| \lesssim 1$, the curves exhibit additional features close to the inner horizon, signaling that the limit $e \to 0$ is not smooth. Lowering the spin suppresses the height of all the features just described.

We then move on to timelike geodesics, whose tangent vector we name u^μ. As before, we choose them to lie on the equatorial plane and to fall into the BH with zero specific angular momentum ($u^\theta = 0,\ L = 0$); we further choose the radial velocity to be zero at infinity ($E = 1$). The contraction

$$G_{\mu\nu}u^\mu u^\nu \tag{4.3.7}$$

yields radial profiles that are qualitatively similar to those of Fig. 4.3 and for this reason we do not report them here. When this quantity is negative, the weak energy condition is violated. Finally, we complement the analysis by computing

$$R_{\mu\nu}u^\mu u^\nu. \tag{4.3.8}$$

Assuming the Einstein equations, $R_{\mu\nu} \propto T_{\mu\nu} - (T/2)g_{\mu\nu}$, hence when Eq. (4.3.8) is negative the strong energy condition is violated. Some results are reported in Fig. 4.4, again for $a/M = 0.9$ and a few illustrative choices for e and b. As in the null case, these observers measure an effective matter content that is practically zero outside of the outer horizon. Large violations of the strong energy condition are measured inside of the inner horizon. At variance with the null case, now the curves exhibit a second positive bump before reaching zero at $r = 0$. Similarly to the previous case, increasing the value of e pushes the large negative trough to the right but does not substantially affect its depth, which is instead controlled by b; the height of the positive bump increases with e. Moreover, for $|e| \lesssim 1$ additional features appear close to the inner horizon. As before, lowering the spin suppresses the magnitude of all these features.

4.3.3 Ergosurfaces

The ergosurfaces are defined by the roots of $g_{tt} = 0$, or equivalently of $r^2 - 2m(r)r + a^2\cos^2\theta = 0$, whose solution can be given in closed form. Since the result is cumbersome, in Fig. 4.5 we show the embedding in Euclidean space of the horizons and ergosurfaces for some illustrative choice of the parameters. The main difference with respect to a Kerr BH is the shape of the inner ergosurface around the poles: values of e closer to the upper and lower bounds in Eq. (4.2.10) correspond to a more pronounced cuspid around the poles; for values of e closer to the lower bound, the inner horizon and ergosurface move close and eventually touch also at the equator; for values of e closer to the upper bound the horizons move closer as previously said. The conformal factor does not affect the ergosurfaces at all.

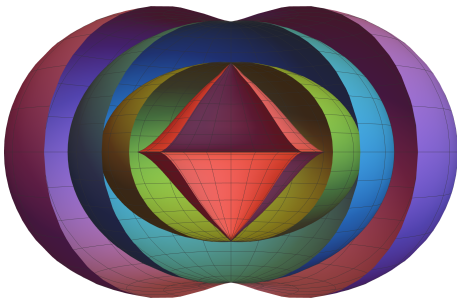

Figure 4.5: Embedding in Euclidean space of the horizons (green and blue surfaces) and ergosurfaces (red and purple surfaces) for $a/M = 0.95$ and $e = 1$.

Finally, let us notice that, since with our choice $m(r_+) = M$, the textbook expression for the maximal efficiency of the Penrose process [163–166] seems to yield the same result as in Kerr:

$$\eta_{\rm max} = 1 - \sqrt{\frac{r_+}{2m(r_+)}} = 1 - \sqrt{\frac{M + \sqrt{M^2 - a^2}}{2M}}\,. \tag{4.3.9}$$

Checking whether this is actually the case would require a more careful analysis of the motion of test particles in our spacetime — an interesting question which however lies outside the scope of this work.

4.3.4 Notable equatorial orbits

In order to characterize the spacetime and its deviations away from Kerr from a phenomenological point of view, we compute the coordinate location of the light ring and the ISCO. We focus on the equatorial plane, where the radial motion is governed by the function (cf. Eq. (4.0.7))

$$\mathcal{R} = E^2 r^2 (r^2 + a^2) - r^2 L^2 + 2m(r) r (aE + L)^2 - \delta \Psi \Delta\,, \tag{4.3.10}$$

with $\delta = 0$ or 1 for null and timelike geodesics, respectively. Circular orbits correspond to $\mathcal{R} = \mathcal{R}' = 0$ and are stable if $\mathcal{R}'' \leqslant 0$. Since the analytical expressions are not particularly illuminating, the values of $r_{\rm LR}$ and $r_{\rm ISCO}$ are computed numerically.

The location of the light ring, which is a null geodesic, does not depend on Ψ. Its fractional deviation from its Kerr analog is shown in Fig. 4.6, as a function of the spin, for some choices of the parameter e. The extrema and sign changes displayed by the curves of Fig. 4.6 are ultimately determined by the behavior of the function $m(r)$ (and its derivative), which is not monotonic. The analogous plot for the ISCO is reported in Fig. 4.7. Contrary to the previous case, $r_{\rm ISCO}$ depends on Ψ, hence the curves in the figure correspond to specific choices of b. In fact, varying the parameter b substantially affects the location of the ISCO, particularly for high spin. The peculiar spike associated to prograde orbits and high spin, in particular, can be entirely explained in terms of the behavior of Ψ: since, as the spin increases, the prograde ISCO shrinks, $r_{\rm ISCO}$ enters deeper into the region where Ψ is markedly different from r^2. In order to further explore the parameter space in the high-spin regime, we set $a = 0.998M$ (roughly the Thorne limit [167]) and let the parameters vary in the ranges $b \in [0, 1]$ and $e \in [-3 - 3M/\sqrt{M^2 - a^2}, 2]$, thereby producing the contour plots of Fig. 4.8.

Despite the much larger interval spanned by e, the gradient of the deviation is dominated by the b component: this is clear for prograde orbits (Fig. 4.8a), but is also true for retrograde orbits (Fig. 4.8b) if e is restricted to take reasonably small values as in Fig. 4.8c. Note, however, that even for spins as high as $a = 0.998M$, except for rather extreme values of the parameters, the ISCO moves less than a few percent in the prograde case and less than a few per mil in the retrograde case.

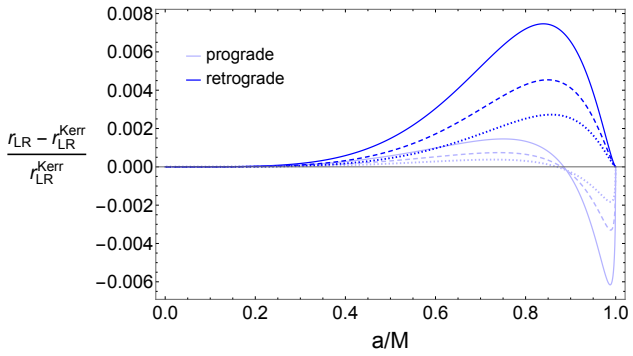

Figure 4.6: Relative difference in the position of the light ring as a function of the spin between Kerr and our spacetime with $e = 0.9$ (dotted lines), $e = 1$ (dashed lines) and $e = 1.1$ (continuous lines). We do not need to specify a value for the conformal parameter b as null geodesics are insensitive to the conformal factor Ψ. While we display only values of e near 1, corrections to the light-ring position actually grow very fast with e and they can be up to order 60% for $e \to 2$. Note also that the extrema and sign changes displayed by the curves are ultimately determined by the behavior of the function $m(r)$ (and its derivative), which is not monotonic.

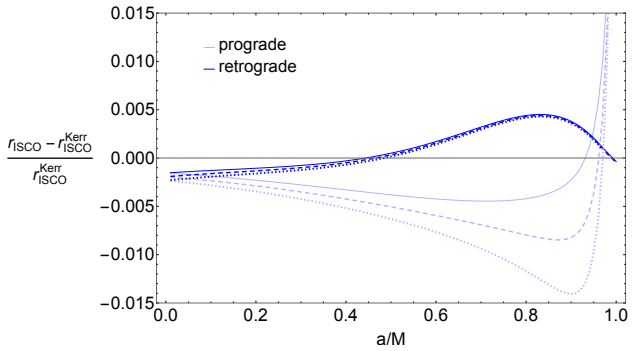

Figure 4.7: Difference in the position of the ISCO between Kerr and our spacetime with $e = 1$ and $b/M^5 = 0.8$ (continuous lines), $b/M^5 = 1$ (dashed lines) and $b/M^5 = 1.2$ (dotted lines). The prograde orbit, lying in a more internal region of the spacetime where the conformal factor is greater, presents larger deviations, particularly for high spin.

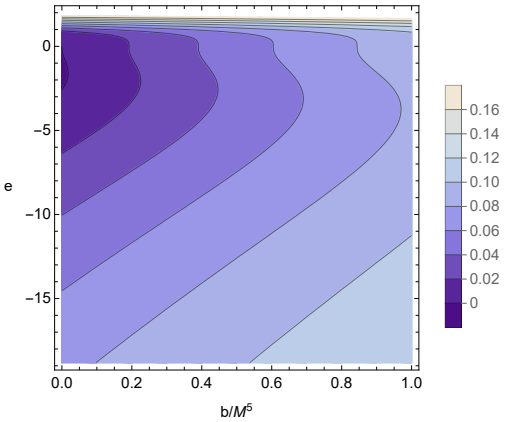

(a) Prograde orbits.

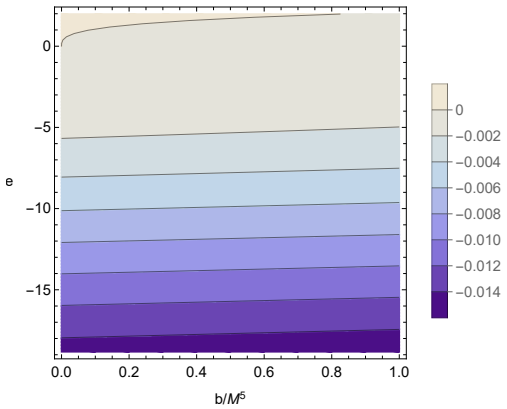

(b) Retrograde orbits.

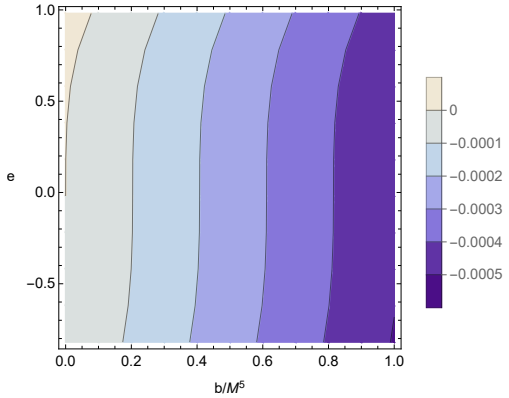

(c) Retrograde orbits, zoom to the region $|e| < 1$ of Fig. 4.8a.

Figure 4.8: Fractional deviation of the ISCO from its Kerr analog, computed as $r_{\rm ISCO}/r_{\rm ISCO}^{\rm Kerr} - 1$. Spin $a/M = 0.998$.

4.4 Conclusions

We built and studied a new regular alternative to Kerr BHs that is stable under classical mass inflation. To construct it, we combined the two most common tools for regularization, in a novel way: we used a mass function to construct a degenerate (zero surface gravity) and thus stable inner horizon, and a conformal factor to regularize the singularity. In general, this procedure leads to a family of metrics, depending on the precise choice of the conformal factor and of $m(r)$.

We decided to focus on a particular form of the conformal factor that accomplishes the regularization in a minimal way and at the same time ensures the non-existence of CTCs and the separability of the equations of motion for test particles. With this choice, the curvature scalars are continuous and tend to zero on the would-be singularity[3] thereby solving a long-standing issue that affects many rotating RBHs. The regularization is controlled by a scale that we parametrize in terms of the quantity b, with dimensions $[M]^5$.

We further took an ansatz for $m(r)$ that is again minimal, in a suitable sense, and fixed the coordinate location of the outer horizon so that it coincides with its Kerr analog. The resulting mass function can be expressed entirely in terms of the coordinate location of the inner horizon, whose deviation from that of Kerr is encoded by the dimensionless quantity e. In the limit $e \to 0$ we obtain the conformal Kerr metric that, though regular, is characterized by the usual surface gravity at the inner horizon (as it should be given that the surface gravity is conformal invariant) and hence is again unstable under mass inflation. However, it is important to notice that our metric cannot indefinitely deviate from the conformal Kerr one since the deviation parameter e must lie in a specific interval in order for the mass function to be everywhere finite and for the horizons to be well ordered ($0 < r_- < r_+$).

Our metric thus depends on a total of four real parameters: the ADM mass M, the spin a, the conformal parameter b and the deviation parameter e. The two additional parameters b and e can be constrained by observations, at least in principle. In particular, e enters at low order in the parametrized post Newtonian expansion of this object gravitational field, possibly influencing its GWs inspiral signal (see Section 5.1); moreover, it affects the orbits of massless test particles and therefore shifts the position of the light ring. Finally e and b both affect the motion of massive test particles, with b having the dominant effect on the location of the ISCO (at least when e is taken to vary in reasonably small ranges) especially at high spins.

Let us stress the remarkable relevance of this fact: given that the conformal and Kerr-deviation parameters might be directly related to quantum-gravitational effects, the possibility to constrain them via observations on the exterior geometry of the BH is further evidence that a new window for quantum-gravity phenomenology might be opening via astrophysical observations.

In conclusion, the rotating RBH geometry proposed here is characterized by a wealth of physically desirable features that make it a plausible candidate for the end point of a gravitational collapse to be contrasted with the Kerr geometry to which it can be made arbitrarily close.

[3] With a slightly different choice, however, the limit can also be made non-zero.

Note however that even if this model is not plagued by classical mass inflation, it would still be subject to the semiclassical instability. Indeed, the timescale of the semiclassical mass inflation seems to depend on the difference between the surface gravity of the two horizons rather then uniquely on the inner horizon one [135]. Thus in order to switch it off one must construct a truly "extremal" RBH for which $k_+ = k_-$. This kind of regularization has been performed in [136]. Note that the RBHs described it this paper are "extremal" ($k_+ = k_- = 0$) but not maximal rotating ($a = M$). Indeed they don't present any constraint on the spin parameter a and for this reason they still represent good candidates to describe the non-maximal rotating astrophysical compact objects we see in our universe.

Part IV

Phenomenological signatures of the regularization

He stepped down,
trying not to look long at her,
as if she were the sun,
yet he saw her, like the sun,
even without looking
— Lev Tolstoj

Chapter 5

Background: gravitational waves from BHs mimickers

The direct detection of gravitational waves announced by the Advanced LIGO team in February 2016, opened a new widow on the Universe and it led to the possibility to investigate the gravitational interaction in the strong field regime. In particular, the GWs signal coming from the coalescence of two compact objects represents a powerful tool for testing the BH paradigm since it carries a lot of information about the merging objects. We expect that the gravitational wave signal originating from regular objects will present potentially observable differences with respect to the signal coming from the coalescence of two singular black holes.

This signal is usually divided into three parts. The first one is the *inspiral*, during which the two objects spiral one towards each other as they lose energy to gravitational radiation. Since this stage is characterised by large distances between the two objects and small velocities, it can be studied in Post-Newtonian approximation in which the Einstein equations are solved performing an expansion in terms of the velocity parameter v/c. The second part is the *merger*, a rapid phase where the two objects merge to create a final remnant. This phase can only be described using numerical simulations that consider the nonlinear aspects of the dynamics. The last phase, called the *ringdown*, is caused by the relaxation of the remnant object to its final, stationary state. It can be studied in perturbation theory, solving for the dynamics of a time-dependent linear perturbation on the spacetime of the final stable object.

In this chapter, we will summarize how this signal can be used to test the nature of the merging objects. For more comprehensive reviews on the topic and for detailed results of these tests on the current observed signals refer to [47, 168–170]. In the successive chapters we will focus specifically on some new results concerning the effects of the singularity regularization on the post-merger signal. We will not deal with the possible phenomenological signatures or the Big Bang regularization, the interested reader can refer to [57–59, 171].

5.1 The Inspiral signal

As we mentioned, the gravitational waveform generated by inspiralling compact binaries moving in quasi-circular orbits can be described in Post Newtonian (PN) approximation, expanding the Einstein equations in terms of the orbital velocity v/c, with each $O([v/c]^{2n})$ being referred to as of nPN order.

In general, PN corrections enter both the amplitude and the phase of the GWs waveform. However corrections in the phase are dominant, especially far from the merger, and they accumulate in the several cicles of the binary inspiral. For this reason PN coefficients up to 3.5PN order are usually considered to model the phase while most waveform models for data analysis keep the amplitude at 0PN order (this is the so called restricted wave approximation). In this set up, the GWs waveform in the frequency domain can be modelled as:

$$h(f) = \frac{1}{D_L}\mathcal{H}(\theta, \phi, \iota, \psi, \mathcal{M}, \eta, f)e^{\Phi(t_c, \phi_c, \mathcal{M}, \eta; f)}, \tag{5.1.1}$$

where

$$\Phi\left(t_c, \varphi_c, \mathcal{M}, \eta; f\right) = 2\pi f t_c - \phi_c - \pi/4 + \sum_{i=0}^{7}\left[\varphi_i + \varphi_{il}\ln f\right] f^{(i-5)/3}. \tag{5.1.2}$$

Here D_L is the luminosity distance to the source, (θ, ϕ) specify the sky position, (ι, ψ) give the orientation of the inspiral plane with respect to the line of sight. $\mathcal{M}$ is the chirp mass and η is the symmetric mass ratio, in terms of the components masses (m_1, m_2) one has $\eta = m_1 m_2/\left(m_1 + m_2\right)^2$ and $\mathcal{M} = \left(m_1 + m_2\right)\eta^{3/5}$. t_c and ϕ_c are respectively the time and phase at coalescence. The precise functional dependence of the phase PN coefficients φ_i and φ_{il} on (M, η) for GR BHs inspirals, can be found in [172]. Note that the only non-vanishing logaritmic coefficients are φ_{5l} and φ_{6l}. For BHs mimickers we expect modifications to these coefficients and to the inspiral signal in general, let us see this more in details.

Multiple moments

In Newtonian gravity, the gravitational potential of a finite density distribution localized in a region R, can be expressed in the exterior of R as a series of spherical harmonics:

$$\Phi(\mathbf{r}) = \int \frac{\rho\left(\mathbf{r}'\right)}{|\mathbf{r} - \mathbf{r}'|} d^3 r' = \sum_{l=0}^{\infty}\sum_{m=-l}^{l}\left(\frac{4\pi}{2l+1}\right) M_{lm}\frac{Y_{lm}(\theta, \varphi)}{r^{l+1}} \tag{5.1.3}$$

where ρ is the mass density and

$$M_{lm} = \int \left(r'\right)^l \rho\left(\mathbf{r}'\right) Y_{lm}^*\left(\theta', \varphi'\right) d^3 r' \tag{5.1.4}$$

are known as *multiple moments*. Here l and m are respectively the angular and azimuthal number labelling each spherical harmonic function (with $l \geqslant 0$ and $|m| \leqslant l$).

This simple description breaks down in general relativity but it is still possible to rigorously define relativistic multiple moments [173, 174]. For stationary and asymptotically flat spacetimes that are smooth enough at infinity [175], it is possible to directly extract the multiple moments from the metric written in a specific class of coordinate systems known as "asymptotically Cartesian and mass centered" (ACMC) [176]. These relativistic multiple moments are divided in two sets: the mass multiple moments M_{lm} that in the Newtonian limit reduce to the aforementioned Newtonian multiple moments and the current multiple moments S_{lm} that have no Newtonian analog. All the multiple moments of a singular black hole in GR can be written in terms of only two parameters that are the mass M and angular momentum J:

$$M_l^{BH} + iS_l^{BH} = M^{l+1}(iJ/M^2)^l \tag{5.1.5}$$

where we put implicitly $m = 0$ since all the moments with different m vanish for axisymmentric objects. Note that for spherically symmetric BHs, the only non vanishing moment is the mass M_0.

There is no reason for this simple multipolar structure to hold also for a generic compact object like the regular BHs and horizonless exotic objects we described in the previous chapters. Still, for a good mimicker of GR BHs, we can assume that deviations from GR values are perturbative. Hence, we can parametrize the multiple moments of a generic compact objects as:

$$M_{lm} = M_l^{BH} + \delta M_{lm} \quad S_{lm} = S_l^{BH} + \delta S_{lm} \tag{5.1.6}$$

The multipolar structure of an object influence the inspiral signal, modifying the PN structure of the GWs waveform at different orders. The lowest order contribution is the quadrupole moment which enters at 2PN order. However, to really put constraints on δM_{20} is challenging due to the fact that the 2PN term in the GW waveform depends also on the binary components spins, which have not been measured accurately so far. The future space mission LISA is expected to provide accurate measurements of the quadrupole and of a large set of high-order multipole moments. In particular, the inspiral signal coming from extreme mass ratio binaries is expected to put stronger bounds on the multipolar structure of the central supermassive object because in these systems the small secondary object performs a large number of cycles before the merger.

Tidal heating

During the coalescence of two compact objects, part of the energy and angular momentum is lost through GWs emission at infinity. If the inspiraling objects posses an horizon, additional energy and angular momentum are absorbed by the horizon. This effect is known as tidal heating (TH). Horizonless alternatives to BHs, on the other hand, are not expected to absorb any significant amount of GWs. This absence of tidal heating can leave a detectable imprint in the inspiral signal, in particular for extreme-mass ratio binaries. In this case the secondary object moves on geodesical orbits, with orbital parameters evolving adiabatically because of the energy and angular momentum loss. Even if the energy loss at the horizon is subleading with respect to the one at infinity, it can still impact the phase

of the orbits (and hence of the GWs signal) in a detectable way, especially if the central object is highly spinning.

Tidal deformability

During the coalescence of a compact binary system, the gravitational field of each component acts as a tidal field on its companion, inducing a deformation in the spacetime that can be encoded in the appearance of "tidal-induced multipole moments". A weak tidal field can be decomposed into the polar tidal field moments $\mathcal{E}_{lm}$ and the axial tidal field moments $\mathcal{B}_{lm}$.

In the non-rotating case, the ratio between the multipole moments and the tidal field moments that induces them defines the tidal Love numbers of the body:

$$k_E^{(l)} \propto \frac{1}{M^{2l+1}} \frac{M_{lm}}{\mathcal{E}_{lm}} \quad , \quad k_B^{(l)} \propto \frac{1}{M^{2l+1}} \frac{S_{lm}}{\mathcal{B}_{lm}} \tag{5.1.7}$$

For a rotating object, the coupling between its angular momentum and the polar (or axial) tidal field moments generates current (or mass) multipole moments in accordance with specific selection rules [177–180]. Consequently, this phenomenon enables the definition of new categories of "rotational tidal Love numbers" for rotating bodies.

In vacuum GR the Love numbers of BHs are precisely zero both in the spherical symmetric case [181, 182] and in the rotating case [183–185]. However, this is not necessarily true for alternative regular compact objects. For example, the tidal Love numbers of most horizonless objects have been shown to be generally nonzero and approach zero in the black hole limit [186].

A non vanishing tidal deformability modifies the phase of the inspiral signal at 5PN order. This effect can provide a way to test the nature of the emitting objects, especially in the signal coming from extreme mass ratio binaries.

5.2 The Post-merger signal

The Ringdown

The ringdown refers to the GWs signal emitted by a compact object when it is perturbed by any process, for example its own formation through the coalescence of a binary system.

It can be studied in perturbation theory by expressing the metric as $g_{\mu\nu} = g^0_{\mu\nu} + h_{\mu\nu}$ and solving the Einstein equations at first order in $h_{\mu\nu}$. Here, $g^0_{\mu\nu}(t, r, \theta, \phi)$ represents the background metric of the compact object in its final stable state, while $h_{\mu u}(t, r, \theta, \phi)$ denotes a minor perturbation. By exploiting the symmetries of the spacetime, it is possible, at least in vacuum GR, to separate the angular part from the radial one in the resulting differential equations. This simplification reduces the problem to solving a Schrodinger-like equation for certain scalar functions $\psi(r, t)$ related to the radial part of the perturbation functions in $h_{\mu\nu}$, while the angular part will be given by the spheroidal harmonics $\mathcal{Y}_{lm}(\theta, \varphi)$.

Through an harmonic decomposition of the time dependence one can express these scalar functions as $\psi_{lm}(r, t) = \sum_n e^{-i\omega_{lmn}t}\psi_{lmn}(r)$. Then, the equations for the radial

part generically reads:

$$\frac{\mathrm{d}^2\psi_{lmn}}{\mathrm{d}r_*^2} + \left(\omega_{lmn}^2 - V_{lm}\right)\psi_{lmn} = 0\,, \tag{5.2.1}$$

where r_* is the tortoise coordinate $dr_*^2 = g^0_{rr}/g^0_{tt}dr^2$.

Upon imposing suitable boundary conditions, such equations are satisfied by a discrete set of complex frequencies ω_{lmn} called quasinormal modes (QNMs) and labeled by the overtone number $n \geqslant 0$ (in addition to the angular and azimuthal number of the corresponding spheroidal harmonics $l \geqslant 0$ and m with $|m| \leqslant l$).

Note that in spherical symmetry, the spheroidal harmonics becomes spherical harmonics $Y_{lm}(\theta, \varphi)$ that can be divided in the axial and polar sector accordingly to their behavior under parity transformations ($\theta \to \pi - \theta$ and $\varphi \to \pi + \varphi$). Correspondingly also the QNMs frequencies can be divided in the polar and axial sector, however for vaccum GR, that is for the Schwarschild metric, the spectra of frequencies in the two sectors coincide, this is referred to as isospectrality of polar and axial quasinormal modes. Furthermore, for the Schwarschild metric, the potential in equation 5.2.1 and consequently the QNMs frequencies ω_n depend only on the angular number l, this is referred to as azymuthal degeneracy.

For additional technical details on perturbation theory, refer to [187–191] and references therein, see also Section 6.6 for perturbations on general spherically symmetric spacetimes.

For the uniqueness theorems, the QNMs frequencies of GR black holes can depend only on two parameters: the mass and spin of the emitting object, i.e. of the final BH formed after the merger. This means that in principle measuring two modes (two complex frequencies) is sufficient to test the hypothesis that the emitting object is a singular GR black hole. Furthermore, the QNMs of various regular BH mimickers have been computed in literature [192–197], allowing for model-based tests of the ringdown.

In practice, precision tests of the nature of the emitting objects will probably require the detection of several ringdown events with the large SNRs expected from third generation ground based detectors, or from the space-based Laser Interferometer Space Antenna (LISA).

This idea of viewing the QNMs spectrum of a compact object as a unique fingerprint of spacetime dynamics (in analogy with atomic spectra), is usually referred to as BH spectroscopy.

Echoes

Horizonless ultra-compact objects are expected to produce an additional signal after the ringdown. This signal consists of a series of secondary pulses with progressively smaller amplitudes. The presence of these echoes of the prompt ringdown is caused by the different form of the potential in the equation of motion 5.2.1 for gravitational perturbations. In Fig. 5.1 we can see that in the black hole (or regular black hole) case the potential presents only a maximum near the photon sphere radius ($\sim 3M$ for a Schwarschild BH). When the GWs radiation is scattered on this potential peak, it is partially reflected towards infinity producing the usual prompt ringdown and partially trasmitted in the interior region where is completely lost in the horizon. If the object is horizonless, the potential presents an additional reflecting barrier. If the surface of the object can reflect in some

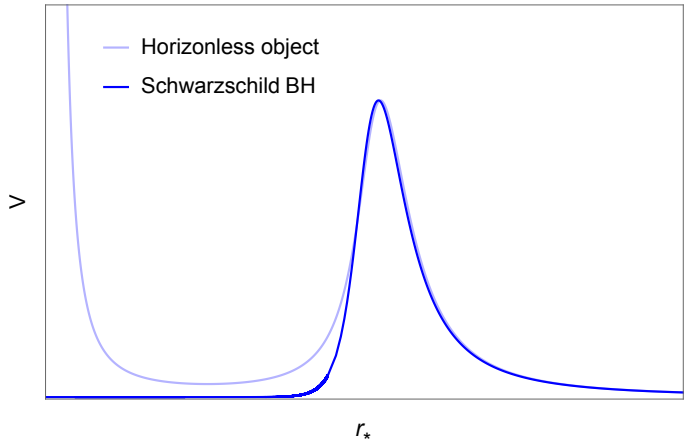

Figure 5.1: Potential for gravitational perturbations (Eq. (5.2.1)). In the black hole case the potential vanish at both $r_* \to \pm\infty$ while for horizoless objects an additional reflective barrier is present at the surface of the object or at its center.

way the gravitational radiation, this barrier will be at its radius. This can happen, for example, in modified theories of gravity in which the graviton reflects effectively on a hard wall [198], or in presence of particular quantum effects [199]. If instead, the gravitational radiation can travel through the interior of the object, the barrier will be located at its center. In both cases, when GWs are scattered on the photon sphere of such horizonless spacetimes, the part of the radiation that is transmitted towards the interior is not lost, it is semi-trapped between the potential peak and the barrier, slowly leaking out towards infinity each time it hits the potential peak at the photon sphere.

The amplitude of the produced echoes depends on the reflection coefficient (R_{BH}) and transmission coefficient (T_{BH}) of the wave coming from the left of the photon sphere and on the reflectivity R of the additional barrier (the surface or the center). After each bounce in the cavity between the barrier and the photon sphere, the GWs perturbation acquires a factor RR_{BH}, each time it passes trough the potential peak it aquires a factor T_{BH}. The photon-sphere barrier acts as a frequency-dependent high-pass filter. For this reason, while the initial ringdown frequencies can be very similiar to the BH QNMs frequencies, each following GWs echo exhibits a lower frequency content. The time delay between echoes is given by the light-crossing time between the potential peak and the reflective boundary. In spherical symmetric spacetime it reads:

$$\Delta t_{\rm echo} \approx 2M - 4M\sigma - 4M\ln(2\sigma) + t_{\rm int} \tag{5.2.2}$$

where the first three terms on the r.h.s. are associated to the travelling time between the surface at $r_0 = 2M(1+\sigma)$ and the photon sphere while t_{int} is the travelling time to cross the object interior.

This picture is obtained in perturbation theory at linear level. However, as we will see in Chapter 7, non linear interactions and backreaction can play a significant role in this contest and so drastically change the echoes signal.

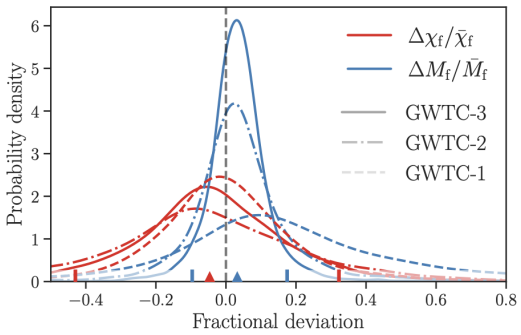

Figure 5.2: Distributions on the remnant mass (blue) and spin (red) fractional deviation parameters obtained by combining the GWTC-3 events (solid trace). For comparison, we also show the results obtained using GWTC-2 (dot dashed traces) and GWTC-1 (dashed) events. The vertical dashed line shows the GR prediction. Triangles mark the GWTC-3 medians, and vertical small bars the symmetric 90% credible intervals. From Ref. [170]

5.3 Performing tests on the gravitational waves signal

We have seen that the gravitational waves signal coming from the coalescence of regular BH mimickers could present several deviations with respect to the one coming from singular BHs mergers. In this section we will briefly explain how the signal is analysed to search for these deviations.

5.3.1 Inspiral-merger-rindown consistency test

A method to verify that a gravitational waveform aligns with the expectations for singular GR black holes is to analyse the complete inspiral-merger-ringdown signal. Unfortunately, predictions for the signal coming from the merger phase (that is a highly non-linear phase) for objects other that GR BHs are practically unknown (however, some notable exceptions include studies on the evolution of boson stars and axion stars [43, 200–203]).

Nonetheless, it is still possible to perform a model-independent null test comparing the mass and spin estimates of the final remnant derived in the GR framework from the inspiral and postinspiral segments of the waveform. Indeed, if General Relativity accurately represents both the adiabatic and nonlinear stages, the parameters estimated from each phase should match within the statistical uncertainties. One usually define the two deviation parameters:

$$\frac{\Delta M_f}{M_f} = 2\frac{M_f^{\rm insp} - M_f^{\rm postinsp}}{M_f^{\rm insp} + M_f^{\rm postinsp}}, \quad \frac{\Delta \chi_f}{\chi_f} = 2\frac{\chi_f^{\rm insp} - \chi_f^{\rm postinsp}}{\chi_f^{\rm insp} + \chi_f^{\rm postinsp}}. \tag{5.3.1}$$

Where M_f and χ_f are the estimated final mass and final dimensionless spin of the remenant BH.

This inspiral-merger-ringdown consistency test has been applied to events listed in the third LIGO-Virgo GWs transient catalog with an SNR > 6 in both the inspiral (low-frequency phase) and postinspiral (high-frequency phase). To achieve this, they divided

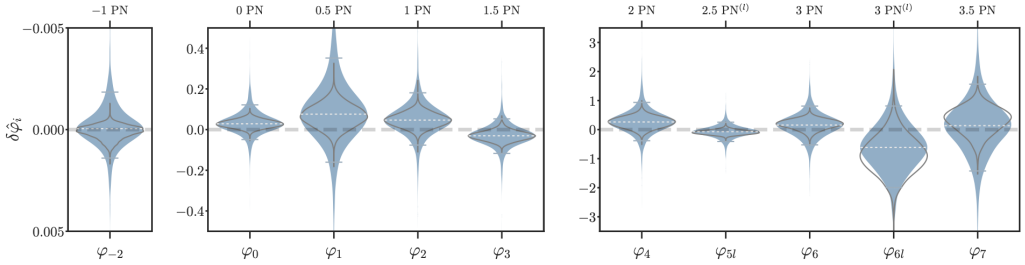

Figure 5.3: Combined GWTC-3 results for the parametrized deviation coefficients of the inspiral phase. Filled distributions represent the results obtained hierarchically combining all events. This method allows the deviation coefficients to assume different values for different events. Unfilled black curves represent the distributions obtained by assuming the same value of the deviation parameters across all events. Horizontal ticks and dashed white lines mark the 90% credible intervals and median values obtained with the hierarchical analysis. From Ref. [170]

the GWs signal into two parts in the frequency domain at some cutoff frequency $f_c^{\rm IMR}$ related to the ISCO of the assumed remnant Kerr BH. The results for the measurements are

$$\frac{\Delta M_f}{M_f} = 0.03^{+0.14}_{-0.13}, \quad \frac{\Delta \chi_f}{\chi_f} = -0.05^{+0.37}_{-0.38},$$

which are compatible with a GR signal within the statistical uncertainties [169]. In Fig. 5.2 we show also the results obtained with the previous first two transient catalogs.

5.3.2 Parametrized tests

Another way to search for deviations from GR in the GWs signal is to put constraints on parametric deformations of the GWs waveform predicted by GR, without relying on any specific alternative theory of gravity. In this framework [204, 205], the deviations from GR are modeled as fractional changes δp_i in the parameters p_i entering the GWs signal as $p_i \to (\delta p_i + 1)p_i$. These fractional changes are then constrained by the data to check the consistency with the GR values.

For example, we saw that the early-inspiral phase can be analytically described up to the order $(v/c)^7$ and thus can be parametrized in terms of the PN coefficients φ_j for $j = 0, \ldots, 7$, as well as the logarithmic terms φ_{jl} for $j = 5, 6$. Moreover, a phenomenological pre-Newtonian coefficient φ_{-2}, denoting an effective -1PN term, is usually included to describe the possible contribution due to emission of dipolar radiation, which is absent in GR.

We can conduct two types of analyses: a single-parameter analysis, where only one of the parameters is allowed to vary freely while the others remain fixed at their GR values, and a multiple-parameter analysis, where all parameters are free to vary simultaneously. The multiple-parameter analysis takes into account correlations between parameters and offers a more conservative (but less informative) measure of the compatibility between an individual GWs event and GR.

Fig. 5.3 shows the constraints on the PN parameters obtained combining events of the third transient catalog LIGO/VIRGO and allowing the coefficients to vary only one at a

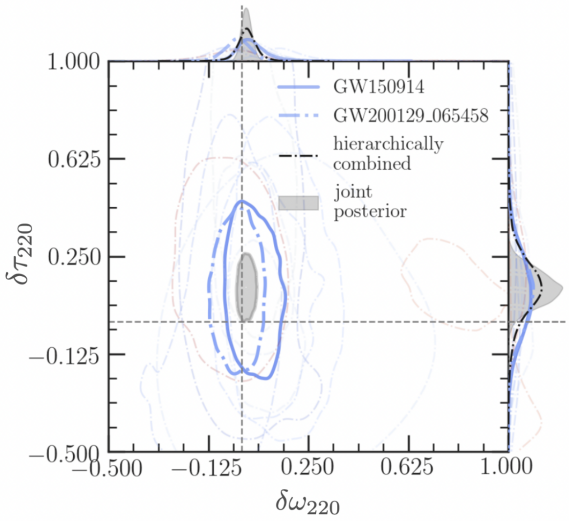

Figure 5.4: The 90% credible levels of the posterior probability distribution of the fractional deviations in the frequency and damping time of the $l = 2$,$m = 2$,$n = 0$ mode, and their corresponding one-dimensional marginalized posterior distributions, for events from the first three observing runs passing a SNR threshold of 8 in both the pre and post-merger signal. Posteriors for the individual events GW150914 and GW200129-065458 are separately shown. The joint constraints obtained multiplying the posteriors (given a flat prior) from individual events are given by the filled grey contours, while the hierarchical method of combination (see caption of Fig. 5.3) yields the black dot dashed curves in the 1D marginalized posteriors. Adapted from Ref. [170].

time. We can see that all the results are consistent with the GR prediction with at least 90% credibility.

Another particularly powerful parameterized test of the nature of the emitting objects is the BH spectroscopy. As we mentioned in Section 5.2 it consists in parametrizing the ringdown part of the signal in terms of the QNMs frequencies in order to search for deviations with respect to the Kerr spectrum. For a null test of GR using uniquely the ringdown you need to detect at least two modes (two complex frequencies) and these are usually parametrized as:

$$\omega^{(J)} = \mathrm{Re}[\omega^{(J)}] = \omega^{(J)}_{\mathrm{Kerr}}(1 + \delta\omega^{(J)}), \tag{5.3.2}$$

$$\tau^{(J)} = \mathrm{Im}[\omega^{(J)}] = \tau^{(J)}_{\mathrm{Kerr}}(1 + \delta\tau^{(J)}) \tag{5.3.3}$$

where $(J) = l, m, n$ labels the considered mode.

In order to obtain more precise results from this analysis, one can try to combine information from different events to achieve better statistics. There are different methods in order to stack multiple events, important examples are the Tiger method (Test Infrastructure for GR) [205, 206] and the Coherent Mode Stacking [207]. In Chapter 6 we will use and briefly discuss another of these methods: the Parspec framework [208]. A general discussion on BH spectroscopy with multiple observations is beyond the scope of this work, a complete review on the topic is [209].

Combining the events of the third GWs transient catalog, constraints on the fractional deviations in the frequency and the damping time of the least-damped quasinormal mode

has been obtained [210]: $\delta\hat{\omega}_{220} = 0.03^{+0.10}_{-0.09}$ and $\delta\hat{\tau}_{220} = 0.10^{+0.44}_{-0.39}$. The probability distributions from which these estimations come from are shown in Fig. 5.4 with black dot dashed curves.

5.3.3 Searches for echoes

The presence of echoes in the late-time GWs signal is a clear distinctive feature of horizonless objects. Several approaches have been developed to model echoes and to search for them in the late GWs signal. The first time-domain echo template was proposed in [211]. It is based on a standard GR inspiral-merger-ringdown template $\mathcal{M}$ and five extra free parameters:

$$h(t) = A\sum_{i=0}^{\infty}(-1)^{i+1}\gamma^{i}\mathcal{M}(t + t_{\rm merger} + t_{\rm echo} - i\Delta t_{\rm echo}, t_0) \tag{5.3.4}$$

where $\mathcal{M}(t, t0) = \Theta(t, t0)\mathcal{M}(t)$ with Θ is a smooth cut-off function. The five free parameters are: the time-delay between successive echoes $\Delta t_{\rm echo}$; the time of arrival of the first echo $t_{\rm echo}$, that depends on non-linear dynamics near the merger; the cut-off time t_0, which quantifies the part of the GR merger template used to produce the echoes; the (frequency-dependent) damping factor of successive echoes $\gamma \in [0, 1]$; the overall amplitude of the echo template A. The $(-1)^i$ term represents the phase inversion of the waveform in each pulse. This implies that Dirichlet boundary conditions are assumed on the reflecting barrier (or, more generally, that the reflection coefficient is real and negative [212]). The phase inversion does not hold for Neumann-like boundary conditions. Extensions of the original template have been developed in [213, 214].

A more phenomenological time-domain model was suggested in [215] that employs a superposition of sine-Gaussians with multiple free parameters. While this model is quite generic, it is burdened by a bigger number of parameters, many of which could be unnecessarily independent.

A frequency-domain template for nonspinning compact objects was built in [212] by approximating the BH potential with a Pöschl-Teller potential and assuming that the source is localized in space. This template depends only on two physical parameter of the horizonless compact object: the reflection coefficient R of the reflective barrier, which can be in general a complex function of the frequency, and the width d of the cavity between the potential peak and the reflective surface, which is directly related to the compactness of the object.

Another search technique with Fourier windows [216–219] exploit the fact that the echoes should pile up at specific frequencies (those implied by the cavity delay time) which are nearly equally spaced.

Some unmodeled searches have also been performed. As instance, a "morphology-independent" analyses, based on the superposition of generalized wavelets adapted from burst searches was proposed and performed in [220, 221].

Note that all the generic modeling of echoes described until now assume equal-spacing between the echoes. In Chapter 7 we will see that, if the effects of non-linear interactions are taken into account, this approximation fails to be adequate, see also [222, 223] for other scenarios involving variable spacing between echoes.

Preliminary evidence suggesting the presence of GWs echoes in the postmerger stage of binary coalescences observed by Advanced LIGO and Advanced Virgo during the first two observing runs has been reported [211, 216, 224]. Nonetheless, the statistical significance of these GWs echoes has been considered low and consistent with noise [225, 226]. Recently, some negative searches have been performed [221, 227, 228]. Additionally, the LIGO/Virgo Collaboration conducted a specific search for echoes within the events listed in the second and third GWs transient catalogs, but found no evidence of GWs echoes [169, 229].

Third-generation gravitational detectors [19–27] are expected to present higher signal-to-noise-ratio in the ringdown (O(100)-O(1000)), potentially allowing to detect GWs echoes or to put strong constraints on horizonless models.

Chapter 6

The ringdown signal: from regular black holes to horizonless objects

In this chapter we investigate the ringdown, i.e. the QNM spectrum, of regular spherically symmetric spacetimes.

We study both test-field perturbations and linear gravitational perturbations. For the latter study, we interpret these metrics as solutions of GR coupled to some suitable matter source [68–71, 230]. This description, although not unique, makes possible the investigation of *gravitational* perturbations, getting above the study of test-field perturbation on a fixed background.

As a general feature, the QNMs spectra for the regular models that we have considered present deviations from the spectrum of a Schwarzschild BH. Assuming that the effect of rotation in more realistic models does not change the picture significantly, we find that for sufficiently large values of the regularization parameter, and for gravitational-wave events with large signal-to-noise ratio, these deviations could be detectable with next generation detectors [19, 25, 231].

The chapter is organized as follows. In Section 6.1 we describe the two specific models considered in the analysis, their main features and field sources. In Section 6.2 we illustrate the study of perturbations on these spacetimes, we report the obtained field equations and the methods used to find the corresponding QNMs. In Section 6.3 we show and comment our results, while in Section 6.4 we discuss how the differences between the obtained spectrum for regular models and the spectrum of singular BHs could be detectable stacking multiple events. The technical details of the derivation of the perturbative equations are given in the appendix.

6.1 Models

Let us report again the generic form of the line element for a regular spherically symmetric spacetimes described in Section 3.1, making the "gauge" choice $h(r) = r^2$:

$$ds^2 = -e^{-2\phi(r)} f(r)\, \mathrm{d}t^2 + \frac{\mathrm{d}r^2}{f(r)} + r^2 \left(\mathrm{d}\theta^2 + \sin^2\theta\, \mathrm{d}\varphi^2\right), \quad f(r) = 1 - \frac{2m(r)}{r}\,. \tag{6.1.1}$$

We recall that simply connected solutions are described by this line element with

$\phi(r) = 0$ and some given mass function $m(r)$ depending on a regularization parameter ℓ.

Multiple connected solutions are instead obtained putting $\phi(r) \neq 0$. As examples of the two possible families of regular geometries, in this chapter we consider the Bardeen and SV models:

$$\text{Bardeen:} \qquad \phi(r) = 0\,, \qquad m(r) = M\frac{r^3}{(r^2+\ell^2)^{3/2}}\,, \tag{6.1.2}$$

$$\text{Simpson–Visser:} \quad \phi(r) = \frac{1}{2}\ln\left(1-\frac{\ell^2}{r^2}\right)\,, \quad m(r) = M\left(1-\frac{\ell^2}{r^2}\right)+\frac{\ell^2}{2r}\,. \tag{6.1.3}$$

We saw in Chapter 1 that these two families of solutions pretty much cover all the possible regularized, spherically symmetric, static, BH spacetimes. [1] Furthermore, depending on the value of ℓ, they can also describe ultra-compact, horizonless, objects [232] which will also be considered in this study.

6.1.1 Horizons and photon spheres

A first relevant observation for our analysis is that the Bardeen-like and SV models have very different features when interpolating from RBHs to horizonless objects. However, in both cases, there exist two special values of the regularization parameter ℓ, say $\ell_{\rm ext}$ and $\ell_{\rm light}$ with $\ell_{\rm ext} < \ell_{\rm light}$, which determine the existence and position of horizons and photon spheres. This is visually illustrated by comparing Fig. 6.1, where the horizon and photon-sphere structure of the spacetimes is represented according to the value of ℓ.

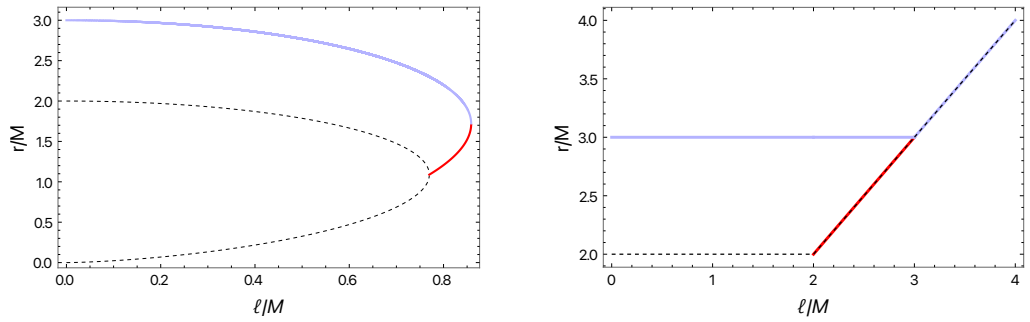

Figure 6.1: Radii of the photon spheres (solid red lines for the inner stable one and solid purple line the outer unstable one) and horizons (dashed black line) for the Bardeen (left panel) and SV (right panel) metric. For the Bardeen metric the two horizons merge for $\ell = 4M/3\sqrt{3}$ giving way to a stable photon sphere inside the usual unstable one. For $\ell = \frac{48M}{25\sqrt{5}}$ the two photon spheres finally merge leaving a simple compact object. For the SV metric the horizon becomes a wormhole throat for $\ell = 2M$ over which a stable photon sphere resides. For $\ell = 3M$ the two photon spheres merge and the wormhole throat becomes an unstable photon sphere.

On the one hand, for $\ell < \ell_{\rm ext}$ a Bardeen-like line element describes a RBH with two horizons and one unstable photon sphere; for $\ell = \ell_{\rm ext}$ the spacetime becomes an extremal RBH, in which the two horizons and the unstable photon sphere coincide; for

[1] We also found spacetimes with an asymptotic regularization of the singular behavior, here we stick to the more physically realistic ones in which the regularizing effects are supposed to act on a finite region of spacetime.

$\ell_{\rm ext} < \ell < \ell_{\rm light}$ the horizon disappears, the spacetime describes an ultracompact object with two photon spheres whose distance decreases with increasing values of ℓ, and one of them is stable. Finally, for $\ell > \ell_{\rm light}$ the two photon spheres disappear and nor stable or unstable null circular orbits are anymore possible around the object. In particular, for the Bardeen model those special values read $\ell_{\rm ext}/M = \frac{4}{3\sqrt{3}}$ and $\ell_{\rm light}/M = \frac{48}{25\sqrt{5}}$.

On the other hand, the SV metric for $\ell < 2M$ describes a RBH geometry with a single horizon shielding a one-way spacelike throat, surrounded by an unstable photon sphere; for $\ell = 2M$ the spacetime represents a one-way wormhole with an extremal null throat and two photon spheres, one of which is stable and located at the throat; for $2M < \ell < 3M$ the wormhole becomes traversable both ways, the throat at

$$r = \ell$$

is timelike and there are two accessible photon spheres; for $\ell > 3M$ the spacetime has only one unstable photon sphere located at the throat $r = \ell$.

6.1.2 Field sources

As already explained, the above introduced static solutions, can be considered the outcome of a transient regularization of the gravitational collapse due to quantum gravity. The implicitly assumption is that such non-classical regime gives way, at late times, to a stationary configuration that should be a solution a some gravitational theory: a low energy, effective field theory limit of quantum gravity, whatever this might be. As our solutions mimic GR ones better and better as one gets away from the objects cores, so we do expect that any such effective field theory of gravity should be encoding deviations from GR in strong gravity regimes. Also, it is well known that such theories can often be recast as GR with non-trivial, and sometimes exotic, matter sources. It is hence reasonable to explore the interpretation of our geometries as solutions of GR and check their associated matter content as this is a crucial step for considering their behavior under perturbations.

Within GR, the effective stress-energy tensor associated with the line element (6.1.1) is given by its Einstein tensor, *i.e.*, $T^{\mu}{}_{\nu} = G^{\mu}{}_{\nu}/8\pi$. Then, for any given RBH model, one might question *a posteriori* the existence of some matter distribution yielding the same stress-energy tensor.

Notice that the Einstein tensor computed from Eq. (6.1.1) has three independent components, meaning that the matter source cannot be uniquely a scalar field (for which $T^{t}{}_{t} = T^{\theta}{}_{\theta}$), nor an electromagnetic field (for which $T^{t}{}_{t} = T^{r}{}_{r}$).

Nonetheless, when $\phi(r) = 0$, $G^{t}{}_{t} = G^{r}{}_{r}$ and Bardeen-like RBHs are often interpreted as solutions of GR coupled to some non-linear electrodynamics with action [68, 69]

$$\mathcal{S} = \int \mathrm{d}^4x\, \sqrt{-g}\left(\frac{1}{16\pi}R - \frac{1}{4\pi}\mathcal{L}(F)\right), \tag{6.1.4}$$

where the electromagnetic Lagrangian is a non-linear function of the electromagnetic field strength $F = \frac{1}{4}F_{\mu\nu}F^{\mu\nu}$, with $F_{\mu\nu} = 2\nabla_{[\mu}A_{\nu]}$ being A_{μ} the electromagnetic potential. The Maxwell field is frequently assumed purely magnetic and its magnetic charge coincides with the regularization parameter, which implies that the only non-vanishing component of the Maxwell field is $F_{\theta\varphi} = \ell \sin\theta$ (alternatively, the only non-vanishing component of

the potential is $A_\varphi = \ell\cos\theta$) and $F = \ell^2/2r^4$.

The modified Maxwell field equation

$$\nabla_\mu \left(\mathcal{L}_F F^{\alpha\mu}\right) = 0\,, \tag{6.1.5}$$

being $\mathcal{L}_F \equiv \partial\mathcal{L}/\partial F$, is trivially satisfied, while the gravitational equations

$$G_{\mu\nu} = 2\left(\mathcal{L}_F F_\mu{}^\lambda F_{\nu\lambda} - g_{\mu\nu}\mathcal{L}\right), \tag{6.1.6}$$

imply that the electromagnetic Lagrangian is given in term of the metric functions of the spacetime as in Eq. (6.1.1) (with $\phi = 0$)

$$\mathcal{L}(F) = \frac{m'}{r^2}, \tag{6.1.7}$$

where $r = r(F)$.

In particular, for the model considered in this work

$$\mathcal{L}_{\text{Bardeen}} = \frac{3M}{\ell^3}\left(\frac{\sqrt{2\ell^2 F}}{1+\sqrt{2\ell^2 F}}\right)^{5/2}. \tag{6.1.8}$$

On the other hand, when $\phi \neq 0$, to model the source it is necessary to introduce other matter fields. In particular, the SV spacetime could be sourced by a combination of non-linear electrodynamics and a self-interacting scalar field [70, 71].

$$\mathcal{S} = \int \mathrm{d}^4x\,\sqrt{-g}\left(\frac{1}{16\pi}R - \frac{1}{4\pi}\mathcal{L}(F) - \frac{\varepsilon}{2}(\partial\Phi)^2 - V(\Phi)\right), \tag{6.1.9}$$

where $\varepsilon = \pm 1$, and the positive (negative) sign corresponds to a canonical (phantom) scalar field with positive (negative) kinetic energy.

Even in this case, we assume the Maxwell field to be purely magnetic with its magnetic charge equal to the regularization parameter, so that the modified Maxwell equation is trivially satisfied. The computation of the gravitational field equations

$$G_{\mu\nu} = 2\left(\mathcal{L}_F F_\mu{}^\lambda F_{\nu\lambda} - g_{\mu\nu}\mathcal{L}\right) + 8\pi\left[\varepsilon\partial_\mu\Phi\partial_\nu\Phi - g_{\mu\nu}\left(\frac{\varepsilon}{2}(\partial\Phi)^2 + V(\Phi)\right)\right], \tag{6.1.10}$$

reveals that the scalar field is phantom and satisfies

$$\Phi'^2 = \frac{\phi'}{4\pi r}\,, \tag{6.1.11}$$

the derivative of the electromagnetic Lagrangian reads

$$\mathcal{L}_F = \frac{r^2\left[r^2 f'' - 3r^2 f'\phi' - 2f\left(r^2\phi'' - r^2\phi'^2 + r\phi' + 1\right) + 2\right]}{4\ell^2}\,, \tag{6.1.12}$$

which, once integrated, can be substituted in the expression for the scalar potential

$$V[\Phi(r)] = \frac{1 - rf' + f\left(r\phi' - 1\right) - 2r^2\mathcal{L}}{8\pi r^2}\,. \tag{6.1.13}$$

Finally, the Klein–Gordon equation is a consequence of the Einstein equations.

In particular, using the metric functions for the SV spacetime we get

$$\mathcal{L}_{\rm SV} = \frac{6M}{5}\left(\frac{2F^5}{\ell^2}\right)^{1/4}, \quad \Phi_{\rm SV} = \frac{1}{\sqrt{4\pi}}\operatorname{arccot}\left(\frac{\sqrt{r^2-\ell^2}}{\ell}\right), \tag{6.1.14}$$

$$V_{\rm SV} = \frac{M\sin^5\left(\sqrt{4\pi}\,\Phi\right)}{10\pi\ell^3}\,. \tag{6.1.15}$$

Notice that we have used a different convention with respect to Ref. [70], in particular we have chosen the scalar field to vanish at spatial infinity.

6.2 Study of perturbations

Assuming the gravito-scalar-magnetic interpretation given in Section 6.1.2, we can study the full effect of linear perturbations expanding the metric and the matter fields around their background values. According to their parity symmetry, even or odd, the metric and matter perturbations can be decomposed respectively in polar and axial contributions. However since the background metric and the background scalar field are even, while the background magnetic field is odd, axial electromagnetic perturbations and polar scalar perturbations are coupled to polar gravitational perturbations, while polar electromagnetic perturbations are coupled solely to axial gravitational perturbations (being impossible to have axial scalar perturbations).

If this parity coupling is not taken into account, as it commonly happened in several recent investigations [233–239], one obtains an incompatible system of equations for the perturbation functions, which admits only a trivial solution. This has been quite systematically overlooked in the previously mentioned literature, discarding one of the three obtained equations, tacitly assuming that it can be obtained from the other two. To understand the fine details, the interested reader can follow the full derivation of the perturbative equations in Section 6.6 and in particular the comment in Footnote 3. On the other hand, other authors have analyzed linear perturbations carefully, but specialized to non-linear electrodynamics without scalar fields or viceversa [240–245]. Our perturbative analysis extends these results to a generic spacetime described by the line element (6.1.1), interpreted as an exact solution of GR coupled to non-linear electrodynamics and scalar fields.

6.2.1 Full perturbative analysis

For each parity sector, gravitational, scalar and electromagnetic harmonic perturbations satisfy a system of coupled non-homogeneous wave equations, which schematically read

$$\frac{\mathrm{d}^2\mathcal{I}}{\mathrm{d}r_*^2} + \left(\omega^2 - V_{\mathcal{I}}\right)\mathcal{I} + \sum_{\mathcal{J}\neq\mathcal{I}} c_{\mathcal{I},\mathcal{J}}\,\mathcal{J} = 0\,, \tag{6.2.1}$$

where r_* is the tortoise coordinate defined as $\mathrm{d}r_*/\mathrm{d}r \equiv \mathrm{e}^{\phi}/f$, for $\mathcal{I},\mathcal{J} = \{\mathcal{A},\mathcal{E}\}$ in the sector in which axial gravitational perturbations are coupled to polar electromagnetic perturbations, and $\mathcal{I},\mathcal{J} = \{\mathcal{P},\mathcal{B},\mathcal{S}\}$ in the sector in which polar gravitational, axial elec-

tromagnetic and polar scalar perturbations are coupled. The variables $\{\mathcal{A}, \mathcal{P}, \mathcal{B}, \mathcal{E}, \mathcal{S}\}$ are given combinations of the metric, the electromagnetic potential, and the scalar field perturbation functions and their derivatives. The potentials $V_{\mathcal{I}}$ and the coefficients $c_{\mathcal{I},\mathcal{J}}$ are given functions of the background metric and fields, and also depend on the harmonic number l associated to the spherical-harmonics expansion.

For the sake of conciseness, we have only summarised the outcome of such full perturbative analysis, which is instead explicitly carried on in Section 6.6. The latter turns out to be quite involved and dependent on the details of the matter distribution so, as a complementary analysis, we also present in what follows a test-field perturbations analysis which, albeit less accurate, has the merit to avoid assumptions on the matter distribution supporting the geometry. In Section 6.3 we shall see that, reassuringly, the outcomes between the two kinds of analysis turn out to be qualitatively in agreement.

6.2.2 Test-field perturbations

The previous analysis relies on the interpretation of our metrics as solutions of GR coupled with some exotic matter. If instead we want to study the ringdown without specifying the matter distribution of our spacetime, test-field perturbations represent a simple but informative proxy. Often, the first step is to consider scalar field perturbations on top of these spacetimes. For spherically symmetric spacetimes, it is possible to extend the analysis to other spin-s fields, to include *axial* spin-2 perturbations [246].

The crucial point made in such analyses is that standard matter fields — such as canonical scalars and Maxwellian electric fields — couple with the *polar* gravitational perturbations, while in the axial sector the source stress-energy tensor is left unperturbed. If true this would imply that spin-2 test fields analysis could already capture some features of the gravitational QNMs spectrum. However, this is not the case for a purely magnetic source, and one should be then careful in drawing conclusions.

Within this context, the perturbative equation for scalar, electromagnetic and gravitational axial perturbations for the spacetime described by Eq. (6.1.1) reads [246, 247]

$$\frac{\mathrm{d}^2\psi_s}{\mathrm{d}r_*^2} + \left(\omega^2 - V_s\right)\psi_s = 0\,, \tag{6.2.2}$$

where ψ_s is related to the spin-s perturbation field, the tortoise coordinate r_* is still defined as $\mathrm{d}r_*/\mathrm{d}r \equiv \mathrm{e}^{\phi}/f$, and the potential depends on the spin-weight of the perturbation and the metric functions:

$$V_s = f\,\mathrm{e}^{-2\phi}\left[\frac{l(l+1)}{r^2} + \frac{2\left(1-s^2\right)m}{r^3} - (1-s)\left(\frac{2m'}{r^2} + \frac{f\phi'}{r}\right)\right]. \tag{6.2.3}$$

6.2.3 Computation of the quasinormal modes

We now want to solve Eqs. (6.2.1) and (6.2.2) for ω, to compute the quasinormal modes frequencies, *i.e.* the late-time response of the compact object to an initial perturbation that is localized in space. After providing suitable boundary conditions, we use standard and matrix-valued direct integration techniques [248, 249] for the test-field case and for the full gravitational case, respectively.

For the RBH cases, the two boundaries from which we integrate are spatial infinity, where we impose the solution to be a purely outgoing wave, and the horizon, where we impose the solution to be a purely ingoing wave.

For the horizonless cases, we still impose the solution to be purely outgoing at spatial infinity, but for the other boundary condition we make a different choice for the two families. The Bardeen-like metrics with $\ell > \ell_{\rm ext}$ describe ultracompact stars thus we impose regularity conditions at the origin. Note that in this way we are assuming that the test field perturbations can travel through the entire object with negligible interaction with matter (while in the gravitational perturbations case such interaction is self-contained in the equations of motion). Of course, this assumption may at this point seem unjustified, it is nonetheless the only one that we can do without introducing a specific, and at this stage arbitrary, coupling between the object's matter and our test field (see however our comment about absorption below). The SV metric with $\ell > 2M$ represents instead a traversable wormhole. Its throat, differently from a horizon, is traversable in both directions. Since the geometry on the two sides of the wormhole throat is symmetric, we assume that the perturbation will inherit the symmetry of the background. This assumption translates into perfect reflection at the throat, which we implement by demanding the perturbation to vanish there, *i.e.* $\psi(\ell) = 0$.

Both the above assumptions can in principle be modified, e.g. for the Bardeen-like ultra-compact objects we could introduce an absorption coefficient associated to the star matter or in the wormhole case we could assume asymmetric stimulation of the wormhole mouth. We leave these extensions of the present study for future investigations.

The direct integration method we used requires an initial guess for the value of the quasinormal mode frequency. While in the RBH case we track the mode continuously starting from its "quasi-Schwarzschild" value obtained for small values of ℓ, in the ultracompact case because of the discontinuity in the boundary conditions (there is no horizon) and the large values of ℓ, we do not have any value as a reference to start from. Thus we explored carefully the (ω_I, ω_R) plane in order to find the mode with smaller imaginary part, that is the fundamental one.

6.3 Results

In what follows we report the QNMs spectra for the considered two families of spherically symmetric regular spacetimes. We focus on the quadrupolar $l = 2$ fundamental mode, which is the dominant one in the gravitational-wave ringdown signal. Note however, that in the ultracompact horizonless cases, these QNMs become dominant only in the late-time ringdown signal being preceded by a first part of the signal that is similar to the Schwarzschild one [250].

For test-field perturbations we explore both the RBH and horizonless branches. For the Bardeen metric we vary the regularization parameter from $\ell = 0$, that is Schwarzschild, to roughly the maximum value for which the object still possesses a photon sphere. In the SV spacetime a photon sphere is always present at the throat and thus there is no upper bound on the value of the regularization parameter, so we let it span in $[0, 3.5M]$. We show our results in Figs. 6.2 and 6.3.

Let us note that some results in the test-field approximation were already present in

literature, in a specific branch and for specific values of s. Our results are in agreement with those presented *e.g.* in Refs. [251–255]. For the full perturbative analysis the computation in the horizonless branch presents some technical difficulties and numerical instabilities, therefore we only report the more solid results for the RBH branch, shown in Figs. 6.4 and 6.5. However, in advance with the discussion in Section 6.4, we only need the numerical values of gravitational QNMs in the RBH branch to assess the possible detectability of these deviations with the next generation of gravitational-wave detectors.

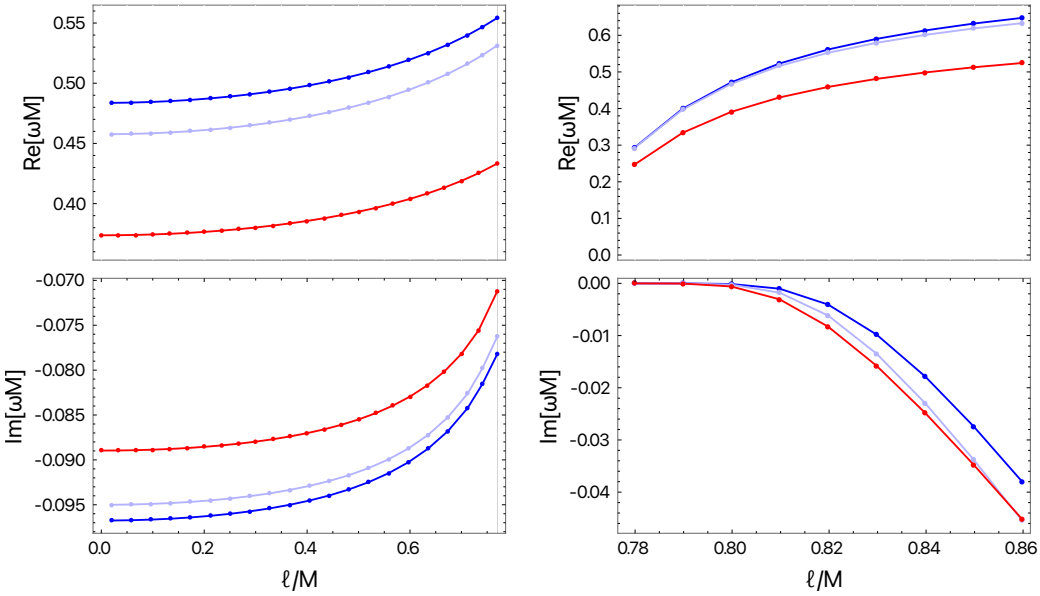

Figure 6.2: Quadrupolar $l = 2$ fundamental mode of the Bardeen metric for test-field perturbations, $s = 0$ (blue), $s = 1$ (light purple) and $s = 2$ (red). On the left results for values of ℓ in the RBH branch that is from $\ell = 0$ (Schwarzschild) to $\ell = \ell_{\rm ext} = \frac{4}{3\sqrt{3}}M$ (extremal RBH). On the right results for values of ℓ in the horizonless branch ($\ell > \ell_{\rm ext}$). Note that, in this branch, for values of the regularization parameter near (but not equal to) the extremal one, the imaginary part is extremely small and thus we have very long living modes this is not true for the extremal RBH case, indicated by the vertical line in the left panel.

Regular Black holes

	Bardeen			Simpson–Visser		
	Test $s=2$	Axial	Polar	Test $s=2$	Axial	Polar
$\ell/M=0.2$						
Δ_R	0.0075	−0.0012	0.0037	$-3\cdot10^{-5}$	−0.0002	−0.0005
Δ_I	0.0045	0.0090	0.0090	0.0022	0.0044	0.0044
$\ell/M=0.6$						
Δ_R	0.0808	0.0069	0.0297	−0.0003	−0.0163	−0.0067
Δ_I	0.0674	0.0776	0.0810	0.0236	0.0292	0.0292
$\ell/M=1.6$						
Δ_R				−0.0053	−0.0690	−0.0428
Δ_I				0.1798	0.1854	0.1776

Horizonless compact objects

	Bardeen	Simpson–Visser
	Test $s=2$	Test $s=2$
$\delta=0.05$		
Δ_R	0.1380	−0.1801
Δ_I	0.9712	0.9970
$\delta=0.10$		
Δ_R	0.3613	−0.0310
Δ_I	0.6441	0.9015
$\delta=0.20$		
Δ_R		0.0482
Δ_I		0.5913

Table 6.1: Relative deviations from the quadrupolar fundamental Schwarzschild frequency $\Delta_{R/I}=\frac{\omega_{R/I}-\omega^{\rm S}_{R/I}}{|\omega^{\rm S}_{R/I}|}$ with $\omega^{\rm S}M=0.37367-0.08896\mathrm{i}$, for $s=2$ test-field and linear gravitational perturbations, both in the axial and polar sectors, for selected valued of the regularization parameter. For the Bardeen metric there are no results for $\ell/M=1.6$ and $\delta=0.2$, with $\delta\equiv\ell/\ell_{\rm ext}-1$, since for those values of compactness the spacetime not only lose the presence of the horizon but even of a photon sphere. For both spacetimes results for axial and polar gravitational perturbations are not reported for horizonless configurations because of the numerical issues present in this branch. Looking at the test field case, it is easy to see the large increment of Δ_I passing from the RBH configurations to the horizonless ones for small δ.

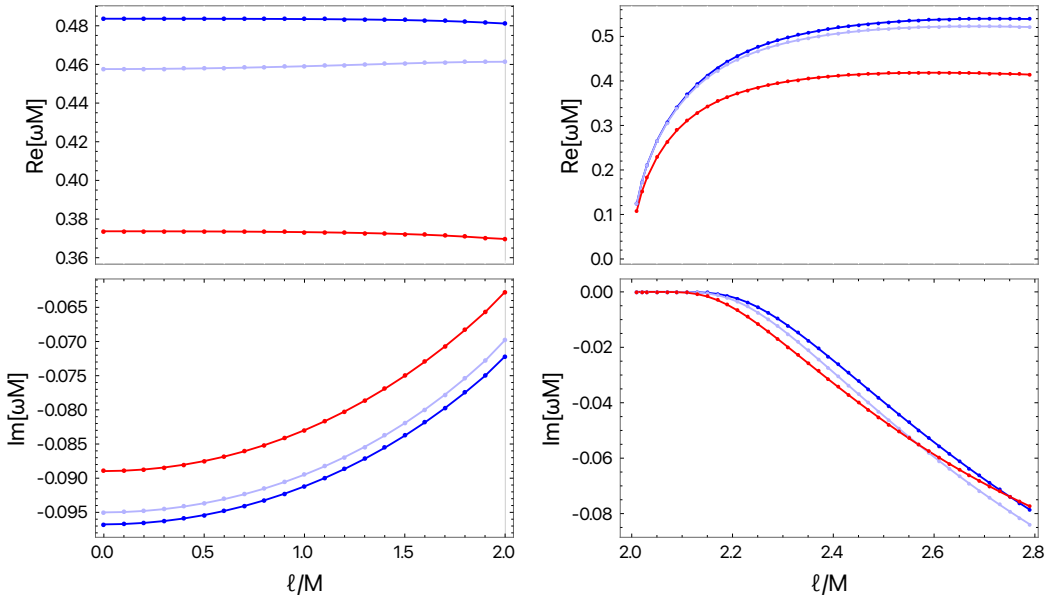

Figure 6.3: Quadrupolar $l = 2$ fundamental mode of the SV metric for test-field perturbations, $s = 0$ (blue), $s = 1$ (light purple) and $s = 2$ (red). On the left results for values of ℓ in the RBH branch, that is from $\ell = 0$ (Schwarzschild) to $\ell = 2M$ (one-way wormhole with an extremal null throat). On the right results for values of ℓ in the horizonless branch ($\ell > 2M$). It is worth noticing the relative flatness of the real part curves which highlights weak deviations from the singular GR solution behavior recovered for $\ell = 0$. Note that, in the horizonless branch (right panel), for values of the regularization parameter near (but not equal to) the extremal one, the imaginary part is extremely small and thus we have very long living modes, this is not true for the extremal RBH case, indicated by the vertical line in the left panel.

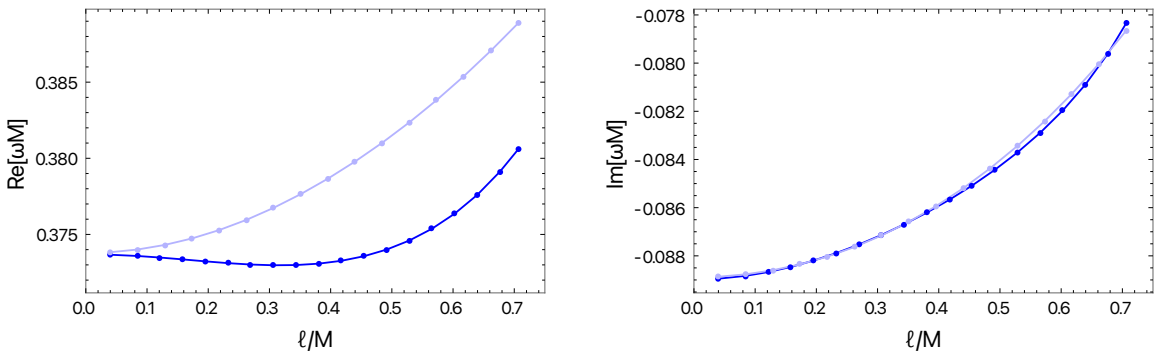

Figure 6.4: Axial (blue) and polar (light purple) $l = 2$ gravitational mode for the Bardeen metric for values of ℓ in the RBH branch that is from $\ell = 0$ (Schwarzschild) to $\ell = \ell_{\text{ext}} = \frac{4}{3\sqrt{3}}M$ (extremal RBH).

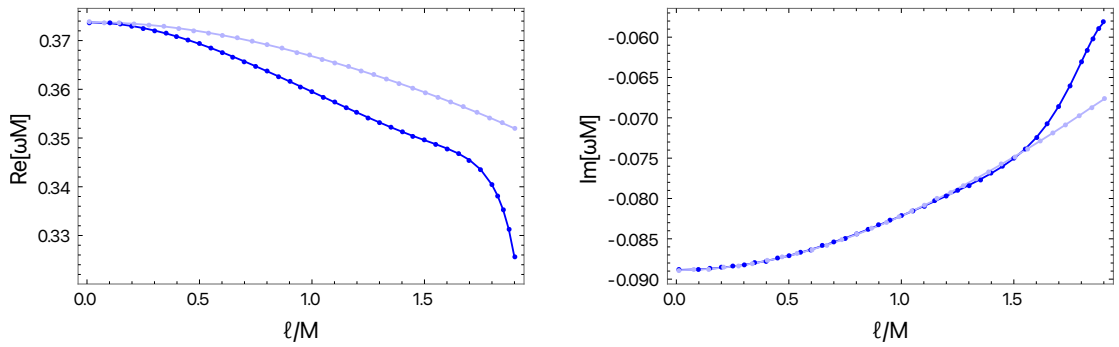

Figure 6.5: Axial (blue) and polar (light purple) $l = 2$ gravitational mode for the SV metric for values of ℓ in the RBH branch that is from $\ell = 0$ (Schwarzschild) to $\ell = 2M$ (one-way wormhole with an extremal null throat).

6.3.1 Summary

The results for the two families of regular models presents some differences. For what regards test-field perturbations, the SV spacetime seems to be a better mimicker since, given a certain value of the regularizing parameter ℓ, its spectrum is more similar to the Schwarzschild one (i.e $|(\omega_{SV} - \omega_S)/\omega_S| < |(\omega_{Bard} - \omega_S)/\omega_S|$). We must say however that, for SV, ℓ can span a bigger intervals of values and thus the spectrum can reach higher deviations from Schwarzschild in the imaginary part (some numerical examples are reported in Table 6.1). Furthermore the corrections to the real part of the frequency in the RBHs branch are negative (except for $s = 1$) while for the Bardeen spacetime are always positive. The reason for this is clear in Schutz-Will WKB approximation [256] in which $\omega_R \sim V(r_{peak})^{1/2}$ (where r_{peak} is the location of the maximum of the potential). Indeed, compared to the Schwarzschild spacetime, the peak of the potential in the SV spacetime is smaller, whereas in the Bardeen spacetime it is higher. This holds for any spin s of the perturbation except for $s = 1$. Indeed, for this value of the spin, in the test-field approximation $V^{\rm SV}(r_{peak}) = V^{\rm Schw}(r_{peak})$ and the small positive corrections in the QNMs of the SV spacetime are only due to the different location of the peak in tortoise coordinates.
For what regards full gravitational perturbations instead, the real part of the frequency for SV RBHs presents stronger deviations from the Schwarzschild one in the axial sector.

For both families of regular models, in the ultracompact branch we found long living modes associated to the trapping of perturbations near the stable photon sphere. The damping time grows exponentially with the harmonic number and it is longer for values of the regularization parameter near the extremal case, that is for more compact configurations. This is not surprising, a more efficient trapping is expected in these cases since there is more distance between the two photon spheres and a deeper potential well. The aforementioned conclusions stand robust within our framework; however, it is crucial to note that they may be influenced by potential interactions between the test field and matter (e.g., through an absorption coefficient). This consideration is particularly significant as the stable photon sphere seats comfortably within the region where the matter stress-energy tensor is non-negligible [232].

Finally, we also found that the isospectrality between the axial and the polar sector is broken for both families, mainly in the real part of the frequencies, with deviations that, as expected, are greater for greater values of the regularization parameter.

6.3.2 A connection between the photon sphere instability and the Aretakis instability?

We found that also in our new class of horizonless ultracompact objects there are long living perturbations modes, associated to the presence of a stable photon sphere. As explained in Section 3.4.2 this is usually assumed to be the hint of a non-linear instability.[2] Indeed the presence of these long living modes in the frequency decomposition is associated with a total perturbation in time domain that decay slower than $1/t$ and this leads to the breaking of linear approximation.

The continuity between RBHs and horizonless objects of our models enlighten the fact that stable photon sphere responsible for this instability is already present in the limiting case of extremal RBHs (for $\ell = \ell_{ext}$) and and its position (in Eddington–Finkelstein coordinates) coincides with that of the extremal horizon [232, 257]. Actually, this is a general feature of any extremal horizon: it coincides with an extreme point of the potential in the equation for null geodesics [258–260]. Interestingly, this case is conjectured to be affected by another type of instability, the so-called Aretakis instability [261, 262] which appears to be connected to conserved quantities of extremal horizons.

Presently, and differently from the photon sphere instability, the Aretakis instability lacks of a sound physical interpretation. In [263, 264] it has been tentatively connected to the presence of null geodesics trapped near the horizon, that is geodesics that orbit arbitrarily many times around the horizon before falling in. If this connection will be confirmed then it will strongly suggest that the Aretakis instability should be interpreted as a special case of the photon sphere one.

However, we have here to notice that the former has been proven to hold also for extremal Kerr BHs [262] albeit for these BHs the photon sphere at the horizon is actually unstable. Of course, also in this case one can observe geodesics that orbit arbitrarily many times around the horizon before falling in, like it happens around any unstable photon sphere, but, usually, this is not associated to any new instability.

Furthermore, from our previous analysis, it is clear that the damping times for extremal RBHs are of the same order of magnitude of that for sub-extremal ones, while ultracompact objects with stable photon sphere presents very long living modes with damping times several order bigger. This seems to suggest that the photon sphere instability is not triggered or partially suppressed for extremal RBHs. Probably this is due to the fact that an extremal horizon, being an horizon, is not a true stable orbit but can be considered a metastable photon sphere (see Fig. 6.6). The presence of an horizon, even if extremal, introduces a source of dissipation: indeed the energy that enters the horizon is completely lost.

[2] Note however that, as already remarked, our results were obtained by neglecting the possible interactions of the perturbation with matter. Indeed, it can be shown that generically the matter content of these spacetimes is not negligible at the location of the stable photon sphere [232]. If this matter absorbs part of the energy carried by the perturbation, the instability would be most probably tamed.

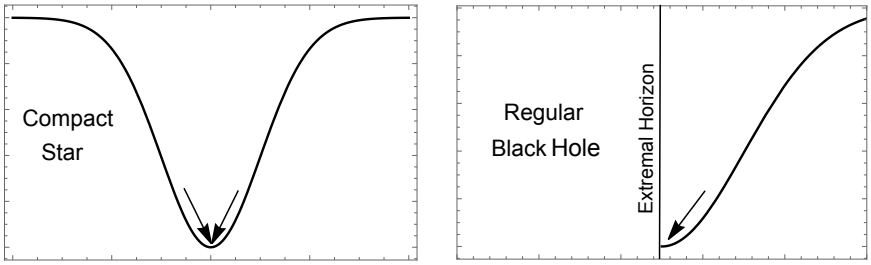

Figure 6.6: Difference between a true stable photon sphere present in the spacetime of compact horizonless objects (left panel) and the "stable" photon sphere present at the horizon of extremal BHs and RBHs (right panel). The first one causes a real trapping of modes while in the second case the "trapped" modes pass through the horizon in the BH region.

In conclusion, at the moment there seems to be no ground for a claim that the Aretakis instability is the limit of the instability associated to stable photon spheres for ultra-compact objects when an extremal trapping horizon forms.

6.4 Detectability

At this point one may wonder if these QNMs can be distinguished from the QNMs of singular GR BHs in the observed gravitational-wave ringdown signals. In other words, will we ever be able to prove that the merging objects that produce a given ringdown signal are not singular GR BHs but RBHs? and how many observations we have to combine to do that?

As a preliminary answer to the above questions, we report here results obtained within a particular framework for BH spectroscopy, the Parspec framework [208]. One can take this initial analysis as a proof of principle of detectability of these corrections to BHs QNMs.

6.4.1 Parspec framework

Parspec is an observable-based parametrization of the ringdown signal of rotating BHs beyond GR, it was developed for BH solutions in modified gravity but can be adapted to our phenomenological models of RBHs. We will give here a brief description of this framework.

Let us assume $i = 1, \ldots, N$ independent ringdown detections, for which q QNMs are measured. Each mode of the i-th source is parametrized as

$$\omega_i^{(J)} := \mathrm{Re}[\omega_i^{(J)}] = \frac{1}{M_i} \sum_{k=0}^{D} \chi_i^n \omega_J^{(k)} \left(1 + \gamma_i \delta\omega_J^{(k)}\right), \tag{6.4.1}$$

$$\tau_i^{(J)} := \frac{1}{\mathrm{Im}[\omega_i^{(J)}]} = M_i \sum_{k=0}^{D} \chi_i^n \tau_J^{(k)} \left(1 + \gamma_i \delta\tau_J^{(k)}\right), \tag{6.4.2}$$

where $J = 1, 2, ..., q$ labels the mode; M_i and $\chi_i \ll 1$ are the detector-frame mass and spin

of the i-th source; D is the order of the spin expansion; $\omega_J^{(k)}$ and $t_J^{(k)}$ are the dimensionless coefficients of the spin expansion for a Kerr BH in GR; γ_i are dimensionless coupling constants that can depend on the source i but not on the specific mode J, for $\gamma_i \to 0$ the GR BH case is recovered; finally $\delta\omega_J^{(k)}$ and $\delta t_J^{(k)}$ are the "beyond Kerr" corrections, in general since all the source dependence is parametrized in γ_i, these corrections are universal dimensionless numbers.

In our analysis, we will assume that ℓ/M is constant. Under this condition, there will be no dependence of the corrections on the source parameters and thus γ_i can be set to 1. This assumption can seem reasonable in the case of a dynamical process of regularization but it is not necessary correct (see Section 3.3). Relaxing this assumption will probably worsen our results, rendering the most massive sources irrelevant for our analysis. However if one consider instead ℓ to be the fixed parameter, the dependece of the QNMs on M becomes more intricate, as instance bigger mass objects will be regular BHs while smaller objects will be horizonless. We leave the analysis of this case to future work.

We assume perturbative corrections, *i.e.* we assume that $\gamma_i \delta\omega^{(k)} \ll 1$ and $\gamma_i \delta t^{(n)} \ll 1$.

It should be noted that M_i and χ_i are extracted assuming GR BHs, *i.e.* computed from the full inspiral-merger-ringdown waveform within GR. One should extract mass and spin of the BH from the inspiral-merger waveform considering also GR deviations, but this can be very challenging, especially because it requires merger simulations for these RBHs. In this preliminary analysis, we shall assume the shift on the final mass and spin of the source to be negligible.

To construct the probability distribution of the beyond Kerr parameters we use a Bayesian approach: if we indicate with $\bar{\theta}$ the parameters (that in our case are $\delta\omega_J^{(k)}$ and $\delta t_J^{(k)}$) and with $\bar{d}$ a given set of ringdown observations, from the Bayes' theorem we have

$$P(\bar{\theta}|\bar{d}) \propto \mathcal{L}(\bar{d}|\bar{\theta}) P_0(\bar{\theta}) \tag{6.4.3}$$

where $\mathcal{L}(\bar{d}|\bar{\theta})$ is the likelihood function and $P_0(\bar{\theta})$ is the prior on the parameters. Thus from the likelihood we can obtain the full posterior probability distribution $P(\bar{\theta}|\bar{d})$ through a Markov chain Monte Carlo (MCMC) method based on the Metropolis-Hastings algorithm.

For each event, the likelihood is chosen to be Gaussian:

$$\mathcal{L}(\bar{d}|\bar{\theta}) = \mathcal{N}(\vec{\mu_i}, \Sigma_i) \tag{6.4.4}$$

where the vector $\vec{\mu_i}$ is

$$\vec{\mu_i} = (\vec{\mu_i}^{(1)}, ..., \vec{\mu_i}^{(q)})^T \tag{6.4.5}$$

where each $\vec{\mu_i}^J$ is a two component vector that depends on the difference between the observed $J = 1, ..., q$ modes and the parametrized templates in Eq. (6.4.2):

$$\vec{\mu}_i^{(J)} = \begin{bmatrix} \omega_i^{(J)} - \omega_{i,\mathrm{obs}}^{(J)} \\ \tau_i^{(J)} - \tau_{i,\mathrm{obs}}^{(J)} \end{bmatrix}, \tag{6.4.6}$$

and Σ_i is the covariance matrix that includes errors and correlations between the frequen-

cies and damping times of the i-th source.

Since the observed QNMs correspond to different values of l and m, *i.e.* they are "quasi-othonormal", the covariance matrix $\Sigma_i = \mathrm{diag}(\Sigma_i^{(1)}, ..., \Sigma_i^{(q)})$ is block-diagonal with each block corresponding to the J-th mode, and thus the likelihood function can be written as a product of Gaussian distributions:

$$\mathcal{N}(\vec{\mu_i}, \Sigma_i) = \prod_{J=1}^{q} \mathcal{N}(\mu_i^{(J)}, \Sigma_i^{(J)}) \tag{6.4.7}$$

Moreover, since we consider N independent detections, the combined likelihood function of the parameters can be further factorized as:

$$\mathcal{L}(\vec{d}|\vec{\theta}) = \prod_{i=1}^{N} \mathcal{L}_i(\vec{d}|\vec{\theta}) = \prod_{i=1}^{N} \prod_{J=1}^{q} \mathcal{N}(\mu_i^{(J)}, \Sigma_i^{(J)}) \tag{6.4.8}$$

6.4.2 Results

We assume that the masses and spins of the merging objects are measured from the inspiral signal so that we can considered only one ringdown mode ($l = m = 2$) in our analysis, we stick to 0 order in the spin thus we have:

$$\omega_i := \mathrm{Re}[\omega_i] = \frac{1}{M_i}\omega^{(0)} \left(1 + \delta\omega^{(0)}\right), \tag{6.4.9}$$

$$\tau_i := \frac{1}{\mathrm{Im}[\omega_i]} = M_i \tau^{(0)} \left(1 + \delta\tau^{(0)}\right). \tag{6.4.10}$$

where, as already mentioned, we put $\gamma_i = 1$ because we assumed ℓ/M to be the same for every source.

The analysis can be generalized to higher order in the spin once computed the gravitational QNMs for this rotating RBHs.

We considered the signal coming from the merger remnant of N binary coalescences as observed by a ground-based 3G detector (ET in the so-called ET-D configuration [19]). The 2N masses of the binary components are drawn from a log-flat distribution between $[5, 95]\, M_\odot$ and the 2N spins from a uniform distribution between $[-1, 1]$. We do not include supermassive BHs in the range of masses since ET will be poorly sensitive to them. We fix the source distance by choosing the SNR of the mode to be 10^2. We then compute the mass and the spin of the final BH formed after merger using semianalytical relations based on numerical relativity simulations in GR [265]. From the final mass of the source we compute the $l = 2$ frequency and damping time of a RBHs with that mass, we perform the analysis for both Bardeen and SV RBHs. We compute the errors on the modes through a Fisher-matrix approach.

Like we can see in Fig. 6.7, O(100) observations with SNR $\approx 10^2$ are enough to exclude with 90% confidence level the hypotesis of GR singular BHs that is $\delta\omega = \delta\tau = 0$. This even for small, but not Planckian, values of the regularization parameter and for both families of regular models.

For the Bardeen metric, the strongest constraints come from the real part of the frequency in the polar sector: when $\ell > 0.13$ its deviation from Schwarzschild real frequency

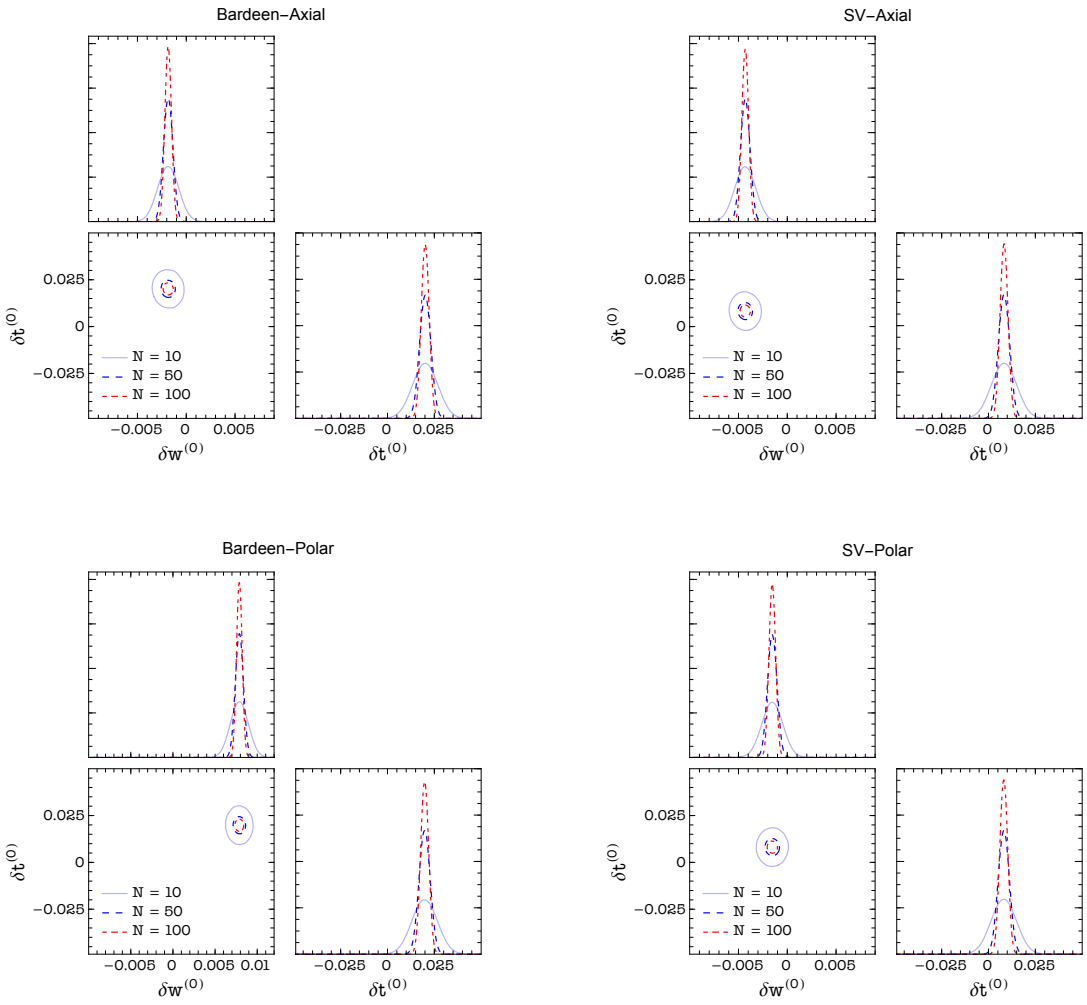

Figure 6.7: Probability distribution functions for corrections to the Schwarzschild $l = m = 2$ mode when we inject as observations axial/polar QNMs of the Bardeen metric with $\ell/M = 0.3$ (left upper/bottom panel) and axial/polar QNMs of the SV metric with $\ell/M = 0.3$ (right upper/bottom panel). Different colors represents results obtained with different numbers N of observed sources.

allows to exclude the GR hypothesis at 90% confidence level. For the SV metric the strongest constraints come from the real part of the frequency in the axial sector and to exclude the GR hypothesis we need $\ell \geqslant 0.19$. Of course these results depend on the number of sources and their SNR. Here we referred to the case of O(100) observations with SNR $\sim 10^2$ which should be routinely available with third generation ground-based detectors [19, 231].

Note that from the posterior probability distributions is also possible to extract a value for the observed $\delta\omega$ and $\delta\tau$ (with associated errors). This should be the value at which the posterior is peaked. Thus if one knows the dependence of these corrections from the regularization parameter ($\delta\omega(\ell)$ and $\delta\tau(\ell)$) it is also possible to infer the value of ℓ from the posterior probability distributions. This dependence could be obtained for example fitting the numerical results for the RBHs QNMs computed in Section 6.3.

6.5 Conclusions

In this chapter we have studied test-field and gravitational perturbations on top of the two possible families of spherically symmetric black-hole mimickers, in particular we considered the Bardeen and SV model. Both families smoothly interpolate between RBHs and horizonless objects depending on the value of the regularization parameter ℓ that enters the metric.

The results for these two families of regular models presents some differences. For what regards test-field perturbations the SV spacetime seems to be a better mimicker since, given a certain value of the regularizing parameter ℓ, its spectrum is more similar to the Schwarzschild one (i.e $|(\omega_{SV} - \omega_S)/\omega_S| < |(\omega_{Bard} - \omega_S)/\omega_S|$). We noticed however, that due to the larger span allowed for ℓ in the SV case, this can produce higher deviations from Schwarzschild in the imaginary part, as explicitly reported in Table 6.1. Furthermore, the corrections to the real part of the frequency in the RBH branch are negative in the SV case while for the Bardeen spacetime are positive. For what regards full gravitational perturbations instead, the real part of the frequency for SV RBHs presents stronger deviations from the Schwarzschild one in the axial sector. We also proved that isospectrality between axial and polar QNMs is broken.

For both families of regular models, in the ultracompact branch, we found long living modes whose damping time grows exponentially with the harmonic index l and is longer for values of the regularization parameter near the extremal case, that is for more compact configurations. These modes are associated with the presence of a stable photon sphere in these spacetime and are usually considered a hint for non-linear instability.

Also the Aretakis instability is expected to affect the extremal RBH case, that is the limiting case between RBHs and horizonless objects. A linear mode analysis is insufficient to confirm it, indeed we find damping times for this case to be of the same order of magnitude of the sub-extremal case.

In general our analysis demonstrates that there are deviations of the QNMs spectrum of these spacetimes from that of a Schwarzschild BH due to the non-zero value of the regularization parameter ℓ. So, we analysed the possible detectability of these deviations in the observed gravitational-wave ringdown signals. The detectability of such deviations depends on several aspects such as: the number of observations, their SNR and obviously

the size of the regularization parameter. Using the Parspec framework for the analysis we showed that these deviations should be detectable in the near future for Bardeen RBHs with $\ell/M > 0.13$ and SV RBHs with $\ell/M > 0.19$. Indeed with about hundred observations with SNR ~ 100, which should be routinely available with third generation ground-based detectors [19, 231], it will be possible to exclude the hypothesis of GR singular BHs with 90% confidence level or to cast constraints on the quantum gravity-induced regularization parameter ℓ. This analysis in only preliminary and we plan to extend it in several ways: using corrections at higher order in the spin, using a more realistic binary population for the sources, and treating also the final mass and spin of the remnant as unknown parameters. We also plan to extend this study on gravitational perturbations to rotating BH mimickers and to better investigate the presumed instability of the extremal case.

In conclusion, in spite of their preliminary nature, the results of these investigations should be taken as a strong encouragement that third generation gravitational-wave experiments have the potential not only to further advance our astrophysical understanding of compact objects but as well to open a new channel into quantum gravity phenomenology.

6.6 Appendix: Derivation of the perturbative equations

To study linear perturbations we start expanding the metric and the matter field around their background values,

$$g_{\mu\nu} = g^{(0)}_{\mu\nu} + h_{\mu\nu}\,, \quad A_\mu = A^{(0)}_\mu + \delta A_\mu\,, \quad \Phi = \Phi^{(0)} + \delta\Phi\,, \tag{6.6.1}$$

where $g^{(0)}_{\mu\nu}$, $A^{(0)}_\mu$ and $\Phi^{(0)}$ represent the background quantities, while $h_{\mu\nu}$, δA_μ and $\delta\Phi$ are small perturbations.

We further decompose the perturbations in spherical harmonics Y^{lm} and separate them in polar and axial parts according to their parity symmetry, *i.e.* $h_{\mu\nu} = h^{\rm polar}_{\mu\nu} + h^{\rm axial}_{\mu\nu}$, and similarly for the matter field. In the Regge–Wheeler gauge, $h_{\mu\nu}$ can be written as

$$h^{\rm polar}_{\mu\nu} = \sum_{l,m} \begin{pmatrix} -f(r)e^{-2\phi(r)}H_0^{lm}(t,r) & H_1^{lm}(t,r) & 0 & 0 \\ H_1^{lm}(t,r) & \frac{H_2^{lm}(t,r)}{f(r)} & 0 & 0 \\ 0 & 0 & r^2K^{lm}(t,r) & 0 \\ 0 & 0 & 0 & r^2\sin^2\theta K^{lm}(t,r) \end{pmatrix} Y^{lm}, \tag{6.6.2}$$

$$h^{\rm axial}_{\mu\nu} = \sum_{l,m} \begin{pmatrix} 0 & 0 & h_0^{lm}(t,r)S^{lm}_\theta & h_0^{lm}(t,r)S^{lm}_\varphi \\ 0 & 0 & h_1^{lm}(t,r)S^{lm}_\theta & h_1^{lm}(t,r)S^{lm}_\varphi \\ h_0^{lm}(t,r)S^{lm}_\theta & h_1^{lm}(t,r)S^{lm}_\theta & 0 & 0 \\ h_0^{lm}(t,r)S^{lm}_\varphi & h_1^{lm}(t,r)S^{lm}_\varphi & 0 & 0 \end{pmatrix}, \tag{6.6.3}$$

being $S^{lm}_b \equiv \left(-Y^{lm}_{,\varphi}/\sin\theta, \sin\theta Y^{lm}_{,\theta}\right)$ with $b = \{\theta, \varphi\}$.

Likewise, we expand the electromagnetic potential as

$$\delta A^{\rm polar}_\mu = \sum_{l,m}\left(\frac{u_1^{lm}(t,r)}{r}Y^{lm}, \frac{u_2^{lm}(t,r)}{rf(r)}Y^{lm}, u_3^{lm}(t,r)Y^{lm}_b\right), \quad \delta A^{\rm axial}_\mu = \sum_{l,m}\left(0,0,u_4^{lm}(t,r)S^{lm}_b\right), \tag{6.6.4}$$

being $Y^{lm}_b \equiv \left(Y^{lm}_{,\theta}, Y^{lm}_{,\varphi}\right)$. Finally, we decompose the scalar perturbation as

$$\delta\Phi = \sum_{l,m}\frac{\delta\Phi^{lm}}{r}\,Y^{lm}\,. \tag{6.6.5}$$

In what follows, we drop the symbol $\sum_{l,m}$ and the superscript lm to avoid cluttering the notation. We also assume harmonic time dependence for the perturbation functions, i.e. for any perturbative quantity $\delta F(t,r)$ we write $\delta F(t,r) = e^{-{\rm i}\omega t}\delta\tilde{F}(r)$, but we will omit the tilde.

The background metric and scalar field are even under parity transformations, while the background magnetic field is odd. Hence, to linear order, the axial gravitational perturbations couple to the polar electromagnetic perturbations (Sector I), while the polar

gravitational perturbations couple to the axial electromagnetic and the polar scalar perturbations (Sector II).

It is relatively easy to check that the equations derived in the next subsections reproduce well known results in the appropriate limits, *e.g.* the Regge–Wheeler–Zerilli gravitational equations for the Schwarzschild spacetime for $\mathcal{L}=0$, $\phi(r)=0$ and $f(r)=1-2M/r$, or those of Ref. [243] for $\phi(r)=0$.

6.6.1 Sector I: axial gravitational–polar electromagnetic

In this sector the axial gravitational perturbations couple with the polar electromagnetic perturbations. Let us begin by considering the modified Maxwell equation for a polar electromagnetic perturbation. At linear order, the field strength squared is unperturbed, $F\approx F^{(0)}$. It follows that when computing linear perturbations the Lagrangian and its derivatives are unperturbed as well, *e.g.* $\mathcal{L}_F\approx\mathcal{L}_{F^{(0)}}$, where $\mathcal{L}_{F^{(0)}}\equiv\partial\mathcal{L}/\partial F^{(0)}$. However, to avoid an excessive cluttering of the equations, in what follows we drop the "(0)" superscript.

The t, r and θ components of the modified Maxwell equation read

$$
\begin{aligned}
&f u_1'' + f\left(\phi' - \frac{2\ell^2\mathcal{L}_{FF}}{r^5\mathcal{L}_F}\right)u_1' + \left(\frac{2\ell^2 f\mathcal{L}_{FF}}{r^6\mathcal{L}_F} - \frac{rf\phi' + l(l+1)}{r^2}\right)u_1 + \mathrm{i}\omega u_2' \\
&+ \mathrm{i}\omega\left(\frac{1}{r} - \frac{f'}{f} - \frac{2\ell^2\mathcal{L}_{FF}}{r^5\mathcal{L}_F} + \phi'\right)u_2 - \frac{l(l+1)\ell}{r^3}h_0 = 0\,, \qquad (6.6.6a)\\
&\mathrm{i}\omega u_1' - \frac{\mathrm{i}\omega u_1}{r} + \left(\frac{l(l+1)\mathrm{e}^{-2\phi}}{r^2} - \frac{\omega^2}{f}\right)u_2 + \frac{l(l+1)\ell f\mathrm{e}^{-2\phi}}{r^3}h_1 = 0\,, \qquad (6.6.6b)\\
&\mathrm{i}\omega r\mathrm{e}^{2\phi}u_1 + rfu_2' - f\left(\frac{2\ell^2\mathcal{L}_{FF}}{r^4\mathcal{L}_F} + r\phi' + 1\right)u_2 + \mathrm{i}\omega\ell\mathrm{e}^{2\phi}h_0 + \ell f^2 h_1' \\
&+ \ell f\left[f' - f\left(\frac{2\ell^2\mathcal{L}_{FF}}{r^5\mathcal{L}_F} + \phi' + \frac{2}{r}\right)\right]h_1 = 0\,. \qquad (6.6.6c)
\end{aligned}
$$

Equation (6.6.6b) can be solved for u_2 and substituting in Eq. (6.6.6a) gives an equation for u_1 with non-homogeneous terms proportional to h_0 and h_1. Equation (6.6.6c) is a consequence of the first two equations.

The independent components of the perturbed axial gravitational equations are the $t\theta$, $r\theta$ and $\theta\varphi$

$$
\begin{aligned}
&fh_0'' + f\phi' h_0' - \frac{2r^2 f\left(r\phi'+1\right) + (l-1)(l+2)r^2 + 4\ell^2\mathcal{L}_F}{r^4}h_0 + \mathrm{i}\omega f h_1' \\
&+ \frac{\mathrm{i}\omega f\left(r\phi'+2\right)}{r}h_1 - \frac{4\ell\mathcal{L}_F}{r^3}u_1 = 0\,, \qquad (6.6.7a)\\
&\mathrm{i}\omega h_0' - \frac{2\mathrm{i}\omega h_0}{r} + \left(\frac{f\mathrm{e}^{-2\phi}\left[(l-1)(l+2)r^2 + 4\ell^2\mathcal{L}_F\right]}{r^4} - \omega^2\right)h_1 + \frac{4\ell\mathcal{L}_F\mathrm{e}^{-2\phi}}{r^3}u_2 = 0\,, \qquad (6.6.7b)\\
&f\mathrm{e}^{-2\phi}h_1' + \mathrm{e}^{-2\phi}\left(f' - f\phi'\right)h_1 + \frac{\mathrm{i}\omega h_0}{f} = 0\,. \qquad (6.6.7c)
\end{aligned}
$$

Solving for h_0 in Eq. (6.6.7c) and substituting in Eq. (6.6.7b) we obtain a dynamical equation for h_1, while Eq. (6.6.7a) is automatically satisfied as a consequence of the previous

equations and the modified Maxwell equations.[3]

To make the four independent equations more readable, it is helpful to introduce a new variable u, which corresponds to the perturbation of the tr component of the Maxwell tensor,

$$u \equiv \frac{\mathrm{i}\omega r u_2 - f\left(u_1 - r u_1'\right)}{r^2 f}\,, \tag{6.6.8}$$

instead of the perturbations of the potential u_1 and u_2.

Taking the first and second derivative of Eq. (6.6.8), solving for u_1' and u_1'', and substituting into Eqs. (6.6.6a) and (6.6.6b) we get

$$\mathcal{L}_F u' + \frac{r^4\mathcal{L}_F\left(r\phi'+2\right) - 2\ell^2\mathcal{L}_{FF}}{r^5}\,u - \frac{l(l+1)\mathcal{L}_F}{r^3 f}\,u_1 - \frac{l(l+1)\ell\mathcal{L}_F}{r^4 f}\,h_0 = 0\,, \tag{6.6.9a}$$

$$\mathrm{i}\omega\mathcal{L}_F u + \frac{l(l+1)\mathcal{L}_F \mathrm{e}^{-2\phi}}{r^3}\,u_2 + \frac{l(l+1)\ell f\mathcal{L}_F \mathrm{e}^{-2\phi}}{r^4}\,h_1 = 0\,. \tag{6.6.9b}$$

Solving Eqs. (6.6.7c), (6.6.9a) and (6.6.9b) for h_0, u_1 and u_2 and substituing in Eq. (6.6.7b), we obtain the gravitational dynamical equation for h_1

$$\begin{aligned} &h_1'' + \left(\tfrac{3f'}{f} - 3\phi' - \tfrac{2}{r}\right) h_1' + \tfrac{4\mathrm{i}\omega\ell\mathcal{L}_F \mathrm{e}^{2\phi}}{l(l+1)f^2}\,u \\ &+ \left(\tfrac{f'^2+\omega^2\mathrm{e}^{2\phi}}{f^2} - \tfrac{l(l+1)-r^2f''+2rf'(2r\phi'+1)-2}{r^2 f} - \phi'' + 2\phi'^2 + \tfrac{2\phi'}{r}\right) h_1 = 0\,, \end{aligned} \tag{6.6.10}$$

while the electromagnetic dynamical equation for u is obtained from Eq. (6.6.8) with the substitutions above and using Section 6.6.1

$$\begin{aligned} u'' + \left(\frac{f'}{f} + \phi' + \frac{4}{r} - \frac{2\ell^2\mathcal{L}_{FF}}{r^5\mathcal{L}_F}\right) u' + \frac{1}{f^2}\Bigg[\omega^2\mathrm{e}^{2\phi} - f\left(\frac{l(l+1) - rf'\left(r\phi'+2\right)}{r^2} + \frac{4\ell^2\mathcal{L}_F}{r^4} + \frac{2\ell^2\mathcal{L}_{FF}f'}{r^5\mathcal{L}_F}\right) \\ + f^2\left(\phi'' + \frac{2r\phi'+2}{r^2} + \frac{6\ell^2\mathcal{L}_{FF}}{r^6\mathcal{L}_F} - \frac{4\ell^4\mathcal{L}_{FF}^2}{r^{10}\mathcal{L}_F^2} + \frac{4\ell^4\mathcal{L}_{FFF}}{r^{10}\mathcal{L}_F}\right)\Bigg] u - \frac{\mathrm{i}l(l+1)\left(l^2+l-2\right)\ell\mathrm{e}^{-2\phi}}{\omega r^6}\,h_1 = 0\,. \end{aligned} \tag{6.6.11}$$

Finally, Section 6.6.1 and Eq. (6.6.11) can be written as wave equations by performing the substitutions $h_1 = r\mathrm{e}^{\phi}\mathcal{A}/f$ and $u = \mathrm{e}^{-\phi}\mathcal{E}/r^2\sqrt{\mathcal{L}_F}$, and by introducing a tortoise-like coordinate $\mathrm{d}r_*/\mathrm{d}r = \mathrm{e}^{\phi}/f$, to get the coupled system

$$\frac{\mathrm{d}^2\mathcal{A}}{\mathrm{d}r_*^2} + \left(\omega^2 - V_{\mathcal{A}}\right)\mathcal{A} + \frac{4\mathrm{i}\omega\ell f\sqrt{\mathcal{L}_F}\mathrm{e}^{-2\phi}}{l(l+1)r^3}\,\mathcal{E} = 0\,, \tag{6.6.12}$$

$$\frac{\mathrm{d}^2\mathcal{E}}{\mathrm{d}r_*^2} + \left(\omega^2 - V_{\mathcal{E}}\right)\mathcal{E} - \frac{\mathrm{i}l(l+1)(l^2+l-2)\ell f\sqrt{\mathcal{L}_F}\mathrm{e}^{-2\phi}}{\omega r^3}\,\mathcal{A} = 0\,, \tag{6.6.13}$$

[3] We stress again that if we had coupled *e.g.* axial gravitational and electromagnetic perturbations as in Refs. [233–239] we would have found an inconsistency. Consider for definiteness the gravitational equations that would have been obtained in this case (for brevity we shall omit them here, but they can be easily found in the previously cited literature). First, one would get a tt component implying the decoupling of gravitational and electromagnetic perturbations. Second, the other independent gravitational equations would provide a system of three coupled equations for h_0 and h_1. However, contrary to what happens for Eqs. (6.6.7a) to (6.6.7c), one of the three equations could be no more deduced from the others, and the only acceptable solution would end up to be the trivial one, *i.e.* $h_0 = h_1 = 0$. A similar argument applies for the modified Maxwell equations.

where

$$V_{\mathcal{A}} = f\mathrm{e}^{-2\phi}\left(\frac{f\phi' - f'}{r} + \frac{(l-1)(l+2)+2f}{r^2}\right), \tag{6.6.14}$$

$$V_{\mathcal{E}} = f\mathrm{e}^{-2\phi}\left[\frac{l(l+1)}{r^2} + \frac{4\ell^2\mathcal{L}_F}{r^4} + \frac{\ell^2\mathcal{L}_{FF}f'}{r^5\mathcal{L}_F} - \frac{f}{r^6}\left(\frac{\ell^2\mathcal{L}_{FF}\left(r\phi'+5\right)}{\mathcal{L}_F} - \frac{3\ell^4\mathcal{L}_{FF}^2}{r^4\mathcal{L}_F^2} + \frac{2\ell^4\mathcal{L}_{FFF}}{r^4\mathcal{L}_F}\right)\right]. \tag{6.6.15}$$

6.6.2 Sector II: polar gravitational–axial electromagnetic–polar scalar

In this sector the polar gravitational perturbations couple with the axial electromagnetic and polar scalar perturbations.

Let us begin with the Klein–Gordon equation

$$\delta\Phi'' - \left(\phi' - \frac{f'}{f}\right)\delta\Phi' + \left(\frac{\omega^2\mathrm{e}^{2\phi}}{f^2} + \frac{\phi'}{r} - \frac{l(l+1)+rf'-r^2V_{\Phi\Phi}}{r^2 f}\right)\delta\Phi + \frac{rV_\Phi H_2}{f} - \left(\frac{\mathrm{i}\omega r\mathrm{e}^{2\phi}}{f}H_1 - \frac{r(H_0'-H_2'+2K')}{2}\right)\Phi' = 0\,. \tag{6.6.16}$$

The field strength squared for an axial perturbation is

$$F \approx F^{(0)} + \delta F = \frac{\ell^2}{2r^4} - \frac{\ell\mathrm{e}^{-\mathrm{i}\omega t}\left[\ell K - l(l+1)u_4\right]Y_{lm}}{r^4}\,. \tag{6.6.17}$$

In this case, when computing linear perturbations to Eq. (6.1.5) we also expand $\mathcal{L}_F$ around $F^{(0)}$, *e.g.* $\mathcal{L}_F \approx \mathcal{L}_{F^{(0)}} + \mathcal{L}_{F^{(0)}F^{(0)}}\,\delta F$, and similarly for higher derivatives.

With the further gauge choice $u_3 = 0$, the θ component of the modified Maxwell equations is the only non-vanishing, and reads

$$u_4'' + \left(\frac{f'}{f} - \frac{2\ell^2\mathcal{L}_{FF}}{r^5\mathcal{L}_F} - \phi'\right)u_4' + \left[\frac{\omega^2\mathrm{e}^{2\phi}}{f^2} - \frac{l(l+1)}{r^2 f}\left(1 + \frac{\ell^2\mathcal{L}_{FF}}{r^4\mathcal{L}_F}\right)\right]u_4 - \frac{\ell(H_0+H_2)}{2r^2 f} + \frac{\ell}{r^2 f}\left(1 + \frac{\ell^2\mathcal{L}_{FF}}{r^4\mathcal{L}_F}\right)K = 0\,. \tag{6.6.18}$$

Lastly, let us consider a polar gravitational perturbation. The $\theta\varphi$ component of the perturbed gravitational equation requires $H_2 = -H_0$.

Using the background equations, the other six independent gravitational equations, namely the tt, tr, $t\varphi$, rr, $r\varphi$ and $\theta\theta$ components, are

$$fK'' + \left(\frac{f'}{2} + \frac{3f}{r}\right)K' - \left(\frac{(l-1)(l+2)}{2r^2} + \frac{2\ell^2\mathcal{L}_F}{r^4}\right)K + \frac{fH_0'}{r} + \frac{2rf' + 2f\left(1-r\phi'\right) + l(l+1)}{2r^2}H_0 + \frac{2l(l+1)\ell\mathcal{L}_F}{r^4}u_4 + \frac{4f\sqrt{\pi r\phi'}}{r^2}\delta\Phi' + \frac{8\pi r^2V_\Phi - 4f\sqrt{\pi r\phi'}}{r^3}\delta\Phi = 0\,, \tag{6.6.19a}$$

$$K' + \left(\frac{1}{r} - \frac{f'}{2f} + \phi'\right) K + \frac{H_0}{r} - \frac{\mathrm{i}l(l+1)H_1}{2r^2\omega} + \frac{4\sqrt{\pi r\phi'}}{r^2}\,\delta\Phi = 0\,, \tag{6.6.20a}$$

$$fH_1' + \left(f' - f\phi'\right) H_1 - \mathrm{i}\omega H_0 + \mathrm{i}\omega K - \frac{4\mathrm{i}\omega\ell\mathcal{L}_F}{r^2}\,u_4 = 0\,, \tag{6.6.20b}$$

$$\left(\frac{f'}{2} + \frac{f}{r} - f\phi'\right) K' + \left(\frac{\omega^2\mathrm{e}^{2\phi}}{f} - \frac{(l-1)(l+2)}{2r^2} - \frac{2\ell^2\mathcal{L}_F}{r^4}\right) K - \frac{2f\left(r\phi'-1\right) - 2rf' + l(l+1)}{2r^2}\,H_0$$
$$- \frac{2\mathrm{i}\omega\mathrm{e}^{2\phi}}{r}\,H_1 + \frac{2l(l+1)\ell\mathcal{L}_F}{r^4}\,u_4 - \frac{4f\sqrt{\pi r\phi'}}{r^2}\,\delta\Phi' + \frac{8\pi r^2 V_\Phi + 4f\sqrt{\pi r\phi'}}{r^3}\,\delta\Phi + \frac{fH_0'}{r} = 0\,, \tag{6.6.20c}$$

$$H_0' + \left(\frac{f'}{f} - 2\phi'\right) H_0 + K' - \frac{\mathrm{i}\omega\mathrm{e}^{2\phi}}{f}\,H_1 - \frac{4\ell\mathcal{L}_F}{r^2}\,u_4' + \frac{8\sqrt{\pi r\phi'}}{r^2}\,\delta\Phi = 0\,, \tag{6.6.20d}$$

$$fH_0'' + \left(2f' + \frac{2f}{r} - 3f\phi'\right) H_0' + \left(\frac{2\left(rf'-1\right) - 2f\left(r\phi'-1\right)}{r^2} - \frac{\omega^2\mathrm{e}^{2\phi}}{f} + \frac{4\ell^2\mathcal{L}_F}{r^4}\right) H_0 + fK''$$
$$+ \left(f' + \frac{2f}{r} - f\phi'\right) K' + \left(\frac{\omega^2\mathrm{e}^{2\phi}}{f} + \frac{4\ell^2\mathcal{L}_F}{r^4} + \frac{4\ell^4\mathcal{L}_{FF}}{r^8}\right) K - 2\mathrm{i}\omega\mathrm{e}^{2\phi}H_1' - \frac{\mathrm{i}\omega\mathrm{e}^{2\phi}\left(rf'+2f\right)}{rf}\,H_1$$
$$- 4l(l+1)\ell\left(\frac{\mathcal{L}_F}{r^4} + \frac{\ell^2\mathcal{L}_{FF}}{r^8}\right) u_4 + \frac{8f\sqrt{\pi r\phi'}}{r^2}\,\delta\Phi' + \frac{16\pi r^2 V_\Phi - 8f\sqrt{\pi r\phi'}}{r^3}\,\delta\Phi = 0\,. \tag{6.6.20e}$$

The off-diagonal equations are first-order differential equations in the metric perturbations and can be solved for H_0', H_1' and K', hence the rr component (6.6.20c) gives an algebraic relation among the metric perturbation functions, which can be used to eliminate H_0 from the other equations.

Using these relations as well as the background equations, Eqs. (6.6.19a) and (6.6.20e) are automatically satisfied. Let $H_1 = \omega R$, then the relevant equations are the tr and $t\varphi$ components, which can be written as a system of two non-homogeneous coupled differential equations

$$\frac{\mathrm{d}K}{\mathrm{d}r} = \alpha_1\,K + \alpha_2\,R + J_1\,, \quad \frac{\mathrm{d}R}{\mathrm{d}r} = \beta_1\,K + \beta_2\,R + J_2\,, \tag{6.6.21}$$

where

$$\alpha_1 = -\frac{1}{2\zeta r^3 f}\left(2fr^2\big(r\phi'\left[2f\left(r\phi'+1\right) + \zeta - 2l(l+1)\right] + \zeta - 2l(l+1) + 2\big)\right.$$
$$\left. -8f\ell^2\mathcal{L}_F - l(l+1)r^2[\zeta - l(l+1)]\right) - \frac{2r\omega^2\mathrm{e}^{2\phi}}{\zeta f}\,, \tag{6.6.22a}$$

$$\alpha_2 = \frac{\mathrm{i}l(l+1)\left[l(l+1) - 2f\left(r\phi'+1\right)\right]}{2\zeta r^2} + \frac{2\mathrm{i}\omega^2\mathrm{e}^{2\phi}}{\zeta}, \tag{6.6.22b}$$

$$\beta_1 = -\frac{4f\left(r^3\phi'\left[f\left(r\phi'+1\right)+\zeta-l(l+1)\right]-[l(l+1)-1]r^2-2\ell^2\mathcal{L}_F\right)+r^2[\zeta-l(l+1)]^2}{2\mathrm{i}\zeta r^2 f^2} + \frac{2\mathrm{i}r^2\omega^2\mathrm{e}^{2\phi}}{\zeta f^2}\,, \tag{6.6.23a}$$

$$\beta_2 = -\frac{2rf\phi'[3\zeta+l(l+1)]+2f[2\zeta+l(l+1)]+[\zeta-l(l+1)][2\zeta+l(l+1)]}{2\zeta rf} + \frac{2r\omega^2\mathrm{e}^{2\phi}}{\zeta f}\,, \tag{6.6.23b}$$

$$J_1 = -\frac{8\ell f\mathcal{L}_F}{\zeta r^2}\,u_4' - \frac{4l(l+1)\ell\mathcal{L}_F}{\zeta r^3}\,u_4 + \frac{8\sqrt{\pi}f\sqrt{r\phi'}}{\zeta r}\,\delta\Phi' - \frac{16\pi r^2 V_\Phi - 4\sqrt{\pi}\sqrt{r\phi'}\left[2f\left(r\phi'+2\right)-l(l+1)\right]}{\zeta r^2}\,\delta\Phi\,, \tag{6.6.23c}$$

$$J_2 = \frac{8\mathrm{i}\ell\mathcal{L}_F}{\zeta r}\,u_4' + \frac{4\mathrm{i}\ell\left[\zeta+l(l+1)\right]\mathcal{L}_F}{\zeta r^2 f}\,u_4 - \frac{8\mathrm{i}\sqrt{\pi}\sqrt{r\phi'}}{\zeta}\,\delta\Phi' - \frac{16\pi r^2 V_\Phi - 4\sqrt{\pi}\sqrt{r\phi'}\left[2f\left(r\phi'+2\right)+\zeta-l(l+1)\right]}{\mathrm{i}\zeta rf}\,\delta\Phi\,, \tag{6.6.23d}$$

and $\zeta(r) = rf' - 2f(2r\phi'+1) + l(l+1)$.

Now, the procedure to obtain the equation that governs polar gravitational perturbations follows Zerilli's original derivation. The task now is to find a new couple of functions $\hat{R}$ and $\hat{H}$ to transform Eq. (6.6.21) into

$$\frac{\mathrm{d}\hat{K}}{\mathrm{d}\hat{r}} = \hat{R} + \hat{J}_1\,, \quad \frac{\mathrm{d}\hat{R}}{\mathrm{d}\hat{r}} = -\left(\omega^2 - V(r)\right)\hat{K} + \hat{J}_2\,, \tag{6.6.24}$$

where the new radial variable $\hat{r}$ is given by $\mathrm{d}\hat{r}/\mathrm{d}r = 1/n(r)$. To find such transformation we write

$$K(r) = g_1(r)\hat{K}(\hat{r}) + g_2(r)\hat{R}(\hat{r})\,, \quad R(r) = k_1(r)\hat{K}(\hat{r}) + k_2(r)\hat{R}(\hat{r})\,, \quad \frac{\mathrm{d}\hat{r}}{\mathrm{d}r} = \frac{1}{n(r)}\,. \tag{6.6.25}$$

Let us introduce the matricial notation

$$\boldsymbol{\psi} = \begin{pmatrix} K \\ R \end{pmatrix}\,, \quad \boldsymbol{A} = \begin{pmatrix} \alpha_1 & \alpha_2 \\ \beta_1 & \beta_2 \end{pmatrix}\,, \quad \hat{\boldsymbol{\psi}} = \begin{pmatrix} \hat{K} \\ \hat{R} \end{pmatrix}\,, \quad \boldsymbol{F} = \begin{pmatrix} g_1 & g_2 \\ k_1 & k_2 \end{pmatrix}\,, \quad \boldsymbol{J} = \begin{pmatrix} J_1 \\ J_2 \end{pmatrix}\,, \tag{6.6.26}$$

then Eq. (6.6.21) can be written as $\mathrm{d}\boldsymbol{\psi}/\mathrm{d}r = \boldsymbol{A}\boldsymbol{\psi} + \boldsymbol{J}$, Eq. (6.6.25) as $\boldsymbol{\psi} = \boldsymbol{F}\hat{\boldsymbol{\psi}}$, which combined with our request Eq. (6.6.24) give the system

$$n\boldsymbol{F}^{-1}\left(\boldsymbol{A}\boldsymbol{F} - \frac{\mathrm{d}\boldsymbol{F}}{\mathrm{d}r}\right) = \begin{pmatrix} 0 & 1 \\ -\omega^2 + V(r) & 0 \end{pmatrix}\,, \tag{6.6.27}$$

together with the new source terms $\hat{\boldsymbol{J}} = n\boldsymbol{F}^{-1}\boldsymbol{J}$.

Equation (6.6.27) represents four equations that relate g_1, g_2, k_1, k_2, n and V in

terms of $\alpha_{1,2}$ and $\beta_{1,2}$. By equating the coefficients of ω^0 and ω^2 we get eight equations, supplemented by the condition $\det \boldsymbol{F} \neq 0$, for six unknown functions. Yet, the system is consistent and admits a solution

$$n(r) = f\mathrm{e}^{-\phi}\,, \tag{6.6.28a}$$

$$g_1(r) = \frac{g_2\mathrm{e}^{-\phi}[rf' + l(l+1)] - 2g_2 f\mathrm{e}^{-\phi}\,(2r\phi' + 1) + 2\mathrm{i}fk_1}{2r}\,, \tag{6.6.28b}$$

$$g_2(r) = \exp\int \mathrm{d}r\,\frac{\phi'\,[rf' + f + l(l+1)] + rf\phi'' - 2rf\phi'^2}{\zeta}\,, \tag{6.6.28c}$$

$$\begin{aligned} k_1(r) = {}& \mathrm{i}\mathrm{e}^{-\phi}\,\frac{1}{2\zeta r^2 f}(g_2[2fr^2\left(r\phi'[2f(r\phi'+1) + \zeta - l(l+1)] + \zeta - (l-1)(l+2) - 4\ell^2\mathcal{L}_F/r^2\right) \\ & + \zeta r^2[\zeta - l(l+1)]] + 2\zeta r^3 f g_2')\,, \end{aligned} \tag{6.6.28d}$$

$$k_2(r) = -\frac{\mathrm{i}rg_2}{f}\,, \tag{6.6.28e}$$

$$\begin{aligned} V(r) = {}& \frac{f\mathrm{e}^{-2\phi}}{\zeta^2 r^2}\Bigg[4f\left(\zeta^2 - \zeta(4\lambda+3) + f[2f + \zeta - 4(\lambda+1)] + 2(\lambda+1)^2 + \frac{2\zeta\ell^4\mathcal{L}_{FF}}{r^6}\right) \\ & + \zeta\left(\zeta^2 - 4\zeta(\lambda+1) + 8(\lambda+1)^2\right) - r^2 f''\Big(\zeta[\zeta - 4(\lambda+1)] + 2f[4f + \zeta - 4(\lambda+1)]\Big) \\ & + 2r^4 f f''^2 - r\phi'\zeta[\zeta - 4(\lambda+1)][\zeta - 2(\lambda+1)] \\ & + r\phi' f(4r^2(\zeta - 5(\lambda+1))f'' + 4f\left(9r^2 f'' - 5\zeta + 28(\lambda+1)\right) - 5\zeta^2 + 36\zeta(\lambda+1) - 72f^2 \\ & - 40(\lambda+1)^2) + 4r^2 f\phi'^2[f\left(5r^2 f'' + 30f + 12\zeta - 34(\lambda+1)\right) \\ & + (\zeta - 4(\lambda+1))(\zeta - 3(\lambda+1))] + 4r^3 f^2\phi'^3[44f + 9\zeta - 24(\lambda+1)] + 48r^4 f^3\phi'^4 \\ & + 8\pi r^3\Phi'[f\left(13r^2 f'' - 26f - 5\zeta + 26(\lambda+1)\right) - 2\zeta[\zeta - 4(\lambda+1)] + 64r^2 f^2\phi'^2 \\ & + 4rf\phi'[29f + 5\zeta - 16(\lambda+1)]]V_\Phi + 8\pi r^4\left(42rf\phi' + \zeta\right)V_\Phi^2 - 2\zeta r^3 f\phi' V_{\Phi\Phi}\Bigg]\,, \end{aligned} \tag{6.6.29a}$$

where we have introduced $\lambda = (l-1)(l+2)/2$. Eq. (6.6.28a) means that the new variable $\hat{r}$ is nothing but the tortoise-like coordinate r_*. The new source terms read

$$\hat{J}_1 = \frac{8f}{\zeta r^2 g_2}\left(\ell\mathcal{L}_F u_4 - \sqrt{\pi r^3\phi'}\delta\Phi\right)\,, \tag{6.6.30}$$

$$\begin{aligned} \hat{J}_2 = {}& -\frac{8f^2\mathrm{e}^{-\phi}}{\zeta r^2 g_2}\Bigg[\ell\mathcal{L}_F u_4' - \frac{1}{\zeta r^3 f}\left(\ell\mathcal{L}_F\left[f\left(r^2\left[\zeta - 2\lambda + 2r(\zeta - \lambda - 1)\phi'\right] - 4\ell^2\mathcal{L}_F\right)\right. \right. \\ & \left. + r^3 f^2\left(r\phi'' + 4r\phi'^2 + 5\phi'\right) - 2\zeta(\lambda+1)r^2\right]\Big)\,u_4 - \sqrt{\pi r^3\phi'}\,\delta\Phi' + \frac{1}{\zeta r^2 f}\left(2\pi\zeta r^4 V_\Phi\right. \\ & \left.\left. - f\sqrt{\pi r\phi'}\left[r^2\left(\zeta + 2\lambda - r[\zeta - 2(\lambda+1)]\phi'\right) + 4\ell^2\mathcal{L}_F\right] + r^3 f^2\sqrt{\pi r\phi'}\left(r\phi'' + 4r\phi'^2 + 5\phi'\right)\right)\,\delta\Phi\Bigg]\,. \end{aligned} \tag{6.6.31}$$

The above system and the source terms simplify when the integral in Eq. (6.6.28c) is given in a closed form, and this depends strongly on the explicit form of the background metric

functions. Remarkably, for $\phi = \phi_0 + \frac{1}{2}\log\left(1-\ell^2/r^2\right)$, with ϕ_0 being an arbitrary constant, as for the SV spacetime, and for *any* choice for f, we find $g_2 = \mathrm{e}^{\phi}$. We assume it in what follows.

Finally, combining Eq. (6.6.24) we get a master equation for the polar gravitational perturbations coupled with the axial electromagnetic and polar scalar perturbations

$$\frac{\mathrm{d}^2\hat{K}}{\mathrm{d}r_*^2} + \left(\omega^2 - V(r)\right)\hat{K} - n\hat{J}_1' - \hat{J}_2 = 0\,. \tag{6.6.32}$$

The very last step is to use the solutions for the gravitational equations to rewrite the Klein–Gordon and modified Maxwell equations; they read

$$\begin{aligned} &u_4'' + \left(\frac{\zeta - 2(\lambda+1)}{rf} - \frac{2\ell^2\mathcal{L}_{FF}}{r^5\mathcal{L}_F} + 3\phi' + \frac{2}{r}\right)u_4' + \frac{8\ell\sqrt{\pi r\phi'}}{\zeta r^3}\left(1 + \frac{\ell^2\mathcal{L}_{FF}}{r^4\mathcal{L}_F}\right)\delta\Phi \\ &+ \left[\frac{\omega^2\mathrm{e}^{2\phi}}{f^2} - \left(1 + \frac{\ell^2\mathcal{L}_{FF}}{r^4\mathcal{L}_F}\right)\left(\frac{8\ell^2\mathcal{L}_F}{\zeta r^4} + \frac{2(\lambda+1)}{fr^2}\right)\right]u_4 + \frac{\ell}{r^2}\left(1 + \frac{\ell^2\mathcal{L}_{FF}}{r^4\mathcal{L}_F}\right)\hat{K}' \\ &+ \ell\left(1 + \frac{\ell^2\mathcal{L}_{FF}}{r^4\mathcal{L}_F}\right)\left(\frac{2\lambda - \zeta - 2r\phi'\left(rf\phi' + f + \zeta - \lambda - 1\right)}{\zeta r^3} + \frac{4\ell^2\mathcal{L}_F}{\zeta r^5} + \frac{\lambda+1}{r^3 f}\right)\hat{K} = 0\,, \end{aligned} \tag{6.6.33}$$

$$\begin{aligned} &\delta\Phi'' + \left(\frac{2f + \zeta - 2(\lambda+1)}{rf} + 3\phi'\right)\delta\Phi' - \frac{2\ell\sqrt{r\phi'}\mathcal{L}_F}{\sqrt{\pi}r^2}\,u_4' \\ &\quad + \left(\frac{\omega^2\mathrm{e}^{2\phi}}{f^2} + \frac{V_{\Phi\Phi}}{f} - \frac{\zeta}{fr^2} + \frac{r\phi' - 2}{r^2}\right)\delta\Phi = 0\,. \end{aligned} \tag{6.6.34}$$

Eqs. (6.6.32) to (6.6.34) can be written as wave equations by introducing new variables

$$\hat{K} = \mathcal{P}\,, \quad u_4 = f_1\mathcal{B} + f_2\mathcal{P} + f_3\mathcal{S}\,, \quad \delta\Phi = g_1\mathcal{S} + g_2\mathcal{P} + g_3\mathcal{B}\,, \tag{6.6.35}$$

where

$$f_1 = \frac{c_1}{\sqrt{\mathcal{L}_F}}\,, \quad f_2 = \frac{\ell}{2r}\,, \quad f_3 = \frac{c_3}{\sqrt{\mathcal{L}_F}}\,, \tag{6.6.36}$$

$$g_1 = \frac{c_3\ell}{\sqrt{\pi}}\int \mathrm{d}r\,\frac{\sqrt{\mathcal{L}_F\phi'}}{r^{3/2}} + c_4\,, \quad g_2 = \frac{\ell^2}{2\sqrt{\pi}}\int \mathrm{d}r\,\frac{\mathcal{L}_F\sqrt{\phi'}}{r^{5/2}} + c_5\,, \quad g_3 = \frac{c_1\ell}{\sqrt{\pi}}\int \mathrm{d}r\,\frac{\sqrt{\mathcal{L}_F\phi'}}{r^{3/2}} + c_6\,, \tag{6.6.37}$$

with $c_1c_4 - c_3c_6 \neq 0$, so that

$$\frac{\mathrm{d}^2\mathcal{I}}{\mathrm{d}r_*^2} + \left(\omega^2 - V_{\mathcal{I}}\right)\mathcal{I} + \sum_{\mathcal{J}\neq\mathcal{I}} c_{\mathcal{I},\mathcal{J}}\,\mathcal{J} = 0\,, \tag{6.6.38}$$

for $\mathcal{I},\mathcal{J} = \{\mathcal{P},\mathcal{B},\mathcal{S}\}$. The potentials $V_{\mathcal{I}}$ and the coefficients $c_{\mathcal{I},\mathcal{J}}$ can be given in closed form REF but they are cumbersome and we do not report them here.

6.6.3 Static perturbations

Static perturbations are easier to derive and we report them for completeness.

In sector I, the modified Maxwell equations for a polar electromagnetic perturbation

can be obtained by taking the $\omega = 0$ limit of Eqs. (6.6.6a) to (6.6.6c), *i.e.*

$$f u_1'' + f\left(\phi' - \frac{2\ell^2 \mathcal{L}_{FF}}{r^5 \mathcal{L}_F}\right) u_1' + \left(\frac{2\ell^2 f \mathcal{L}_{FF}}{r^6 \mathcal{L}_F} - \frac{r f \phi' + l(l+1)}{r^2}\right) u_1 - \frac{l(l+1)\ell}{r^3} h_0 = 0\,, \tag{6.6.39a}$$

$$u_2 + \frac{\ell f}{r} h_1 = 0\,, \tag{6.6.39b}$$

$$r u_2' - \left(\frac{2\ell^2 \mathcal{L}_{FF}}{r^4 \mathcal{L}_F} + r\phi' + 1\right) u_2 + \ell f h_1' + \ell\left[f' - f\left(\frac{2\ell^2 \mathcal{L}_{FF}}{r^5 \mathcal{L}_F} + \phi' + \frac{2}{r}\right)\right] h_1 = 0\,, \tag{6.6.39c}$$

while the Einstein equations for an axial gravitational perturbation can be obtained by taking the $\omega = 0$ limit of Eqs. (6.6.7a) to (6.6.7c), *i.e.*

$$f h_0'' + f\phi' h_0' - \frac{2r^2 f\,(r\phi' + 1) + (l-1)(l+2)r^2 + 4\ell^2 \mathcal{L}_F}{r^4} h_0 - \frac{4\ell \mathcal{L}_F}{r^3} u_1 = 0\,, \tag{6.6.40a}$$

$$\frac{(l-1)(l+2)r^2 + 4\ell^2 \mathcal{L}_F}{r} h_1 + \frac{4\ell \mathcal{L}_F}{f} u_2 = 0\,, \tag{6.6.40b}$$

$$f h_1' + \left(f' - f\phi'\right) h_1 = 0\,. \tag{6.6.40c}$$

Equation (6.6.39b) can be solved for u_2, making Eq. (6.6.39c) automatically satisfied. However, this solution is incompatible with Eqs. (6.6.40b) and (6.6.40c) unless $u_2 = h_1 = 0$. The two equations that govern static perturbations in sector I are therefore Eqs. (6.6.39a) and (6.6.40a).

In sector II, the static Klein–Gordon and modified Maxwell equations can be obtained by the $\omega = 0$ limit of Eqs. (6.6.16) and (6.6.18),

$$\delta\Phi'' - \left(\phi' - \frac{f'}{f}\right)\delta\Phi' + \left(\frac{\phi'}{r} - \frac{l(l+1) + r f' - r^2 V_{\Phi\Phi}}{r^2 f}\right)\delta\Phi + \frac{r V_\Phi H_2}{f} + \frac{r(H_0' - H_2' + 2K')}{2}\Phi' = 0\,, \tag{6.6.41}$$

$$u_4'' + \left(\frac{f'}{f} - \frac{2\ell^2 \mathcal{L}_{FF}}{r^5 \mathcal{L}_F} - \phi'\right) u_4' - \frac{l(l+1)}{r^2 f}\left(1 + \frac{\ell^2 \mathcal{L}_{FF}}{r^4 \mathcal{L}_F}\right) u_4 - \frac{\ell(H_0 + H_2)}{2r^2 f} + \frac{\ell}{r^2 f}\left(1 + \frac{\ell^2 \mathcal{L}_{FF}}{r^4 \mathcal{L}_F}\right) K = 0\,. \tag{6.6.42}$$

Again, the $\theta\varphi$ component of the perturbed gravitational equation requires $H_2 = -H_0$, but the tr component further imposes $H_1 = 0$, leaving four independent gravitational equations,

$$f K'' + \left(\frac{f'}{2} + \frac{3f}{r}\right) K' - \left(\frac{(l-1)(l+2)}{2r^2} + \frac{2\ell^2 \mathcal{L}_F}{r^4}\right) K + \frac{f H_0'}{r} + \frac{2r f' + 2f\,(1 - r\phi') + l(l+1)}{2r^2} H_0 + \frac{2l(l+1)\ell \mathcal{L}_F}{r^4} u_4 + \frac{4f\sqrt{\pi r \phi'}}{r^2}\delta\Phi' + \frac{8\pi r^2 V_\Phi - 4f\sqrt{\pi r\phi'}}{r^3}\delta\Phi = 0\,, \tag{6.6.43a}$$

$$\left(\frac{f'}{2}+\frac{f}{r}-f\phi'\right)K'-\left(\frac{(l-1)(l+2)}{2r^2}+\frac{2\ell^2\mathcal{L}_F}{r^4}\right)K+\frac{fH_0'}{r}-\frac{2f\left(r\phi'-1\right)-2rf'+l(l+1)}{2r^2}H_0$$
$$+\frac{2l(l+1)\ell\mathcal{L}_F}{r^4}u_4-\frac{4f\sqrt{\pi r\phi'}}{r^2}\delta\Phi'+\frac{8\pi r^2V_\Phi+4f\sqrt{\pi r\phi'}}{r^3}\delta\Phi=0\,, \tag{6.6.44a}$$
$$H_0'+\left(\frac{f'}{f}-2\phi'\right)H_0+K'-\frac{4\ell\mathcal{L}_F}{r^2}u_4'+\frac{8\sqrt{\pi r\phi'}}{r^2}\delta\Phi=0\,, \tag{6.6.44b}$$
$$fH_0''+\left(2f'+\frac{2f}{r}-3f\phi'\right)H_0'+\left(\frac{2\left(rf'-1\right)-2f\left(r\phi'-1\right)}{r^2}+\frac{4\ell^2\mathcal{L}_F}{r^4}\right)H_0+fK''$$
$$+\left(\frac{4\ell^2\mathcal{L}_F}{r^4}+\frac{4\ell^4\mathcal{L}_{FF}}{r^8}\right)K-4l(l+1)\ell\left(\frac{\mathcal{L}_F}{r^4}+\frac{\ell^2\mathcal{L}_{FF}}{r^8}\right)u_4+\frac{8f\sqrt{\pi r\phi'}}{r^2}\delta\Phi'$$
$$+\left(f'+\frac{2f}{r}-f\phi'\right)K'+\frac{16\pi r^2V_\Phi-8f\sqrt{\pi r\phi'}}{r^3}\delta\Phi=0\,. \tag{6.6.44c}$$

We now solve Eqs. (6.6.44a) and (6.6.44b) for K and K'. The derivative of Eq. (6.6.44b) with respect to r, together with the background equations and Eq. (6.6.42), gives an equation for K''. Using these relations and the background equations, Eq. (6.6.44c) is identically satisfied. The gravitational perturbation are then described by a non-homogenous differential equation for H_0,

$$fH_0''-\eta_1H_0'-\eta_2H_0+J_3=0\,, \tag{6.6.45}$$

where

$$\eta_1=\frac{4\ell^2}{\Delta}\left(f'-2f\phi'\right)\left(\mathcal{L}_F+\frac{\ell^2\mathcal{L}_{FF}}{r^4}\right)-f'+f\left(\phi'-\frac{2}{r}\right), \tag{6.6.46}$$
$$\eta_2=\frac{4\ell^2}{\Delta}\left(\mathcal{L}_F+\frac{\ell^2\mathcal{L}_{FF}}{r^4}\right)\left(\frac{l(l+1)}{r^2}-4f'\phi'+\frac{f'^2}{f}+\frac{2f\left(r\phi'-1\right)\left(2r\phi'+1\right)}{r^2}\right)-2f'\left(2\phi'+\frac{1}{r}\right)$$
$$+\frac{f'^2}{f}+\frac{2f\left(r\phi'+1\right)\left(2r\phi'-1\right)}{r^2}+\frac{l^2+l+2}{r^2}-\frac{4\ell^2\mathcal{L}_F}{r^4}\,, \tag{6.6.47}$$
$$J_3=-\frac{4\ell}{r^2}\left[\frac{2f\mathcal{L}_F}{r}-\left(f'-\frac{2f\left(r\phi'-1\right)}{r}\right)\left(\frac{4\ell^4\mathcal{L}_F\mathcal{L}_{FF}}{\Delta r^4}+\frac{4\ell^2\mathcal{L}_F^2}{\Delta}+\mathcal{L}_F\right)\right]u_4'$$
$$-\frac{4\ell(l-1)l(l+1)(l+2)}{r^2\Delta}\left(\mathcal{L}_F+\frac{\ell^2\mathcal{L}_{FF}}{r^4}\right)u_4-\frac{32\ell^2f\sqrt{\pi r\phi'}}{r^2\Delta}\left(\mathcal{L}_F+\frac{\ell^2\mathcal{L}_{FF}}{r^4}\right)\delta\Phi'$$
$$-\frac{4}{r}\left[\frac{8\ell^2}{\Delta}\left(\mathcal{L}_F+\frac{\ell^2\mathcal{L}_{FF}}{r^4}\right)\left(\sqrt{\pi r\phi'}\left(\frac{f'}{r}+\frac{f\left(1-2r\phi'\right)}{r^2}\right)-2\pi V_\Phi\right)\right.$$
$$\left.-\frac{\sqrt{\pi}f\left[r\phi''+\phi'\left(2r\phi'+3\right)\right]}{r\sqrt{r\phi'}}\right]\delta\Phi\,, \tag{6.6.48}$$
$$\Delta=(l-1)(l+2)r^2+4\ell^2\mathcal{L}_F\,. \tag{6.6.49}$$

Once the solutions for H_0, u_4 and $\delta\Phi$ are known, the other metric function perturbation

is given by

$$K = -\frac{r^2 f\left[l(l+1) - 4r^2 f'\phi' + 2f\left(r\phi' - 1\right)\left(2r\phi' + 1\right)\right] + r^4 f'^2}{\Delta f} H_0 - \frac{r^4\left(f' - 2f\phi'\right)}{\Delta} H_0' + \frac{16\pi r^3 V_\Phi + 8r\sqrt{\pi r\phi'}\left[f\left(2r\phi' - 1\right) - rf'\right]}{\Delta}\delta\Phi - \frac{8r^2 f\sqrt{\pi r\phi'}}{\Delta}\delta\Phi' + \frac{4\ell l(l+1)\mathcal{L}_F}{\Delta} u_4 + \frac{4\ell r\mathcal{L}_F\left[rf' + 2f(1 - r\phi')\right]}{\Delta} u_4' \,. \tag{6.6.50}$$

Chapter 7

The echoes signal: the role of absorption and backreaction

As we mentioned in Chapter 5, for horizonless compact object the usual GWs ringdown signal is followed by a series of echoes. Usually these are studied in linear perturbation theory, neglecting the possible backreaction of the ECO. This is justified because the energy in the ringdown is small (from two to three orders of magnitude with respect to the mass of the object [266, 267]) and diffused on a wavelength of the order or larger than the ECO radius. However, it can be argued that this linear approximation is actually dangerous since for good BH mimickers the surface of the ECO is very close to the would-be horizon [268]. For this reason, the peeling of geodesics will cause an accumulation of light rays and so a large increase of the perturbation energy density near the surface. Actually, it can be shown that GWs fluxes can even lead to the violation of the hoop conjecture [269] and the collapse of the ECO into a BH [270–272]. Thus it seems clear that non-linear interactions between the ECO and the GWs flux must be considered.

The scope of this chapter is to study possible effects on the echoes waveform due to backreaction and in particular we shall focus on the effect of the echo absorption on behalf of the ECO. Indeed, a perfectly reflecting surface is often just an idealization, we expect instead that part of the radiation can be absorbed by the object for istance through effects of dissipation or viscosity [273]. The introduction of an absorption coefficient for the ECO surface is not only physically reasonable, but it also allows to circumvent some ECO's instabilities as we discussed in Section 3.4. Indeed, it makes the timescale for the onset of these instabilities very long and it can even turn them off [151, 152].

However, until now, the only considered effect of absorption on the echoes waveform is the decreasing of echoes amplitude and energy [152, 274] or the changing of their frequency content in the case of frequency-dependent absorption coefficient [275, 276]. Yet, it should also imply an increase of the central object mass and consequently a change of the spacetime in which echoes are propagating. Similar considerations were done in Ref. [277] in the context of BH ringdown, showing how the change in the BH mass, due to the absorption of a mode excited at early times, causes a shift in the mode spectrum and thus the excitation of additional modes.

In the first part of this chapter, we consider the simple instructive case in which we have no other backreaction effects apart from absorption. We show that this leads to a

non-constant time delay between echoes and thus the loss of the typical quasi-periodicity predicted for these signals. This is particularly interesting if we think that, as mentioned in Section 5.3.3, the strategies used in the searches for echoes in the GWs ringdown are usually based on the aforementioned quasi-periodicity. Indeed, in Ref. [223] it was shown that applying a template with constant time interval between echoes may significantly misinterpret the signals if the variation of this interval is greater than the statistical errors.

In the second part of this investigation, we take into account that, for sufficiently compact central objects, the absorption of part of the GWs flux can increase the mass of the object over the hoop limit $2M \geqslant r_0$. Thus, assuming the stability of these ECOs, some backreaction mechanism must be present so to prevent the formation of a horizon: we consider a scenario in which the absorption coefficient depends on the compactness, and a scenario in which the ECO expands. In both cases we show the effects on the echoes waveform and time delay.

7.1 Set-up

As a proxy to the more general case of gravitational perturbations, here we study the evolution of a minimally coupled massless scalar field Φ propagating in a spherically symmetric ECO spacetime. As commonly assumed, the scalar field does not couple directly to any form of matter that might be present within or outside the ECO. Its action reads

$$S = -\frac{1}{2}\int \mathrm{d}^4x\sqrt{-g}\, g^{\mu\nu}\nabla_\mu\Phi\nabla_\nu\Phi\,. \tag{7.1.1}$$

We do not assume any specific form for the gravitational action and the ECO spacetime is characterized by its initial mass M_0 and radius r_0 greater than its Schwarzschild radius. We remember that we define the compactness parameter of the object as

$$\sigma \equiv \frac{r_0}{2M_0} - 1\,, \tag{7.1.2}$$

which is always positive and goes to zero in the BH limit, *i.e.* $\sigma \to 0$ as $r_0 \to 2M_0$. Independently of the specific ECO model, the spacetime outside its surface is Schwarzschild. For $r > r_0$ we have:

$$\mathrm{d}s^2 = -f(r)\,\mathrm{d}t^2 + \frac{\mathrm{d}r^2}{f(r)} + r^2\left(\mathrm{d}\theta^2 + \sin^2\theta\,\mathrm{d}\varphi^2\right), \quad f(r) = 1 - \frac{2M_0}{r}\,. \tag{7.1.3}$$

Because of spherical symmetry, the Klein–Gordon equation in this spacetime is separable thus we can decompose the field as $\Phi(t,r,\theta,\varphi) = \sum_{lm}\frac{\Psi_{lm}(t,r)}{r}Y_{lm}(\theta,\varphi)$, where Y_{lm} are the scalar spherical harmonics. Then the field equation for each mode $\Psi_{lm}(t,r)$ is (to avoid cluttering, in what follows we drop the lm indexes):

$$\frac{\partial^2\Psi}{\partial t^2} - f^2\frac{\partial^2\Psi}{\partial r^2} - ff'\frac{\partial\Psi}{\partial r} + V(r)\Psi = 0\,, \tag{7.1.4}$$

where a prime represents derivative with respect to the radial coordinate r and

$$V(r) = \left(1 - \frac{2M_0}{r}\right)\left(\frac{2M_0}{r^3} + \frac{l(l+1)}{r^2}\right). \tag{7.1.5}$$

7.1.1 Energy of the perturbation

To compute the energy of the scalar perturbation, we start with the stress-energy tensor stemming from the action in Eq. (7.1.1)

$$T^{\mu\nu} = \nabla^\mu\Phi\nabla^\nu\Phi - \frac{1}{2}g^{\mu\nu}\nabla_\alpha\Phi\nabla^\alpha\Phi\,. \tag{7.1.6}$$

We consider the conserved current $J^\mu = k_\nu T^{\mu\nu}$, where k_ν is the timelike Killing field of the Schwarzschild spacetime. The conserved energy in a three-dimensional hypersurface Σ is then

$$E = \int_\Sigma \mathrm{d}^3x\sqrt{\gamma}\,J^\mu n_\mu\,, \tag{7.1.7}$$

where γ is the induced three-dimensional metric on the hypersurface and n^μ is the normalized vector field orthogonal to Σ. In our case Σ is the hypersurface at $t = \text{const}$ and thus $n^\mu = \nabla^\mu t/|\nabla^\mu t| = k^\mu/\sqrt{f(r)}$. From this, integrating in the angular part, we obtain, *e.g.* in Schwarzschild coordinates

$$E = \frac{1}{2}\int \frac{\mathrm{d}r}{f(r)}\left[\left(\frac{\partial\Psi}{\partial t}\right)^2 + f(r)^2\left(\frac{\partial\Psi}{\partial r}\right)^2 + V(r)\,\Psi^2 - f(r)\frac{\partial}{\partial r}\left(\frac{f(r)}{r}\Psi^2\right)\right]. \tag{7.1.8}$$

These coordinates might look not suitable, as the factor $1/f(r)$ gets divergent as we approach the event horizon. However, while the region Δr in which the field Ψ is diffused shrinks, it — seen by a static observer at infinity – moves slower and contracts as it approaches the horizon, reaching it in an infinite amount of time. The two effects compensate each other, and the energy remains constant.

7.1.2 Varying mass and moving surface

If the object absorbs energy from the scalar field, we have to take into account that its mass can change in time. We assume that at each instant the spacetime can be described by the Schwarzschild metric with a different mass $M_0 \to M(t)$ and $f(r) \to F(t,r) = 1-2M(t)/r$. Then the Klein–Gordon equation, written in terms of the "initial" tortoise coordinate $r_* = r + 2M_0\ln(r/2M_0 - 1)$, becomes:

$$\frac{\partial^2\Psi}{\partial t^2} - \frac{F^2}{f^2}\frac{\partial^2\Psi}{\partial r_*^2} - \frac{F}{f}\left(\frac{\partial F}{\partial r} - \frac{Ff'}{f}\right)\frac{\partial\Psi}{\partial r_*} + V(r,t)\Psi + \frac{1}{F}\frac{\partial F}{\partial t}\frac{\partial\Psi}{\partial t} = 0\,. \tag{7.1.9}$$

where the potential V has been promoted as a function of t and r, and r itself is interpreted as a function of r_*.

In one of the models that we consider the surface of the object moves, and so also the point at which we impose our boundary conditions, *i.e.* $r_0 \to r_0(t)$. Thus to solve the scalar field equation with a time-independent boundary condition we need to choose

a coordinate in which the surface of the object is fixed in time. For example, if the object expand in order to stay at constant compactness then $x = M_0 \ln(r/2M(t) - 1)$ is a good choice. In these coordinates the Klein–Gordon equation reads

$$\frac{\partial^2\Psi}{\partial t^2} - M_0^2\left(\frac{1}{r^2} - \frac{r^2\dot{M}^2}{M^2(r-2M)^2}\right)\frac{\partial^2\Psi}{\partial x^2} - \frac{2\dot{M}M_0 r}{M(r-2M)}\frac{\partial^2\Psi}{\partial t\partial x} + M_0\left(\frac{1}{r^2} - \frac{2M}{r^3} - \frac{r\ddot{M}}{M(r-2M)} + \frac{r(r-4M)\dot{M}^2}{M^2(r-2M)^2}\right)\frac{\partial\Psi}{\partial x} + V(r,t)\Psi = 0\,, \tag{7.1.10}$$

where the time dependence of M is implicit, and r is interpreted as a function of x.

In these coordinates the surface, at which we impose the boundary condition, is always at $x = x_0 = M_0 \ln(r_0/2M_0 - 1)$. Another way to simulate a moving surface is to simply change, at each time step, the point of the numerical grid at which we impose the boundary condition, the two methods bring to the same results.

7.1.3 Numerical set-up

In the numerical simulation reported in the next sections we always consider an $l = 2$ quadrupolar mode and we use as initial condition for Ψ a Gaussian pulse:

$$\frac{\partial\Psi(r,0)}{\partial t} = \Psi_0 \exp\left(-\frac{(r_* - r_c)^2}{2\varsigma^2}\right), \quad \Psi(r,0) = 0\,, \tag{7.1.11}$$

with central value $r_c = 11M_0$ and width $\varsigma = 2M_0$; different initial values lead to similar results. The pulse is initially centered outside the potential barrier $V(r)$, whose peak is at approximately $3M_0$, and it is moving inward. The amplitude Ψ_0 is chosen in order to obtain an impulse with energy of order of the one we expect to be contained in the echoes signals, roughly from two to four orders of magnitude smaller than the mass of the central object [211].

We evolve Ψ in the time domain using a fourth-order Runge–Kutta integrator and computing spatial derivatives with finite-difference approximation of second-order accuracy [278]. A convergence test of the code is shown in Fig. 7.5 and discussed in Section 7.5. The non-trivial boundary conditions that we have imposed for our numerical simulations are described in Section 7.5.1.

During the simulations the mass of the central object increases because of the energy absorbed from the field, at a given time step, by an amount

$$\kappa\,\Delta E(t)\,, \tag{7.1.12}$$

where κ is the absorption coefficient (see definition below) and $\Delta E(t)$ is the field energy present, at time t, in the last spatial bin of our computational domain corresponding to the location of the surface of the central object. The method with which we estimate $\Delta E(t)$ at each instant is explained in Section 7.5.2.

7.2 Echoes: absorption beyond the test field limit

In our first scenario, we evolve Ψ according to Eq. (7.1.9), taking into account that the mass of the compact object can increase during the evolution as a consequence of the energy absorbed from the scalar field. In fact, whatever is the mechanism responsible for absorption, the energy of the field is converted in some other kind of energy inside the object, *e.g.* thermal energy in the case of dissipative/viscous effects, and since all energy "gravitates", this absorption will increase the mass of the object (technically the Misner-Sharp mass at the horizon or the ADM mass of the static object without the perturbation).

We define the absorption coefficient as the fraction of the incoming energy $E_{\rm in}$ that is lost inside the object:

$$\kappa = 1 - \frac{E_{\rm out}}{E_{\rm in}} \,. \tag{7.2.1}$$

Given a certain compactness and absorption coefficient, there exists a maximum flux of energy that the object can sustain without overcoming the hoop limit and collapse into a BH. It follows that if the energy in the GWs flux is bigger than this maximum, the collapse will delay part of the echoes signal. In the examples shown here, we have chosen compactness and absorption coefficients in order to always remain below this limit.

As we already explained in Chapter 5, in linear approximation, the time delay between echoes is the time that light takes to travel from the potential barrier centered around $r_{\rm peak} \approx 3M_0$ to the ECO surface $r_0 = 2M_0(1+\sigma)$ and back,[1] as follows

$$\Delta t_{\rm echo} = 2\int_{r_0}^{r_{\rm peak}} \frac{{\rm d}r}{f(r)} \simeq 2M_0\left[1 - 2\sigma - 2\ln(2\sigma)\right], \tag{7.2.2}$$

where σ is the compactness parameter defined in Eq. (7.1.2).

Nonetheless, if the ECO absorbs a small quantity of energy ΔE from the first echo, increasing its mass as $M_0 \to M = M_0 + \Delta E$ but remaining with the same radius r_0, the ECO compactness parameter for the first and second echoes is different

$$\sigma_{\text{1st echo}} = \frac{r_0}{2M_0} - 1 \,, \quad \sigma_{\text{2nd echo}} = \frac{r_0}{2M} - 1 = \frac{r_0}{2(M_0+\Delta E)} - 1 < \sigma_{\text{1st echo}} \,. \tag{7.2.3}$$

As a consequence, also the time delay of the second echo will be different. We give some numerical examples in Fig. 7.1 and Table 7.1 for selected values of the compactness and absorption parameters.

In these examples and in the plots that we show across the chapter, it is clear that even very small absorption coefficients (of order 0.1%–0.01%) lead to significant changes of the signal. This can seem counterintuitive, given the small amount of energy present in the echoes. The point is that, although the change in the mass is actually small, for very

[1] In reality, it should be taken into account also the interaction time $\Delta t_{\rm int}$ during which the field travels inside the interior of the object and it is partially absorbed (see Eq. (5.2.2)). Here, we assume it to be of the order of the radius of the object and thus negligible with respect to the exterior travel time. However, there exist models in which the interior spacetime is such that $\Delta t_{\rm int}$ becomes dominant [279, 280], one of these examples will be analysed in Chapter 8. Also $\Delta t_{\rm int}$ depends on the compactness parameter. However, the precise dependence on σ is model-dependent and generically not logarithmic.

compact objects it is sufficient to cause a big change in their compactness if the radius remains fixed.

Consider for definiteness an ECO with initial compactness parameter $\sigma_0 = 10^{-7}$: the absorption of the amount of energy $5 \cdot 10^{-8} M_0$ is sufficient to halve its compactness parameter and, as a result, to significantly change the spacetime in which the field is propagating. In this example, the time delay between echoes that depends logarithmic in the compactness parameter, roughly changes from $\Delta t_{\rm echo}/M_0 \approx -4 \ln(2\sigma_0) \approx 61.7$ to $\Delta t_{\rm echo}/M_0 \approx 64.5$.

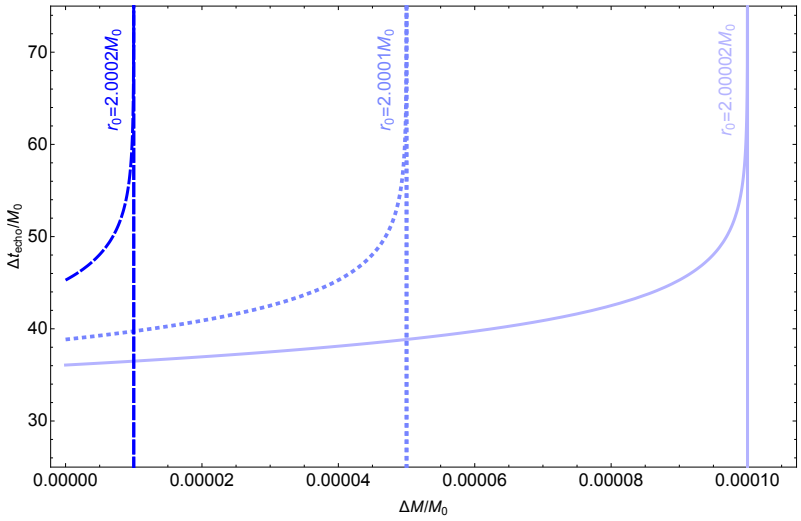

Figure 7.1: Time delay between echoes for fixed position of the surface r_0 and variable mass. The vertical lines represent the asymptotic value of $\Delta M/M_0$ for which the BH limit $r_0 = 2M_0$ is exceeded. All values are reported in units of the initial mass of the object M_0.

In Fig. 7.2 we plot the typical waveform for a Gaussian pulse scattered off an ECO with a small absorption parameter, compared with a perfectly reflecting ECO.

We observe a considerable difference in phase between the two cases due to the aforementioned non-negligible change in the time delay among echoes, in agreement with the analytical estimate of Eq. (7.2.2).

We also note a difference in the amplitude of the signal. The absorption coefficient is too small to produce a visible decreasing of the echoes amplitude, yet the first echo has a smaller amplitude with respect to the perfectly reflecting case, while the subsequent echoes have even bigger amplitudes. To understand this redistribution of energy is convenient to look at the field equation in (t, r_t) coordinates, where r_t is the "time-dependent" tortoise coordinate $r_t = r + 2M(t) \ln(r/2M(t) - 1)$, in which the Klein–Gordon equation remains a simple wave equation apart from some negligible terms proportional to $\dot{M}$ and $\ddot{M}$. Nevertheless, the position of the surface in the r_t coordinate changes with time and gets more negative as the mass increases, since the object is becoming more compact. This means that while the first echo is reflecting on the central object surface, this surface is moving away from it. Since we are in a reference frame in which the field equation is a simple wave equation, a movement of the surface causes a Doppler effect, *i.e.* a decrease of the frequency content of the field. For this reason, a smaller fraction of the first echo

σ_0	$\Delta t_{\rm echo}/M_0$	κ	$E_{\rm 1st\ echo}/M_0$	$\Delta t_1/M_0$	$E_{\rm 2nd\ echo}/M_0$	$\Delta t_2/M_0$
10^{-3}	26.85	6%	10^{-2}	30.54	$0.25 \cdot 10^{-2}$	32.43
10^{-4}	36.07	6%	10^{-3}	39.74	$0.25 \cdot 10^{-3}$	41.62
10^{-5}	45.28	6%	10^{-4}	48.94	$0.25 \cdot 10^{-4}$	50.82
10^{-5}	45.28	0.06%	10^{-2}	48.94	$0.25 \cdot 10^{-2}$	50.82
10^{-6}	54.49	0.06%	10^{-3}	58.15	$0.25 \cdot 10^{-3}$	60.03
10^{-7}	63.70	0.06%	10^{-4}	67.36	$0.25 \cdot 10^{-4}$	69.24

Table 7.1: Given an initial compactness parameter σ_0 we report the expected time delays between echoes $\Delta t_{\rm echo}$ in the case of a perfect reflecting ECO and the true time delay between the first and the second echo Δt_1 and between the second and third echo Δt_2 in the case of an ECO with absorption coefficient κ. These last two time delays are different to respect to $\Delta t_{\rm echo}$ because the partial absorption of the energy contained in the first and second echo changes the compactness of the central object. We assume that the energy in the second echo is approximately a quarter of that of the first one. All values are reported in units of the initial mass of the object M_0.

will pass through the high-pass filter potential centered at $r_{\rm peak}$, while a greater fraction of it will be bounced back forming the subsequent echoes that therefore will have a greater amplitude with respect to the perfectly reflecting case. Also the absorption of the second and third echoes causes an increase of the mass and thus a movement of the surface during the reflection, but the effect is quite negligible with respect to the previous increase of amplitude.

7.3 Echoes: absorption and backreaction scenarios

In realistic situations, the energy absorbed from the ringdown signal might be enough to cause the collapse of the ECO into a BH. Thus, if we want the object to be stable, we have to take into account some mechanisms that prevent the collapse, whose details depend obviously on the physics of the object and the specific gravitational field equations. To have a glimpse on the possible effects on the signal, while remaining agnostic about the novel physics supporting the ECO, we consider here some simple model-independent scenarios.

7.3.1 Asymptotic compactness

As a first scenario, the object is allowed to absorb energy varying its compactness up to a certain limit, say until its surface is at a Planck length from the would-be horizon. This corresponds to a compactness parameter of order of $\sigma_{\rm Planck} \approx 10^{-40}$ for stellar mass objects ($M \approx 10^2 M_\odot$). This situation is particularly reasonable because the ringdown signal comes from objects that have just been formed in a binary coalescence, thus it is not obvious that they are already in their definitive stable configuration.

Technically, this situation can occur when the ECO absorption coefficient depends on

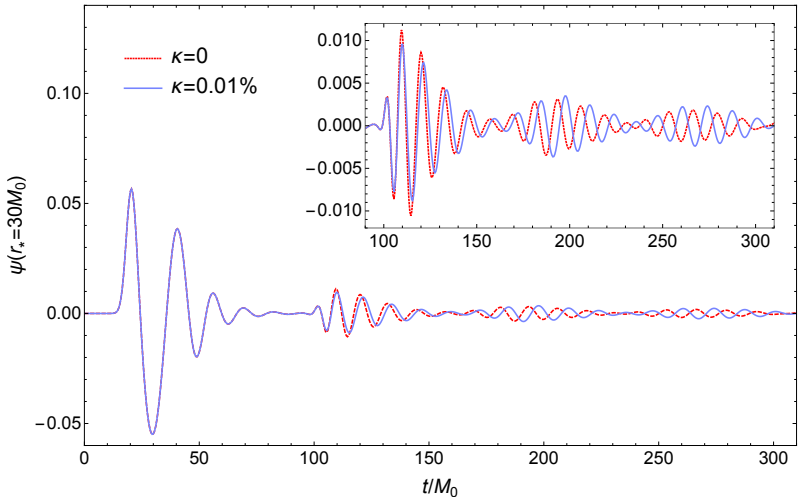

Figure 7.2: Quadrupolar waveform extracted at $r_* = 30M_0$. The initial Gaussian pulse has energy $E = 4.4 \cdot 10^{-3} M_0$ and it is scattered off an ECO with initial compactness parameter $\sigma = 10^{-7}$, *i.e.* $r_0 = 2.0000002 M_0$. The red dashed line shows the case of a perfectly reflecting object, while the purple solid line shows the case in which the surface of the object absorbs incoming radiation with an absorption efficiency of 0.01%.

its compactness and goes to zero as $\sigma \to \sigma_{\rm Planck}$. The effects on the echoes waveform will depend on the initial value of the absorption coefficient, on the velocity with which it goes to zero and on the value of the asymptotic compactness. If the absorption coefficient varies very slowly, we obtain the same results of constant absorption, analyzed in the previous section, and no other backreaction. When instead the absorption coefficient goes rapidly to zero, only the first echo will be partially absorbed and the time delay will soon stabilize to a constant value. Among several possible choices, in our computations we have considered this functional form for the absorption coefficient

$$\kappa(\sigma) = \alpha \left(1 - \tanh \frac{\beta}{\sigma - \sigma_{\rm Planck}} \right), \tag{7.3.1}$$

which varies slowly when the compactness is far from the Planck value, and goes smoothly to zero for $\sigma \to \sigma_{\rm Planck}$. The parameters α and β represent, respectively, the initial value and the velocity with which κ goes to zero. At each step of the simulation

$$\sigma(t + \Delta t) = \frac{r_0}{2M(t) + \kappa(\sigma(t)) \Delta E(t)} - 1, \tag{7.3.2}$$

such that as $\sigma(t) \to \sigma_{\rm Planck}$, we have $\kappa(\sigma) \to 0$ and thus $\sigma(t + \Delta t) = \sigma(t)$.

In Fig. 7.3 we plot the typical waveform for a Gaussian pulse scattered off an ECO with a compactness-depending absorption parameter, compared with a perfectly reflecting ECO.

The top and middle panels show our results for, respectively, $\alpha = \{0.05, 2 \cdot 10^{-4}\}$ and $\beta = \sigma_0 \cdot 10^{-3}$, with $\sigma_0 = 10^{-7}$. In the first case the initial absorption coefficient is $\kappa_0 \approx 5\%$. With an incoming Gaussian pulse of energy $E \approx 10^{-3} M_0$, this κ_0 is sufficient to reach a very high compactness, and thus a negligible absorption coefficient, already during the absorption of the very first part of the first echo. For this reason, we observe that the

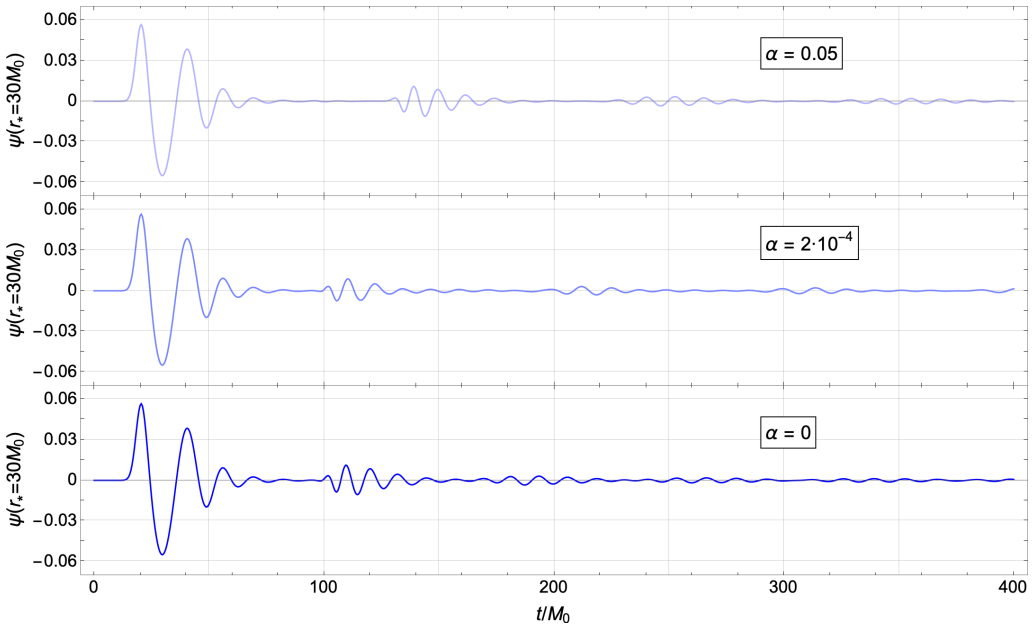

Figure 7.3: Quadrupolar waveform extracted at $r_* = 30M_0$. The initial Gaussian pulse has energy $E = 4.4 \cdot 10^{-3} M_0$ and it is scattered off an ECO with initial compactness parameter $\sigma = 10^{-7}$, *i.e.* $r_0 = 2.0000002 M_0$. We show results for a compactness-dependent absorption parameter (top and middle panels, for selected values of the parameter α introduced in Eq. (7.3.1) and $\beta = \sigma \cdot 10^{-3}$) and for a perfectly reflecting ECO (bottom panel).

time delay among the echoes is approximately constant even if it is larger than in the perfectly reflecting case shown in the bottom panel. In the second case, the absorption coefficient is approximately constant and $\kappa_0 \approx 0.02\%$ during the absorption of the first echo, while it becomes negligible only during the absorption of the third echo. This leads to non-constant time delays among the first echoes.

We want to mention another possible scenario in which the change in the compactness stops when the object reaches a limiting value: the absorption coefficient is constant but, once the asymptotic compactness is reached, the ECO starts expanding to remain in the same equilibrium configuration. In this case, the first part of the signal will have larger time delays but this increment of $\Delta t_{\rm echo}$ will stop once the expansion starts. The reason for this will be clear in the next section.

7.3.2 Expansion

In another backreaction scenario, to remain stable, the ECO compensates the absorption by expanding. A reasonable way to model the expansion is to assume that its radius moves in order to maintain the same initial compactness, according to the following prescription (in Schwarzschild coordinates)

$$\frac{r_0(t+\Delta t)}{2\left(M(t)+\Delta E\right)} \stackrel{!}{=} \frac{r_0(t)}{2M(t)} = \sigma_0 + 1\,, \tag{7.3.3}$$

where ΔE is the amount of energy absorbed from the scalar field in the time interval Δt.

In this case, the sole dependence on time in Eq. (7.2.2) is a linear dependence on $M(t)$ and thus the time delays among echoes will be approximately always the same, as in the perfectly reflecting case. Obviously, this is true only if the expansion happens fast enough for the object to be approximately at the same constant compactness at each instant — note that this could even require superluminal expansion [270].

Alternatively, there might be a transient phase throughout the object has already absorbed energy but has not expanded enough to reach the original compactness. The duration τ of the transient phase is crucial to determine the effect that it produces on the signal. If τ is much smaller than the light crossing time between the surface and the potential, *i.e.* $\tau \ll \Delta t_{\rm echo}$, when the second echo arrives on the surface, the object will have already recovered its initial compactness and thus no visible shift in the time delay will be produced. On the other hand, when $\tau > \Delta t_{\rm echo}$, the time delay between the first and the second echo will be longer than in the perfectly reflecting case because the second echo will arrive on the surface when the compactness is still different from the initial one. Then, while the object continues to expand, it also continues to absorb small amounts of energy from subsequent echoes, thus it will reach its initial compactness only when the energy of these echoes will become negligible. However, we expect its compactness to become closer and closer to the initial one, and thus the time delay among these subsequent echoes to become smaller and smaller until it reaches the value corresponding to the initial compactness. In Fig. 7.4 we plot the waveform for a Gaussian pulse off an ECO whose surface expands linearly, compared with a perfectly reflecting ECO. In this example we have chosen the expansion rate v such that the surface moves as $r_0(t) = r_0 + v\Delta t$ and the compactness is modelled as

$$\sigma(t + \Delta t) = \frac{r_0 + v\Delta t}{2M(t) + \kappa(\sigma(t))\Delta E(t)} - 1\,, \tag{7.3.4}$$

such that the initial compactness is reached after a transient phase $\tau \approx 65 M_0 \geqslant \Delta t_{\rm echo}$ with respect to the beginning of the absorption.

Before closing a final comment is in order. In the previous scenario we have assumed a BH-like relation between the instantaneous radius and mass, *i.e.* a direct proportionality $r_0(t) \propto M(t)$. However, the relation between the radius and the mass of star-like compact objects can be more involved, implying that the compactness of these objects can be different for different values of the mass — see *e.g.* Fig. 1 of Ref. [280]. Nonetheless, we are here considering ultra-compact objects which are good BH mimickers and as such they are expected to be characterized by a BH-like behavior. It is however worth mentioning that assuming $r_0(t)$ to be a more general function of $M(t)$ would imply that the expanding ECO would experience a change in its compactness parameter. This, in turn, would lead to a variation of the time delay among echoes, and to a breaking of the aforementioned degeneracy with the perfectly reflecting case.

7.4 Conclusions

In this chapter we have analyzed the response of an ECO against scalar perturbations to discuss possible effects of non-linear interactions on the echoes signal. In the first part, we have let the central compact object absorb part of the incoming radiation, resulting

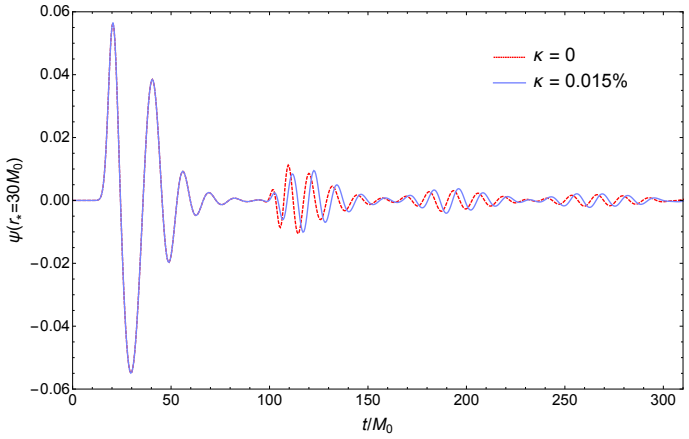

Figure 7.4: Quadrupolar waveform extracted at $r_* = 30M_0$. The initial Gaussian pulse has energy $E = 4.4 \cdot 10^{-3} M_0$ and it is scattered off an ECO with initial compactness parameter $\sigma = 10^{-7}$, *i.e.* $r_0 = 2.0000002 M_0$. The red dashed line shows the case of a perfectly reflecting object, while the purple solid line shows the case in which the surface of the object absorbs incoming radiation with an absorption efficiency of 0.015% and it expands to achieve the initial compactness in a finite amount of time.

in an increase in its mass and leading to changes in the spacetime in which the scalar field propagates. The most important effect of this on the echo waveform is the loss of the quasi-periodicity of the signal. In fact, the absorption of each echo changes the mass and thus the compactness of the object, and as a result, it increases the time delay among echoes which depends logarithmically on the compactness. If the absorption continues without any other backreaction of the object, the time delay will continue to increase. However, the energy of the nth echo is smaller than the previous ones, hence the change in the time delays becomes more and more negligible and it stabilizes to a constant value, unless the ECO collapses into a BH and no other echoes are produced.

In the second part we have considered some possible model-independent scenarios in which the object reacts to the absorption to prevent its collapse into a BH. In the first scenario, the ECO can increase its compactness only up to a certain limiting value. This can happen in at least two different ways: (i) the ECO absorption coefficient decreases for increasing compactness, going to zero when the asymptotic compactness is reached; (ii) the absorption coefficient is constant but once the asymptotic compactness is reached the object starts to expand in order to remain in the same equilibrium configuration. The characteristic feature of this scenario is that the time delay between echoes gets longer and longer until it stabilizes to a constant value corresponding to the time delay of an object with the asymptotic compactness. In the second scenario, the ECO expands instantaneously in order to prevent the collapse. If the expansion rate maintains the same initial compactness, the resulting signal will have constant time delays among echoes like in the case of a perfectly reflecting ECO. However, this type of expansion is an idealization and physically we expect that the original compactness is not recovered instantly but only after a transient phase. When the transient phase is much shorter than the time delay between echoes, the effects on the waveform are negligible; while when it is comparable or greater than the time delay, the interval among echoes in the resulting signal is initially

bigger than in the perfect reflecting case but then gets shorter, until it reaches the value corresponding to the time delay of the object at its initial compactness. It might also be possible that the mass-radius relation for these objects is not linear as for BHs, and that stable configurations have different compactness for different values of the mass. In this case, the object will not expand at constant compactness, breaking the degeneracy with the perfectly reflecting case.

At this point, one can wonder whether these changes in the time delay are actually detectable, or whether the signal can still be approximated as quasi-periodic. First of all, we emphasize that in all cases analyzed here the change in the time delay is a feature of the first part of the signal. The number of echoes interested by this effect depends on the initial compactness, the absorption coefficient and the damping factor between echoes, *i.e.* the difference in amplitude among subsequent echoes. Anyway, thanks to its bigger amplitude, it is the first part of the signal that is more likely detectable.

The time delay between the signal and the first echo is subjected to more uncertainties because it can be affected by non-linear physics during the merger. Thus the observable for which the effect of absorption might be more important and non-negligible is usually the difference between the first two time delays: Δt_2 between the first and second echo and Δt_3 between the second and third echo. As an example, consider an ECO with mass M_0, initial compactness $\sigma = 10^{-5}$, an absorption coefficient $\kappa = 0.06\%$ and assume that the energy carried by the first echo is $E_{\rm echo} \approx 10^{-2} M_0$ with a damping factor between the first and second echo $\gamma = 0.35$: the resulting relative difference in the time delays turns out to be $\Delta t_{12} = (\Delta t_2 - \Delta t_1)/\Delta t_2 \approx 5.7\%$.[2] Note that in this example, since the total absorbed energy is $E_{\rm tot} = \kappa \sum_{n=0}^{\infty} \gamma^n E_{\rm echo}$, the hoop limit $r_0 = 2M_0$ is never reached. Obviously, the difference Δt_{12} can be larger if we choose parameters that do not prevent the overcoming of the hoop limit after the absorption of some of the first echoes.

Finally, we have not considered the possible effects of a frequency-dependent absorption coefficient. As subsequent echoes contains smaller frequencies to respect to the previous ones, if the ECO absorbs only higher frequencies than a given critical energy scale, like in the case of Boltzmann reflectivity [275], subsequent echoes will be less absorbed and the absorption can even become negligible after some echoes. However, excluding a possible expansion of the object, it seems that the above described mechanism would additionally require a non-trivial dependence of the critical energy scale on the compactness of the object in order to avoid the formation of an horizon. We leave this to future investigations.

In conclusion, we think that the possible phenomenology exposed by this investigation should be taken into account in future searches for echoes in ringdown signals. In fact, the strategies adopted in these searches are usually based on the quasi-periodicity of the echoes signal [211, 281], a feature that we showed can be partially lost in more realistic scenarios. This seems to indicate that future generic searches for echoes, agnostic to any specific model of BH mimickers, should give way to more model-dependent analyses which would take into account the stability, or meta-stability, of such objects. Last but not least, the relevance of such findings appears to deserve an extension to gravitational perturbations, and possibly even more relevantly, to rotating geometries. We hope that this study will then stimulate further investigations and help elaborate a more refined searching strategy.

[2] Taking into account an interaction time $\Delta t_{\rm int} \approx 4M_0$ during which the field travels inside the interior of the object, modifies the relative difference as $\Delta t_{12} \approx 5.3\%$.

7.5 Appendix: Numerical implementation

In our simulations we have evolved the scalar field using a fourth-order Runge–Kutta integrator and computing spatial derivatives with finite-difference approximation of second-order accuracy [278]. To validate our code we have checked the conservation of the energy and the matching with the time delays computed analytically. We have also performed a convergence study to guarantee that the numerical resolution is high enough. In the left panel of Fig. 7.5 we observe that, until the mass of the central object is constant, we find the expected second order convergence. However, the right panel of Fig. 7.5 shows that as the field arrives at the surface and absorption is taken into account, the discrete *linear* increase of the mass parameter at each time step introduces a dominant linear error.

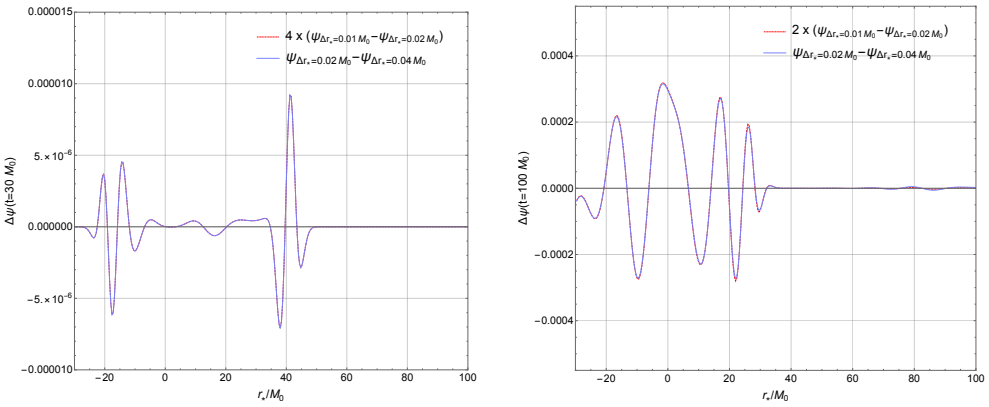

Figure 7.5: Left: Convergence study of the evolution of the scalar field at time $t = 30M_0$, when the mass parameter is still constant. The purple line shows the difference between results obtained with low ($\Delta t = \Delta r_* = 0.04M_0$) and medium ($\Delta t = \Delta r_* = 0.02M_0$) resolutions, while the red line shows the difference between results obtained with medium and high ($\Delta t = \Delta r_* = 0.01M_0$) resolutions multiplied by 4, the expected factor for second-order convergence. Right: Convergence study of the evolution of the scalar field at time $t = 100M_0$, when the mass is changed discretely at each time step, introducing a linear error. The purple line shows the difference between results obtained with low ($\Delta t = \Delta r_* = 0.04M_0$) and medium ($\Delta t = \Delta r_* = 0.02M_0$) resolutions, while the red line shows the difference between results obtained with medium and high ($\Delta t = \Delta r_* = 0.01M_0$) resolutions multiplied by 2, the expected factor for linear convergence. In our simulations we always use higher resolution, *i.e.* $\Delta t = \Delta r_* = 0.001M_0$.

7.5.1 Boundary conditions

The boundary conditions for the scenarios investigated in this work are non-trivial. As usual, we impose purely outgoing (*i.e.* perfectly absorbing) boundary conditions at the outer boundary. This is because in real physical systems there is no outer boundary and the radiation escapes away at infinity. To do so, we simply impose the condition

$$\frac{\partial \Psi}{\partial t} + \frac{\partial \Psi}{\partial x} = 0 \tag{7.5.1}$$

at the outer boundary of our computational domain.

However, differently from the BH case, at the ECO surface r_0 we need to impose *partially* reflecting boundary conditions, to account for absorption. One way to implement it is to insert a fictitious, dissipative region of length l behind r_0 and then a perfectly reflecting boundary condition at $r_0 - l$, so that looking at the reflected wave only from r_0 onwards it will have an effective smaller amplitude. The dissipation, in turn, can be implemented through two possible methods. One is to switch on a dissipative term in this region through perfect matched layers [282]. The other method is to pause the simulation at an instant in which the whole part of the field that has to be reflected is present inside the fictitious region, then for each point of the region we replace $\Psi(r)$ with $(1-\kappa)^{1/2}\Psi(r)$ before the simulation stars over. In any case, the fictitious dissipative region, will cause a delay in the reflection that can be either deleted in the final results or can be interpreted as the interaction time between the massive object and the scalar wave. If the central object is compact enough, as in the cases considered here, this replacement with $(1-\kappa)^{1/2}\Psi(r)$ can be done also without inserting any fictitious region, simply stopping the simulation when the part of the field that has to be reflected is in the region between the potential and the surface.

We also checked that we obtain the same results if we simply impose Dirichlet boundary conditions and multiply each nth echo for $(1-\kappa)^{n/2}$ at the end of the simulation. We have used this last simple implementation for all the simulations presented here in which the absorption coefficient is constant. This method has already been studied and applied even in the frequency domain *e.g.* in Refs. [283, 284].

Note also that, given the small absorption coefficients used in this work, the effect on the echoes amplitude is negligible.

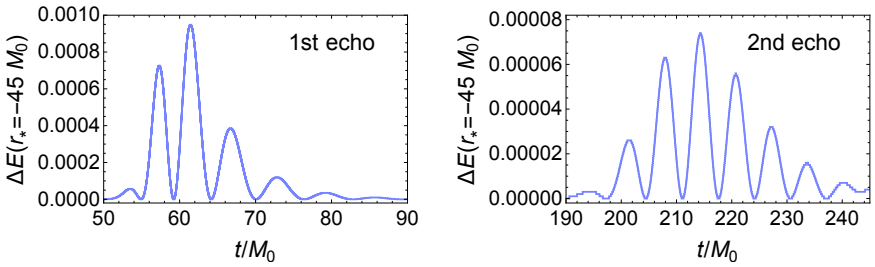

Figure 7.6: Energy present in the spatial bin between $r_* = -45.001M_0$ and $r_* = -45M_0$ for the first two echoes of a quadrupolar Gaussian pulse in the spacetime of an ECO with compactness $\sigma = 2.3 \cdot 10^{-16}$.

7.5.2 Absorbed energy

During the multiple reflections of echoes, the central object absorbs part of the energy of the scalar field and its mass increases, at a given time step, by an amount $\kappa\,\Delta E(t)$, where κ is the absorption coefficient defined in Eq. (7.2.1) and $\Delta E(t)$ is the field energy present, at time t, in the last spatial bin of our computational domain corresponding to the location of the surface of the central object.

For this reason we need to know the energy distribution of the echoes that arrive at the surface. To obtain this distribution we run a simulation in which the central object is very compact, precisely we put the surface at $r_* = -70M_0$. Then we look at the energy that pass

through a fixed point, distant from the reflecting surface to avoid possible deformations and interference with the reflecting wave. Precisely we chose to evaluate the energy at $r_* = -45M_0$. Since the field moves on light rays $\mathrm{d}r_* = \mathrm{d}t$, these energy distribution in time is equivalent to the spatial energy distribution.

The results obtained in this way for the first two echoes are shown in Fig. 7.6. Taking into account the right time shift due to the different position of the surface in the true simulations, we obtain the energy that arrive at the object for each instant.

Note however that the results are poorly influenced by the precise distribution of the energy but basically depends only on the time of arrival of the echo, its spread and its total energy.

Chapter 8

Sensitivity to the inner quantum core: the ringdown of semiclassical stars

In this Chapter we investigate some (often) overlooked aspects related to the ringdown of exotic compact objects. In particular, we study the sensitivity of the ringdown signal to the properties of their innermost regions. We present results obtained both in frequency and time domain, highlighting the connection between long living QNMs associated to the presence of a stable lightring and the echoes signal.

For this investigation we center the analysis on a particular family of static and spherically symmetric exotic compact objects recently found within the framework of quantum field theory in curved spacetimes [38, 39]. These so-called "semiclassical stars" are a well-motivated model of horizonless compact objects, as they do not require of any new physics beyond quantum vacuum polarization. Such solutions are particular suitable for this analysis since they exhibit an (approximately) Schwarzschild exterior together with a modified interior composed of a constant-density classical fluid and the cloud of vacuum polarization generated by the star itself. By varying their classical density, it is possible to modify the interior metric without affecting the exterior, which has a clear effect in the QNMs frequencies and the echo waveform.

In this model, as the compactness of the star is increased, quantum vacuum effects allow to smoothly surpass the Buchdahl limit, opening a window towards studying the properties of exotic compact objects in the black hole limit.

Let us written the line element of these "semiclassical stars" in the following form:

$$ds^2 = -f(r)dt^2 + q(r)dr^2 + r^2 d\Omega^2, \tag{8.0.1}$$

where $d\Omega^2$ is the line element of the unit sphere. We define the compactness function as $C(r) \equiv 1 - q(r)^{-1} = 2m(r)/r$, whit $m(r)$ the so-called Misner-Sharp mass [83, 84]. In order to find a regular solution, the authors in [38, 39] incorporated the renormalized stress-energy tensor (RSET) of massless scalar fields describing quantum vacuum polarization — an effect expected to be present in any compact star [285–287] — to the Einstein

equations, so that

$$G^{\mu}{}_{\nu} = 8\pi \left(T^{\mu}{}_{\nu} + M_{\rm P}^2 \langle \hat{T}^{\mu}{}_{\nu} \rangle \right) , \tag{8.0.2}$$

where we recall that we are using geometric units $c = G = 1$ and thus $\hbar = M_{\rm P}^2$.

Eq. (8.0.2) takes into account that the physical vacuum of a static star corresponds to the Boulware vacuum [288] in quantum field theory (whereas the classical vacuum stress energy tensor would be simply zero). Note that the classical stress-energy tensor (SET) of the star matter, which we take to be a constant-density fluid [289], and the RSET are conserved independently; they only influence each other through their impact on the spacetime.

Noticeably, by taking equations (8.0.2) as a modified theory of gravity to find their self-consistent solutions, the authors [38, 39] obtained a new type of star supported by an interior nucleus of negative energy density. When their compactness is small, vacuum polarization contributes as a perturbative correction over the classical constant-density solution. However, as compactness approaches the Buchdahl limit $C(r_0) = 2M/r_0 = 8/9$ (here M is the ADM mass and r_0 is the total radius of the star), which the Schwarzschild star saturates [290], the RSET grows in magnitude and modifies the interior structure. As a consequence, semiclassical stars were found to not exhibit an upper bound to their compactness, but rather to be able to exist also for the compactness range $8/9 < C(r_0) < 1$. Thus they can serve as a well-motivated black hole mimicker worth bringing under phenomenological scrutiny.

A distinctive observational feature that only emerges in ultra-compact stars is the presence of gravitational-wave echoes. Stars with $C(r_0) > 2/3$ develop outer and inner light rings, which correspond to the presence of unstable and stable circular photon orbits, respectively. When the system is perturbed and the light-crossing time between the two light rings is large enough, echoes can be individually resolved in the late-time waveform associated to matter fields. In frequency domain, the signal can also be studied via a complementary analysis involving the QNMs of the system. Since the time delay between echoes and the associated QNMs are both sensitive to the interior properties of the star [291, 292], echo detection [293] could constitute not only a direct observation of horizonless objects more compact than neutron stars, but also a way to extract details about their interior physical properties.

Two additional comments are pertinent at this stage. The first comment is related to the presence of an additional scale, $M_{\rm P}$, in the semiclassical equations (8.0.2). The introduction of quantum effects breaks the scale invariance of the Schwarzschild interior solution, meaning that the time delay between echoes (and the quasinormal mode frequencies themselves) does not increase linearly with M as the scale separation between M and $M_{\rm P}$ increases. This has clear implications on the detectability of echoes which, as we will show, would become extremely delayed for semiclassical stars surpassing the Buchdahl limit.

The second comment is related to the spacetime at $r = 0$, where absence of curvature singularities implies the metric functions must obey the expansions

$$q = 1 + q_2 r^2 + O(r^3), \quad f = f_0 + f_2 r^2 + O(r^3). \tag{8.0.3}$$

We will say that the core of the star is "de-Sitter-like" (dSl) if $q_2 < 0$ and $f_2 > 0$ and

"anti-de-Sitter-like" (AdSl) if $q_2 > 0$ and $f_2 < 0$ (the cores are strict de-Sitter or anti-de-Sitter only if $f = q^{-1}$), or "mixed" otherwise. The characteristics of the central core are relevant for echo detection since, in stars with $f_0 \ll f(r_0) = 1 - 2M/r_0$, the dominant contribution to echo delay comes from a neighbourhood of $r = 0$. This property was observed in constant-density solutions [294] and is preserved in their semiclassical version. Consequently, modifications of the metric in the central regions of the star (for example, changing from an AdSl to a dSl core) have phenomenological consequences. Since the central regions of extremely compact objects would be an adequate place where to search for new physics beyond semiclassical gravity, it is reasonable to think of gravitational-wave echoes as messengers carrying information about the quantum-gravitational regime.

In this chapter, we present a primer on the phenomenology of semiclassical stars. Although our analysis is clearly model-dependent, the wide range of compactness values and the diversity of interior structures displayed by the semiclassical star model (allowing for AdSl and mixed cores) allows to address more general physical questions about the phenomenology of exotic compact objects. In Sec. 8.1 we present the classical, uniform-density solution together with its semiclassical counterpart. In Sec. 8.2 we analyze the propagation of spin 2 test fields perturbations, showing the qualitative differences that arise as the star is made more compact. Complementarily, we obtain the fundamental quasinormal modes of these stars and their scaling with the compactness in Sec. 8.3. In Sec. 8.4 we detail how modifications in the central regions of these stars affects both the delay between echoes and the QNMs frequencies. We furthermore discuss about the connection between the presence of echoes in the time domain and of long-living modes in the frequency domain and we comment on how both phenomena suggest the necessity of taking into account non-linear effects. We conclude with some further comments in Sec. 8.5.

8.1 The semiclassical star model

The existence of upper compactness bounds in stars, as well as their specific values, depends on the properties and equation of state obeyed by the fluid [295–298]. The simplest stellar model, or constant-density star [289], saturates the hypotheses of the Buchdahl theorem (see Chapter 1) and its compactness is bounded from above by $C(r_0) < 8/9$. For clarity, we briefly review the model here.

The SET of the star is modeled as an isotropic perfect fluid

$$T^{\mu}_{\ \nu} = (\rho + p)\, u^{\mu} u_{\nu} + p \delta^{\mu}_{\nu}, \tag{8.1.1}$$

with p and ρ denoting the pressures and energy density measured by an observer comoving with the fluid with 4-velocity u^{μ}. Assuming a metric of the form (8.0.1) the covariant conservation of the SET (8.1.1) implies

$$\nabla_{\mu} T^{\mu}_{r} = p' + \frac{f'}{2f}(\rho + p) = 0. \tag{8.1.2}$$

If we assume a uniform energy density fluid

$$\rho(r) \equiv \rho = \text{const}, \tag{8.1.3}$$

we can solve Eqs. (8.0.2) with $M_{\rm P} = 0$ and seek for a metric matching the Schwarzschild one at the star surface $r = r_0$. Such interior metric can be found to be

$$\begin{aligned} ds^2 = &-\frac{1}{4}\left(3\sqrt{1-C(r_0)} - \sqrt{1-r^2C(r_0)/r_0^2}\right)^2 dt^2 \\ &+ \left(1-r^2C(r_0)/r_0^2\right)^{-1} dr^2 + r^2 d\Omega^2. \end{aligned} \tag{8.1.4}$$

It is straightforward to check from the above equation that $f = 0$ at $r = 0$ for $C(r_0) = 8/9$. By means of the conservation relation (8.1.2) which, for constant-density fluid, can be integrated to $p = \rho\left(\sqrt{\frac{f(r_0)}{f(r)}} - 1\right)$, this translates into a diverging pressure at the center, which is tantamount to say that for this solution, any finite pressure will not be able to support the star beyond the $C(r_0) = 8/9$ compactness. This is, in a nutshell, the so called Buchdahl's limit.

In what follows, while still assuming the equation of state (8.1.3) for the classical fluid, we shall be interested in solving the full semiclassical Eqs. (8.0.2) incorporating the RSET as an additional matter source. Obtaining the RSET in spherically symmetric spacetimes is a complicated procedure requiring, beyond renormalization, also an accurate numerical computation for the modes in which the quantum field is decomposed. While efforts have been devoted to calculating RSETs in black hole spacetimes [299–302], this computation is yet to be attained in stellar spacetimes if not via analytical approximations. While exact RSETs can be found numerically, this still hinders a proper treatment of their backreaction on the classical geometry [303].

Following this motivation, in [39] a novel approximation — particularly adapted to stellar spacetimes — for the RSET of massless minimally coupled scalar fields was developed. Remarkably, within such framework semiclassically stable star were found. Here, we omit the technical details, as they can be easily found in the original publication, and just present the form of the tt and rr components of the so obtained semiclassical stellar equations (8.0.2)

$$\begin{aligned} \frac{q'}{q} = &-\frac{q-1}{r} + 8\pi r q\rho + \frac{M_{\rm P}^2}{48\pi r}\left\{-\frac{83}{20r^2q} + \frac{1}{15r^2}\left(105 + 136\pi r^2\rho + 504\pi r^2 p\right)\right. \\ &-\frac{q}{30r^2}\left[63 + 1054\pi r^2\rho + 7488\pi^2 r^4\rho^2 + 49\pi r^2\left(53 + 940\pi r^2\rho\right)p + 56832\pi^2 r^4 p^2\right] \\ &-\frac{q^2}{15r^2}\left(1 + 8\pi r^2 p\right)^2\left(3 - 616\pi r^2\rho - 1080\pi r^2 p\right) - \frac{11h^3}{20r^2}\left(1 + 8\pi r^2 p\right)^4 \\ &\left.+8\pi\left(\rho + p\right)\log\left[\lambda^2 f\right]\left[-1 + q\left(1 + 2\pi r^2\rho + 26\pi r^2 p\right) - q^2\left(1 + 8\pi r^2 p\right)^2\right]\right\}, \end{aligned} \tag{8.1.5}$$

$$
\begin{aligned}
\frac{f'}{f} =& \frac{q-1}{r} + 8\pi r q p + \frac{M_{\rm P}^2}{48\pi r}\left\{-\frac{5}{4r^2 q} + \frac{1}{15r^2}\left(21 - 108\pi r^2\rho - 764\pi r^2 p\right)\right. \\
&+\frac{q}{30r^2}\left[23 - 4\pi r^2\rho\left(3 + 20\pi r^2\rho\right) + 320\pi r^2\left(5 - 12\pi r^2\rho\right) + 11904\pi^2 r^4 p^2\right] \\
&-\frac{q^2}{15r^2}\left(1 + 8\pi r^2 p\right)^2\left(11 - 180\pi r^2\rho - 228\pi r^2 p\right) - \frac{11q^3}{60r^2}\left(1 + 8\pi r^2 p\right)^4 \\
&\left.+4\pi\left(\rho + p\right)\log\left[\lambda^2 f\right]\left[\frac{11}{3} - \frac{q}{3}\left(3 + 12\pi r^2\rho + 20\pi r^2 p\right) - q^2\left(1 + 8\pi r^2 p\right)^2\right]\right\}, \quad (8.1.6)
\end{aligned}
$$

where λ is an arbitrary parameter, introduced by the renormalization prescription, which was implicitly defined as

$$
\log\left[\lambda^2 f(r_0)\right] = \frac{q(r_0)\left[15q(r_0) - 40\pi r_0^2\rho - 6\right] - 9}{q(r_0)\left[5q(r_0) + 24\pi r_0^2\rho + 6\right] - 11} \tag{8.1.7}
$$

so to allow for a smooth matching between the interior and exterior solutions [39].

A quick glance at the above equations shows that the right-hand sides of Eqs. (8.1.5, 8.1.6) contain corrections proportional to $M_{\rm P}^2$ that qualitatively estimate quantum vacuum polarization effects. For stars of small compactness, for which $p \ll \rho$, semiclassical effects amount to a perturbative correction over the classical solution. However, when compactness approaches the Buchdahl limit, in which $p \gg \rho$, terms $\propto p^4$ in (8.1.5, 8.1.6) overcome their $O(M_{\rm P}^2)$ suppression, modifying the stellar solutions in a non-perturbative way and allowing to surpass the Buchdahl limit.

Eqs. (8.1.5, 8.1.6) reduce to their counterparts in vacuum by taking $p = \rho = 0$. At sufficiently large distances, the metric obeys the expansions

$$
\begin{aligned}
f &= 1 - \frac{2M}{r} + \frac{M_{\rm P}^2 M^2}{90\pi r^4} + O\left(\frac{M_{\rm P}^2 M^3}{r^5}\right), \\
q &= \left[1 - \frac{2M}{r} - \frac{M_{\rm P}^2 M^2}{6\pi r^4} + O\left(\frac{M_{\rm P}^2 M^3}{r^5}\right)\right]^{-1}.
\end{aligned} \tag{8.1.8}
$$

Notice that the semiclassical solution is asymptotically flat because we are evaluating the RSET in the Boulware state, which reduces to the Minkowski vacuum in the asymptotic regions. With these boundary conditions, the vacuum equations are integrated (assuming $M > 0$) from a sufficiently large fiducial radius until some radius $r_0 > 2M$ where the surface of the star is placed. Then, starting from $r = r_0$, Eqs. (8.1.5, 8.1.6) are integrated inwards with the boundary conditions

$$
p|_{r=r_0} = 0, \quad \rho = \text{const} = \rho_0, \tag{8.1.9}
$$

where the value of ρ_0 compatible with a regular metric must be found numerically [39]. The surface compactness of the star is given by $C(r_0) = 1 - q(r_0)^{-1}$ and can take values in the interval $C(r_0) \in (0, 1)$.

Not all values of ρ_0 are compatible with a regular metric: numerical explorations reveal that for *any* $C(r_0) < 1$ there exists a critical density $\rho_0 = \rho_{\rm c}$ that corresponds to the regular solution with smallest ρ_0. For $\rho_0 < \rho_{\rm c}$ we find solutions with naked curvature singularities, whereas for $\rho_0 \geqslant \rho_{\rm c}$ we obtain fully regular spacetimes. Since the space

of parameters is large, we have summarized these cases in Table 8.1. In the following sections, our analyses will be restricted to critical stars ($\rho_0 = \rho_c$), which display a core of the AdSl type. The phenomenology associated to super-critical stars ($\rho_0 > \rho_c$), which have cores of the mixed type instead, will be explored in Section 8.4.

ρ \ $C(r_0)$	$C(r_0) < 8/9$	$C(r_0) = 8/9$	$C(r_0) > 8/9$
$\rho_0 < \rho_c$	Sub-critical Sub-Buchdahl	Sub-critical Buchdahl	Sub-critical Super-Buchdahl
$\rho_0 = \rho_c$	Critical Sub-Buchdahl	Critical Buchdahl	Critical Super-Buchdahl
$\rho_0 > \rho_c$	Super-critical Sub-Buchdahl	Super-critical Buchdahl	Super-critical Super-Buchdahl

Table 8.1: Table depicting the various families of semiclassical stars, depending on their energy density ρ_0 and their surface compactness $C(r_0)$. The grey cells correspond to singular solutions. In dark blue (critical solutions), we have regular stars with an AdSl core, while in light blue (super-critical solutions) we find stars with mixed cores. In both cases the solutions can approach the black hole limit arbitrarily.

Figure 8.1 shows the metric functions of a critical semiclassical star with $M/M_P = 10$ and $C(r_0) = 0.98$, far surpassing the Buchdahl limit. Note that, in this work, we take stars of such small sizes to simplify numerical analyses. Nonetheless, we checked that the interior properties of semiclassical stars do not suffer any qualitative modification for larger M/M_P ratios. Therefore, we can safely extrapolate the conclusions of this study to stars of astrophysical size.

As compactness is increased beyond $C(r_0) = 8/9$, the mass function $m(r) = \frac{r}{2}(1 - q(r)^{-1}) = \frac{r}{2}C(r)$ inside the stars solutions becomes increasingly negative. This effect is a direct consequence of the negative energy densities generated by the RSET, which grow in negativity as central pressures increase. All in all, semiclassical stars are a well-motivated extension of constant-density stars beyond their maximum compactness bound. Once vacuum polarization effects allow the Buchdahl threshold to be surpassed, we find no further compactness limits. In the upcoming sections we will explore the phenomenology associated to the propagation of test fields on these stars.

8.2 Critical solutions: Time domain analysis

In this section we study the time evolution of a test field in the spacetime described in Section 8.1. Since we are using a test-field approximation, we are neglecting any coupling between our perturbation field and the perturbations of the matter present in our spacetime. For uniform density stars in GR, the axial matter perturbations vanish [304–306], this means that test-field perturbations with $s = 2$ describe accurately the axial sector of gravitational waves. Since for compactness $C(r_0) < 8/9$ semiclassical corrections are perturbative, we expect the test field limit to be a good approximation also in the semiclassical case. For stars with $C(r_0) > 8/9$ instead, the RSET is non-negligible and the coupling between its perturbations and our field perturbation could lead to non-negligible

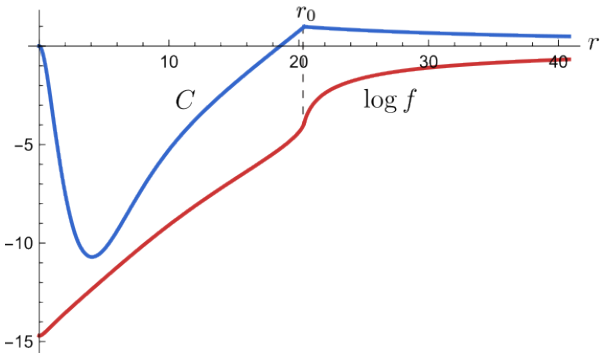

Figure 8.1: Numerical solution of a critical semiclassical star with $C(r_0) = 0.98$, $M/M_{\rm P} = 10, \rho = \rho_{\rm c} \simeq 0.00112 M_{\rm P}^{-2}$. The blue curve is the compactness function $C(r) = 1 - q(r)^{-1}$ and the red curve corresponds to $\log f(r)$. The stellar geometry is regular at $r = 0$, its surface is located at $r_0 \approx 20.42 M_{\rm P}$, and the spacetime for $r > r_0$ is very close to the Schwarzschild solution. The distinctive features of semiclassical stars are their negative mass interiors (recall that $C(r) = 2m(r)/r$) and their monotonously decreasing $f(r)$, which produces large redshifts on outgoing null rays.

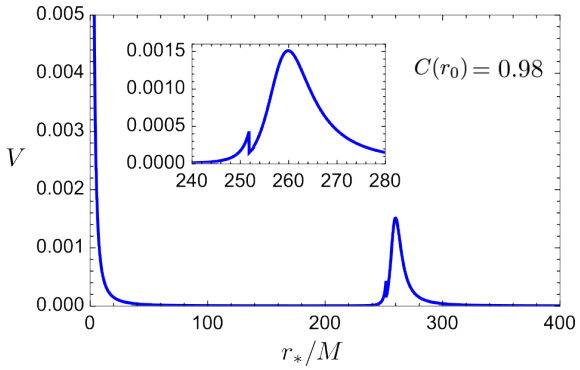

Figure 8.2: Potential of the test-field equation for $s = l = 2$ and compactness $C(r_0) = 0.98$. The inset is a zoom on the discontinuity of the potential at the star's surface. The finite jump in the potential indicates the position of the star surface. Such discontinuity is linked with the finite jump in ρ at the surface, and poses no problem for the numerical evolution of test fields.

corrections. Unfortunately, it is not possible at the moment to investigate this further since our RSET approximation corresponds to a vacuum-expectation value obtained under the assumptions of staticity and spherical symmetry, and is thus not adequate in time-dependent or non-spherical situations. However, we expect that our qualitative conclusions about test-field perturbations will be valid also for the true coupled gravitational fields.

We recall that, because of the spherical symmetry, we can decompose the field into the radial part and angular part, the latter being expressed in terms of spherical harmonics. Then the equation for the radial part of scalar, electromagnetic and gravitational test-field perturbations is [246, 247]:

$$\frac{\partial^2 \psi}{\partial t^2} - \frac{{\rm d}^2 \psi_s}{{\rm d} r_*^2} + V_s \psi_s = 0 \,, \tag{8.2.1}$$

where the tortoise coordinate r_* is defined as

$$dr_* = \sqrt{\frac{q}{f}}dr, \tag{8.2.2}$$

and s is the spin of the test-field, l is the harmonic index and the potential reads

$$V(r) = \frac{f(r)s(s-1)}{r^2 q(r)} + \frac{f(r)(l(l+1)-s(s-1))}{r^2} + \frac{(s-1)(q'(r)f(r)-q(r)f'(r)}{2rq(r)^2} \tag{8.2.3}$$

The shape of $V(r)$ is reported in Fig. 8.2 for a reference value of the compactness. We solved Eq. (8.2.1) using a fourth-order Runge–Kutta integrator and computing spatial derivatives with finite-difference approximation of second-order in accuracy. In the numerical simulation reported in this section we always consider an $l = 2$ quadrupolar mode and we use as initial condition for ψ a Gaussian pulse:

$$\psi(r,0) = \psi_0 \exp\left(-\frac{(r_* - r_*^c)^2}{2\varsigma^2}\right), \tag{8.2.4}$$

$$\frac{\partial\psi(r,0)}{\partial t} = -\psi_0 \frac{(r_* - r_*^c)}{\varsigma^2} \exp\left(-\frac{(r_* - r_*^c)^2}{2\varsigma^2}\right), \tag{8.2.5}$$

with central value $r_*^c = r_*(r^c) = r_*(250M)$ and width $\varsigma = 2M$; different initial values lead to similar results. The pulse is initially centered outside the peak of the potential $V(r)$, and moves inwards.

8.2.1 Time delay between echoes

For sufficiently compact semiclassical stars, as for every other ultra-compact object with an exterior region well-approximated by (or exactly described by) the Schwarzschild metric, the signal in time domain is given by an initial response pulse that is very similar (or identical) to the one expected from Schwarschild black holes followed by a series of echoes. As we already mentioned, the distance between them is given by the light-crossing time between the potential peak and the reflective boundary. In some models, the perturbation is assumed to be reflected at the surface of the object, leading to a logarithmic dependence of the light-crossing time (or time-delay) with the compactness $\sigma = C(r_0)^{-1} - 1$ (see Chapter 5 and Chapter 7). However, a complete reflection of gravitational waves at the surface is not realistic and one expects instead that the perturbation (or a part of it) can travel through the interior of the object. In spherical symmetry, this translates into a reflective boundary condition at the center $r = 0$.

In this case the full formula for the time delay between echoes (assuming a Schwarzschild exterior) is given by Eq. (5.2.2), that in terms of $C(r_0)$ reads

$$\Delta t_{\rm echo} = 2M - 4M(C(r_0)^{-1} - 1) - 4M \ln\left[2\left(C(r_0)^{-1} - 1\right)\right] + \Delta t_{\rm int}\,. \tag{8.2.6}$$

We recall that the first three terms on the r.h.s. are associated to the travelling time between the surface and the light ring while $\Delta t_{\rm int}$ is the travelling time to cross the star. Normally $\Delta t_{\rm int}$ has been neglected in the extant literature assuming a low curvature interior. However this is not the case for our semiclassical solutions where indeed in the

interior a very large (but finite) time delay is suffered by exiting waves. This can be easily seen by a direct calculation using the modified geometry.

The light-crossing time a light ray emanating from the photon sphere and getting reflected at $r = 0$ needs to reach the photon sphere back is

$$\Delta t_{\rm echo} = 2\int_0^{r_{\rm ph}} \sqrt{\frac{q}{f}}dr \tag{8.2.7}$$

When $f(0) \ll f(r_0)$ and f decreases monotonically towards the center, the dominant contribution to the crossing time comes from the large time delays suffered by light rays at the innermost regions of the star. This implies that the logarithmic dependence of the crossing time on $C(r_0)^{-1} - 1$ (that came exclusively from the exterior of the object) becomes a sub-leading contribution.

The magnitude of the time delay for the semiclassical star model depends on both the compactness $C(r_0)$ and the ratio $M/M_{\rm P}$ between the mass of the object and the Planck mass $M_{\rm P}$, which enters the solution through the renormalized stress-energy tensor. Semiclassical corrections introduce a new length scale that spoils the scale invariance of the classical solution.

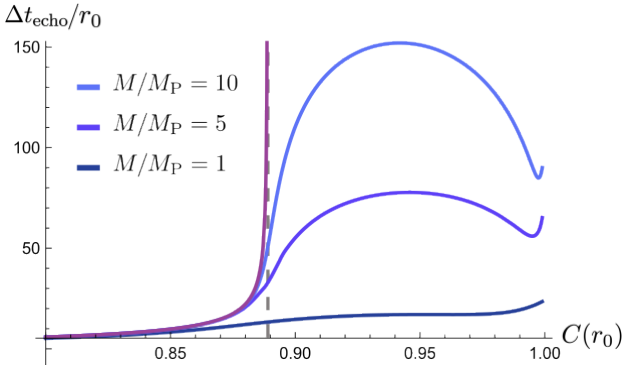

Figure 8.3: Light-crossing time in terms of the compactness for the classical constant density star (purple line) and semiclassical stars with $M/M_{\rm P} = \{10, 5, 1\}$ (blue lines from top to bottom, respectively). Semiclassical solutions are not scale invariant. The origin of the plateau reached by the light crossing time for sufficiently high compactness is discussed in the text.

Figure 8.3 displays the qualitative dependency of the crossing time on both compactness and scale separation. Regarding the dependence on the compactness, we observe an initial growth of the crossing time with $C(r_0)$ until a maximum value is reached, followed by a subsequent decrease. This behaviour is caused by the decrease of values of the functions q and f in the stellar interior as $C(r_0)$ increases. A Decrease in f leads to larger time delays, while a decrease in q can be linked to a shrinking of the proper volume. These effects are perceived by null rays and compensate themselves causing, beyond certain $C(r_0) > 8/9$ value, a decrease of the crossing time with the compactness.

Regarding the dependence on scale separation between the ADM mass and the Planck mass, considering the realistic case of a stellar mass object with $M/M_{\rm P} \gg 1$, we see that for low values of the compactness, $C(r_0) < 8/9$, the quantity $\Delta t_{\rm echo}/r_0$ approaches the classical solution value and is hence basically independent on $M/M_{\rm P}$. For very compact

objects, $C(r_0) > 8/9$, the crossing time $\Delta t_{\rm echo}/r_0$ grows instead linearly with $M/M_{\rm P}$. In between both regimes lies the separatrix $C(r_0) = 8/9$, for which $\Delta t_{\rm echo}/r_0 \propto (M/M_{\rm P})^{\alpha}$, with $\alpha \in (0, 1)$. These scalings are valid for all the three cases of sub-critical, critical and super-critical density. This scaling of the crossing time, as we will see below, has crucial implications for the observability of the echo signal.

Figure 8.4 shows three numerical integrations of Eq. (8.2.1) for stars with the same $M/M_{\rm P}$ and increasing compactness. As it is customary for exotic compact objects, the time delay between echoes grows with the compactness (although this is not always true, see Fig. 8.3), and they become clearly identifiable as isolated events when the star is super-Buchdahl. Because of the linear dependence of the time delay with M/M_p, after the initial black-hole like response, the subsequent echoes would suffer an extremely large time delay that would make them essentially impossible to identify as part of the original signal [294], at least for super-Buchdahl objects with masses much larger than the Planck mass.

Of course this is a feature of this particular model of semiclassical stars, already in the same semiclassical set-up it is possible to construct different models starting from classical matter fluids obeying other, more realistic equations of state instead of using the simple constant density profile. It is not clear yet if this particular scaling of the time delay found here will be shared by other models.

8.3 Critical solutions: Frequency domain analysis

We shall now move to study the same $s = 2$ test-field perturbations in the frequency domain. This means that we will solve Eq. (8.2.1) assuming an ansatz of the form

$$\psi(t, r) = e^{i\omega t}\phi(r), \tag{8.3.1}$$

where ϕ obeys the boundary conditions

$$\begin{aligned} &\phi \simeq e^{i\omega r}, \quad r \to \infty, \\ &\phi \simeq r^{1+l}, \quad r \to 0. \end{aligned} \tag{8.3.2}$$

Numerous methods have been developed for obtaining the quasinormal modes of black hole and stellar spacetimes (see [307, 308] and references therein), whose utility depends on the details of the system under consideration. Here, we implement the direct calculation developed by Chandrasekhar and Detweiler [309]. While its implementation is straightforward, this method suffers from instabilities that originate from a large sensitivity in the solution to the radius where the ingoing boundary conditions are imposed [310]. Despite its limitations, it is possible to generate reliable and precise results for the axial QNMs of semiclassical stars and to compare them with their classical counterparts. Throughout this section we take $M/M_{\rm P} = 1$.

For what regards the boundary conditions at large r, let us remember that our metric is characterized by the asymptotic behaviour set by the expansions (8.1.8). Henceforth,

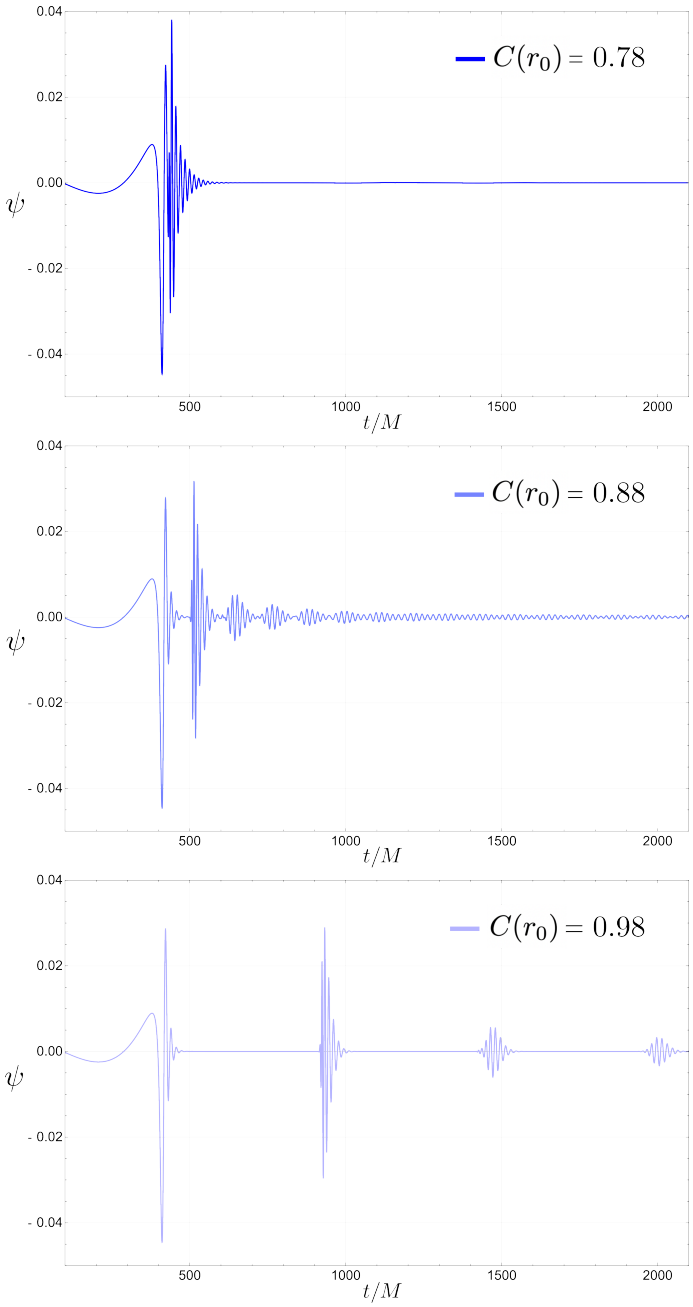

Figure 8.4: Signal received by an observer at $r = 250M$ outside a semiclassical star with $M/M_{\rm P} = 10$ for different values of the compactness $C(r_0)$. The initial signal is a Gaussian pulse centered outside the potential peak. We observe an initial Schwarzschild-like signal associated to the peak of the potential followed by a series of echoes, whose separation increases with the compactness.

for the ingoing mode we have assumed an asymptotic series solution of the form

$$\phi = e^{i\omega r}\left(\frac{r}{2M} - 1\right)^{2Mi\omega}\sum_{n=0}^{\infty}\frac{c_n}{r^n}, \tag{8.3.3}$$

and solved for the c_n coefficients order by order, so obtaining

$$c_1 = \frac{l\,(1+l)\,i}{2\omega} c_0,$$
$$c_2 = \frac{(1-l)\,l\,(1+l)\,(2+l) + 12Mi\omega}{8\omega^2} c_0, \tag{8.3.4}$$

as the lowest-order coefficients, with $c_0 = 1$.

At small r, the metric obeys instead the expansions (8.0.3) and we can then find the following series solution for the outgoing mode

$$\phi = r^l \sum_{m=1}^{\infty} d_m r^m, \tag{8.3.5}$$

where, for the lowest-order terms, we obtain

$$d_2 = 0, \quad d_3 = -\frac{\omega^2 + (f_2 - f_0 q_2 l)\,(2+l)}{2f_0\,(3+2l)} d_1,$$
$$d_4 = -\frac{-3f_3 + f_0 q_3\,(1+2l)}{12 f_0} d_1, \tag{8.3.6}$$

with $d_1 = 1$.

Using these boundary conditions, we shift the value of ω until we find the one that guarantees a vanishing of the Wronskian between the ingoing and outgoing modes at some radius $r_{\rm m} > r_0$. In this way, we obtained the fundamental frequency of the $l = 2$ mode and observed how its value changes with the compactness. Figures 8.5 and 8.6 show the real part and the logarithm of the imaginary part of the fundamental QNMs frequency, respectively. The corresponding values of the classical, constant density solution are shown for comparison. We have tested our method comparing with the results in [305] for constant density stars. For classical stars, we observe a drop in the accuracy of the method as we approach the Buchdahl limit, but the values for the QNMs frequencies of the last two points shown in Figs. 8.5 and 8.6 are nonetheless accurate within one order of magnitude. For semiclassical stars, the QNMs frequency values obtained are accurate at least to three decimal places under changes in the matching radius $r_{\rm m}$ in the entire range of compactness values explored.

It is easy to see that the QNMs frequencies of the classical and semiclassical solutions are characterized by quite distinct behaviours. In the first case, both ω_R and ω_I tend to 0 in the Buchdahl limit. This behaviour is associated to the divergence of the crossing time in this limit, which produces an infinite time delay between echoes [294]. In the semiclassical solution, however, the QNMs frequencies start departing from their classical counterparts as the Buchdahl limit is approached, since in proximity of such limit semiclassical effects become relevant. As discussed, the latter also lead to a breakdown of scale invariance introducing a dependence of the frequencies on $M/M_{\rm P}$. Finally, let us notice that between the Buchdahl and the black hole limits, axial QNMs frequencies reach a plateau, not increasing significantly. We have not explored what happens in the $C(r_0) \to 1$ limit since the features of the solutions in this regime rely strongly on the details of the approximation adopted for the RSET.

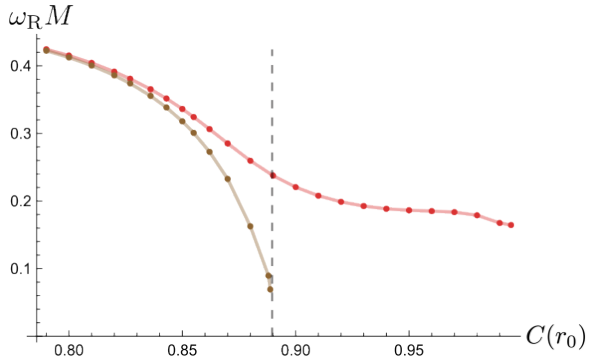

Figure 8.5: Real part of the QNMs frequencies in terms of the compactness for the classical and semiclassical models (brown and red, respectively). The classical frequencies approach 0 in the Buchdahl limit, while the semiclassical ones have finite values in all the range $C(r_0) < 1$. We have taken $M = M_{\mathrm{P}} = 1$.

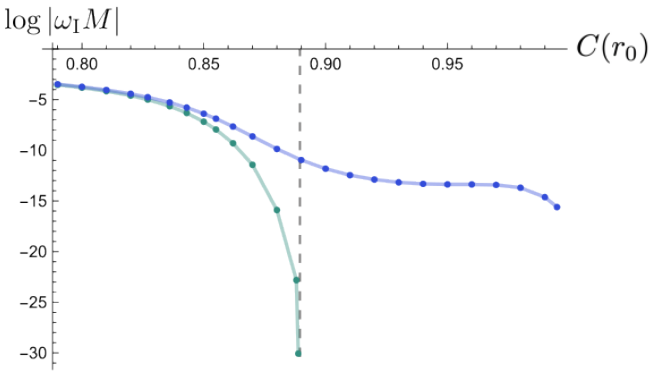

Figure 8.6: Logarithm of the imaginary part of the QNMs frequencies in terms of the compactness for the classical and semiclassical models (green and blue, respectively). The classical frequencies approach 0 in the Buchdahl limit, while the semiclassical ones have finite values in all the range $C(r_0) < 1$. The presence of small imaginary part is indicative of long-lived modes and potential non-linear instabilities [311]. Notice the similarity in behaviour with respect to the real parts in Fig. 8.5. We have taken $M = M_{\mathrm{P}} = 1$.

8.4 Sensitivity to the internal properties of compact objects

Phenomenological studies of black hole mimickers spacetimes attempt to be agnostic about the interior properties of such objects by imposing a (partial or total) reflective boundary condition at their surface [312–314]. This restricts echoes and, in general, the ringdown signal, to be only probes of the spacetime geometry between the surface and the light ring. However, it is clear that a more physical scenario would allow for perturbations to travel through the entire object, and consequently to carry out information about its internal structure. For a spherically symmetric spacetime this assumption would translate into reflective boundary conditions being imposed at the center of the object rather than at its surface. Remarkably, by doing so, the ringdown signal becomes also a probe of the innermost regions where quantum effects are expected to be stronger.

In this section we compare the phenomenology of compact objects with the same exterior spacetime but different central regions, showing that echoes and QNMs are indeed sensitive to the internal structure and hence indirectly to the quantum effects avoiding singular behaviours at the object core. As particular examples, we take a sub-family of semiclassical stars with increasing classical energy density and the Dymnikova metric.

8.4.1 Super-critical semiclassical stars

For a star of a given mass M and compactness $C(r_0)$, the semiclassical stellar equations (8.1.5, 8.1.6) allow to freely adjust the value of the classical density ρ_0. In previous sections, all our considerations have been restricted to critical solutions, i.e., those with $\rho_0 = \rho_c$ (see Table 8.1), for which the central pressure is a global maximum and the region near $r = 0$ is of the AdSl type. By taking $\rho_0 > \rho_c$, we can generate regular stellar solutions of the same mass and compactness, but whose central pressure has a local minimum at the center, this feature being reproduced by cores of the dSl type.

Figures 8.7 and 8.8 show respectively the interior metric function $f(r)$ and $C(r) = 1 - q(r)^{-1}$ for several super-critical solutions. Note that all super-critical solutions have an identical vacuum exterior and only differ in their interior properties.

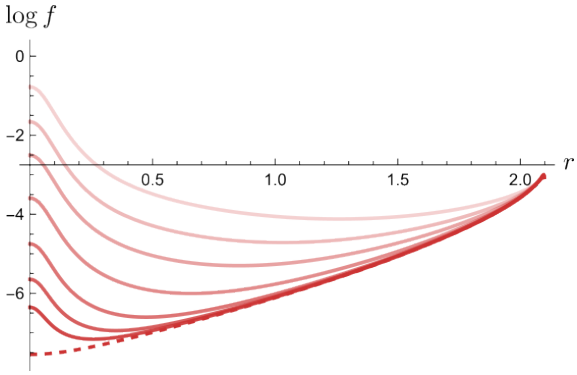

Figure 8.7: Logarithm of the redshift function f in terms of the radius for stars with $M = M_P = 1$ and $C(r_0) = 0.99$. The dashed line denotes the critical solution with $\rho_c \simeq 0.055 M_P^{-2}$. From darker to lighter shades, the curves correspond to super-critical solutions with $\rho_0/\rho_c = \{1.001, 1.004, 1.015, 1.04, 1.1, 1.25, 1.6\}$. Increasing ρ_0 diminishes the redshift suffered by light rays at the center appreciably.

Although there is no change in the position of the outer light ring, the modification of the stellar interior affects the crossing time (hence the time delay between echoes) as well as the QNMs frequencies. Particularly, the crossing time diminishes as ρ_0 increases (Fig. 8.9), while the QNMs frequencies increase (Figs. 8.10 and 8.11).

Indeed, inserting expansions (8.0.3) in the potential (8.2.3) for $s = 2$, $l = 2$, we have

$$V = \frac{6 f_0}{r^2} + O(r^0), \tag{8.4.1}$$

hence different densities correspond to different values of f_0, meaning changes in the slopes of the centrifugal barrier at $r = 0$ that, as we see in Fig. 8.12, affect the phase of the echoes and cause a slightly different modulation of their amplitude with time.

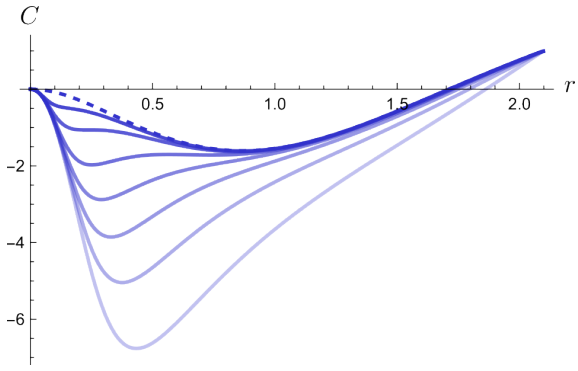

Figure 8.8: Compactness function $C(r)$ in terms of the radius for stars with $M = M_{\rm P} = 1$ and $C(r_0) = 0.99$. The dashed line denotes the critical solution with $\rho_{\rm c} \simeq 0.055 M_{\rm P}^{-2}$. From darker to lighter shades, the curves correspond to super-critical solutions with $\rho_0/\rho_{\rm c} = \{1.001, 1.004, 1.015, 1.04, 1.1, 1.25, 1.6\}$. Increasing ρ_0 generates a deeper and broader negative mass interior.

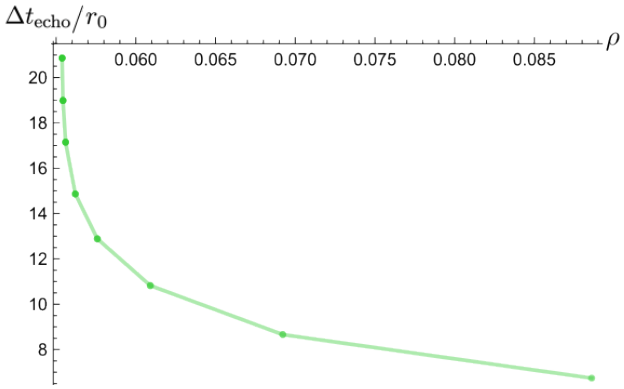

Figure 8.9: Light-crossing time in terms of the density of super-critical solutions with $M = M_{\rm P} = 1$ and $C(r_0) = 0.99$. As the star becomes super-critical, the crossing time decreases appreciably. This behaviour affects the QNMs frequencies, increasing their values with ρ (see Figs. 8.10 and 8.11).

8.4.2 Dymnikova's model

The Dymnikova metric [80, 315] is one of the simply connected, spherically symmetric regular models introduced in Table 3.1.

The line element of this model can be written in the same form of Eq. 8.0.1 with

$$f(r) = 1 - \frac{2m(r)}{r}, \qquad q(r) = 1/f(r)\,, \qquad \text{and} \quad m(r) = M\left[1 - \exp(-\frac{r^3}{2M\ell^2})\right]\,. \tag{8.4.2}$$

Note that, for this model, the range of possible scale separations between M and the regularization parameter ℓ is limited. Indeed, as anticipated, if ℓ/M is too small the metric presents a pair of horizons (as it is indeed a regular black hole), and if ℓ/M is too big the object has no light rings. For this reason the range of parameters for which echoes appear is restricted.

The exterior solution of the Dymnikova's model closely resembles the one of our semi-

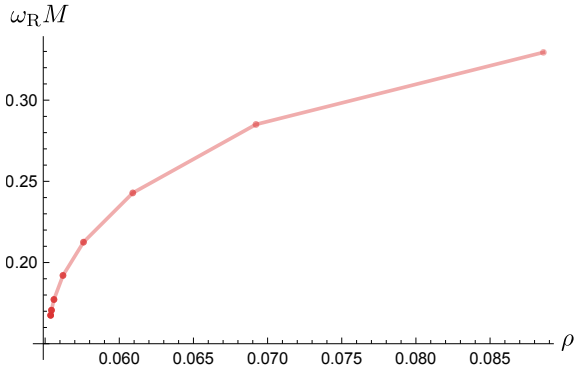

Figure 8.10: Real part of the $l = 2$ fundamental QNMs frequencies for super-critical solutions with $M = M_P = 1$ and $C(r_0) = 0.99$. The frequency values increase with ρ, similarly to the logarithm of the complex part of the QNMs frequency and the inverse of the crossing time (see Figs. 8.11 and 8.9)

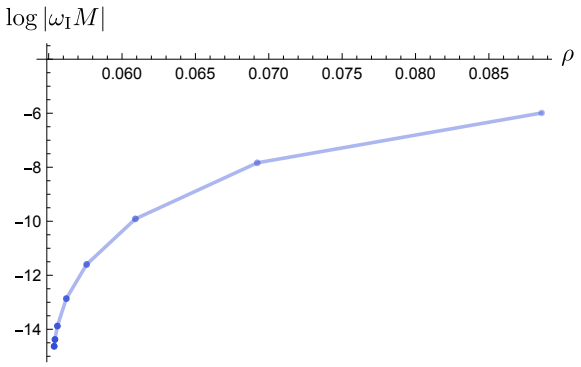

Figure 8.11: Logarithm of the complex part part of the $l = 2$ fundamental QNMs frequencies for super-critical solutions with $M = M_P = 1$ and $C(r_0) = 0.99$. The frequency values increase with ρ in a tendency very similar to the real part of the frequency and the inverse of the crossing time (see Figs. 8.10 and 8.9).

classical model. Both models have nearly the same outer light ring and innermost stable circular orbit position, and the potential for test-field perturbations shares the same shape from the neighborhood of the light ring to infinity. However, the interior region is quite different. Near the center, Dymnikova's metric exhibits a strictly de-Sitter core and the potential for test-field perturbations has a different shape (w.r.t. the semiclassical star) especially near $r = 0$ (see Eq. (8.4.1)).

As a further tests of the sensitivity of echos to the internal structure of the ultra-compact star we can compare the Dymnikova model with semiclassical star solutions characterized by the same light-crossing time between the unstable light ring and the center, i.e. having by construction the same time delay between echoes. Nonetheless, as shown in Fig. 8.12, one can see that the time-domain signal coming from stars with different densities presents some differences within them and with Dymnikova's model. Indeed, signals coming from different models present slightly different modulations in amplitude and very different phases that are due, mainly, to the discrepancies in their potential barrier near $r = 0$.

We therefore conclude that black hole mimickers spacetimes with similar exterior ge-

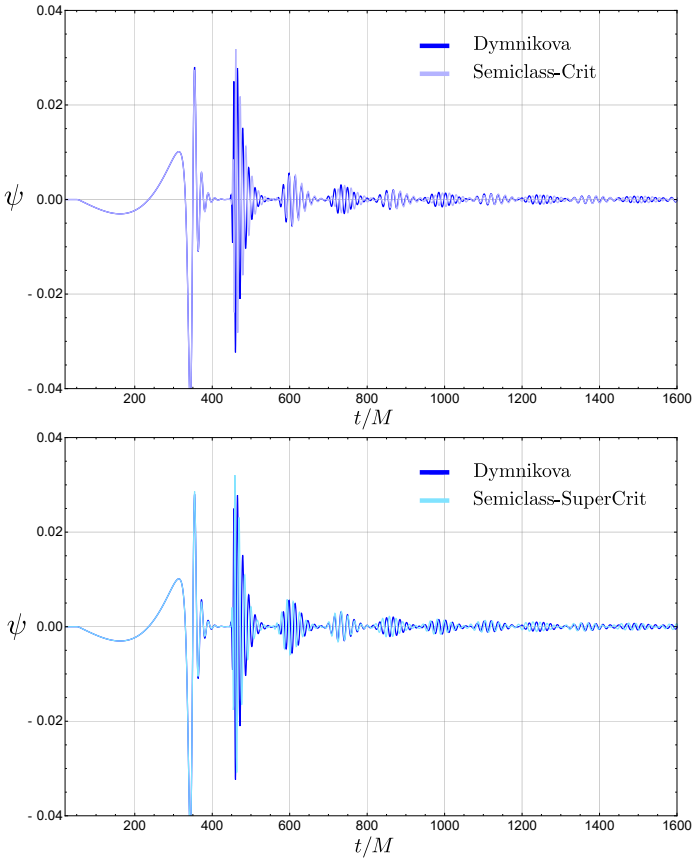

Figure 8.12: Comparison between signals received by an observer at $r = 250M$ outside objects with similar exterior spacetime but different central region and $M/M_{\rm P} = 10$. The initial signal is a gaussian pulse centered outside the potential peak. The Dymnikova model with $\ell = 1.15M$ is compared with semiclassical stars with critical density ρ_c in the upper panel and with super-critical density $\rho = 1.026679\rho_c$ in the bottom panel. These values of ℓ and ρ are chosen in order to have the same Δt_{echo} for the three analysed solutions. In both cases we can note a slight difference in the modulation of the amplitude and a different phase between the two signals. This is due to the slightly different trend of the potential in the region near $r = 0$.

ometry, i.e. nearly sharing the same position for the external light ring, but differing in their interior properties will still produce different ringdown signals. Indeed, this realization can be seen as the ultra-compact star analogue of the even more striking one that regularizations of black hole cores lead to solutions which generically have (even if possibly just slightly) different exteriors w.r.t. the singular solutions of GR (at least modulo nonphysical ad hoc constructions).

8.4.3 Echoes and the stable lightring

We have observed that echoes signal strongly depends on the internal structure of the object. This is because this part of the waveform is associated with the slow leakage of perturbations from the region between the unstable light ring and the central centrifugal barrier (where a stable light ring must always be present [316, 317]). This same process leads to the appearance of long-living modes in the QNMs spectrum, which are considered

indicative of non-linear instabilities [137, 316]. These instabilities appear to be confirmed in some specific models by numerical simulations [140].

Typically, these concerns are not associated with the presence of echoes in the signal. However, it is worth stressing that echoes are the time-domain counterpart of the aforementioned long-living modes and can indeed be reconstructed using the first few overtones [318], with the late-time part of the echo signal being dominated by the fundamental modes. Therefore, it is not surprising that a careful analysis of the echo scenario also leads to the conclusion that non-linear effects and backreaction must play an important role as we explained in Chapter 7.

It is important to note that the long-living modes forming the late part of the echoes signal are due to the extended time required for perturbations to travel several times between the unstable light ring and the reflective barrier. Thus, they can lead to instability only in the case of a sustained continuous flux of perturbations, allowing for a, possibly destabilizing, *accumulation* of energy in the region between the unstable light ring and the reflective barrier.

Finally, we emphasize that while the extremely long time delay between echoes and their consequently probable unobservability (discussed in section 8.2) is a model-dependent feature, the presence of a stable light ring and the consequent semi-trapping of perturbations leading to the appearence of long-living modes is a universal feature of horizonless objects and a necessary condition for the emission of echoes. Therefore, studying the ringdown in a fully non-linear regime would be very useful to understand if we can truly observe echoes and thus probe the innermost regions of these objects.

8.5 Conclusions

In this work, we studied the ringdown signal produced by semiclassical stars, which are regular stellar solutions to the Einstein equations incorporating the expectation value in the Boulware vacuum (the natural vacuum in stellar spacetimes) of the renormalized stress-energy tensor. A distinctive feature of these stars is that the backreaction of vacuum polarization effects allows for the existence of regular stars surpassing the Buchdahl limit. Consequently, they can serve as a novel family of black hole mimickers without requiring new physics beyond GR and quantum field theory in curved spacetimes.

The exterior of these objects corresponds to a perturbatively-corrected Schwarzschild spacetime, maintaining the same asymptotically flat behavior at large distances up to some surface $r = r_0$. However, in the interior region $r < r_0$, if the star's compactness surpasses the Buchdahl limit, the spacetime is significantly modified by semiclassical corrections.

Notably, by varying their compactness $C(r_0)$ and their classical surface density ρ_0, we can modify the internal region of these stars without changing the exterior. This means that the position of the outer light ring and the innermost stable circular orbit remain the same as in the Schwarzschild black hole (up to $O(M_{\rm P}^2)$ corrections). This allowed us to investigate the extent to which the ringdown signal is sensitive to the internal structure of black hole mimickers.

Our time-domain analysis shows that the initial part of the signal is identical to that produced by a Schwarzschild black hole[1], information about the object being a black

[1]This is because the exterior spacetime of semiclassical stars is almost identical to the Schwarzschild

hole mimicker is only carried by the subsequent echoes. Furthermore, we observed that increasing the compactness of the object generally results in echoes being further separated and individually resolved. However, for sufficiently compact objects, the crossing time can decrease with compactness (see Fig. 8.3).

The latest part of the echo signal is dominated by the long-living fundamental QNMs frequencies, which are highly sensitive to the features of the interior metric. We varied these features by increasing the compactness of critical solutions (Figs. 8.5, 8.6) and by exploring super-critical solutions with the same $C(r_0)$ but different ρ_0 (Figs. 8.9, 8.10, 8.11). From our analysis, we conclude that echoes unmistakably carry information about the internal properties of these objects, making even more pressing the question of whether such echoes are truly observable.

We have shown that if perturbations can travel through the object's interior, the time-delay between echoes depends on both the compactness of the object and its internal structure. It also crucially depends on the ratio between the ADM mass M and the Planck mass. For super-Buchdahl stars ($C(r_0) > 8/9$), the ratio $\Delta t_{\rm echo}/r_0$ increases linearly with the quotient $M/M_{\rm P}$, making echoes essentially unobservable for stellar-sized objects. For example, with $C(r_0) \approx 0.90$, values of $\Delta t_{\rm echo}$ of the order of seconds — that might lead to detectable echoes — are possible only for $M \approx 10^{21} M_{\rm P}$, or roughly 10^{-17} solar masses. For a stellar mass object, the part of the signal that crosses the exterior potential barrier and travels towards the object's interior would, in practice, be frozen forever.

Nonetheless, possible mechanisms for observable echoes from such semiclassical stars could include partial reflections at their surface [319, 320] or ringdown signals from extremely light primordial objects [321, 322] or morsels formed during binary mergers [323]. Also, it might be possible to find other observables sensitive to the internal structure of these semiclassical stars, for example in the inspiral-merger part of the signals. We plan to investigate these issues in future work.

It is important to stress that the extremely delayed echo signals here found, could be just a feature of this particular model, where semiclassical effects break the scale invariance of the classical uniform-density solution. Within the same semiclassical framework, other models can be constructed starting from different classical stress-energy sources. For example, the approximations used for the RSET can be applied to fluids with barotropic equations of state [39]. Investigating whether echoes are extremely delayed and thus unobservable also in these other models would be a desirable analysis to carry on in the future.

Another aspect, not considered in this study, is the effect of matter on the signal, as we analyzed test-field perturbations. In the axial sector, classical matter perturbations vanish, but the RSET is non-zero (albeit small) even outside the star's surface, potentially affecting the initial part of the ringdown signal through interactions with quantum matter. Trust in the results obtained with test field perturbations follows from such effects being of $O(M_{\rm P}^2)$.

Finally, despite these various possible future lines of investigation, we want to emphasize a key takeaway from our study of this specific class of semiclassical ultra-compact stars: they provide us with the general lesson that the core of these exotic objects does

spacetime, for some other BH mimickers models, as the Bardeen or Hayward metrics (Table 3.1), the exterior spacetime is slightly different and so is the initial ringdown signal.

matter and that once propagation inside the star core is considered, short-delayed (and potentially observable) echoes are no longer guaranteed. We can see this conclusions "as a curse and a blessing": on the downside, it is evident that testing these objects via echoes will require in the future an in-depth analysis based on the specific exotic star model. On the upside, if such analysis will yield promising results for phenomenology, it will open the door to finally testing quantum gravity effects — hidden in the core of such objects — by observing gravitational waves. Only time will tell.

Part V

Final remarks

This thesis dealt with the construction and phenomenological investigation of regular effective models for describing the early universe and the dark compact objects that we observe in the sky.

We saw that under the reasonable assumptions of this work I, the regularization of cosmological and black holes singularities can be realized through a limited number of local geometries. In the case of a spherical symmetrical black hole, the regularization can lead to simply connected geometries presenting at least an additional inner horizon or to multiple connected geometries presenting an hidden wormhole throat. In the case of an homogeneous and isotropic cosmological spacetime, the regularization can only result in simply connected geometries: a bouncing universe (where the scale factor reaches a minimum in the past before re-expanding), an emergent universe (where the scale factor reaches and maintains a constant value in the past), and asymptotically emergent universe (where the scale factor diminishes continually, asymptotically approaching a constant value in the past). This analysis of cosmological spacetimes has been particularly interesting because of the different symmetries and time-dependence of the considered scenario, indeed in an expanding universe the trapping and defocusing of geodesics are more delicate concepts to study. This analysis opens the path to the study of the regularization of less symmetric time-dependent geometries like rotating black holes.

Then, we saw how it is possible to construct specific examples of metrics that embody these regularizations. For the black hole case, it is also possible to add rotation to these metrics through the so called Newman-Janis procedure. However the rotating simply connected regular black holes present in literature exhibit several issues. In particular, presenting an inner horizon, they are plagued by the mass inflation instability that is an unbounded growth of perturbations near this horizon. At classical level the time-scale of this instability is determined by the inner horizon's surface gravity. We presented a new rotating regular black hole whose inner horizon has zero surface gravity for any value of the

spin parameter, and is therefore stable against classical mass inflation. To construct it we combined two successful strategies for regularizing black holes metrics, i.e. we replaced the mass parameter with a function of the radius to stabilize the inner horizon and we introduce a conformal factor to regularize the singularity. Our metric depends on a total of four real parameters: the ADM mass M , the spin a, the conformal parameter b and the deviation parameter e. The two additional parameters b and e can be constrained by observations since they affect the multipolar structure of the object and the orbits of massless and massive test particles. Given that the conformal and Kerr-deviation parameters might be directly related to quantum-gravitational effects, the possibility to constrain them via observations on the exterior geometry of the BH is further evidence that a new window for quantum-gravity phenomenology might be opening via astrophysical observations.

In general, the possibility to test new (quantum) physics beyond GR through observations is analysed in the last part of this thesis, that is dedicated to the phenomenology of BH mimickers. In particular, we focused on the study of the ringdown signal emitted by such objects.

We studied test-field and gravitational perturbations on two spherically symmetric regular metrics, each representing an example of one of the two possible families of black hole mimickers: the Bardeen metric, which is part of the simply-connected family and interpolates between a multiple horizon black hole and an exotic compact star; and the SV metric, which is part of to the multiple-connected family and interpolates between an hidden wormhole and a traversable wormhole. For both families of regular models, in the horizonless branch, we found long living modes whose damping time grows exponentially with the harmonic index l and is longer for more compact configurations. These modes are associated with the presence of a stable photon sphere in these spacetime and are usually considered a hint for non-linear instability. In general our analysis demonstrates that there are deviations of the QNMs spectrum of these spacetimes from that of a Schwarzschild BH. We analysed the possible detectability of these deviations in the observed gravitational-wave ringdown signals using the Parspec framework [208]. The detectability of such deviations depends on several aspects such as: the number of observations, their SNR and obviously the size of the regularization parameter entering the metric functions. We showed that these deviations should be detectable with the next generation of GWs detectors for macroscopic values of the regularizing parameter. This analysis in only preliminary and we plan to extend it in several ways: using corrections at higher order in the spin, using a more realistic binary population for the sources, and treating also the final mass and spin of the remnant as unknown parameters.

For horizonless mimickers, an additional signal is expected to be emitted after the prompt ringdown. This consists of a series of secondary pulses with progressively smaller amplitude and lower frequency content, called echoes. Echoes are caused by the slowly leaking out of perturbations semi-trapped between the photon sphere and a reflective barrier at the center or the surface of the object. Usually echoes are studied in linear approximation, we discussed the possible effect of back-reaction on this part of the signal. Firstly, we have let the central compact object absorb part of the incoming radiation, resulting in an increase in its mass and leading to changes in the spacetime in which the perturbation propagates. The most important effect of this on the echo waveform is the loss of the quasi-periodicity of the signal. Indeed, the absorption of each echo changes the

mass and thus the compactness of the object, and as a result, it increases the time delay among echoes which depends logaritmically on the compactness. Apart from this simple scenario, we also consider the case in which, in order to preserve its compactness above the black hole limit, the compact object absorption shuts down in a finite amount of time or leads to an expansion. In both these cases we find interesting new features that should be taken into account in future searches. Indeed, the strategies adopted in these searches are usually based on the quasi-periodicity of the echoes signal, a feature that we showed can be partially lost in more realistic scenarios.

Finally we investigated the sensitivity of the ringdown singal to the structure of the innermorst region of the emitting object. For this purpose, we focused on a particular class of static and spherically symmetric exotic compact objects, denominated semiclassical stars [38, 39]. Such solutions are particular suitable for this analysis since they exhibit an (approximately) Schwarzschild exterior together with a modified interior composed of a constant-density classical fluid and the cloud of vacuum polarization generated by the star itself. By varying their classical density, it is possible to modify the interior metric without affecting the exterior.

Often, gravitational perturbations are considered to be reflected at the surface of the compact objects. This restricts echoes and, in general, the ringdown signal, to be only probes of the spacetime geometry near the light ring. If instead gravitational perturbations are assumed to travel thorough the interior object, we found that the echoes signal appears to be very sensitive to the structure of the innermost region of the mimicker, a region where we expect new physics effects to dominate. For the specific model of stellar-sized semiclassical stars, we even found that the interior travel time is sufficiently prolonged to render the echoes effectively unobservable. This analysis makes evident that, even if the emission of observable echoes is not guaranteed for every horizonless mimickers, its potential detection could enable us to explore new (quantum) physics hidden in the core of such objects.

The different investigations presented here, despite their specific focus, provide us with several general insights. These can be summarized in the final message that probing new physics responsible for the putative regularization of spacetime singularities is certainly possible but not guaranteed. Without even thinking about technical or environmental issues [324], the regularization itself could be at the moment inaccessible to us even in principle. As instance, a planckian regularization parameter for our effective models could lead to a ringdown indistinguishable from the one expected from singular BHs and to extremely delayed, unobservable echoes.

The author's opinion is that, despite these uncertainties, it is not only valuable but even necessary to continue perusing the path of quantum gravity phenomenology and the search for new physics in the signal coming from extreme gravitational phenomena. Indeed, at the moment, it represents, if not the most promising, at least one of the very few instruments we have to provide guidance out of the current crisis of fundamental physics.

The author remains hopeful that one day, not too far in the future, we will be able to glimpse the imprints of quantum effects in the GWs signals coming from the merger of compact objects, opening the world to the era of quantum gravity.

Bibliography

[1] B. P. Abbott et al. "Observation of Gravitational Waves from a Binary Black Hole Merger". In: *Phys. Rev. Lett.* 116.6 (2016), p. 061102. DOI: 10.1103/PhysRevLett.116.061102. arXiv: 1602.03837 [gr-qc].

[2] B. P. Abbott et al. "Gravitational Waves and Gamma-rays from a Binary Neutron Star Merger: GW170817 and GRB 170817A". In: *Astrophys. J. Lett.* 848.2 (2017), p. L13. DOI: 10.3847/2041-8213/aa920c. arXiv: 1710.05834 [astro-ph.HE].

[3] B. P. Abbott et al. "Multi-messenger Observations of a Binary Neutron Star Merger". In: *Astrophys. J. Lett.* 848.2 (2017), p. L12. DOI: 10.3847/2041-8213/aa91c9. arXiv: 1710.05833 [astro-ph.HE].

[4] B. P. Abbott et al. "GW170817: Observation of Gravitational Waves from a Binary Neutron Star Inspiral". In: *Phys. Rev. Lett.* 119.16 (2017), p. 161101. DOI: 10.1103/PhysRevLett.119.161101. arXiv: 1710.05832 [gr-qc].

[5] Kazunori Akiyama et al. "First M87 Event Horizon Telescope Results. I. The Shadow of the Supermassive Black Hole". In: *Astrophys. J. Lett.* 875 (2019), p. L1. DOI: 10.3847/2041-8213/ab0ec7. arXiv: 1906.11238 [astro-ph.GA].

[6] Kazunori Akiyama et al. "First M87 Event Horizon Telescope Results. II. Array and Instrumentation". In: *Astrophys. J. Lett.* 875.1 (2019), p. L2. DOI: 10.3847/2041-8213/ab0c96. arXiv: 1906.11239 [astro-ph.IM].

[7] Kazunori Akiyama et al. "First M87 Event Horizon Telescope Results. III. Data Processing and Calibration". In: *Astrophys. J. Lett.* 875.1 (2019), p. L3. DOI: 10.3847/2041-8213/ab0c57. arXiv: 1906.11240 [astro-ph.GA].

[8] Kazunori Akiyama et al. "First M87 Event Horizon Telescope Results. IV. Imaging the Central Supermassive Black Hole". In: *Astrophys. J. Lett.* 875.1 (2019), p. L4. DOI: 10.3847/2041-8213/ab0e85. arXiv: 1906.11241 [astro-ph.GA].

[9] Kazunori Akiyama et al. "First M87 Event Horizon Telescope Results. V. Physical Origin of the Asymmetric Ring". In: *Astrophys. J. Lett.* 875.1 (2019), p. L5. DOI: 10.3847/2041-8213/ab0f43. arXiv: 1906.11242 [astro-ph.GA].

[10] Kazunori Akiyama et al. "First M87 Event Horizon Telescope Results. VI. The Shadow and Mass of the Central Black Hole". In: *Astrophys. J. Lett.* 875.1 (2019), p. L6. DOI: 10.3847/2041-8213/ab1141. arXiv: 1906.11243 [astro-ph.GA].

[11] Kazunori Akiyama et al. "First M87 Event Horizon Telescope Results. VII. Polarization of the Ring". In: *Astrophys. J. Lett.* 910.1 (2021), p. L12. DOI: 10.3847/2041-8213/abe71d. arXiv: 2105.01169 [astro-ph.HE].

[12] Kazunori Akiyama et al. “First M87 Event Horizon Telescope Results. VIII. Magnetic Field Structure near The Event Horizon”. In: *Astrophys. J. Lett.* 910.1 (2021), p. L13. DOI: 10.3847/2041-8213/abe4de. arXiv: 2105.01173 [astro-ph.HE].

[13] Kazunori Akiyama et al. “First Sagittarius A* Event Horizon Telescope Results. I. The Shadow of the Supermassive Black Hole in the Center of the Milky Way”. In: *Astrophys. J. Lett.* 930.2 (2022), p. L12. DOI: 10.3847/2041-8213/ac6674. arXiv: 2311.08680 [astro-ph.HE].

[14] Kazunori Akiyama et al. “First Sagittarius A* Event Horizon Telescope Results. II. EHT and Multiwavelength Observations, Data Processing, and Calibration”. In: *Astrophys. J. Lett.* 930.2 (2022), p. L13. DOI: 10.3847/2041-8213/ac6675. arXiv: 2311.08679 [astro-ph.HE].

[15] Kazunori Akiyama et al. “First Sagittarius A* Event Horizon Telescope Results. III. Imaging of the Galactic Center Supermassive Black Hole”. In: *Astrophys. J. Lett.* 930.2 (2022), p. L14. DOI: 10.3847/2041-8213/ac6429. arXiv: 2311.09479 [astro-ph.HE].

[16] Kazunori Akiyama et al. “First Sagittarius A* Event Horizon Telescope Results. IV. Variability, Morphology, and Black Hole Mass”. In: *Astrophys. J. Lett.* 930.2 (2022), p. L15. DOI: 10.3847/2041-8213/ac6736. arXiv: 2311.08697 [astro-ph.HE].

[17] Kazunori Akiyama et al. “First Sagittarius A* Event Horizon Telescope Results. V. Testing Astrophysical Models of the Galactic Center Black Hole”. In: *Astrophys. J. Lett.* 930.2 (2022), p. L16. DOI: 10.3847/2041-8213/ac6672. arXiv: 2311.09478 [astro-ph.HE].

[18] Kazunori Akiyama et al. “First Sagittarius A* Event Horizon Telescope Results. VI. Testing the Black Hole Metric”. In: *Astrophys. J. Lett.* 930.2 (2022), p. L17. DOI: 10.3847/2041-8213/ac6756. arXiv: 2311.09484 [astro-ph.HE].

[19] M. Punturo et al. “The Einstein Telescope: A third-generation gravitational wave observatory”. In: *Class. Quantum Grav.* 27 (2010). Ed. by Fulvio Ricci, p. 194002. DOI: 10.1088/0264-9381/27/19/194002.

[20] Marica Branchesi et al. “Science with the Einstein Telescope: a comparison of different designs”. In: *JCAP* 07 (2023), p. 068. DOI: 10.1088/1475-7516/2023/07/068. arXiv: 2303.15923 [gr-qc].

[21] Vicky Kalogera et al. “The Next Generation Global Gravitational Wave Observatory: The Science Book”. In: (Nov. 2021). arXiv: 2111.06990 [gr-qc].

[22] Michele Maggiore et al. “Science Case for the Einstein Telescope”. In: *JCAP* 03 (2020), p. 050. DOI: 10.1088/1475-7516/2020/03/050. arXiv: 1912.02622 [astro-ph.CO].

[23] David Reitze et al. “Cosmic Explorer: The U.S. Contribution to Gravitational-Wave Astronomy beyond LIGO”. In: *Bull. Am. Astron. Soc.* 51.7 (2019), p. 035. arXiv: 1907.04833 [astro-ph.IM].

[24] B. Sathyaprakash et al. "Scientific Objectives of Einstein Telescope". In: *Class. Quant. Grav.* 29 (2012). Ed. by Mark Hannam et al. [Erratum: Class.Quant.Grav. 30, 079501 (2013)], p. 124013. DOI: 10.1088/0264-9381/29/12/124013. arXiv: 1206.0331 [gr-qc].

[25] Pau Amaro-Seoane et al. "Laser Interferometer Space Antenna". In: (Feb. 2017). arXiv: 1702.00786 [astro-ph.IM].

[26] K. G. Arun et al. "New horizons for fundamental physics with LISA". In: *Living Rev. Rel.* 25.1 (2022), p. 4. DOI: 10.1007/s41114-022-00036-9. arXiv: 2205.01597 [gr-qc].

[27] Enrico Barausse et al. "Prospects for Fundamental Physics with LISA". In: *Gen. Rel. Grav.* 52.8 (2020), p. 81. DOI: 10.1007/s10714-020-02691-1. arXiv: 2001.09793 [gr-qc].

[28] Eric Poisson. *A Relativist's Toolkit: The Mathematics of Black-Hole Mechanics*. Cambridge University Press, Dec. 2009. DOI: 10.1017/CBO9780511606601.

[29] Robert M. Wald. *General Relativity*. Chicago, USA: Chicago Univ. Pr., 1984. DOI: 10.7208/chicago/9780226870373.001.0001.

[30] Roger Penrose. "Gravitational collapse and space-time singularities". In: *Phys. Rev. Lett.* 14 (1965), pp. 57–59. DOI: 10.1103/PhysRevLett.14.57.

[31] S. W. Hawking and R. Penrose. "The Singularities of gravitational collapse and cosmology". In: *Proc. Roy. Soc. Lond. A* 314 (1970), pp. 529–548. DOI: 10.1098/rspa.1970.0021.

[32] Raúl Carballo-Rubio et al. "Geodesically complete black holes". In: *Phys. Rev. D* 101 (2020), p. 084047. DOI: 10.1103/PhysRevD.101.084047. arXiv: 1911.11200 [gr-qc].

[33] Carlos Barceló, Raúl Carballo-Rubio, and Luis J. Garay. "Mutiny at the white-hole district". In: *Int. J. Mod. Phys. D* 23.12 (2014), p. 1442022. DOI: 10.1142/S021827181442022X. arXiv: 1407.1391 [gr-qc].

[34] Hal M. Haggard and Carlo Rovelli. "Quantum-gravity effects outside the horizon spark black to white hole tunneling". In: *Phys. Rev. D* 92.10 (2015), p. 104020. DOI: 10.1103/PhysRevD.92.104020. arXiv: 1407.0989 [gr-qc].

[35] Pawel O. Mazur and Emil Mottola. "Gravitational vacuum condensate stars". In: *Proc. Nat. Acad. Sci.* 101 (2004), pp. 9545–9550. DOI: 10.1073/pnas.0402717101. arXiv: gr-qc/0407075.

[36] Pawel O. Mazur and Emil Mottola. "Gravitational Condensate Stars: An Alternative to Black Holes". In: *Universe* 9.2 (2023), p. 88. DOI: 10.3390/universe9020088. arXiv: gr-qc/0109035.

[37] Matt Visser and David L. Wiltshire. "Stable gravastars: An Alternative to black holes?" In: *Class. Quantum Grav.* 21 (2004), pp. 1135–1152. DOI: 10.1088/0264-9381/21/4/027. arXiv: gr-qc/0310107.

[38] Julio Arrechea et al. "Semiclassical relativistic stars". In: *Sci. Rep.* 12.1 (2022), p. 15958. DOI: 10.1038/s41598-022-19836-8. arXiv: 2110.15808 [gr-qc].

[39] Julio Arrechea et al. “Ultracompact horizonless objects in order-reduced semiclassical gravity”. In: (Oct. 2023). arXiv: 2310.12668 [gr-qc].

[40] Samir D. Mathur. “The Fuzzball proposal for black holes: An Elementary review”. In: *Fortsch. Phys.* 53 (2005), pp. 793–827. DOI: 10.1002/prop.200410203. arXiv: hep-th/0502050 [hep-th].

[41] Taishi Ikeda et al. “Black-hole microstate spectroscopy: Ringdown, quasinormal modes, and echoes”. In: *Phys. Rev. D* 104 (6 2021), p. 066021. DOI: 10.1103/PhysRevD.104.066021. URL: https://link.aps.org/doi/10.1103/PhysRevD.104.066021.

[42] Philippe Jetzer. “Boson stars”. In: *Phys. Rept.* 220 (1992), pp. 163–227. DOI: 10.1016/0370-1573(92)90123-H.

[43] Steven L. Liebling and Carlos Palenzuela. “Dynamical boson stars”. In: *Living Rev. Rel.* 15 (2012), p. 6. DOI: 10.12942/lrr-2012-6. arXiv: 1202.5809 [gr-qc].

[44] Matt Visser. *Lorentzian wormholes: From Einstein to Hawking*. 1995. ISBN: 978-1-56396-653-8.

[45] M. S. Morris, K. S. Thorne, and U. Yurtsever. “Wormholes, Time Machines, and the Weak Energy Condition”. In: *Phys. Rev. Lett.* 61 (1988), pp. 1446–1449. DOI: 10.1103/PhysRevLett.61.1446.

[46] Hans A. Buchdahl. “General Relativistic Fluid Spheres”. In: *Phys. Rev.* 116 (1959), p. 1027. DOI: 10.1103/PhysRev.116.1027.

[47] Vitor Cardoso and Paolo Pani. “Testing the nature of dark compact objects: A status report”. In: *Living Rev. Rel.* 22.1 (2019), p. 4. DOI: 10.1007/s41114-019-0020-4. arXiv: 1904.05363 [gr-qc].

[48] Steven Weinberg. *Gravitation and Cosmology: Principles and Applications of the General Theory of Relativity*. New York: John Wiley and Sons, 1972. ISBN: 978-0-471-92567-5, 978-0-471-92567-5.

[49] George F. R. Ellis. “Closed trapped surfaces in cosmology”. In: *Gen. Rel. Grav.* 35 (2003), pp. 1309–1319. DOI: 10.1023/A:1024508831299. arXiv: gr-qc/0304039.

[50] G. F. R. Ellis and T. Rothman. “Lost horizons”. In: *Am. J. Phys.* 61.10 (1993), pp. 883–893. DOI: 10.1119/1.17400.

[51] Tamara M. Davis and Charles H. Lineweaver. “Expanding confusion: common misconceptions of cosmological horizons and the superluminal expansion of the universe”. In: *Publ. Astron. Soc. Austral.* 21 (2004), p. 97. DOI: 10.1071/AS03040. arXiv: astro-ph/0310808.

[52] George F. R. Ellis and Roy Maartens. “The emergent universe: Inflationary cosmology with no singularity”. In: *Class. Quant. Grav.* 21 (2004), pp. 223–232. DOI: 10.1088/0264-9381/21/1/015. arXiv: gr-qc/0211082.

[53] Emanuele Alesci et al. “Cosmological singularity resolution from quantum gravity: the emergent-bouncing universe”. In: *Phys. Rev. D* 96.4 (2017), p. 046008. DOI: 10.1103/PhysRevD.96.046008. arXiv: 1612.07116 [gr-qc].

[54] J. B. Hartle and S. W. Hawking. "Wave Function of the Universe". In: *Phys. Rev. D* 28 (1983). Ed. by Li-Zhi Fang and R. Ruffini, pp. 2960–2975. DOI: 10.1103/PhysRevD.28.2960.

[55] Julian Barbour, Tim Koslowski, and Flavio Mercati. "Identification of a gravitational arrow of time". In: *Phys. Rev. Lett.* 113.18 (2014), p. 181101. DOI: 10.1103/PhysRevLett.113.181101. arXiv: 1409.0917 [gr-qc].

[56] James Hartle and Thomas Hertog. "Arrows of Time in the Bouncing Universes of the No-boundary Quantum State". In: *Phys. Rev. D* 85 (2012), p. 103524. DOI: 10.1103/PhysRevD.85.103524. arXiv: 1104.1733 [hep-th].

[57] Robert Brandenberger et al. "Fluctuations through a Vibrating Bounce". In: *Phys. Rev. D* 97.4 (2018), p. 043504. DOI: 10.1103/PhysRevD.97.043504. arXiv: 1711.08370 [hep-th].

[58] Francesco Gozzini and Francesca Vidotto. "Primordial Fluctuations From Quantum Gravity". In: *Front. Astron. Space Sci.* 7 (2021), p. 629466. DOI: 10.3389/fspas.2020.629466. arXiv: 1906.02211 [gr-qc].

[59] Luis J. Garay, Mercedes Martín-Benito, and Eduardo Martín-Martínez. "Echo of the Quantum Bounce". In: *Phys. Rev. D* 89.4 (2014), p. 043510. DOI: 10.1103/PhysRevD.89.043510. arXiv: 1308.4348 [gr-qc].

[60] M. Novello and S. E. Perez Bergliaffa. "Bouncing Cosmologies". In: *Phys. Rept.* 463 (2008), pp. 127–213. DOI: 10.1016/j.physrep.2008.04.006. arXiv: 0802.1634 [astro-ph].

[61] Abhay Ashtekar and Parampreet Singh. "Loop Quantum Cosmology: A Status Report". In: *Class. Quant. Grav.* 28 (2011), p. 213001. DOI: 10.1088/0264-9381/28/21/213001. arXiv: 1108.0893 [gr-qc].

[62] Damien A. Easson and Joseph E. Lesnefsky. "Eternal Universes". In: (Apr. 2024). arXiv: 2404.03016 [hep-th].

[63] Sandip P. Trivedi. "Semiclassical extremal black holes". In: *Phys. Rev. D* 47 (10 1993), pp. 4233–4238. DOI: 10.1103/PhysRevD.47.4233. URL: https://link.aps.org/doi/10.1103/PhysRevD.47.4233.

[64] Francisco S. N. Lobo et al. "Novel black-bounce spacetimes: wormholes, regularity, energy conditions, and causal structure". In: *Phys. Rev. D* 103.8 (2021), p. 084052. DOI: 10.1103/PhysRevD.103.084052. arXiv: 2009.12057 [gr-qc].

[65] E. Zakhary and C. B. G. Mcintosh. "A Complete Set of Riemann Invariants". In: *Gen. Rel. Grav.* 29.5 (1997), pp. 539–581. DOI: 10.1023/a:1018851201784.

[66] Ramón Torres. *Regular rotating black holes: A review*. 2022. arXiv: 2208.12713 [gr-qc].

[67] Cosimo Bambi. *Regular Black Holes*. Springer Series in Astrophysics and Cosmology. Springer Singapore, 2023. DOI: 10.1007/978-981-99-1596-5. arXiv: 2307.13249 [gr-qc].

[68] Eloy Ayon-Beato and Alberto Garcia. "The Bardeen model as a nonlinear magnetic monopole". In: *Phys. Lett. B* 493 (2000), pp. 149–152. DOI: 10.1016/S0370-2693(00)01125-4. arXiv: gr-qc/0009077.

[69] Kirill A. Bronnikov. *Regular black holes sourced by nonlinear electrodynamics*. Nov. 2022. arXiv: 2211.00743 [gr-qc].

[70] Kirill A. Bronnikov and Rahul Kumar Walia. "Field sources for Simpson-Visser spacetimes". In: *Phys. Rev. D* 105.4 (2022), p. 044039. DOI: 10.1103/PhysRevD.105.044039. arXiv: 2112.13198 [gr-qc].

[71] Manuel E. Rodrigues and Marcos V. de S. Silva. "Source of black bounces in general relativity". In: *Phys. Rev. D* 107.4 (2023), p. 044064. DOI: 10.1103/PhysRevD.107.044064. arXiv: 2302.10772 [gr-qc].

[72] Milko Estrada and Rodrigo Aros. "A new class of regular black holes in Einstein Gauss-Bonnet gravity with localized sources of matter". In: *Phys. Lett. B* 844 (2023), p. 138090. DOI: 10.1016/j.physletb.2023.138090. arXiv: 2305.17233 [gr-qc].

[73] José Tarciso S. S. Junior and Manuel E. Rodrigues. "Coincident $f(\mathbb{Q})$ gravity: black holes, regular black holes, and black bounces". In: *Eur. Phys. J. C* 83.6 (2023), p. 475. DOI: 10.1140/epjc/s10052-023-11660-2. arXiv: 2306.04661 [gr-qc].

[74] Kimet Jusufi. "Regular black holes in Verlinde's emergent gravity". In: *Annals Phys.* 448 (2023), p. 169191. DOI: 10.1016/j.aop.2022.169191. arXiv: 2208.12979 [gr-qc].

[75] Allah Ditta et al. "Thermal properties of Simpson–Visser Minkowski core regular black holes solution in Verlinde's emergent gravity". In: *Phys. Dark Univ.* 43 (2024), p. 101418. DOI: 10.1016/j.dark.2023.101418.

[76] Shin'ichi Nojiri and G. G. L. Nashed. "Hayward black hole in scalar-Einstein-Gauss-Bonnet gravity in four dimensions". In: *Phys. Rev. D* 108.2 (2023), p. 024014. DOI: 10.1103/PhysRevD.108.024014. arXiv: 2306.14162 [gr-qc].

[77] Breno L. Giacchini and Ivan Kolář. "Toward regular black holes in sixth-derivative gravity". In: (June 2024). arXiv: 2406.00997 [gr-qc].

[78] James M. Bardeen. "Non-Singular General Relativistic Gravitational Collapse". In: *Proceedings of the International Conference GR5*. Tblisi, U.S.S.R., 1968.

[79] Sean A. Hayward. "Formation and Evaporation of Non-Singular Black Holes". In: *Phys. Rev. Lett.* 96.3 (2006), p. 031103. ISSN: 0031-9007, 1079-7114. DOI: 10.1103/PhysRevLett.96.031103. arXiv: gr-qc/0506126.

[80] Irina Dymnikova. "Vacuum Nonsingular Black Hole". In: *Gen. Relativ. Gravit.* 24 (1992), pp. 235–242. ISSN: 0001-7701. DOI: 10.1007/BF00760226.

[81] Zhong-Ying Fan and Xiaobao Wang. "Construction of regular black holes in general relativity". In: *Phys. Rev. D* 94.12 (2016), p. 124027. DOI: 10.1103/PhysRevD.94.124027. arXiv: 1610.02636 [gr-qc].

[82] Ana Bokulic et al. "Lagrangian reverse engineering for regular black holes". In: *Phys. Lett. B* 854 (2024), p. 138750. DOI: 10.1016/j.physletb.2024.138750. arXiv: 2311.17151 [gr-qc].

[83] Charles W. Misner and David H. Sharp. "Relativistic equations for adiabatic, spherically symmetric gravitational collapse". In: *Phys. Rev.* 136 (1964), B571–B576. DOI: 10.1103/PhysRev.136.B571.

[84] Jr. Hernandez Walter C. and Charles W. Misner. "Observer Time as a Coordinate in Relativistic Spherical Hydrodynamics". In: 143 (1966), p. 452. DOI: 10.1086/148525.

[85] Roberto Casadio, Andrea Giusti, and Jorge Ovalle. "Quantum rotating black holes". In: *JHEP* 05 (2023), p. 118. DOI: 10.1007/JHEP05(2023)118. arXiv: 2303.02713 [gr-qc].

[86] Roberto Casadio, Alexander Kamenshchik, and Jorge Ovalle. "From black hole mimickers to black holes". In: *Phys. Rev. D* 109.2 (2024), p. 024042. DOI: 10.1103/PhysRevD.109.024042. arXiv: 2401.03980 [gr-qc].

[87] Tian Zhou and Leonardo Modesto. "Geodesic incompleteness of some popular regular black holes". In: *Phys. Rev. D* 107.4 (2023), p. 044016. DOI: 10.1103/PhysRevD.107.044016. arXiv: 2208.02557 [gr-qc].

[88] Chen Lan and Yi-Fan Wang. "Singularities of regular black holes and the monodromy method for asymptotic quasinormal modes*". In: *Chin. Phys. C* 47.2 (2023), p. 025103. DOI: 10.1088/1674-1137/aca07c. arXiv: 2205.05935 [gr-qc].

[89] Sushant G. Ghosh. "A nonsingular rotating black hole". In: *Eur. Phys. J. C* 75.11 (2015), p. 532. DOI: 10.1140/epjc/s10052-015-3740-y. arXiv: 1408.5668 [gr-qc].

[90] Naoki Tsukamoto. "Black hole shadow in an asymptotically-flat, stationary, and axisymmetric spacetime: The Kerr–Newman and rotating regular black holes". In: *Phys. Rev. D* 97.6 (2018), p. 064021. DOI: 10.1103/PhysRevD.97.064021. arXiv: 1708.07427 [gr-qc].

[91] Rahul Kumar and Sushant G. Ghosh. "Black hole parameter estimation from its shadow". In: *Astrophys. J.* 892 (2020), p. 78. DOI: 10.3847/1538-4357/ab77b0. arXiv: 1811.01260 [gr-qc].

[92] Rahul Kumar, Amit Kumar, and Sushant G. Ghosh. "Testing rotating regular metrics as candidates for astrophysical black holes". In: *Astrophys. J.* 896.1 (2020), p. 89. DOI: 10.3847/1538-4357/ab8c4a. arXiv: 2006.09869 [gr-qc].

[93] Alex Simpson and Matt Visser. "The Eye of the Storm: A Regular Kerr Black Hole". In: 03.2022 (2022), p. 011. DOI: 10.1088/1475-7516/2022/03/011. arXiv: 2111.12329.

[94] Alex Simpson and Matt Visser. "Black-bounce to traversable wormhole". In: 2019.02 (2019), p. 042. DOI: 10.1088/1475-7516/2019/02/042. arXiv: 1812.07114 [gr-qc].

[95] S. V. Bolokhov, K. A. Bronnikov, and M. V. Skvortsova. "Magnetic black universes and wormholes with a phantom scalar". In: *Class. Quant. Grav.* 29 (2012), p. 245006. DOI: 10.1088/0264-9381/29/24/245006. arXiv: 1208.4619 [gr-qc].

[96] K. A. Bronnikov and P. A. Korolyov. "Magnetic wormholes and black universes with invisible ghosts". In: *Grav. Cosmol.* 21.2 (2015), pp. 157–165. DOI: 10.1134/S0202289315020024. arXiv: 1503.02956 [gr-qc].

[97] K. A. Bronnikov and J. C. Fabris. "Regular phantom black holes". In: *Phys. Rev. Lett.* 96 (2006), p. 251101. DOI: 10.1103/PhysRevLett.96.251101. arXiv: gr-qc/0511109.

[98] E T. Newman et al. "Metric of a Rotating, Charged Mass". In: *J. Math. Phys.* 6 (1965), pp. 918–919. DOI: 10.1063/1.1704351.

[99] Naresh Dadhich and Sushant G. Ghosh. "Rotating black hole in Einstein and pure Lovelock gravity". In: (July 2013). arXiv: 1307.6166 [gr-qc].

[100] Sushant G. Ghosh, Sunil D. Maharaj, and Uma Papnoi. "Radiating Kerr-Newman black hole in $f(R)$ gravity". In: *Eur. Phys. J. C* 73.6 (2013), p. 2473. DOI: 10.1140/epjc/s10052-013-2473-z. arXiv: 1208.3028 [gr-qc].

[101] Francesco Caravelli and Leonardo Modesto. "Spinning Loop Black Holes". In: *Class. Quant. Grav.* 27 (2010), p. 245022. DOI: 10.1088/0264-9381/27/24/245022. arXiv: 1006.0232 [gr-qc].

[102] Devin Hansen and Nicolas Yunes. "Applicability of the Newman-Janis Algorithm to Black Hole Solutions of Modified Gravity Theories". In: *Phys. Rev. D* 88.10 (2013), p. 104020. DOI: 10.1103/PhysRevD.88.104020. arXiv: 1308.6631 [gr-qc].

[103] Cosimo Bambi and Leonardo Modesto. "Rotating regular black holes". In: *Phys. Lett. B* 721 (2013), pp. 329–334. DOI: 10.1016/j.physletb.2013.03.025. arXiv: 1302.6075 [gr-qc].

[104] Jacopo Mazza, Edgardo Franzin, and Stefano Liberati. "A novel family of rotating black hole mimickers". In: *JCAP* 04 (2021), p. 082. DOI: 10.1088/1475-7516/2021/04/082. arXiv: 2102.01105 [gr-qc].

[105] S. P. Drake and Peter Szekeres. "Uniqueness of the Newman-Janis algorithm in generating the Kerr-Newman metric". In: *Gen. Rel. Grav.* 32 (2000), pp. 445–458. DOI: 10.1023/A:1001920232180. arXiv: gr-qc/9807001.

[106] Philip Beltracchi and Paolo Gondolo. "Physical interpretation of Newman-Janis rotating systems. II. General systems". In: *Phys. Rev. D* 104.12 (2021), p. 124067. DOI: 10.1103/PhysRevD.104.124067. arXiv: 2108.02841 [gr-qc].

[107] Del Rajan and Matt Visser. "Cartesian Kerr–Schild variation on the Newman–Janis trick". In: *Int. J. Mod. Phys. D* 26.14 (2017), p. 1750167. DOI: 10.1142/S021827181750167X. arXiv: 1601.03532 [gr-qc].

[108] Rafael Ferraro. "Untangling the Newman-Janis algorithm". In: *Gen. Rel. Grav.* 46 (2014), p. 1705. DOI: 10.1007/s10714-014-1705-3. arXiv: 1311.3946 [gr-qc].

[109] Nima Arkani-Hamed, Yu-tin Huang, and Donal O'Connell. "Kerr black holes as elementary particles". In: *JHEP* 01 (2020), p. 046. DOI: 10.1007/JHEP01(2020)046. arXiv: 1906.10100 [hep-th].

[110] Alfredo Guevara et al. "A worldsheet for Kerr". In: *JHEP* 03 (2021), p. 201. DOI: 10.1007/JHEP03(2021)201. arXiv: 2012.11570 [hep-th].

[111] E. T. Newman and A. I. Janis. "Note on the Kerr spinning particle metric". In: *J. Math. Phys.* 6 (1965), pp. 915–917. DOI: 10.1063/1.1704350.

[112] Mustapha Azreg-Aïnou. "From static to rotating to conformal static solutions: Rotating imperfect fluid wormholes with(out) electric or magnetic field". In: *Eur. Phys. J. C* 74.5 (2014), p. 2865. DOI: 10.1140/epjc/s10052-014-2865-8. arXiv: 1401.4292 [gr-qc].

[113] Mustapha Azreg-Aïnou. "Generating rotating regular black hole solutions without complexification". In: *Phys. Rev. D* 90.6 (2014), p. 064041. DOI: 10.1103/PhysRevD.90.064041. arXiv: 1405.2569 [gr-qc].

[114] Astrid Eichhorn and Aaron Held. "From a locality-principle for new physics to image features of regular spinning black holes with disks". In: *JCAP* 05 (2021), p. 073. DOI: 10.1088/1475-7516/2021/05/073. arXiv: 2103.13163 [gr-qc].

[115] Astrid Eichhorn and Aaron Held. "Image features of spinning regular black holes based on a locality principle". In: *Eur. Phys. J. C* 81.10 (2021), p. 933. DOI: 10.1140/epjc/s10052-021-09716-2. arXiv: 2103.07473 [gr-qc].

[116] Astrid Eichhorn, Aaron Held, and Philipp-Vincent Johannsen. "Universal signatures of singularity-resolving physics in photon rings of black holes and horizonless objects". In: *JCAP* 01 (2023), p. 043. DOI: 10.1088/1475-7516/2023/01/043. arXiv: 2204.02429 [gr-qc].

[117] Irina Dymnikova and Evgeny Galaktionov. "Basic Generic Properties of Regular Rotating Black Holes and Solitons". In: *Adv. Math. Phys.* 2017 (2017), p. 1035381. DOI: 10.1155/2017/1035381.

[118] Hideki Maeda. "Quest for realistic non-singular black-hole geometries: regular-center type". In: *JHEP* 11 (2022), p. 108. DOI: 10.1007/JHEP11(2022)108. arXiv: 2107.04791 [gr-qc].

[119] Edgardo Franzin et al. "Charged black-bounce spacetimes". In: 07.2021 (2021), p. 036. DOI: 10.1088/1475-7516/2021/07/036. arXiv: 2104.11376 [gr-qc].

[120] Carlo Rovelli and Francesca Vidotto. "Planck stars". In: *Int. J. Mod. Phys. D* 23.12 (2014), p. 1442026. DOI: 10.1142/S0218271814420267. arXiv: 1401.6562 [gr-qc].

[121] Daniele Malafarina. "Classical collapse to black holes and quantum bounces: A review". In: *Universe* 3.2 (2017), p. 48. DOI: 10.3390/universe3020048. arXiv: 1703.04138 [gr-qc].

[122] Julio Arrechea and Carlos Barceló. "Stellar equilibrium on a physical vacuum soil". In: *Int. J. Mod. Phys. D* 32.14 (2023), p. 2342006. DOI: 10.1142/S0218271823420063. arXiv: 2305.07939 [gr-qc].

[123] Julio Arrechea et al. "Schwarzschild geometry counterpart in semiclassical gravity". In: *Phys. Rev. D* 101.6 (2020), p. 064059. DOI: 10.1103/PhysRevD.101.064059. arXiv: 1911.03213 [gr-qc].

[124] Julio Arrechea et al. "Reissner–Nordström geometry counterpart in semiclassical gravity". In: *Class. Quant. Grav.* 38.11 (2021), p. 115014. DOI: 10.1088/1361-6382/abf628. arXiv: 2102.03544 [gr-qc].

[125] Clément Berthiere, Debajyoti Sarkar, and Sergey N. Solodukhin. "The fate of black hole horizons in semiclassical gravity". In: *Phys. Lett. B* 786 (2018), pp. 21–27. DOI: 10.1016/j.physletb.2018.09.027. arXiv: 1712.09914 [hep-th].

[126] Bob Holdom and Jing Ren. "Not quite a black hole". In: *Phys. Rev. D* 95 (8 2017), p. 084034. DOI: 10.1103/PhysRevD.95.084034. URL: https://link.aps.org/doi/10.1103/PhysRevD.95.084034.

[127] Eric Poisson and W. Israel. "Inner-horizon instability and mass inflation in black holes". In: *Phys. Rev. Lett.* 63 (1989), pp. 1663–1666. DOI: 10.1103/PhysRevLett.63.1663.

[128] Amos Ori. "Inner structure of a charged black hole: An exact mass-inflation solution". In: *Phys. Rev. Lett.* 67 (1991), pp. 789–792. DOI: 10.1103/PhysRevLett.67.789.

[129] Alfio Bonanno, Amir-Pouyan Khosravi, and Frank Saueressig. "Regular black holes with stable cores". In: *Phys. Rev. D* 103.12 (2021), p. 124027. DOI: 10.1103/PhysRevD.103.124027. arXiv: 2010.04226 [gr-qc].

[130] Alfio Bonanno, Amir-Pouyan Khosravi, and Frank Saueressig. "Regular evaporating black holes with stable cores". In: *Phys. Rev. D* 107.2 (2023), p. 024005. DOI: 10.1103/PhysRevD.107.024005. arXiv: 2209.10612 [gr-qc].

[131] Raúl Carballo-Rubio et al. "On the viability of regular black holes". In: 07.2018 (2018), p. 023. DOI: 10.1007/JHEP07(2018)023. arXiv: 1805.02675 [gr-qc].

[132] Raúl Carballo-Rubio et al. "Inner horizon instability and the unstable cores of regular black holes". In: *JHEP* 05 (2021), p. 132. DOI: 10.1007/JHEP05(2021)132. arXiv: 2101.05006 [gr-qc].

[133] Carlos Barceló et al. "Black hole inner horizon evaporation in semiclassical gravity". In: *Class. Quant. Grav.* 38.12 (2021), p. 125003. DOI: 10.1088/1361-6382/abf89c. arXiv: 2011.07331 [gr-qc].

[134] Carlos Barceló et al. "Classical mass inflation versus semiclassical inner horizon inflation". In: *Phys. Rev. D* 106.12 (2022), p. 124006. DOI: 10.1103/PhysRevD.106.124006. arXiv: 2203.13539 [gr-qc].

[135] Tyler McMaken. "Semiclassical instability of inner-extremal regular black holes". In: *Phys. Rev. D* 107.12 (2023), p. 125023. DOI: 10.1103/PhysRevD.107.125023. arXiv: 2303.03562 [gr-qc].

[136] Francesco Di Filippo, Stefano Liberati, and Matt Visser. "Fully extremal black holes: a black hole graveyard?" In: (May 2024). arXiv: 2405.08069 [gr-qc].

[137] Vitor Cardoso et al. "Light rings as observational evidence for event horizons: long-lived modes, ergoregions and nonlinear instabilities of ultracompact objects". In: *Phys. Rev. D* 90.4 (2014), p. 044069. DOI: 10.1103/PhysRevD.90.044069. arXiv: 1406.5510 [gr-qc].

[138] Felicity C. Eperon, Harvey S. Reall, and Jorge E. Santos. "Instability of supersymmetric microstate geometries". In: *JHEP* 10 (2016), p. 031. DOI: 10.1007/JHEP10(2016)031. arXiv: 1607.06828 [hep-th].

[139] Joe Keir. "Slowly decaying waves on spherically symmetric spacetimes and ultracompact neutron stars". In: *Class. Quant. Grav.* 33.13 (2016), p. 135009. DOI: 10.1088/0264-9381/33/13/135009. arXiv: 1404.7036 [gr-qc].

[140] Pedro V. P. Cunha et al. "Exotic Compact Objects and the Fate of the Light-Ring Instability". In: *Phys. Rev. Lett.* 130.6 (2023), p. 061401. DOI: 10.1103/PhysRevLett.130.061401. arXiv: 2207.13713 [gr-qc].

[141] Valentin Boyanov et al. "Pseudospectrum of horizonless compact objects: A bootstrap instability mechanism". In: *Phys. Rev. D* 107.6 (2023), p. 064012. DOI: 10.1103/PhysRevD.107.064012. arXiv: 2209.12950 [gr-qc].

[142] John L. Friedman. "Ergosphere instability". In: *Commun. Math. Phys.* 63.3 (1978), pp. 243–255. DOI: 10.1007/BF01196933.

[143] N. Comins and B. F. Schutz. "On the Ergoregion Instability". In: *Proceedings of the Royal Society of London Series A* 364.1717 (Dec. 1978), pp. 211–226. DOI: 10.1098/rspa.1978.0196.

[144] Shin'ichirou Yoshida and Yoshiharu Eriguchi. "Ergoregion instability revisited - a new and general method for numerical analysis of stability". In: 282.2 (Sept. 1996), pp. 580–586. DOI: 10.1093/mnras/282.2.580.

[145] John L. Friedman. "Ergosphere instability". In: *Communications in Mathematical Physics* 63.3 (Oct. 1978), pp. 243–255. DOI: 10.1007/BF01196933.

[146] A. Vilenkin. "Exponential Amplification of Waves in the Gravitational Field of Ultrarelativistic Rotating Body". In: *Phys. Lett. B* 78 (1978), pp. 301–303. DOI: 10.1016/0370-2693(78)90027-8.

[147] Vitor Cardoso et al. "Ergoregion instability of ultracompact astrophysical objects". In: *Phys. Rev. D* 77 (2008), p. 124044. DOI: 10.1103/PhysRevD.77.124044. arXiv: 0709.0532 [gr-qc].

[148] Vitor Cardoso et al. "Instability of hyper-compact Kerr-like objects". In: *Class. Quant. Grav.* 25 (2008), p. 195010. DOI: 10.1088/0264-9381/25/19/195010. arXiv: 0808.1615 [gr-qc].

[149] Cecilia B. M. H. Chirenti and Luciano Rezzolla. "On the ergoregion instability in rotating gravastars". In: *Phys. Rev. D* 78 (2008), p. 084011. DOI: 10.1103/PhysRevD.78.084011. arXiv: 0808.4080 [gr-qc].

[150] Enrico Barausse et al. "The stochastic gravitational-wave background in the absence of horizons". In: *Class. Quantum Grav.* 35.20 (2018), 20LT01. DOI: 10.1088/1361-6382/aae1de. arXiv: 1805.08229 [gr-qc].

[151] Elisa Maggio, Paolo Pani, and Valeria Ferrari. "Exotic compact objects and how to quench their ergoregion instability". In: *Phys. Rev. D* 96.10 (2017), p. 104047. DOI: 10.1103/PhysRevD.96.104047. arXiv: 1703.03696 [gr-qc].

[152] Elisa Maggio et al. "Ergoregion instability of exotic compact objects: Electromagnetic and gravitational perturbations and the role of absorption". In: *Phys. Rev. D* 99.6 (2019), p. 064007. DOI: 10.1103/PhysRevD.99.064007. arXiv: 1807.08840 [gr-qc].

[153] Raúl Carballo-Rubio et al. “Regular black holes without mass inflation instability”. In: *J. High Energy Phys.* 09.2022 (2022), p. 118. DOI: 10.1007/JHEP09(2022)118. arXiv: 2205.13556 [gr-qc].

[154] Cosimo Bambi, Leonardo Modesto, and Leslaw Rachwał. “Spacetime completeness of non-singular black holes in conformal gravity”. In: *JCAP* 05 (2017), p. 003. DOI: 10.1088/1475-7516/2017/05/003. arXiv: 1611.00865 [gr-qc].

[155] Kimet Jusufi et al. “Rotating regular black holes in conformal massive gravity”. In: *Phys. Rev. D* 101.4 (2020), p. 044035. DOI: 10.1103/PhysRevD.101.044035. arXiv: 1911.07520 [gr-qc].

[156] J. v. narlikar and A. k. kembhavi. “Space-Time Singularities and Conformal Gravity”. In: *Lett. Nuovo Cim.* 19 (1977), pp. 517–520. DOI: 10.1007/BF02748215.

[157] Mustapha Azreg-Aïnou. “Generating Rotating Regular Black Hole Solutions without Complexification”. In: *Phys. Rev. D* 90.6 (2014), p. 064041. ISSN: 1550-7998, 1550-2368. DOI: 10.1103/PhysRevD.90.064041. arXiv: 1405.2569.

[158] Mustapha Azreg-Aïnou. “Regular and conformal regular cores for static and rotating solutions”. In: *Phys. Lett. B* 730 (2014), pp. 95–98. ISSN: 03702693. DOI: 10.1016/j.physletb.2014.01.041. arXiv: 1401.0787.

[159] Mustapha Azreg-Aïnou. “From Static to Rotating to Conformal Static Solutions: Rotating Imperfect Fluid Wormholes with(out) Electric or Magnetic Field”. In: *Eur. Phys. J. C* 74.5 (2014), p. 2865. ISSN: 1434-6044, 1434-6052. DOI: 10.1140/epjc/s10052-014-2865-8. arXiv: 1401.4292.

[160] Cosimo Bambi, Leonardo Modesto, and Lesław Rachwał. “Spacetime Completeness of Non-Singular Black Holes in Conformal Gravity”. In: 05.2017 (2017), p. 003. DOI: 10.1088/1475-7516/2017/05/003. arXiv: 1611.00865.

[161] F. D. Ryan. “Gravitational waves from the inspiral of a compact object into a massive, axisymmetric body with arbitrary multipole moments”. In: *Phys. Rev. D* 52 (1995), pp. 5707–5718. DOI: 10.1103/PhysRevD.52.5707.

[162] S. W. Hawking and G. F. R. Ellis. *The Large Scale Structure of Space-Time*. Cambridge Monographs on Mathematical Physics. Cambridge: Cambridge University Press, 1973. ISBN: 978-0-521-09906-6. DOI: 10.1017/CBO9780511524646.

[163] R. Penrose and R. M. Floyd. “Extraction of rotational energy from a black hole”. In: *Nat. Phys. Sci.* 229.6 (1971), pp. 177–179. ISSN: 2058-1106. DOI: 10.1038/physci229177a0.

[164] James M. Bardeen, William H. Press, and Saul A. Teukolsky. “Rotating black holes: Locally nonrotating frames, energy extraction, and scalar synchrotron radiation”. In: *Astrophys. J.* 178 (1972), pp. 347–370. DOI: 10.1086/151796.

[165] Robert M. Wald. “Energy limits on the Penrose process”. In: *Astrophys. J.* 191 (1974), pp. 231–234. ISSN: 0004-637X. DOI: 10.1086/152959.

[166] A. Kovetz and T. Piran. “The efficiency of the Penrose process”. In: *Lett. Nuovo Cimento* 12.2 (1975). [Erratum: Lett. Nuovo Cimento **12**, 560 (1975)], pp. 39–42. ISSN: 1827-613X. DOI: 10.1007/BF02813727.

[167] Kip S. Thorne. "Disk accretion onto a black hole. 2. Evolution of the hole." In: *Astrophys. J.* 191 (1974), pp. 507–520. DOI: 10.1086/152991.

[168] Elisa Maggio, Paolo Pani, and Guilherme Raposo. "Testing the nature of dark compact objects with gravitational waves". In: (May 2021). arXiv: 2105.06410 [gr-qc].

[169] R. Abbott et al. "Tests of General Relativity with GWTC-3". In: (Dec. 2021). arXiv: 2112.06861 [gr-qc].

[170] Abhirup Ghosh. "Summary of Tests of General Relativity with GWTC-3". In: *56th Rencontres de Moriond on Gravitation*. Apr. 2022. arXiv: 2204.00662 [gr-qc].

[171] D. Battefeld and Patrick Peter. "A Critical Review of Classical Bouncing Cosmologies". In: *Phys. Rept.* 571 (2015), pp. 1–66. DOI: 10.1016/j.physrep.2014.12.004. arXiv: 1406.2790 [astro-ph.CO].

[172] Chandra Kant Mishra et al. "Parametrized tests of post-Newtonian theory using Advanced LIGO and Einstein Telescope". In: *Phys. Rev. D* 82 (2010), p. 064010. DOI: 10.1103/PhysRevD.82.064010. arXiv: 1005.0304 [gr-qc].

[173] Robert P. Geroch. "Multipole moments. II. Curved space". In: *J. Math. Phys.* 11 (1970), pp. 2580–2588. DOI: 10.1063/1.1665427.

[174] R. O. Hansen. "Multipole moments of stationary space-times". In: *J. Math. Phys.* 15 (1974), pp. 46–52. DOI: 10.1063/1.1666501.

[175] Daniel R. Mayerson. "Gravitational multipoles in general stationary spacetimes". In: *SciPost Phys.* 15.4 (2023), p. 154. DOI: 10.21468/SciPostPhys.15.4.154. arXiv: 2210.05687 [gr-qc].

[176] K. S. Thorne. "Multipole Expansions of Gravitational Radiation". In: *Rev. Mod. Phys.* 52 (1980), pp. 299–339. DOI: 10.1103/RevModPhys.52.299.

[177] Eric Poisson. "Tidal deformation of a slowly rotating black hole". In: *Phys. Rev. D* 91.4 (2015), p. 044004. DOI: 10.1103/PhysRevD.91.044004. arXiv: 1411.4711 [gr-qc].

[178] Paolo Pani et al. "Tidal deformations of a spinning compact object". In: *Phys. Rev. D* 92.2 (2015), p. 024010. DOI: 10.1103/PhysRevD.92.024010. arXiv: 1503.07365 [gr-qc].

[179] Philippe Landry and Eric Poisson. "Tidal deformation of a slowly rotating material body. External metric". In: *Phys. Rev. D* 91 (2015), p. 104018. DOI: 10.1103/PhysRevD.91.104018. arXiv: 1503.07366 [gr-qc].

[180] Philippe Landry. "Tidal deformation of a slowly rotating material body: Interior metric and Love numbers". In: *Phys. Rev. D* 95.12 (2017), p. 124058. DOI: 10.1103/PhysRevD.95.124058. arXiv: 1703.08168 [gr-qc].

[181] Taylor Binnington and Eric Poisson. "Relativistic theory of tidal Love numbers". In: *Phys. Rev. D* 80 (2009), p. 084018. DOI: 10.1103/PhysRevD.80.084018. arXiv: 0906.1366 [gr-qc].

[182] Norman Gürlebeck. "No-hair theorem for Black Holes in Astrophysical Environments". In: *Phys. Rev. Lett.* 114.15 (2015), p. 151102. DOI: 10.1103/PhysRevLett.114.151102. arXiv: 1503.03240 [gr-qc].

[183] Horng Sheng Chia. "Tidal deformation and dissipation of rotating black holes". In: *Phys. Rev. D* 104.2 (2021), p. 024013. DOI: 10.1103/PhysRevD.104.024013. arXiv: 2010.07300 [gr-qc].

[184] Alexandre Le Tiec and Marc Casals. "Spinning Black Holes Fall in Love". In: *Phys. Rev. Lett.* 126.13 (2021), p. 131102. DOI: 10.1103/PhysRevLett.126.131102. arXiv: 2007.00214 [gr-qc].

[185] Alexandre Le Tiec, Marc Casals, and Edgardo Franzin. "Tidal Love Numbers of Kerr Black Holes". In: *Phys. Rev. D* 103.8 (2021), p. 084021. DOI: 10.1103/PhysRevD.103.084021. arXiv: 2010.15795 [gr-qc].

[186] Vitor Cardoso et al. "Testing strong-field gravity with tidal Love numbers". In: *Phys. Rev. D* 95.8 (2017). [Addendum: Phys.Rev.D 95, 089901 (2017)], p. 084014. DOI: 10.1103/PhysRevD.95.084014. arXiv: 1701.01116 [gr-qc].

[187] Tullio Regge and John A. Wheeler. "Stability of a Schwarzschild singularity". In: *Phys. Rev.* 108 (1957), pp. 1063–1069. DOI: 10.1103/PhysRev.108.1063.

[188] F. J. Zerilli. "Gravitational field of a particle falling in a schwarzschild geometry analyzed in tensor harmonics". In: *Phys. Rev. D* 2 (1970), pp. 2141–2160. DOI: 10.1103/PhysRevD.2.2141.

[189] S. A. Teukolsky. "Rotating black holes - separable wave equations for gravitational and electromagnetic perturbations". In: *Phys. Rev. Lett.* 29 (1972), pp. 1114–1118. DOI: 10.1103/PhysRevLett.29.1114.

[190] Hans-Peter Nollert. "TOPICAL REVIEW: Quasinormal modes: the characteristic 'sound' of black holes and neutron stars". In: *Class. Quant. Grav.* 16 (1999), R159–R216. DOI: 10.1088/0264-9381/16/12/201.

[191] Emanuele Berti, Vitor Cardoso, and Andrei O. Starinets. "Quasinormal modes of black holes and black branes". In: *Class. Quant. Grav.* 26 (2009), p. 163001. DOI: 10.1088/0264-9381/26/16/163001. arXiv: 0905.2975 [gr-qc].

[192] R. A. Konoplya and A. Zhidenko. "Wormholes versus black holes: quasinormal ringing at early and late times". In: *JCAP* 12 (2016), p. 043. DOI: 10.1088/1475-7516/2016/12/043. arXiv: 1606.00517 [gr-qc].

[193] Paolo Pani et al. "Gravitational wave signatures of the absence of an event horizon. I. Nonradial oscillations of a thin-shell gravastar". In: *Phys. Rev. D* 80 (2009), p. 124047. DOI: 10.1103/PhysRevD.80.124047. arXiv: 0909.0287 [gr-qc].

[194] Taishi Ikeda et al. "Black-hole microstate spectroscopy: Ringdown, quasinormal modes, and echoes". In: *Phys. Rev. D* 104.6 (2021), p. 066021. DOI: 10.1103/PhysRevD.104.066021. arXiv: 2103.10960 [gr-qc].

[195] Elisa Maggio et al. "How does a dark compact object ringdown?" In: *Phys. Rev. D* 102.6 (2020), p. 064053. DOI: 10.1103/PhysRevD.102.064053. arXiv: 2006.14628 [gr-qc].

[196] S. Yoshida, Y. Eriguchi, and T. Futamase. "Quasinormal modes of boson stars". In: *Phys. Rev. D* 50 (1994), pp. 6235–6246. DOI: 10.1103/PhysRevD.50.6235.

[197] R. A. Konoplya. "How to tell the shape of a wormhole by its quasinormal modes". In: *Phys. Lett. B* 784 (2018), pp. 43–49. DOI: 10.1016/j.physletb.2018.07.025. arXiv: 1805.04718 [gr-qc].

[198] Naritaka Oshita and Niayesh Afshordi. "Probing microstructure of black hole spacetimes with gravitational wave echoes". In: *Phys. Rev. D* 99.4 (2019), p. 044002. DOI: 10.1103/PhysRevD.99.044002. arXiv: 1807.10287 [gr-qc].

[199] Qingwen Wang, Naritaka Oshita, and Niayesh Afshordi. "Echoes from Quantum Black Holes". In: *Phys. Rev. D* 101.2 (2020), p. 024031. DOI: 10.1103/PhysRevD.101.024031. arXiv: 1905.00446 [gr-qc].

[200] Vitor Cardoso et al. "Gravitational-wave signatures of exotic compact objects and of quantum corrections at the horizon scale". In: *Phys. Rev. D* 94.8 (2016), p. 084031. DOI: 10.1103/PhysRevD.94.084031. arXiv: 1608.08637 [gr-qc].

[201] Miguel Bezares, Carlos Palenzuela, and Carles Bona. "Final fate of compact boson star mergers". In: *Phys. Rev. D* 95.12 (2017), p. 124005. DOI: 10.1103/PhysRevD.95.124005. arXiv: 1705.01071 [gr-qc].

[202] Miguel Bezares et al. "Gravitational waves and kicks from the merger of unequal mass, highly compact boson stars". In: *Phys. Rev. D* 105.6 (2022), p. 064067. DOI: 10.1103/PhysRevD.105.064067. arXiv: 2201.06113 [gr-qc].

[203] Katy Clough, Tim Dietrich, and Jens C. Niemeyer. "Axion star collisions with black holes and neutron stars in full 3D numerical relativity". In: *Phys. Rev. D* 98.8 (2018), p. 083020. DOI: 10.1103/PhysRevD.98.083020. arXiv: 1808.04668 [gr-qc].

[204] T. G. F. Li et al. "Towards a generic test of the strong field dynamics of general relativity using compact binary coalescence". In: *Phys. Rev. D* 85 (2012), p. 082003. DOI: 10.1103/PhysRevD.85.082003. arXiv: 1110.0530 [gr-qc].

[205] Michalis Agathos et al. "TIGER: A data analysis pipeline for testing the strong-field dynamics of general relativity with gravitational wave signals from coalescing compact binaries". In: *Phys. Rev. D* 89.8 (2014), p. 082001. DOI: 10.1103/PhysRevD.89.082001. arXiv: 1311.0420 [gr-qc].

[206] J. Meidam et al. "Testing the no-hair theorem with black hole ringdowns using TIGER". In: *Phys. Rev. D* 90.6 (2014), p. 064009. DOI: 10.1103/PhysRevD.90.064009. arXiv: 1406.3201 [gr-qc].

[207] Huan Yang et al. "Black hole spectroscopy with coherent mode stacking". In: *Phys. Rev. Lett.* 118.16 (2017), p. 161101. DOI: 10.1103/PhysRevLett.118.161101. arXiv: 1701.05808 [gr-qc].

[208] Andrea Maselli et al. "Parametrized ringdown spin expansion coefficients: a data-analysis framework for black-hole spectroscopy with multiple events". In: *Phys. Rev. D* 101.2 (2020), p. 024043. DOI: 10.1103/PhysRevD.101.024043. arXiv: 1910.12893 [gr-qc].

[209] Emanuele Berti et al. “Extreme Gravity Tests with Gravitational Waves from Compact Binary Coalescences: (II) Ringdown”. In: *Gen. Rel. Grav.* 50.5 (2018), p. 49. DOI: 10.1007/s10714-018-2372-6. arXiv: 1801.03587 [gr-qc].

[210] Abhirup Ghosh, Richard Brito, and Alessandra Buonanno. “Constraints on quasinormal-mode frequencies with LIGO-Virgo binary–black-hole observations”. In: *Phys. Rev. D* 103.12 (2021), p. 124041. DOI: 10.1103/PhysRevD.103.124041. arXiv: 2104.01906 [gr-qc].

[211] Jahed Abedi, Hannah Dykaar, and Niayesh Afshordi. “Echoes from the Abyss: Tentative evidence for Planck-scale structure at black hole horizons”. In: *Phys. Rev. D* 96.8 (2017), p. 082004. DOI: 10.1103/PhysRevD.96.082004. arXiv: 1612.00266 [gr-qc].

[212] Adriano Testa and Paolo Pani. “Analytical template for gravitational-wave echoes: signal characterization and prospects of detection with current and future interferometers”. In: *Phys. Rev. D* 98.4 (2018), p. 044018. DOI: 10.1103/PhysRevD.98.044018. arXiv: 1806.04253 [gr-qc].

[213] Hiroyuki Nakano et al. “Black hole ringdown echoes and howls”. In: *PTEP* 2017.7 (2017), 071E01. DOI: 10.1093/ptep/ptx093. arXiv: 1704.07175 [gr-qc].

[214] Qingwen Wang and Niayesh Afshordi. “Black hole echology: The observer’s manual”. In: *Phys. Rev. D* 97.12 (2018), p. 124044. DOI: 10.1103/PhysRevD.97.124044. arXiv: 1803.02845 [gr-qc].

[215] Andrea Maselli, Sebastian H. Völkel, and Kostas D. Kokkotas. “Parameter estimation of gravitational wave echoes from exotic compact objects”. In: *Phys. Rev. D* 96.6 (2017), p. 064045. DOI: 10.1103/PhysRevD.96.064045. arXiv: 1708.02217 [gr-qc].

[216] Randy S. Conklin, Bob Holdom, and Jing Ren. “Gravitational wave echoes through new windows”. In: *Phys. Rev. D* 98.4 (2018), p. 044021. DOI: 10.1103/PhysRevD.98.044021. arXiv: 1712.06517 [gr-qc].

[217] Randy S. Conklin and Bob Holdom. “Gravitational wave echo spectra”. In: *Phys. Rev. D* 100.12 (2019), p. 124030. DOI: 10.1103/PhysRevD.100.124030. arXiv: 1905.09370 [gr-qc].

[218] Randy S. Conklin and Niayesh Afshordi. “Boltzmann Meets Lorentz: A Surrogate Model for Black Hole Echoes”. In: (Dec. 2021). arXiv: 2201.00027 [gr-qc].

[219] Di Wu et al. “Model-independent search for the quasinormal modes of gravitational wave echoes”. In: *Phys. Rev. D* 108.12 (2023), p. 124006. DOI: 10.1103/PhysRevD.108.124006. arXiv: 2308.01017 [gr-qc].

[220] Ka Wa Tsang et al. “A morphology-independent data analysis method for detecting and characterizing gravitational wave echoes”. In: *Phys. Rev. D* 98.2 (2018), p. 024023. DOI: 10.1103/PhysRevD.98.024023. arXiv: 1804.04877 [gr-qc].

[221] Ka Wa Tsang et al. “A morphology-independent search for gravitational wave echoes in data from the first and second observing runs of Advanced LIGO and Advanced Virgo”. In: *Phys. Rev. D* 101.6 (2020), p. 064012. DOI: 10.1103/PhysRevD.101.064012. arXiv: 1906.11168 [gr-qc].

[222] Yu-Tong Wang et al. "Are gravitational wave ringdown echoes always equal-interval?" In: *Eur. Phys. J. C* 78.6 (2018), p. 482. DOI: 10.1140/epjc/s10052-018-5974-y. arXiv: 1802.02003 [gr-qc].

[223] Yu-Tong Wang et al. "On echo intervals in gravitational wave echo analysis". In: *Eur. Phys. J. C* 79.9 (2019), p. 726. DOI: 10.1140/epjc/s10052-019-7234-1. arXiv: 1904.00212 [gr-qc].

[224] Jahed Abedi and Niayesh Afshordi. "Echoes from the Abyss: A highly spinning black hole remnant for the binary neutron star merger GW170817". In: *JCAP* 11 (2019), p. 010. DOI: 10.1088/1475-7516/2019/11/010. arXiv: 1803.10454 [gr-qc].

[225] Julian Westerweck et al. "Low significance of evidence for black hole echoes in gravitational wave data". In: *Phys. Rev. D* 97.12 (2018), p. 124037. DOI: 10.1103/PhysRevD.97.124037. arXiv: 1712.09966 [gr-qc].

[226] Alex B. Nielsen et al. "Parameter estimation and statistical significance of echoes following black hole signals in the first Advanced LIGO observing run". In: *Phys. Rev. D* 99.10 (2019), p. 104012. DOI: 10.1103/PhysRevD.99.104012. arXiv: 1811.04904 [gr-qc].

[227] R. K. L. Lo, T. G. F. Li, and A. J. Weinstein. "Template-based Gravitational-Wave Echoes Search Using Bayesian Model Selection". In: *Phys. Rev. D* 99.8 (2019), p. 084052. DOI: 10.1103/PhysRevD.99.084052. arXiv: 1811.07431 [gr-qc].

[228] Nami Uchikata et al. "Searching for black hole echoes from the LIGO-Virgo Catalog GWTC-1". In: *Phys. Rev. D* 100.6 (2019), p. 062006. DOI: 10.1103/PhysRevD.100.062006. arXiv: 1906.00838 [gr-qc].

[229] R. Abbott et al. "Tests of general relativity with binary black holes from the second LIGO-Virgo gravitational-wave transient catalog". In: *Phys. Rev. D* 103.12 (2021), p. 122002. DOI: 10.1103/PhysRevD.103.122002. arXiv: 2010.14529 [gr-qc].

[230] K. A. Bronnikov. "Black bounces, wormholes, and partly phantom scalar fields". In: *Phys. Rev. D* 106.6 (2022), p. 064029. DOI: 10.1103/PhysRevD.106.064029. arXiv: 2206.09227 [gr-qc].

[231] Benjamin P Abbott et al. "Exploring the Sensitivity of Next Generation Gravitational Wave Detectors". In: *Class. Quantum Grav.* 34.4 (2017), p. 044001. DOI: 10.1088/1361-6382/aa51f4. arXiv: 1607.08697 [astro-ph.IM].

[232] Raúl Carballo-Rubio et al. *A connection between regular black holes and horizonless ultracompact stars*. Nov. 2022. arXiv: 2211.05817 [gr-qc].

[233] S. C. Ulhoa. "On Quasinormal Modes for Gravitational Perturbations of Bardeen Black Hole". In: *Braz. J. Phys.* 44 (2014), pp. 380–384. DOI: 10.1007/s13538-014-0209-7. arXiv: 1303.3143 [gr-qc].

[234] Sahel Dey and Sayan Chakrabarti. "A note on electromagnetic and gravitational perturbations of the Bardeen de Sitter black hole: quasinormal modes and greybody factors". In: *Eur. Phys. J. C* 79.6 (2019), p. 504. DOI: 10.1140/epjc/s10052-019-7004-0. arXiv: 1807.09065 [gr-qc].

[235] Bobir Toshmatov et al. "Electromagnetic perturbations of black holes in general relativity coupled to nonlinear electrodynamics". In: *Phys. Rev. D* 97.8 (2018), p. 084058. DOI: 10.1103/PhysRevD.97.084058. arXiv: 1805.00240 [gr-qc].

[236] Bobir Toshmatov, Zdeněk Stuchlík, and Bobomurat Ahmedov. "Electromagnetic perturbations of black holes in general relativity coupled to nonlinear electrodynamics: Polar perturbations". In: *Phys. Rev. D* 98.8 (2018), p. 085021. DOI: 10.1103/PhysRevD.98.085021. arXiv: 1810.06383 [gr-qc].

[237] Bobir Toshmatov et al. "Relaxations of perturbations of spacetimes in general relativity coupled to nonlinear electrodynamics". In: *Phys. Rev. D* 99.6 (2019), p. 064043. DOI: 10.1103/PhysRevD.99.064043. arXiv: 1903.03778 [gr-qc].

[238] Ying Zhao et al. *The Quasinormal Modes and Isospectrality of Bardeen (Anti-) de Sitter Black Holes*. June 2023. arXiv: 2306.02332 [gr-qc].

[239] Chen Wu. "Quasinormal frequencies of gravitational perturbation in regular black hole spacetimes". In: *Eur. Phys. J. C* 78.4 (2018), p. 283. DOI: 10.1140/epjc/s10052-018-5764-6.

[240] K. A. Bronnikov, R. A. Konoplya, and A. Zhidenko. "Instabilities of wormholes and regular black holes supported by a phantom scalar field". In: *Phys. Rev. D* 86 (2012), p. 024028. DOI: 10.1103/PhysRevD.86.024028. arXiv: 1205.2224 [gr-qc].

[241] Claudia Moreno and Olivier Sarbach. "Stability properties of black holes in self-gravitating nonlinear electrodynamics". In: *Phys. Rev. D* 67 (2003), p. 024028. DOI: 10.1103/PhysRevD.67.024028. arXiv: gr-qc/0208090.

[242] Eliana Chaverra et al. "Black holes in nonlinear electrodynamics: Quasinormal spectra and parity splitting". In: *Phys. Rev. D* 93.12 (2016), p. 123013. DOI: 10.1103/PhysRevD.93.123013. arXiv: 1605.04003 [gr-qc].

[243] Kimihiro Nomura, Daisuke Yoshida, and Jiro Soda. "Stability of magnetic black holes in general nonlinear electrodynamics". In: *Phys. Rev. D* 101.12 (2020), p. 124026. DOI: 10.1103/PhysRevD.101.124026. arXiv: 2004.07560 [gr-qc].

[244] Kimihiro Nomura and Daisuke Yoshida. "Quasinormal modes of charged black holes with corrections from nonlinear electrodynamics". In: *Phys. Rev. D* 105.4 (2022), p. 044006. DOI: 10.1103/PhysRevD.105.044006. arXiv: 2111.06273 [gr-qc].

[245] Kun Meng and Shao-Jun Zhang. "Gravito-electromagnetic perturbations and QNMs of regular black holes". In: *Class. Quant. Grav.* 40.19 (2023), p. 195024. DOI: 10.1088/1361-6382/acf3c6. arXiv: 2210.00295 [gr-qc].

[246] A. J. M. Medved, Damien Martin, and Matt Visser. "Dirty black holes: Quasinormal modes for 'squeezed' horizons". In: *Class. Quantum Grav.* 21 (2004), pp. 2393–2405. DOI: 10.1088/0264-9381/21/9/013. arXiv: gr-qc/0310097.

[247] Max Karlovini. "Axial perturbations of general spherically symmetric space-times". In: *Class. Quant. Grav.* 19 (2002), pp. 2125–2140. DOI: 10.1088/0264-9381/19/8/305. arXiv: gr-qc/0111066.

[248] S. Chandrasekhar and Steven L. Detweiler. "The quasi-normal modes of the Schwarzschild black hole". In: *Proc. Roy. Soc. Lond. A* 344 (1975), pp. 441–452. DOI: 10.1098/rspa.1975.0112.

[249] Paolo Pani. "Advanced Methods in Black-Hole Perturbation Theory". In: *Int. J. Mod. Phys. A* 28 (2013). Ed. by V. Cardoso et al., p. 1340018. DOI: 10.1142/S0217751X13400186. arXiv: 1305.6759 [gr-qc].

[250] Vitor Cardoso, Edgardo Franzin, and Paolo Pani. "Is the gravitational-wave ringdown a probe of the event horizon?" In: *Phys. Rev. Lett.* 116.17 (2016). [Erratum: Phys. Rev. Lett. **117**, 089902 (2016)], p. 171101. DOI: 10.1103/PhysRevLett.116.171101. arXiv: 1602.07309 [gr-qc].

[251] Bobir Toshmatov et al. "Quasinormal modes of test fields around regular black holes". In: *Phys. Rev. D* 91.8 (2015), p. 083008. DOI: 10.1103/PhysRevD.91.083008. arXiv: 1503.05737 [gr-qc].

[252] M. S. Churilova and Z. Stuchlik. "Ringing of the regular black-hole/wormhole transition". In: *Class. Quant. Grav.* 37.7 (2020), p. 075014. DOI: 10.1088/1361-6382/ab7717. arXiv: 1911.11823 [gr-qc].

[253] Edgardo Franzin et al. "Scalar perturbations around rotating regular black holes and wormholes: Quasinormal modes, ergoregion instability, and superradiance". In: *Phys. Rev. D* 105.12 (2022), p. 124051. DOI: 10.1103/PhysRevD.105.124051. arXiv: 2201.01650 [gr-qc].

[254] R. A. Konoplya, D. Ovchinnikov, and B. Ahmedov. "Bardeen spacetime as a quantum corrected Schwarzschild black hole: Quasinormal modes and Hawking radiation". In: (July 2023). arXiv: 2307.10801 [gr-qc].

[255] Leonardo Balart, Grigoris Panotopoulos, and Ángel Rincón. "Regular charged black holes, energy conditions and quasinormal modes". In: *Fortschr. Phys.* 2023 (2023), p. 2300075. DOI: 10.1002/prop.202300075. arXiv: 2309.01910 [gr-qc].

[256] Bernard F. Schutz and Clifford M. Will. "BLACK HOLE NORMAL MODES: A SEMIANALYTIC APPROACH". In: *Astrophys. J. Lett.* 291 (1985), pp. L33–L36. DOI: 10.1086/184453.

[257] Raúl Carballo-Rubio et al. *Singularity-free gravitational collapse: From regular black holes to horizonless objects*. Jan. 2023. arXiv: 2302.00028 [gr-qc].

[258] Fech Scen Khoo and Yen Chin Ong. "Lux in obscuro: Photon Orbits of Extremal Black Holes Revisited". In: *Class. Quantum Grav.* 33.23 (2016). [Erratum: Class. Quantum Grav. 34, 219501 (2017)], p. 235002. DOI: 10.1088/0264-9381/33/23/235002. arXiv: 1605.05774 [gr-qc].

[259] James M. Bardeen, William H. Press, and Saul A Teukolsky. "Rotating black holes: Locally nonrotating frames, energy extraction, and scalar synchrotron radiation". In: *Astrophys. J.* 178 (1972), p. 347. DOI: 10.1086/151796.

[260] Parthapratim Pradhan and Parthasarathi Majumdar. "Circular Orbits in Extremal Reissner Nordstrom Spacetimes". In: *Phys. Lett. A* 375 (2011), pp. 474–479. DOI: 10.1016/j.physleta.2010.11.015. arXiv: 1001.0359 [gr-qc].

[261] Stefanos Aretakis. "Stability and Instability of Extreme Reissner-Nordström Black Hole Spacetimes for Linear Scalar Perturbations I". In: *Commun. Math. Phys.* 307 (2011), pp. 17–63. DOI: 10.1007/s00220-011-1254-5. arXiv: 1110.2007 [gr-qc].

[262] Stefanos Aretakis. "Horizon Instability of Extremal Black Holes". In: *Adv. Theor. Math. Phys.* 19 (2015), pp. 507–530. DOI: 10.4310/ATMP.2015.v19.n3.a1. arXiv: 1206.6598 [gr-qc].

[263] Samuel E. Gralla, Arun Ravishankar, and Peter Zimmerman. "Horizon Instability of the Extremal BTZ Black Hole". In: 05.2020 (2020), p. 094. DOI: 10.1007/JHEP05(2020)094. arXiv: 1911.11164 [gr-qc].

[264] Arun Ravishankar. "On the Horizon Instability of Extremal Black Holes and Black Branes". PhD thesis. Arizona U., 2021.

[265] James Healy, Carlos O. Lousto, and Yosef Zlochower. "Remnant mass, spin, and recoil from spin aligned black-hole binaries". In: *Phys. Rev. D* 90.10 (2014), p. 104004. DOI: 10.1103/PhysRevD.90.104004. arXiv: 1406.7295 [gr-qc].

[266] Vishal Baibhav et al. "Black hole spectroscopy: Systematic errors and ringdown energy estimates". In: *Phys. Rev. D* 97.4 (2018), p. 044048. DOI: 10.1103/PhysRevD.97.044048. arXiv: 1710.02156 [gr-qc].

[267] Enrico Barausse, Viktoriya Morozova, and Luciano Rezzolla. "On the mass radiated by coalescing black-hole binaries". In: *Astrophys. J.* 758 (2012). [Erratum: Astrophys.J. 786, 76 (2014)], p. 63. DOI: 10.1088/0004-637X/758/1/63. arXiv: 1206.3803 [gr-qc].

[268] Raúl Carballo-Rubio et al. "Phenomenological aspects of black holes beyond general relativity". In: *Phys. Rev. D* 98.12 (2018), p. 124009. DOI: 10.1103/PhysRevD.98.124009. arXiv: 1809.08238 [gr-qc].

[269] Kip S. Thorne. "Nonspherical gravitational collapse—a short review". In: *Magic Without Magic: John Archibald Wheeler*. Ed. by J. Klauder. San Francisco, US: Freeman, 1972, pp. 231–243.

[270] Raúl Carballo-Rubio, Pawan Kumar, and Wenbin Lu. "Seeking observational evidence for the formation of trapping horizons in astrophysical black holes". In: *Phys. Rev. D* 97.12 (2018), p. 123012. DOI: 10.1103/PhysRevD.97.123012. arXiv: 1804.00663 [gr-qc].

[271] Andrea Addazi, Antonino Marcianò, and Nicolás Yunes. "Gravitational Instability of Exotic Compact Objects". In: *Eur. Phys. J. C* 80.1 (2020), p. 36. DOI: 10.1140/epjc/s10052-019-7575-9. arXiv: 1905.08734 [gr-qc].

[272] Baoyi Chen et al. *Instability of exotic compact objects and its implications for gravitational-wave echoes*. Feb. 2019. arXiv: 1902.08180 [gr-qc].

[273] F. Paul Esposito. "Absorption of Gravitational Energy by a Viscous Compressible Fluid". In: *Astrophys. J.* 165 (Mar. 1971), p. 165. DOI: 10.1086/150884.

[274] Elisa Maggio et al. "Analytical model for gravitational-wave echoes from spinning remnants". In: *Phys. Rev. D* 100.6 (2019), p. 064056. DOI: 10.1103/PhysRevD.100.064056. arXiv: 1907.03091 [gr-qc].

[275] Naritaka Oshita, Qingwen Wang, and Niayesh Afshordi. "On reflectivity of quantum black hole horizons". In: 04.2020 (2020), p. 016. DOI: 10.1088/1475-7516/2020/04/016. arXiv: 1905.00464 [hep-th].

[276] Sumanta Chakraborty et al. "Implications of the quantum nature of the black hole horizon on the gravitational-wave ringdown". In: *Phys. Rev. D* 106.2 (2022), p. 024041. DOI: 10.1103/PhysRevD.106.024041. arXiv: 2202.09111 [gr-qc].

[277] Laura Sberna et al. "Nonlinear effects in the black hole ringdown: Absorption-induced mode excitation". In: *Phys. Rev. D* 105.6 (2022), p. 064046. DOI: 10.1103/PhysRevD.105.064046. arXiv: 2112.11168 [gr-qc].

[278] Sam R. Dolan, Leor Barack, and Barry Wardell. "Self force via m-mode regularization and 2+1D evolution: II. Scalar-field implementation on Kerr spacetime". In: *Phys. Rev. D* 84 (2011), p. 084001. DOI: 10.1103/PhysRevD.84.084001. arXiv: 1107.0012 [gr-qc].

[279] Paolo Pani and Valeria Ferrari. "On gravitational-wave echoes from neutron-star binary coalescences". In: *Class. Quantum Grav.* 35.15 (2018), 15LT01. DOI: 10.1088/1361-6382/aacb8f. arXiv: 1804.01444 [gr-qc].

[280] Guilherme Raposo et al. "Anisotropic stars as ultracompact objects in general relativity". In: *Phys. Rev. D* 99.10 (2019), p. 104072. DOI: 10.1103/PhysRevD.99.104072. arXiv: 1811.07917 [gr-qc].

[281] Jing Ren and Di Wu. "Gravitational wave echoes search with combs". In: *Phys. Rev. D* 104.12 (2021), p. 124023. DOI: 10.1103/PhysRevD.104.124023. arXiv: 2108.01820 [gr-qc].

[282] Jean-Pierre Berenger. "A perfectly matched layer for the absorption of electromagnetic waves". In: *J. Comput. Phys.* 114.2 (1994), pp. 185–200. ISSN: 0021-9991. DOI: 10.1006/jcph.1994.1159.

[283] Vitor Cardoso, Valentino F. Foit, and Matthew Kleban. "Gravitational wave echoes from black hole area quantization". In: 08.2019 (2019), p. 006. DOI: 10.1088/1475-7516/2019/08/006. arXiv: 1902.10164 [hep-th].

[284] Zachary Mark et al. "A recipe for echoes from exotic compact objects". In: *Phys. Rev. D* 96.8 (2017), p. 084002. DOI: 10.1103/PhysRevD.96.084002. arXiv: 1706.06155 [gr-qc].

[285] William A. Hiscock. "Gravitational vacuum polarization around static spherical stars". In: *Phys. Rev. D* 37 (8 1988), pp. 2142–2150. DOI: 10.1103/PhysRevD.37.2142. URL: https://link.aps.org/doi/10.1103/PhysRevD.37.2142.

[286] Ignacio A. Reyes and Giovanni Maria Tomaselli. "Quantum field theory on compact stars near the Buchdahl limit". In: *Phys. Rev. D* 108.6 (2023), p. 065006. DOI: 10.1103/PhysRevD.108.065006. arXiv: 2301.00826 [gr-qc].

[287] Ignacio A. Reyes. "Trace anomaly and compact stars". In: (Aug. 2023). arXiv: 2308.07363 [gr-qc].

[288] David G. Boulware. "Quantum field theory in Schwarzschild and Rindler spaces". In: *Phys. Rev. D* 11 (6 1975), pp. 1404–1423. DOI: 10.1103/PhysRevD.11.1404. URL: https://link.aps.org/doi/10.1103/PhysRevD.11.1404.

[289] Karl Schwarzschild. "On the gravitational field of a sphere of incompressible fluid according to Einstein's theory". In: *Sitzungsber. Preuss. Akad. Wiss. Berlin (Math. Phys.)* 1916 (1916), pp. 424–434. arXiv: physics/9912033 [physics.hist-ph].

[290] H. A. Buchdahl. "General Relativistic Fluid Spheres". In: *Phys. Rev.* 116 (4 1959), pp. 1027–1034. DOI: 10.1103/PhysRev.116.1027. URL: https://link.aps.org/doi/10.1103/PhysRev.116.1027.

[291] Vitor Cardoso et al. "Light rings as observational evidence for event horizons: Long-lived modes, ergoregions and nonlinear instabilities of ultracompact objects". In: *Phys. Rev. D* 90 (4 2014), p. 044069. DOI: 10.1103/PhysRevD.90.044069. URL: https://link.aps.org/doi/10.1103/PhysRevD.90.044069.

[292] Guangzhou Guo et al. "Echoes from hairy black holes". In: *JHEP* 06 (2022), p. 073. DOI: 10.1007/JHEP06(2022)073. arXiv: 2204.00982 [gr-qc].

[293] Jahed Abedi, Hannah Dykaar, and Niayesh Afshordi. "Echoes from the Abyss: Tentative evidence for Planck-scale structure at black hole horizons". In: *Phys. Rev. D* 96.8 (2017), p. 082004. DOI: 10.1103/PhysRevD.96.082004. arXiv: 1612.00266 [gr-qc].

[294] Aaron Zimmerman, Richard N. George, and Yanbei Chen. "Rogue echoes from exotic compact objects". In: (June 2023). arXiv: 2306.11166 [gr-qc].

[295] Paschalis Karageorgis and John G. Stalker. "Sharp bounds on 2m/r for static spherical objects". In: *Class. Quant. Grav.* 25 (2008), p. 195021. DOI: 10.1088/0264-9381/25/19/195021. arXiv: 0707.3632 [gr-qc].

[296] Hakan Andreasson. "Sharp bounds on 2m/r of general spherically symmetric static objects". In: *J. Diff. Eq.* 245 (2008), pp. 2243–2266. DOI: 10.1016/j.jde.2008.05.010. arXiv: gr-qc/0702137.

[297] Alfredo Urbano and Hardi Veermäe. "On gravitational echoes from ultracompact exotic stars". In: *JCAP* 04 (2019), p. 011. DOI: 10.1088/1475-7516/2019/04/011. arXiv: 1810.07137 [gr-qc].

[298] Guilherme Raposo et al. "Anisotropic stars as ultracompact objects in general relativity". In: *Phys. Rev. D* 99 (10 2019), p. 104072. DOI: 10.1103/PhysRevD.99.104072. URL: https://link.aps.org/doi/10.1103/PhysRevD.99.104072.

[299] K. W. Howard and P. Candelas. "Quantum Stress Tensor in Schwarzschild Space-Time". In: *Phys. Rev. Lett.* 53 (5 1984), pp. 403–406. DOI: 10.1103/PhysRevLett.53.403. URL: https://link.aps.org/doi/10.1103/PhysRevLett.53.403.

[300] Paul R. Anderson, William A. Hiscock, and David A. Samuel. "Stress-energy tensor of quantized scalar fields in static spherically symmetric spacetimes". In: *Phys. Rev. D* 51 (8 1995), pp. 4337–4358. DOI: 10.1103/PhysRevD.51.4337. URL: https://link.aps.org/doi/10.1103/PhysRevD.51.4337.

[301] Adam Levi and Amos Ori. "Versatile Method for Renormalized Stress-Energy Computation in Black-Hole Spacetimes". In: *Phys. Rev. Lett.* 117 (23 2016), p. 231101. DOI: 10.1103/PhysRevLett.117.231101. URL: https://link.aps.org/doi/10.1103/PhysRevLett.117.231101.

[302] Peter Taylor, Cormac Breen, and Adrian Ottewill. "Mode-sum prescription for the renormalized stress energy tensor on black hole spacetimes". In: *Phys. Rev. D* 106.6 (2022), p. 065023. DOI: 10.1103/PhysRevD.106.065023. arXiv: 2201.05174 [gr-qc].

[303] Eanna E. Flanagan and Robert M. Wald. "Does back reaction enforce the averaged null energy condition in semiclassical gravity?" In: *Phys. Rev. D* 54 (1996), pp. 6233–6283. DOI: 10.1103/PhysRevD.54.6233. arXiv: gr-qc/9602052.

[304] Kip S. Thorne and Alfonso Campolattaro. *Non-Radial Pulsation of General-Relativistic Stellar Models. I. Analytic Analysis for L ¿= 2*. Sept. 1967. DOI: 10.1086/149288.

[305] Subrahmanyan Chandrasekhar and V. Ferrari. "On the non-radial oscillations of a star". In: *Proc. Roy. Soc. Lond. A* 432 (1991). Ed. by K. C. Wali, pp. 247–279. DOI: 10.1098/rspa.1991.0016.

[306] Hans-Peter Nollert. "Quasinormal modes: the characteristic 'sound' of black holes and neutron stars". In: *Classical and Quantum Gravity* 16 (1999), R159 –R216. URL: https://api.semanticscholar.org/CorpusID:123577194.

[307] Kostas D. Kokkotas and Bernd G. Schmidt. "Quasinormal modes of stars and black holes". In: *Living Rev. Rel.* 2 (1999), p. 2. DOI: 10.12942/lrr-1999-2. arXiv: gr-qc/9909058.

[308] Roman A. Konoplya et al. "Stable Schwarzschild stars as black-hole mimickers". In: *Phys. Rev. D* 100.4 (2019), p. 044027. DOI: 10.1103/PhysRevD.100.044027. arXiv: 1905.08097 [gr-qc].

[309] S. Chandrasekhar and S. Detweiler. "The Quasi-Normal Modes of the Schwarzschild Black Hole". In: *Proceedings of the Royal Society of London Series A* 344.1639 (Aug. 1975), pp. 441–452. DOI: 10.1098/rspa.1975.0112.

[310] C. Molina et al. "Gravitational signature of Schwarzschild black holes in dynamical Chern-Simons gravity". In: *Phys. Rev. D* 81 (2010), p. 124021. DOI: 10.1103/PhysRevD.81.124021. arXiv: 1004.4007 [gr-qc].

[311] Edgardo Franzin, Stefano Liberati, and Vania Vellucci. "From regular black holes to horizonless objects: quasi-normal modes, instabilities and spectroscopy". In: *JCAP* 01 (2024), p. 020. DOI: 10.1088/1475-7516/2024/01/020. arXiv: 2310.11990 [gr-qc].

[312] Vitor Cardoso and Paolo Pani. "Testing the nature of dark compact objects: a status report". In: *Living Rev. Rel.* 22.1 (2019), p. 4. DOI: 10.1007/s41114-019-0020-4. arXiv: 1904.05363 [gr-qc].

[313] Elisa Maggio, Maarten van de Meent, and Paolo Pani. "Extreme mass-ratio inspirals around a spinning horizonless compact object". In: *Phys. Rev. D* 104 (10 2021), p. 104026. DOI: 10.1103/PhysRevD.104.104026. URL: https://link.aps.org/doi/10.1103/PhysRevD.104.104026.

[314] Elisa Maggio. "Probing the Horizon of Black Holes with Gravitational Waves". In: *Lect. Notes Phys.* 1017 (2023), pp. 333–346. DOI: 10.1007/978-3-031-31520-6_9. arXiv: 2310.07368 [gr-qc].

[315] Irina Dymnikova. "Cosmological term as a source of mass". In: *Class. Quant. Grav.* 19 (2002), pp. 725–740. DOI: 10.1088/0264-9381/19/4/306. arXiv: gr-qc/0112052.

[316] Pedro V. P. Cunha, Emanuele Berti, and Carlos A. R. Herdeiro. "Light-Ring Stability for Ultracompact Objects". In: *Phys. Rev. Lett.* 119.25 (2017), p. 251102. DOI: 10.1103/PhysRevLett.119.251102. arXiv: 1708.04211 [gr-qc].

[317] Francesco Di Filippo. "On the nature of inner light-rings". In: (Apr. 2024). arXiv: 2404.07357 [gr-qc].

[318] Guangzhou Guo et al. "Echoes from hairy black holes". In: *JHEP* 06 (2022), p. 073. DOI: 10.1007/JHEP06(2022)073. arXiv: 2204.00982 [gr-qc].

[319] W. H. Press. "On gravitational conductors, waveguides, and circuits." In: *General Relativity and Gravitation* 11.2 (Oct. 1979), pp. 105–109. DOI: 10.1007/BF00756582.

[320] Fabio S. Bemfica, Marcelo M. Disconzi, and Jorge Noronha. "First-Order General-Relativistic Viscous Fluid Dynamics". In: *Phys. Rev. X* 12.2 (2022), p. 021044. DOI: 10.1103/PhysRevX.12.021044. arXiv: 2009.11388 [gr-qc].

[321] Bernard J. Carr. "The Primordial black hole mass spectrum". In: *Astrophys. J.* 201 (1975), pp. 1–19. DOI: 10.1086/153853.

[322] Alexandre Arbey. "Primordial black holes, a small review". In: *58th Rencontres de Moriond on Very High Energy Phenomena in the Universe*. May 2024. arXiv: 2405.08624 [gr-qc].

[323] Giacomo Cacciapaglia, Stefan Hohenegger, and Francesco Sannino. "Measuring Hawking Radiation from Black Hole Morsels in Astrophysical Black Hole Mergers". In: (May 2024). arXiv: 2405.12880 [astro-ph.HE].

[324] Anuradha Gupta et al. "Possible Causes of False General Relativity Violations in Gravitational Wave Observations". In: (May 2024). arXiv: 2405.02197 [gr-qc].